EUROPEAN ORGANIZATION FOR NUCLEAR RESEARCH

CERN-PH-EP-2018–XXX
October 30, 2018

Light isovector resonances in $\pi^- p \to \pi^-\pi^-\pi^+ p$ at 190 GeV/c

The COMPASS Collaboration

Abstract

We have performed the most comprehensive resonance-model fit of $\pi^-\pi^-\pi^+$ states using the results of our previously published partial-wave analysis (PWA) of a large data set of diffractive-dissociation events from the reaction $\pi^- + p \to \pi^-\pi^-\pi^+ + p_{\text{recoil}}$ with a 190 GeV/c pion beam. The PWA results, which were obtained in 100 bins of three-pion mass, $0.5 < m_{3\pi} < 2.5\,\text{GeV}/c^2$, and simultaneously in 11 bins of the reduced four-momentum transfer squared, $0.1 < t' < 1.0\,(\text{GeV}/c)^2$, are subjected to a resonance-model fit using Breit-Wigner amplitudes to simultaneously describe a subset of 14 selected waves using 11 isovector light-meson states with $J^{PC} = 0^{-+}$, 1^{++}, 2^{++}, 2^{-+}, 4^{++}, and spin-exotic 1^{-+} quantum numbers. The model contains the well-known resonances $\pi(1800)$, $a_1(1260)$, $a_2(1320)$, $\pi_2(1670)$, $\pi_2(1880)$, and $a_4(2040)$. In addition, it includes the disputed $\pi_1(1600)$, the excited states $a_1(1640)$, $a_2(1700)$, and $\pi_2(2005)$, as well as the resonancelike $a_1(1420)$. We measure the resonance parameters mass and width of these objects by combining the information from the PWA results obtained in the 11 t' bins. We extract the relative branching fractions of the $\rho(770)\pi$ and $f_2(1270)\pi$ decays of $a_2(1320)$ and $a_4(2040)$, where the former one is measured for the first time. In a novel approach, we extract the t' dependence of the intensity of the resonances and of their phases. The t' dependence of the intensities of most resonances differs distinctly from the t' dependence of the nonresonant components. For the first time, we determine the t' dependence of the phases of the production amplitudes and confirm that the production mechanism of the Pomeron exchange is common to all resonances. We have performed extensive systematic studies on the model dependence and correlations of the measured physical parameters.

PACS numbers: 11.80.Et, 13.25.Jx, 13.85.Hd, 14.40.Be
Keywords: experimental results, magnetic spectrometer; hadron spectroscopy, meson, light; CERN Lab; CERN SPS; COMPASS; beam, pi-, 190 GeV/c; pi-, hadroproduction, meson resonance; pi-, diffraction, dissociation; pi-, multiple production, (pi+ 2pi-); target, hydrogen; pi-p, inelastic scattering, exclusive reaction; pi- p –> p pi+ 2pi-; partial-wave analysis; isobar model; hadronic decay, amplitude analysis; mass spectrum, (pi+ 2pi-); spin, density matrix; momentum transfer dependence, slope; data analysis method; scalar meson, isoscalar; pseudoscalar meson, isovector; vector meson, isovector; axial-vector meson, isovector; tensor meson; f0(500); rho(770); f0(980); f2(1270); f0(1500); rho3(1690); a1(1260); a2(1320); a1(1420); pi1(1600); a1(1640); pi2(1670); a2(1700); pi(1800); pi2(1880); pi2(2005); a4(2040)

(submitted to Physical Review D)

The COMPASS Collaboration

M. Aghasyan[24], M.G. Alexeev[25], G.D. Alexeev[7], A. Amoroso[25,26], V. Andrieux[28,20], N.V. Anfimov[7], V. Anosov[7], A. Antoshkin[7], K. Augsten[7,18], W. Augustyniak[29], A. Austregesilo[15], C.D.R. Azevedo[1], B. Badełek[30], F. Balestra[25,26], M. Ball[3], J. Barth[4], R. Beck[3], Y. Bedfer[20], J. Bernhard[12,9], K. Bicker[15,9], E. R. Bielert[9], R. Birsa[24], M. Bodlak[17], P. Bordalo[11,a], F. Bradamante[23,24], A. Bressan[23,24], M. Büchele[8], V.E. Burtsev[27], W.-C. Chang[21], C. Chatterjee[6], M. Chiosso[25,26], I. Choi[28], A.G. Chumakov[27], S.-U. Chung[15,b], A. Cicuttin[24,c], M.L. Crespo[24,c], S. Dalla Torre[24], S.S. Dasgupta[6], S. Dasgupta[23,24], O.Yu. Denisov[26,#], L. Dhara[6], S.V. Donskov[19], N. Doshita[32], Ch. Dreisbach[15], W. Dünnweber[d], R.R. Dusaev[27], M. Dziewiecki[31], A. Efremov[7], P.D. Eversheim[3], M. Faessler[d], A. Ferrero[20], M. Finger[17], M. Finger jr.[17], H. Fischer[8], C. Franco[11], N. du Fresne von Hohenesche[12,9], J.M. Friedrich[15,#], V. Frolov[7,9], E. Fuchey[20,e], F. Gautheron[2], O.P. Gavrichtchouk[7], S. Gerassimov[14,15], J. Giarra[12], I. Gnesi[25,26], M. Gorzellik[8,f], A. Grasso[25,26], A. Gridin[7], M. Grosse Perdekamp[28], B. Grube[15,#], T. Grussenmeyer[8], A. Guskov[7], F. Haas[15], D. Hahne[4], G. Hamar[24], D. von Harrach[12], R. Heitz[28], F. Herrmann[8], N. Horikawa[16,g], N. d'Hose[20], C.-Y. Hsieh[21,h], S. Huber[15], S. Ishimoto[32,i], A. Ivanov[25,26], T. Iwata[32], V. Jary[18], R. Joosten[3], P. Jörg[8], K. Juraskova[18], E. Kabuß[12], A. Kerbizi[23,24], B. Ketzer[3], G.V. Khaustov[19], Yu.A. Khokhlov[19,j], Yu. Kisselev[7], F. Klein[4], J.H. Koivuniemi[2,28], V.N. Kolosov[19], K. Kondo[32], I. Konorov[14,15], V.F. Konstantinov[19], A.M. Kotzinian[26,k], O.M. Kouznetsov[7], Z. Kral[18], M. Krämer[15], F. Krinner[15], Z.V. Kroumchtein[7,*], Y. Kulinich[28], F. Kunne[20], K. Kurek[29], R.P. Kurjata[31], I.I. Kuznetsov[27], A. Kveton[18], A.A. Lednev[19,*], E.A. Levchenko[27], M. Levillain[20], S. Levorato[24], Y.-S. Lian[21,l], J. Lichtenstadt[22], R. Longo[25,26], V.E. Lyubovitskij[27], A. Maggiora[26], A. Magnon[28], N. Makins[28], N. Makke[24,c], G.K. Mallot[9], S.A. Mamon[27], B. Marianski[29], A. Martin[23,24], J. Marzec[31], J. Matoušek[23,24,17], H. Matsuda[32], T. Matsuda[13], G.V. Meshcheryakov[7], M. Meyer[28,20], W. Meyer[2], Yu.V. Mikhailov[19], M. Mikhasenko[3], E. Mitrofanov[7], N. Mitrofanov[7], Y. Miyachi[32], A. Moretti[23], A. Nagaytsev[7], F. Nerling[12], D. Neyret[20], J. Nový[18,9], W.-D. Nowak[12], G. Nukazuka[32], A.S. Nunes[11], A.G. Olshevsky[7], I. Orlov[7], M. Ostrick[12], D. Panzieri[26,m], B. Parsamyan[25,26], S. Paul[15], J.-C. Peng[28], F. Pereira[1], M. Pešek[17], M. Pešková[17], D.V. Peshekhonov[7], N. Pierre[12,20], S. Platchkov[20], J. Pochodzalla[12], V.A. Polyakov[19], J. Pretz[4,n], M. Quaresma[11], C. Quintans[11], S. Ramos[11,a], C. Regali[8], G. Reicherz[2], C. Riedl[28], N.S. Rogacheva[7], D.I. Ryabchikov[19,15], A. Rybnikov[7], A. Rychter[31], R. Salac[18], V.D. Samoylenko[19], A. Sandacz[29], C. Santos[24], S. Sarkar[6], I.A. Savin[7], T. Sawada[21], G. Sbrizzai[23,24], P. Schiavon[23,24], T. Schlüter[d], S. Schmeing[15], H. Schmieden[4], K. Schönning[9,o], E. Seder[20], A. Selyunin[7], L. Silva[11], L. Sinha[6], S. Sirtl[8], M. Slunecka[7], J. Smolik[7], A. Srnka[5], D. Steffen[9,15], M. Stolarski[11], O. Subrt[9,18], M. Sulc[10], H. Suzuki[32,g], A. Szabelski[23,24,29] T. Szameitat[8,f], P. Sznajder[29], M. Tasevsky[7], S. Tessaro[24], F. Tessarotto[24], A. Thiel[3], J. Tomsa[17], F. Tosello[26], V. Tskhay[14], S. Uhl[15], B.I. Vasilishin[27], A. Vauth[9], J. Veloso[1], A. Vidon[20], M. Virius[18], S. Wallner[15], M. Wilfert[12], J. ter Wolbeek[8,f], K. Zaremba[31], P. Zavada[7], M. Zavertyaev[14], E. Zemlyanichkina[7], M. Ziembicki[31]

[1] University of Aveiro, Department of Physics, 3810-193 Aveiro, Portugal
[2] Universität Bochum, Institut für Experimentalphysik, 44780 Bochum, Germany[p,q]
[3] Universität Bonn, Helmholtz-Institut für Strahlen- und Kernphysik, 53115 Bonn, Germany[p]
[4] Universität Bonn, Physikalisches Institut, 53115 Bonn, Germany[p]
[5] Institute of Scientific Instruments, AS CR, 61264 Brno, Czech Republic[r]
[6] Matrivani Institute of Experimental Research & Education, Calcutta-700 030, India[s]
[7] Joint Institute for Nuclear Research, 141980 Dubna, Moscow region, Russia
[8] Universität Freiburg, Physikalisches Institut, 79104 Freiburg, Germany[p,q]
[9] CERN, 1211 Geneva 23, Switzerland

[10] Technical University in Liberec, 46117 Liberec, Czech Republic[r]
[11] LIP, 1000-149 Lisbon, Portugal[t]
[12] Universität Mainz, Institut für Kernphysik, 55099 Mainz, Germany[p]
[13] University of Miyazaki, Miyazaki 889-2192, Japan[u]
[14] Lebedev Physical Institute, 119991 Moscow, Russia
[15] Technische Universität München, Physik-Department, 85748 Garching, Germany[p,d]
[16] Nagoya University, 464 Nagoya, Japan[u]
[17] Charles University in Prague, Faculty of Mathematics and Physics, 18000 Prague, Czech Republic[r]
[18] Czech Technical University in Prague, 16636 Prague, Czech Republic[r]
[19] NRC "Kurchatov Institute", IHEP, 142281 Protvino, Russia
[20] IRFU, CEA, Université Paris-Saclay, 91191 Gif-sur-Yvette, France[q]
[21] Academia Sinica, Institute of Physics, Taipei 11529, Taiwan[v]
[22] Tel Aviv University, School of Physics and Astronomy, 69978 Tel Aviv, Israel[w]
[23] University of Trieste, Department of Physics, 34127 Trieste, Italy
[24] Trieste Section of INFN, 34127 Trieste, Italy
[25] University of Turin, Department of Physics, 10125 Turin, Italy
[26] Torino Section of INFN, 10125 Turin, Italy
[27] Tomsk Polytechnic University, 634050 Tomsk, Russia[x]
[28] University of Illinois at Urbana-Champaign, Department of Physics, Urbana, Illinois 61801-3080, USA[y]
[29] National Centre for Nuclear Research, 00-681 Warsaw, Poland[z]
[30] University of Warsaw, Faculty of Physics, 02-093 Warsaw, Poland[z]
[31] Warsaw University of Technology, Institute of Radioelectronics, 00-665 Warsaw, Poland[z]
[32] Yamagata University, Yamagata 992-8510, Japan[u]

[#]Corresponding authors
[*]Deceased
[a] Also at Instituto Superior Técnico, Universidade de Lisboa, Lisbon, Portugal
[b] Also at Department of Physics, Pusan National University, Busan 609-735, Republic of Korea and at Physics Dept., Brookhaven National Laboratory, Upton, NY 11973, USA
[c] Also at Abdus Salam ICTP, 34151 Trieste, Italy
[d] Supported by the DFG cluster of excellence 'Origin and Structure of the Universe' (www.universe-cluster.de) (Germany)
[e] Supported by the Laboratoire d'excellence P2IO (France)
[f] Supported by the DFG Research Training Group Programmes 1102 and 2044 (Germany)
[g] Also at Chubu University, Kasugai, Aichi 487-8501, Japan[u]
[h] Also at Department of Physics, National Central University, 300 Jhongda Road, Jhongli 32001, Taiwan
[i] Also at KEK, 1-1 Oho, Tsukuba, Ibaraki 305-0801, Japan
[j] Also at Moscow Institute of Physics and Technology, Moscow Region, 141700, Russia
[k] Also at Yerevan Physics Institute, Alikhanian Br. Street, Yerevan, Armenia, 0036
[l] Also at Department of Physics, National Kaohsiung Normal University, Kaohsiung County 824, Taiwan
[m] Also at University of Eastern Piedmont, 15100 Alessandria, Italy
[n] Present address: RWTH Aachen University, III. Physikalisches Institut, 52056 Aachen, Germany
[o] Present address: Uppsala University, Box 516, 75120 Uppsala, Sweden
[p] Supported by BMBF - Bundesministerium für Bildung und Forschung (Germany)
[q] Supported by FP7, HadronPhysics3, Grant 283286 (European Union)

[r] Supported by MEYS, Grant LG13031 (Czech Republic)
[s] Supported by SAIL (CSR) and B.Sen fund (India)
[t] Supported by FCT - Fundação para a Ciência e Tecnologia, COMPETE and QREN, Grants CERN/FP 116376/2010, 123600/2011 and CERN/FIS-NUC/0017/2015 (Portugal)
[u] Supported by MEXT and JSPS, Grants 18002006, 20540299, 18540281 and 26247032, the Daiko and Yamada Foundations (Japan)
[v] Supported by the Ministry of Science and Technology (Taiwan)
[w] Supported by the Israel Academy of Sciences and Humanities (Israel)
[x] Supported by the Russian Federation program "Nauka" (Contract No. 0.1764.GZB.2017) (Russia)
[y] Supported by the National Science Foundation, Grant no. PHY-1506416 (USA)
[z] Supported by NCN, Grant 2015/18/M/ST2/00550 (Poland)

Contents

I Introduction

The excitation spectrum of bound quark-antiquark states that are composed of u, d, and s quarks, i.e., light-quark mesons, has regained interest in recent years. Excited light-quark mesons are currently studied extensively in high-flux fixed-target experiments with hadrons at CERN [1] and with photons at Jefferson Lab [2,3]. They are also produced, for example, in multibody decays of heavy-quark mesons and in e^+e^- collisions with initial-state radiation. Both processes are studied, for example, at BESIII [4], *BABAR* [5], and Belle [5]. Recently, the formulation of QCD on the lattice has gained new momentum because it now also addresses light-meson decays; see e.g., Refs. [6–9]. In the future, this will lead to more realistic predictions for masses and widths of excited hadrons. Hence obtaining more precise experimental knowledge of the properties of light mesons has become important. Despite many decades of research, the spectroscopic information coming from different experiments is sometimes inconsistent or even controversial. Extensive discussions of the light-meson sector can be found in Refs. [10–16].

Light-meson states are characterized by spin J, parity P, charge conjugation C,[a] and isospin I quantum numbers. The mesons are grouped into $\mathrm{SU}(3)_{\mathrm{flavor}}$ multiplets that contain states with the same J^P quantum numbers. In this paper, we restrict ourselves to isovector mesons with masses below about $2.1\,\mathrm{GeV}/c^2$, which decay into three charged pions and hence have negative G parity. The Particle Data Group (PDG) provides a complete listing of the known states [10]. Figure 1 shows a summary of recent measurements of masses and widths of these states grouped by their J^{PC} quantum numbers. For each resonance, the four most recent entries from the PDG are confronted with the results that will be presented in this work. For some states, the variation of the resonance parameters extracted from different experiments is by far larger than the statistical uncertainties of the individual measurements. In many cases, these variations originate from different analysis methods and model assumptions. Substantial differences among the measurements are found, for example, for the parameters of the a_1 ground state, $a_1(1260)$, and the first excited states of the a_1 and the a_2, $a_1(1640)$ and $a_2(1700)$. The situation is similar for the $\pi_1(1600)$, which has "exotic" $J^{PC} = 1^{-+}$ quantum numbers that are forbidden for ordinary $q\bar{q}'$ quark-model states in the nonrelativistic limit. The resonance interpretation of the $\pi_1(1600)$ signal is controversial, in particular in the $\rho(770)\pi$ decay mode that will be addressed in this analysis. For all states discussed here, we exploit the observed dependence of the production amplitudes on the squared four-momentum transfer in order to better separate resonant and nonresonant contributions. We also extract branching-fraction ratios for the $\rho(770)\pi$ and $f_2(1270)\pi$ decays of $a_2(1320)$ and $a_4(2040)$.

The COMPASS Collaboration has already published properties of isovector 3π resonances with masses in the range between 1.1 and $2.1\,\mathrm{GeV}/c^2$, produced in pion scattering off a solid-lead target [17,18]. In particular, we reported in Ref. [17] the observation of the spin-exotic $\pi_1(1600)$ in the $\rho(770)\pi$ decay mode. Our recent observation of a new axial-vector resonancelike structure, the $a_1(1420)$, with the same quantum numbers as the elusive $a_1(1260)$ [19] has spurred much work on the interpretation of states (including heavy-quark states), for which the assignment to quark-model multiplets is unclear; see e.g., Refs. [20–29]. The present study uses the same data but yields more accurate resonance parameters.

This work is based on the world's largest data set to date on diffractively produced mesons decaying into three charged pions. The data were obtained by the COMPASS experiment and were already presented in detail in Ref. [30]. They contain exclusive events from the inelastic

[a] Although the C parity is not defined for the charged states considered here, it is customary to quote the J^{PC} quantum numbers of the corresponding neutral partner state in the isospin triplet. The C parity can be generalized to the G parity, $G \equiv C\,e^{i\pi I_y}$, which is a multiplicative quantum number that is defined for the nonstrange states of a meson multiplet. Here, I_y is the y component of the isospin.

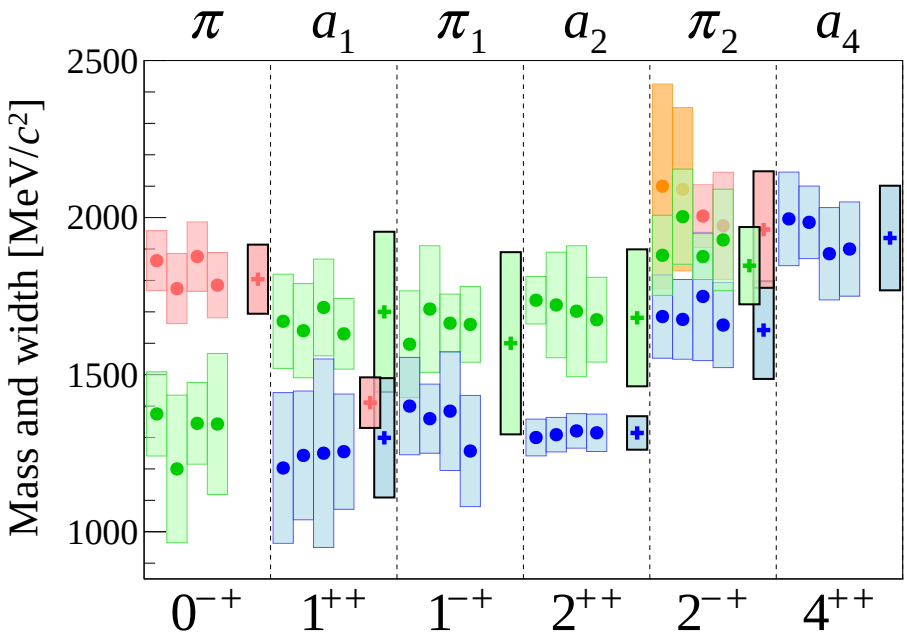

FIG. 1: Masses and widths of light isovector mesons with positive C parity and a 3π decay mode. For each resonance, the four most recent measurements of masses (circles) and widths (vertical size of boxes), as listed by the PDG [10], are compared to the masses and widths obtained in this analysis (crosses and black-framed boxes, respectively). The measurements are grouped according to the J^{PC} quantum numbers of the states. Higher excitations with the same J^{PC} are shown in different colors.

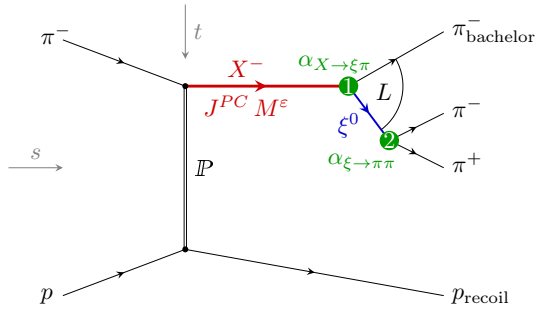

FIG. 2: Diffractive dissociation of a beam pion on a target proton into the $\pi^-\pi^-\pi^+$ final state via an intermediate 3π state X^-. The decay of X^- is described using the isobar model, which assumes that the decay proceeds via an intermediate $\pi^-\pi^+$ state ξ^0, the so-called isobar. At the two decay vertices, the couplings $\alpha_{X\to\xi\pi}$ (vertex 1) and $\alpha_{\xi\to\pi\pi}$ (vertex 2) appear, which are in general complex numbers.

reaction

$$\pi^- + p \to \pi^-\pi^-\pi^+ + p_{\text{recoil}}, \tag{1}$$

which was induced by a 190 GeV/c π^- beam impinging on a liquid-hydrogen target. The recoiling target proton is denoted by p_{recoil}. In such single-diffractive reactions, the target particle stays intact and the beam pion is excited via the exchange of a Pomeron with the target nucleon to a short-lived intermediate state X^- that then decays into $\pi^-\pi^-\pi^+$ as shown in Fig. 2.

Reaction (1) depends on two Mandelstam variables: the squared $\pi^- p$ center-of-mass energy s, which is fixed by the beam energy, and the squared four-momentum t transferred by the Pomeron.

It is convenient to define the *reduced four-momentum transfer squared*

$$t' \equiv |t| - |t|_{\min} \geq 0, \text{ where } |t|_{\min} \approx \left(\frac{m_{3\pi}^2 - m_\pi^2}{2|\vec{p}_{\text{beam}}|} \right)^2 \tag{2}$$

is the minimum absolute value of the four-momentum transfer needed to excite the beam pion to a 3π state with invariant mass $m_{3\pi}$. The beam momentum $\vec{p}_{\text{beam}}$ is defined in the laboratory frame. The analysis is limited to the kinematic range $0.1 < t' < 1.0\,(\text{GeV}/c)^2$. Typical values of $|t|_{\min}$ are well below $10^{-3}\,(\text{GeV}/c)^2$ for the 3π mass range from 0.5 to $2.5\,\text{GeV}/c^2$ considered in this analysis.

Since reaction (1) is dominated by Pomeron exchange,[b] isospin and G parity of the beam pion are conserved so that the quantum numbers of the intermediate state X^- are restricted[c] to $I^G = 1^-$. This limits the analysis to meson states that belong to the π_J and a_J families.[d] The X^- decay is assumed to proceed independently of the X^- production; i.e., the amplitude for the process factorizes into production and decay amplitudes.

In our previous publication [30], the data were subjected to a partial-wave analysis (PWA) of the outgoing 3π system. The employed PWA model relies on the isobar model, which describes the $X^- \to \pi^-\pi^-\pi^+$ decay as a sequence of two two-body decays, $X^- \to \xi^0\pi^-$ and $\xi^0 \to \pi^-\pi^+$ via intermediate $\pi^-\pi^+$ states ξ^0, the so-called *isobars* (see Fig. 2). Each isobar is characterized by its $I^G\,J^{PC}$ quantum numbers and an assumed dependence of its decay amplitude on the $\pi^-\pi^+$ invariant mass $m_{\pi^-\pi^+}$, which in the simplest case is a Breit-Wigner amplitude representing a $\pi\pi$ resonance.

The PWA model used in Ref. [30] assumed that the data are a mixture of interfering contributions of various partial waves that are defined by the quantum numbers of the X^- and their decay modes. This set of partial waves included six different isobars, and we allowed for total spins $0 \leq J \leq 6$ and orbital angular momenta $0 \leq L \leq 6$ between the isobars and the bachelor π^-. Independent fits of the set of partial-wave amplitudes to the data were carried out in 1100 $(m_{3\pi}, t')$ bins without applying model assumptions about the resonance content of the 3π system. We refer to this first step that was performed prior to the present analysis as *mass-independent analysis*. The results of a PWA fit in a given $(m_{3\pi}, t')$ bin were represented in terms of a spin-density matrix that contains all information about the partial-wave amplitudes and their mutual interferences that can be extracted from the data. This mass-independent analysis is a prerequisite to searching for 3π resonances produced in reaction (1), which can be identified only if we combine the information contained in the spin-density matrices over a wide range of $m_{3\pi}$.

In this paper, the results of the mass-independent analysis from Ref. [30] are used as input for a resonance-model fit, which is also referred to as *mass-dependent fit*. In this second analysis step, we search for 3π resonances that contribute to the intermediate X^- states by modeling the $m_{3\pi}$ dependence of the earlier extracted spin-density matrices over a wide range of $m_{3\pi}$. Resonances appear as characteristic structures in the $m_{3\pi}$ dependence not only of the moduli squared of the partial-wave amplitudes, i.e., in the *partial-wave intensities*, but also of the mutual interference terms of the partial waves. In addition to the product of the moduli of the partial-wave amplitudes, an interference term contains information about the relative phase between a pair of waves. The change of a relative phase with increasing $m_{3\pi}$ is called *phase motion*. The fit model assumes that the partial-wave amplitudes can be described by a coherent sum of Breit-Wigner amplitudes representing the resonances and amplitudes that describe nonresonant components. In a novel

[b] The Pomeron is a quasiparticle with vacuum quantum numbers and therefore has $I^G = 0^+$.

[c] We do not consider flavor-exotic states with isospin 2.

[d] Note that due to parity conservation, a_0 states cannot decay into $\pi^-\pi^-\pi^+$.

approach, we extend this analysis technique that was used in most of the previous analyses (see e.g., Refs. [17, 31–34]) by including for the first time to our knowledge the information on the dependence of the partial-wave amplitudes on t' in the fit. By requiring that the shape parameters of the resonances are independent of t', a better separation of the resonant and nonresonant components is achieved, which is a substantial improvement over previous analyses.

Most of the details on the event selection and the mass-independent analysis have already been presented in our previous publication [30]. Therefore, we give in Sec. II only a brief summary of the basic features of the experimental setup and the event selection. Section III contains a discussion of those details of the mass-independent analysis from Ref. [30] that are relevant for the resonance-model fit. In Sec. IV, we explain the fit model and the employed fitting method. Because of the large number of events, statistical uncertainties of the extracted resonance parameters are negligible compared to systematic uncertainties. Hence we performed extensive systematic studies, which are described in Sec. V. The results of the resonance-model fit are presented and discussed in Sec. VI grouped by the J^{PC} quantum numbers of the resonances. This includes a comparison of the obtained resonance parameters with world data and a discussion of the extracted t' spectra of the resonant and nonresonant components. The t' dependence of the relative phases of the wave components is discussed in Sec. VII. In Sec. VIII, we summarize our findings. The appendixes contain the details about an alternative description of the nonresonant contributions, about alternative formulations of the χ^2 function that is minimized to determine the resonance parameters, and about the systematic uncertainties of the extracted resonance parameters. The supplemental material in Secs. E and F contains the amplitude data that enter in the resonance-model fit, the full fit result, and additional information required to perform the resonance-model fit. The data required to perform the resonance-model fit are provided in computer-readable format at [35].

II Experimental setup and event selection

The experimental setup and the data selection criteria are described in detail in Refs. [30, 36]. Here, we give only a brief summary.

The COMPASS experiment [1, 37] is located at the M2 beam line of the CERN Super Proton Synchrotron. The data used for the analysis presented in this paper were recorded in the year 2008. A beam of negatively charged hadrons with 190 GeV/c momentum and 96.8 % π^- content was incident on a 40 cm long liquid-hydrogen target that was surrounded by a recoil-proton detector (RPD). Incoming pions were identified using a pair of beam Cherenkov detectors (CEDARs) that were placed in the beam line upstream of the target. Outgoing charged particles were detected by the tracking system, and their momenta were determined using two large-aperture dipole magnets. The large-acceptance high-precision two-stage magnetic spectrometer was well suited for investigating high-energy reactions at low to intermediate values of the reduced four-momentum transfer squared t'. For the present analysis, t' was chosen to be in the range from 0.1 to 1.0 $(\text{GeV}/c)^2$, where the lower bound is dictated by the acceptance of the RPD and the upper bound by the decrease of the number of events with increasing t'.

Data were recorded using a trigger based on a recoil-proton signal in the RPD in coincidence with an incoming beam particle and no signal in the veto counters (see Sec. II B in Ref. [30]). In the analysis, we require a production vertex located within the target volume. This vertex must have one incoming beam pion and three outgoing charged particles. The sum of the energies of the outgoing particles, E_{sum}, is required to be equal to the average beam energy within 2 standard deviations $\sigma_{E_{\text{sum}}}$, i.e., within ± 3.78 GeV. Contributions from double-diffractive processes, in which also the target proton is excited, are suppressed by the RPD and veto trigger signals and by

requiring exactly one recoil particle detected in the RPD that is back-to-back with the outgoing $\pi^-\pi^-\pi^+$ system in the plane transverse to the beam (transverse momentum balance; see Sec. II C in Ref. [30]). Events are disregarded if the incoming beam particle is identified by the CEDARs as a kaon. If at least one of the three forward-going particles is identified by the ring-imaging Cherenkov detector (RICH) as not being a pion, the event is also rejected. In addition, we require Feynman-x of the fastest final-state π^- to be below 0.9 for rapidity differences between the fast π^- and the slower $\pi^-\pi^+$ pair in the range from 2.7 to 4.5. This suppresses the small contamination by centrally produced $\pi^-\pi^+$ final states in the analyzed mass range (see Sec. II C in Ref. [30]). The selected kinematic region of $0.5 < m_{3\pi} < 2.5\,\text{GeV}/c^2$ and $0.1 < t' < 1.0\,(\text{GeV}/c)^2$ contains a total of 46×10^6 exclusive events that enter into the partial-wave analysis (see Sec. III).

III Partial-wave decomposition

We use a two-step procedure for the determination of the spectrum of 3π resonances produced in the reaction $\pi^- + p \to \pi^-\pi^-\pi^+ + p_\text{recoil}$. In the first analysis step published in Ref. [30], a partial-wave decomposition was performed independently in 100 $m_{3\pi}$ bins each divided into 11 t' bins, which serves as input for the resonance-model fit presented in this paper. The PWA method and the results are discussed in detail in Ref. [30]. Here, we summarize the facts relevant for the resonance-model fit, which is introduced in Sec. IV.

Our basic assumption for the PWA model is that resonances dominate the 3π intermediate states X^- that are produced in the scattering process. We therefore describe the process as an inelastic two-body scattering reaction $\pi^- + p \to X^- + p_\text{recoil}$ with subsequent decay of X^- into the three final-state pions, $X^- \to \pi^-\pi^-\pi^+$.

For fixed center-of-mass energy $\sqrt{s}$, the kinematic distribution of the final-state particles depends on $m_{3\pi}$, t', and a set of five additional phase-space variables represented by τ. The latter fully describes the three-body decay. The set of variables used in our analysis is defined in Sec. III A of Ref. [30]. For the reaction $\pi^- + p \to \pi^-\pi^-\pi^+ + p_\text{recoil}$, a perfect detector with unit acceptance would measure the intensity distribution

$$\mathcal{I}(m_{3\pi}, t', \tau) \equiv \frac{\mathrm{d}N}{\mathrm{d}m_{3\pi}\,\mathrm{d}t'\,\mathrm{d}\varphi_3(m_{3\pi},\tau)} \propto \frac{\mathrm{d}\sigma_{\pi^-+p\to\pi^-\pi^-\pi^++p_\text{recoil}}}{\mathrm{d}m_{3\pi}\,\mathrm{d}t'\,\mathrm{d}\varphi_3(m_{3\pi},\tau)} \propto m_{3\pi}\left|\mathcal{M}_{fi}(m_{3\pi}, t', \tau)\right|^2, \quad (3)$$

where N is the number of events, $\mathrm{d}\varphi_3$ the five-dimensional differential Lorentz-invariant three-body phase-space element of the three outgoing pions, $\mathrm{d}\sigma_{\pi^-+p\to\pi^-\pi^-\pi^++p_\text{recoil}}$ the differential cross section for the measured process, and $\mathcal{M}_{fi}$ the transition matrix element from the initial to the final state.[e] The right-hand side of Eq. (3) is derived from Fermi's golden rule as given e.g., in Ref. [38]. We factorize the phase space of the four outgoing particles into the two-body phase space for X^- and p_recoil and the three-body phase space for the decay $X^- \to \pi^-\pi^-\pi^+$, which introduces the factor $m_{3\pi}$. The differential two-body phase space element is expressed in terms of t'. All constant factors have been dropped from the right-hand side of Eq. (3). It is worth noting that, since $\mathcal{I}$ is differential in the three-body phase-space element, it is independent of the particular choice of the variables τ.[f]

[e] To simplify notation, the term $|\mathcal{M}_{fi}|^2$ is assumed to include incoherent sums, e.g., over the helicities of the particles with nonzero spin [see Eq. (5)].

[f] The simplest parametrization of the differential three-body phase-space element is in terms of the energies of two of the final-state particles, e.g., E_1 and E_3, and the Euler angles (α, β, γ) that define the spatial orientation of the plane that is formed by the daughter particles in the X^- rest frame:

$$\mathrm{d}\varphi_3(m_{3\pi}, \underbrace{E_1, E_3, \alpha, \beta, \gamma}_{\equiv\tau}) \propto \mathrm{d}E_1\,\mathrm{d}E_3\,\mathrm{d}\alpha\,\mathrm{d}\cos\beta\,\mathrm{d}\gamma$$

For different choices of τ, the respective Jacobians have to be taken into account.

Since we assume that the 3π intermediate state is dominated by resonances, the production of X^- can be treated independently of its decay (see Fig. 2). The amplitude for a particular intermediate state X^- therefore factorizes into two terms: (i) the *transition amplitude* $\mathcal{T}(m_{3\pi}, t')$, which encodes the $m_{3\pi}$-dependent strength and phase of the production of a state X^- with specific quantum numbers, and (ii) the *decay amplitude* $\Psi(m_{3\pi}, \tau)$, which describes the decay of X^- into a particular $\pi^-\pi^-\pi^+$ final state.

As demonstrated in Ref. [30], we observe dominant contributions of resonances in the $\pi^-\pi^+$ subsystem of the $\pi^-\pi^-\pi^+$ final state. Therefore, we factorize the three-body decay amplitude into two two-body decay terms (see Fig. 2). This factorization is known as the *isobar model*[g] and the intermediate neutral $\pi^-\pi^+$ state ξ^0 is called the *isobar*. In the first two-body decay, $X^- \to \xi^0\pi^-$, a relative orbital angular momentum L appears. The orbital angular momentum in the isobar decay $\xi^0 \to \pi^-\pi^+$ is equal to the spin of the isobar. For a given three-pion mass, the decay amplitude accounts for the deviation of the kinematic distribution of the three outgoing pions from the isotropic phase-space distribution and is specified by the quantum numbers of X^- (isospin I, G parity, spin J, parity P, C parity, and the spin projection M) and its decay mode (ξ, L). For convenience, we introduce the partial-wave index

$$a \equiv (I^G, J^{PC}, M, \xi, L). \tag{4}$$

We describe the decay $X^- \to \xi^0\pi^-$ in the Gottfried-Jackson rest frame of the X^- (see Sec. III A in Ref. [30]), where the quantization axis is chosen along the beam direction, and we employ the *reflectivity basis*, where positive and negative values of the spin projection M are combined to yield amplitudes characterized by $M \geq 0$ and by the reflectivity quantum number $\varepsilon = \pm 1$ [40]. The reflectivity ε is the eigenvalue of the reflection through the X^- production plane. In the high-energy limit, ε corresponds to the naturality of the exchange in the scattering process such that $\varepsilon = +1$ corresponds to natural spin parity of the exchanged Reggeon, i.e., $J^P = (\text{odd})^-$ or $(\text{even})^+$ transfer to the beam particle. Conversely, $\varepsilon = -1$ corresponds to unnatural spin parity of the exchanged Reggeon, i.e., $J^P = (\text{even})^-$ or $(\text{odd})^+$ transfer to the beam particle.

The isobar-model decay amplitudes are calculable using the helicity formalism up to the unknown complex-valued couplings $\alpha_{X\to\xi\pi}$ and $\alpha_{\xi\to\pi\pi}$, which appear at each decay vertex (see Fig. 2). Assuming that these couplings do not depend on the kinematics, they are moved from the decay amplitudes into the transition amplitudes. The transition and decay amplitudes redefined in this way are represented by $\overline{\mathcal{T}}_a(m_{3\pi}, t')$ and $\overline{\Psi}_a(m_{3\pi}, \tau)$. It is worth noting that due to this redefinition, the transition amplitudes $\overline{\mathcal{T}}_a$ depend not only on the X^- quantum numbers but also on the X^- decay mode. Details are explained in Sec. III B of Ref. [30].

We model the intensity distribution $\mathcal{I}(m_{3\pi}, t', \tau)$ of the final-state particles in Eq. (3) as a truncated series of partial waves, which are denoted by the index a as defined in Eq. (4). The $N^{\varepsilon}_{\text{waves}}$ partial-wave amplitudes for the contributing intermediate X^- states and their decays are summed coherently:

$$\mathcal{I}(m_{3\pi}, t', \tau) = \sum_{\varepsilon=\pm1} \sum_{r=1}^{N^{\varepsilon}_r} \left| \sum_{a}^{N^{\varepsilon}_{\text{waves}}} \overline{\mathcal{T}}^{r\varepsilon}_a(m_{3\pi}, t')\, \overline{\Psi}^{\varepsilon}_a(m_{3\pi}, \tau) \right|^2 + \overline{\mathcal{T}}^2_{\text{flat}}(m_{3\pi}, t'). \tag{5}$$

In the above formula,[h] the contributions to the intensity distribution corresponding to reflectivity ε and *rank index* r (see next paragraph) are summed incoherently. The former is due to parity conservation that forbids interference of states with different reflectivities [40]. We also introduced

[g] An early detailed discussion can be found in Ref. [39].

[h] Equation (5) corresponds to Eq. (17) in Ref. [30]. The explicit factor $m_{3\pi}$ that appears on the right-hand side of Eq. (3) is absorbed into $\overline{\mathcal{T}}^{r\varepsilon}_a(m_{3\pi}, t')$.

Table 1: Borders of the 11 nonequidistant t' bins, in which the partial-wave analysis is performed. The intervals are chosen such that each bin contains approximately 4.6×10^6 events. Only the last range from 0.449 to 1.000 $(\mathrm{GeV}/c)^2$ is subdivided further into two bins.

Bin	1	2	3	4	5	6	
t' $[(\mathrm{GeV}/c)^2]$	0.100	0.113	0.127	0.144	0.164	0.189	0.220

Bin	7	8	9	10	11	
t' $[(\mathrm{GeV}/c)^2]$	0.220	0.262	0.326	0.449	0.724	1.000

an additional incoherently added wave that is isotropic in the three-body phase space and is referred to as *flat wave*. The purpose of this wave is to absorb intensity of events with three uncorrelated pions in the final state, e.g., nonexclusive background. The corresponding transition amplitude $\overline{\mathcal{T}}_{\mathrm{flat}}$ is real-valued.[i]

Several processes, e.g., spin-flip and spin-nonflip processes or the excitation of baryon resonances at the target vertex, may disturb the coherence of the intermediate states. Incoherence may also be introduced by integrating over large ranges of t', if intermediate states are produced with different dependences on t'. Incoherences are incorporated by the additional rank index r for the transition amplitudes, which is summed over incoherently [see Eq. (5)]. In general, the *rank* N_r may be different in the two reflectivity sectors, i.e., N_r^ε.

The goal of the partial-wave analysis is to extract the unknown transition amplitudes in Eq. (5) from the data. The $\overline{\mathcal{T}}_a^{r\varepsilon}$ contain information about the intermediate 3π resonances. Since the $m_{3\pi}$ dependence of the transition amplitudes is unknown, the event sample is divided into $m_{3\pi}$ bins that are chosen to be much narrower than the width of typical hadronic resonances. The analyzed mass range $0.5 < m_{3\pi} < 2.5\,\mathrm{GeV}/c^2$ is subdivided into 100 equidistant $m_{3\pi}$ bins with a width of $20\,\mathrm{MeV}/c^2$. Within each mass bin, the $m_{3\pi}$ dependence of the amplitudes is assumed to be negligible, so that the transition amplitudes only depend on t'.

We do not know *a priori* the t' dependence of the transition amplitudes. In previous analyses, it was often assumed that the $m_{3\pi}$ and t' dependences are uncorrelated and the t' dependence was modeled by real functions $g_a^\varepsilon(t')$. These functions were extracted from the analyzed data sample by integrating over wide $m_{3\pi}$ ranges, often only for groups of waves. We have shown in Ref. [30] that for the process under study this assumption is not valid. The t' dependence of the intensity of individual waves depends on $m_{3\pi}$ and may differ significantly from wave to wave. This agrees with previous studies of diffractive dissociation of pions (see e.g., Refs. [17, 31, 41, 42]), which revealed contributions of nonresonant background processes such as the Deck effect [43]. The nonresonant processes typically exhibit $m_{3\pi}$ and t' dependences that are different from those of resonances. In particular, the analyses presented in Refs. [31, 41] showed the importance of the kinematic variable t' in a partial-wave analysis of the diffractively produced 3π system and illustrated the power of accounting for the different t' dependences of the reaction mechanisms and also of the different resonances. Therefore, for each $m_{3\pi}$ bin the partial-wave decomposition was performed independently in 11 nonequidistant t' slices of the analyzed range $0.1 < t' < 1.0\,(\mathrm{GeV}/c)^2$ as listed in Table 1. Within each t' bin, we assumed the transition amplitudes to be independent of t'. In this work, we further develop this approach to better disentangle resonant and nonresonant components (see Secs. IV and VII).

In order to simplify notation, we consider the intensity in Eq. (5) in a particular $(m_{3\pi}, t')$ bin. Within this kinematic bin, $m_{3\pi}$ and t' are considered to be constant, and hence $\mathcal{I}$ is only a

[i] The decay amplitude $\overline{\Psi}_{\mathrm{flat}}(m_{3\pi}, \tau)$ of the flat wave is a constant and was set to unity.

function of the set τ of phase-space variables.

In the resonance-model fit, special care has to be taken about the normalization of the transition amplitudes. A consistent normalization that makes the transition amplitudes comparable across different experiments is achieved by normalizing the decay amplitudes to the integrals I^{ε}_{aa}, which are the diagonal elements of the integral matrix

$$I^{\varepsilon}_{ab}(m_{3\pi}) \equiv \int \mathrm{d}\varphi_3(\tau; m_{3\pi})\, \overline{\Psi}^{\varepsilon}_{a}(\tau; m_{3\pi})\, \overline{\Psi}^{\varepsilon\,*}_{b}(\tau; m_{3\pi}), \tag{6}$$

where a and b are wave indices as defined in Eq. (4). We define[j]

$$\Psi^{\varepsilon}_{a}(\tau; m_{3\pi}) \equiv \frac{\overline{\Psi}^{\varepsilon}_{a}(\tau; m_{3\pi})}{\sqrt{I^{\varepsilon}_{aa}(m_{3\pi})}}. \tag{9}$$

The normalization of the transition amplitudes is determined by the expression for the number of events N_{pred} predicted for the $(m_{3\pi}, t')$ bin by the model in Eq. (5):

$$N_{\mathrm{pred}}(m_{3\pi}, t') = \int \mathrm{d}\varphi_3(\tau; m_{3\pi})\, \mathcal{I}(\tau; m_{3\pi}, t'). \tag{10}$$

Based on Eq. (9), the transition amplitudes are redefined according to[k]

$$\mathcal{T}^{r\varepsilon}_{a}(m_{3\pi}, t') \equiv \overline{\mathcal{T}}^{r\varepsilon}_{a}(m_{3\pi}, t')\, \sqrt{I^{\varepsilon}_{aa}(m_{3\pi})}, \tag{12}$$

so that $\mathcal{I}$ remains unchanged. Using the fact that the decay amplitudes Ψ^{ε}_{a} are normalized via Eqs. (7) and (9), Eq. (10) reads

$$N_{\mathrm{pred}} = \sum_{\varepsilon=\pm1} \left\{ \sum_{a}^{N^{\varepsilon}_{\mathrm{waves}}} \sum_{r=1}^{N^{\varepsilon}_{r}} \left|\mathcal{T}^{r\varepsilon}_{a}\right|^2 + 2 \sum_{a<b}^{N^{\varepsilon}_{\mathrm{waves}}} \mathrm{Re}\left[\sum_{r=1}^{N^{\varepsilon}_{r}} \mathcal{T}^{r\varepsilon}_{a}\, \mathcal{T}^{r\varepsilon\,*}_{b} \frac{I^{\varepsilon}_{ab}}{\sqrt{I^{\varepsilon}_{aa}}\,\sqrt{I^{\varepsilon}_{bb}}} \right] \right\} + \mathcal{T}^{2}_{\mathrm{flat}}. \tag{13}$$

We introduce the *spin-density matrix* for the $(m_{3\pi}, t')$ bin,

$$\varrho^{\varepsilon}_{ab}(m_{3\pi}, t') \equiv \sum_{r=1}^{N^{\varepsilon}_{r}} \mathcal{T}^{r\varepsilon}_{a}(m_{3\pi}, t')\, \mathcal{T}^{r\varepsilon\,*}_{b}(m_{3\pi}, t'), \tag{14}$$

which represents the full information that can be obtained about the X^- states. The parameter N^{ε}_{r} is the *rank* of the spin-density matrix. With the above, Eq. (13) simplifies to

$$N_{\mathrm{pred}} = \sum_{\varepsilon=\pm1} \left\{ \underbrace{\sum_{a}^{N^{\varepsilon}_{\mathrm{waves}}} \varrho^{\varepsilon}_{aa}}_{\text{Intensities}} + \underbrace{\sum_{a<b}^{N^{\varepsilon}_{\mathrm{waves}}} 2\,\mathrm{Re}\left[\varrho^{\varepsilon}_{ab} \frac{I^{\varepsilon}_{ab}}{\sqrt{I^{\varepsilon}_{aa}}\,\sqrt{I^{\varepsilon}_{bb}}} \right]}_{\text{Overlaps}} \right\} + \mathcal{T}^{2}_{\mathrm{flat}}. \tag{15}$$

[j] Since the decay amplitude $\overline{\Psi}_{\mathrm{flat}}$ of the flat wave was set to unity, the corresponding normalized decay amplitude is given by

$$\Psi_{\mathrm{flat}}(\tau; m_{3\pi}) \equiv \frac{1}{\sqrt{V_{\varphi_3}(m_{3\pi})}} \tag{7}$$

with

$$V_{\varphi_3}(m_{3\pi}) \equiv \int \mathrm{d}\varphi_3(\tau; m_{3\pi}). \tag{8}$$

[k] Similarly, the transition amplitude of the flat wave is redefined based on Eq. (7):

$$\mathcal{T}_{\mathrm{flat}}(m_{3\pi}, t') \equiv \overline{\mathcal{T}}_{\mathrm{flat}}(m_{3\pi}, t')\, \sqrt{V_{\varphi_3}(m_{3\pi})}. \tag{11}$$

From this equation, we can derive an interpretation for the spin-density matrix elements. The diagonal elements $\varrho^{\varepsilon}_{aa}$ are the *partial-wave intensities*, i.e., the expected number of events in wave a.[l] The off-diagonal elements $\varrho^{\varepsilon}_{ab}$, which contain information about the relative phase between waves a and b, contribute to the so-called *overlaps*, which are the number of events originating from the interference between waves a and b.[m] Limiting the summation in Eq. (15) to a subset of partial waves yields the expected number of events in these waves including all interferences. Such sums will be denoted as *coherent sums* of partial waves in the following text.

We used an extended maximum-likelihood approach [44] to determine the unknown transition amplitudes $\mathcal{T}^{r\varepsilon}_{a}$ by fitting the model intensity $\mathcal{I}(\tau)$ of Eq. (5) to the measured τ distribution, in narrow bins of $m_{3\pi}$ and t'. The extended likelihood function for a $(m_{3\pi}, t')$ bin,[n]

$$\mathcal{L} = \underbrace{\frac{\overline{N}^{N}\, e^{-\overline{N}}}{N!}}_{\substack{\text{Poisson}\\ \text{probability}}} \prod_{i=1}^{N} \underbrace{\frac{\mathcal{I}(\tau_i)}{\overline{N}}}_{\substack{\text{Probability}\\ \text{for event } i}}, \tag{16}$$

contains a Poisson term for the actually *observed* number of events $N(m_{3\pi}, t')$ and the number of events

$$\overline{N}(m_{3\pi}, t') = \int \mathrm{d}\varphi_3(\tau; m_{3\pi})\, \eta(\tau; m_{3\pi}, t')\, \mathcal{I}(\tau; m_{3\pi}, t') \tag{17}$$

that is *expected* to be observed by the detector. Via this term, the detection efficiency $\eta(\tau; m_{3\pi}, t')$ of the experimental setup is taken into account by the PWA model. In addition, Eq. (17) together with Eqs. (7) and (9) ensures the correct normalization of the transition amplitudes according to Eqs. (11) and (12). This also fixes the normalization of the diagonal elements of the spin-density matrix in Eq. (14) to the acceptance-corrected number of events in the particular wave.

In principle, the partial-wave expansion in Eq. (5) includes an infinite number of waves. In practice, the expansion series has to be truncated. We thus have to define a *wave set* describing the data sufficiently well, without too many free parameters. We included $[\pi\pi]_S$, $\rho(770)$, $f_0(980)$, $f_2(1270)$, $f_0(1500)$, and $\rho_3(1690)$ as isobars in the fit model, where $[\pi\pi]_S$ represents a parametrization of the broad component of the $\pi\pi$ S-wave, which dominates the $m_{\pi^-\pi^+}$ spectrum from low to intermediate two-pion masses and exhibits a slow phase motion (see Fig. 10 in Ref. [30]). This selection of isobars is based on features observed in the $\pi^-\pi^+$ invariant mass spectrum (see Ref. [30]) and on analyses of previous experiments [17, 41, 42, 45–47]. Based on the six isobars, we have constructed a set of 88 partial waves, i.e., 80 waves with reflectivity $\varepsilon = +1$, seven waves with $\varepsilon = -1$, and a noninterfering flat wave representing three uncorrelated pions (see Table IX in Appendix A of Ref. [30] for a complete list). This wave set is the largest used so far in a PWA of the $\pi^-\pi^-\pi^+$ final state. It includes partial waves with spin $J \leq 6$, orbital angular momentum $L \leq 6$, and spin projection $M = 0$, 1, and 2. The wave set consists mainly of positive-reflectivity waves, which is expected due to Pomeron dominance at high energies. As discussed in Ref. [30], it was found that the ranks $N_r^{(\varepsilon=+1)} = 1$ and $N_r^{(\varepsilon=-1)} = 2$ describe the data well. In the reflectivity basis, partial waves are completely defined by the wave index a, as given in Eq. (4), and the reflectivity ε. For the remaining text, we adopt the *partial-wave notation* $J^{PC}M^{\varepsilon}[\text{isobar}]\pi L$.

The *total intensity* of all partial waves is defined as the total number of acceptance-corrected events as given by Eq. (10). The *relative intensity* of a particular partial wave, as e.g., listed in

[l] For a real experiment, this corresponds to the acceptance-corrected number of events.

[m] For constructive interference, this number is positive; for destructive interference, it is negative.

[n] For better readability, we do not explicitly write the $m_{3\pi}$ and t' dependences.

Table 2 in Sec. IV, is defined as the ratio of its intensity integral over the analyzed range $0.5 < m_{3\pi} < 2.5\,\mathrm{GeV}/c^2$ and the corresponding integral of the total intensity. Owing to interference effects between the waves, i.e., overlaps, this value is in general different from the contribution of a wave to the total intensity.[o] Hence in our fit, the relative intensities of all 88 partial waves add up to 105.3 % instead of 100 %.

As shown in Ref. [30], the waves with negative reflectivity corresponding to unnatural-parity exchange processes contribute only 2.2 % to the total intensity and do not interfere with the positive-reflectivity waves. This dominance of natural-parity exchange processes is consistent with the expected dominance of the Pomeron contribution at COMPASS energies. In this paper, we only consider a selection of positive-reflectivity partial waves.

IV Resonance-model fit

The goal of the analysis described in this paper is to extract 3π resonances contributing to the reaction $\pi^- + p \to \pi^-\pi^-\pi^+ + p_{\mathrm{recoil}}$ and to determine their quantum numbers and parameters, i.e., masses and widths. The starting point of the analysis is the spin-density matrix $\varrho_{ab}(m_{3\pi}, t')$ as defined in Eq. (14). It has been extracted from the data in the first step of the analysis by performing a partial-wave decomposition independently in 100 bins of $m_{3\pi}$ and 11 bins of t' for each $m_{3\pi}$ bin using a model with 88 waves (see Ref. [30] and Sec. III).

For the resonance extraction presented here, we select a subset of waves that exhibit resonance signals in their intensity spectra and in their phase motions. Some waves contain well-known resonances that are used as an interferometer to study the resonance content of more interesting waves, such as the spin-exotic $1^{-+}1^+\rho(770)\pi P$ wave. All selected waves have positive reflectivity. Since the spin-density submatrix of the $\varepsilon = +1$ waves was chosen to have rank 1, we will drop reflectivity and rank indices from Eq. (14) and from all formulas that will follow below. We therefore write

$$\varrho_{ab}(m_{3\pi}, t') = \mathcal{T}_a(m_{3\pi}, t')\,\mathcal{T}_b^*(m_{3\pi}, t'). \tag{18}$$

For the selected waves, the $m_{3\pi}$ and t' dependences of the corresponding elements of the spin-density submatrix in Eq. (18) are parametrized in terms of the transition amplitudes. The fit model must therefore reproduce not only the measured partial-wave intensities but also their mutual interferences. Performing the analysis on the amplitude level greatly improves the sensitivity for potential resonance signals. We employ a parametrization similar to the ones used by previous analyses (see e.g., Refs. [17, 31, 32, 34, 47, 48]). In the following, model quantities will be distinguished from the corresponding measured quantities by a hat ("$\widehat{\ }$").

We model the transition amplitudes $\mathcal{T}_a(m_{3\pi}, t')$ as the product of an amplitude $\mathcal{P}(m_{3\pi}, t')$, which accounts for the overall strength of the production of a 3π system with mass $m_{3\pi}$ at a given t' (see Sec. IV A), and a term that coherently sums over possible resonance propagators and nonresonant background contributions of the 3π system with quantum numbers defined by the wave index a [see Eq. (4)]. The model $\widehat{\mathcal{T}}_a$ for the measured transition amplitude $\mathcal{T}_a$ for wave a is

$$\widehat{\mathcal{T}}_a(m_{3\pi}, t') = \sqrt{I_{aa}(m_{3\pi})}\,\sqrt{m_{3\pi}}\,\mathcal{P}(m_{3\pi}, t') \sum_{j \,\in\, \mathbb{S}_a} \mathcal{C}_a^j(t')\,\mathcal{D}_j(m_{3\pi}, t'; \zeta_j). \tag{19}$$

Here, I_{aa} is the *decay phase-space volume* of wave a as defined in Eq. (6). This factor enters, because the partial-wave intensities $|\mathcal{T}_a|^2$ are normalized via Eq. (12) to represent the acceptance-corrected number of events in wave a. The factor $\sqrt{m_{3\pi}}$ results from the splitting of the four-body

[o] The relative intensities include effects from interference due to Bose symmetrization of the two indistinguishable final-state π^-.

phase space of the final-state particles in Eq. (3). The functions $\mathcal{D}_j(m_{3\pi}, t'; \zeta_j)$ are the *dynamical amplitudes* that represent the resonant or nonresonant wave components, which are enumerated by the index j. The coherent sum runs over the subset $\mathbb{S}_a$ of the indices of those wave components that we assume to appear in wave a. The dynamical amplitudes depend on the set ζ_j of *shape parameters*, which are e.g., the masses and widths in the case of resonance components. It should be stressed that if the same wave component $\mathcal{D}_j(m_{3\pi}, t'; \zeta_j)$ appears in several partial waves, which must have the same J^{PC} quantum numbers, it has the same values of the shape parameters ζ_j. The coefficients $\mathcal{C}_a^j(t')$ in Eq. (19) are the so-called *coupling amplitudes*. They collect the unknown parts of the model, which are the t' dependences of the production strengths and phases of the X^- and the complex-valued couplings, $\alpha_{X\to\xi\pi}$ and $\alpha_{\xi\to\pi\pi}$, which appear at the two vertices in the isobar decay chain.

Based on Eq. (19), we can formulate the model for the spin-density submatrix of the selected waves

$$\begin{aligned}\widehat{\varrho}_{ab}(m_{3\pi}, t') &= \widehat{\mathcal{T}}_a(m_{3\pi}, t')\, \widehat{\mathcal{T}}_b^*(m_{3\pi}, t') \\ &= \sqrt{I_{aa}(m_{3\pi})}\, \sqrt{I_{bb}(m_{3\pi})}\, m_{3\pi}\, \left|\mathcal{P}(m_{3\pi}, t')\right|^2 \\ &\quad \times \left[\sum_{j\,\in\,\mathbb{S}_a} \mathcal{C}_a^j(t')\, \mathcal{D}_j(m_{3\pi}, t'; \zeta_j)\right] \left[\sum_{k\,\in\,\mathbb{S}_b} \mathcal{C}_b^k(t')\, \mathcal{D}_k(m_{3\pi}, t'; \zeta_k)\right]^*,\end{aligned} \tag{20}$$

which describes the $m_{3\pi}$ and t' dependences of the measured spin-density matrix elements $\varrho_{ab}(m_{3\pi}, t')$. The free parameters to be determined by the resonance-model fit are the coupling amplitudes $\mathcal{C}_a^j(t')$ and the shape parameters ζ_j.

In Eq. (20) we extended the commonly used ansatz for the parametrization of the spin-density matrix to explicitly include the t' dependence. In particular, the coupling amplitudes $\mathcal{C}_a^j(t')$ are allowed to take different values in each t' bin. This novel approach allows us to perform for the first time a t'-resolved resonance-model fit. The t' information that was extracted in the mass-independent analysis performed in the first analysis step (see Sec. III) is exploited here to better separate the resonant and nonresonant contributions by allowing them to have different t' dependences. The resonance-model fit yields as additional results the t' dependence of the intensity and the production phases of the wave components (see Secs. IV C and VII).

Assuming factorization of production and decay of the intermediate 3π state X^-, the resonant amplitudes $\mathcal{D}_j^{\mathrm{R}}(m_{3\pi}; \zeta_j^{\mathrm{R}})$, which represent the on-shell propagators of the produced 3π resonances, should be independent of t'. This is in particular true for the corresponding shape parameters ζ_j^{R} of the resonant amplitudes, i.e., the masses and widths of the resonances. This constraint is built into the model by using the same shape parameters across all t' bins. Only the strengths and coupling phases of the resonant components, which are represented by the $\mathcal{C}_a^j(t')$, can be chosen freely by the fit for each individual t' bin. We exploit the factorization of production and decay further for the case, where a resonance appears in several partial waves, which have the same $J^{PC}\, M^{\varepsilon}$ quantum numbers. These waves represent different decay modes of the same X^- state and differ only in the isobar ξ^0 or the orbital angular momentum L. The resonant amplitude is expected to follow the same t' dependence in these partial waves. This is built into the model by fixing the t' dependence $\mathcal{C}_b^j(t')$ of a resonance j that appears in wave b to the t' dependence $\mathcal{C}_a^j(t')$ that this resonance has in wave a via

$$\mathcal{C}_b^j(t') = {}_b\mathcal{B}_a^j\, \mathcal{C}_a^j(t'). \tag{21}$$

This replaces the set of independent coupling amplitudes $\mathcal{C}_b^j(t')$ for wave b by a single t'-independent complex-valued *branching amplitude* ${}_b\mathcal{B}_a^j$ as a free fit parameter. This quantity represents the

relative strength and phase of the two decay modes of resonance j. The constraint expressed by Eq. (21) significantly reduces the number of free parameters and was also found to stabilize the fit (see Secs. V and VI).

In general, the above assumptions do not hold for the nonresonant amplitudes $\mathcal{D}_j^{\mathrm{NR}}(m_{3\pi}, t'; \zeta_j^{\mathrm{NR}})$. The shape of their $m_{3\pi}$ distribution may vary with t' and may also depend on the X^- quantum numbers and decay mode. Therefore, for each wave in the fit, a separate nonresonant component is added to the model. Although the nonresonant amplitudes may have an explicit t' dependence, the shape parameters ζ_j^{NR} are kept the same across all t' bins.

A Fit model

Ideally, the resonance model would describe the $m_{3\pi}$ dependence of the full 88×88 spin-density matrix obtained from the PWA fit in the first analysis step. However, in practice such a fit would require very large computing resources owing to the large number of free parameters. In addition, some partial waves, which mostly have small relative intensities, are affected by imperfections in the PWA model. These imperfections may cause artifacts at the stage of the mass-independent analysis that the physical model is not able to describe. Thus the resonance-model fit is commonly performed using only a selected submatrix of the spin-density matrix. For the present analysis, we selected a subset of 14 waves that are listed in Table 2 out of the 88 waves used in the partial-wave decomposition (see Table IX in Appendix A of Ref. [30]). Compared to previous analyses of the 3π final state this constitutes the so far largest wave set included in a resonance-model fit. The sum of the relative intensities (see definition in Sec. III) of the 14 waves is 56.8 %, whereas the coherent sum of these waves amounts to 57.9 %. The intensity distributions of the waves are discussed in detail in Ref. [30] with the exception of the spin-exotic $1^{-+}1^+\rho(770)\pi P$ wave. The waves contain signals of the well-known resonances $a_1(1260)$, $a_2(1320)$, $\pi_2(1670)$, $\pi(1800)$, $\pi_2(1880)$, and $a_4(2040)$, which appear as peaks in the intensity distributions of the partial waves with the corresponding quantum numbers. In addition, the set of selected waves includes a clear signal of the novel resonancelike $a_1(1420)$, which was first reported in Ref. [19], and potential signals of the less well-known or disputed states $\pi_1(1600)$, $a_1(1640)$, and $a_2(1700)$. In the development of the analysis model it was found that a third $J^{PC} = 2^{-+}$ resonance, the $\pi_2(2005)$, is required to describe the data.

1 Parametrization of the dynamical amplitudes for resonances

The selected 14 waves are described using the resonance model of Eq. (20) with six a_J-like and five π_J-like resonances. The resonances are parametrized using relativistic Breit-Wigner amplitudes [49],

$$\mathcal{D}_j^{\mathrm{R}}(m_{3\pi}; \underbrace{m_j, \Gamma_j}_{\equiv \zeta_j^{\mathrm{R}}}) = \frac{m_j\, \Gamma_j}{m_j^2 - m_{3\pi}^2 - i\, m_j\, \Gamma_{j,\mathrm{tot}}(m_{3\pi})}, \tag{22}$$

with the mass-dependent total width $\Gamma_{j,\mathrm{tot}}(m_{3\pi})$. The shape parameters to be determined by the fit are mass m_j and width Γ_j of the resonance j. For most resonances, the decay modes and relative branching fractions are not or only poorly known. In these cases, we approximate the mass-dependent width by a constant:

$$\Gamma_{j,\mathrm{tot}}(m_{3\pi}) \approx \Gamma_j. \tag{23}$$

Only for $a_1(1260)$ and $a_2(1320)$ are different parametrizations used. Due to the large width of the $a_1(1260)$, we use the Bowler parametrization [Eq. (9) in Ref. [50]] to account for the variation

of the decay phase space across the resonance width:

$$\Gamma_{a_1(1260),\mathrm{tot}}(m_{3\pi}) = \Gamma_{a_1(1260)} \frac{I_{aa}(m_{3\pi})}{I_{aa}(m_{a_1(1260)})} \frac{m_{a_1(1260)}}{m_{3\pi}} \tag{24}$$

with $a = 1^{++}0^{+}\rho(770)\pi S$. Here, I_{aa} is the decay phase-space volume of the $1^{++}0^{+}\rho(770)\pi S$ wave calculated according to Eq. (6), which takes into account the finite width of the $\rho(770)$, the angular-momentum barrier factor in the $\rho(770)$ decay, and the Bose symmetrization of the decay amplitude.

For the $a_2(1320)$, we approximate the total width by assuming that it is saturated by the two dominant decay modes, $\rho(770)\pi$ and $\eta\pi$, both in a D wave [51, 52],[p]

$$\Gamma_{a_2(1320),\mathrm{tot}}(m_{3\pi}) = \Gamma_{a_2(1320)} \frac{m_{a_2(1320)}}{m_{3\pi}} \left[(1-x) \frac{q_{\rho\pi}(m_{3\pi})}{q_{\rho\pi}(m_{a_2(1320)})} \frac{F_2^2\left(q_{\rho\pi}(m_{3\pi})\right)}{F_2^2\left(q_{\rho\pi}(m_{a_2(1320)})\right)} + x \frac{q_{\eta\pi}(m_{3\pi})}{q_{\eta\pi}(m_{a_2(1320)})} \frac{F_2^2\left(q_{\eta\pi}(m_{3\pi})\right)}{F_2^2\left(q_{\eta\pi}(m_{a_2(1320)})\right)} \right]. \tag{25}$$

In Eq. (25), we neglect the width of the $\rho(770)$ and use the quasi-two-body approximation, where $q_{\xi\pi}$ is the two-body breakup momentum in the decay $X^- \to \xi^0\pi^-$. It is given by

$$q_{\xi\pi}^2(m_{3\pi}) = \frac{\left[m_{3\pi}^2 - (m_\pi + m_\xi)^2\right]\left[m_{3\pi}^2 - (m_\pi - m_\xi)^2\right]}{4m_{3\pi}^2} \tag{26}$$

with m_ξ being the mass of the isobar ξ^0.[q] The $F_\ell(q_{\xi\pi})$ terms in Eq. (25) are the Blatt-Weisskopf angular-momentum barrier factors [53], which take into account the centrifugal-barrier effect caused by the orbital angular momentum $\ell = 2$ between the bachelor π^- and the $\rho(770)$ or the η. We use the parametrization of von Hippel and Quigg [54] as given in Sec. IV A of Ref. [30] with a range parameter of $q_R = 200\,\mathrm{MeV}/c$.[r] We approximate the relative branching fraction between both $a_2(1320)$ decay modes by setting $x = 0.2$.[s]

2 Parametrization of the dynamical amplitudes for nonresonant components

For each of the 14 selected partial waves, a separate nonresonant component is included in the fit model. We adopt a phenomenological parametrization for the nonresonant amplitude in the form of a Gaussian in the two-body breakup momentum q of the decay that was inspired by Ref. [55]. We extend this parametrization to have a more flexible threshold behavior and to include an explicit empirical t' dependence:

$$\mathcal{D}_j^{\mathrm{NR}}(m_{3\pi}, t'; \underbrace{b, c_0, c_1, c_2}_{\equiv\, \zeta_j^{\mathrm{NR}}}) = \left[\frac{m_{3\pi} - m_{\mathrm{thr}}}{m_{\mathrm{norm}}}\right]^b e^{-(c_0 + c_1 t' + c_2 t'^2)\, \tilde{q}_{\xi\pi}^2(m_{3\pi})}. \tag{27}$$

Here, b and the c_i are the free shape parameters for the nonresonant component j.[t] The parameters m_{norm} and m_{thr} are the same for all nonresonant components and are empirically

[p] We neglect the additional mass dependence of the $a_2(1320)$ width that would be induced by the $\omega\pi\pi$ and $K\overline{K}$ decay modes, which have branching fractions of $10.6 \pm 3.2\,\%$ and $4.9 \pm 0.8\,\%$, respectively [10].

[q] For the $a_2(1320)$, the lower bound of the fitted $m_{3\pi}$ range was chosen such that $q_{\rho\pi}^2 > 0$.

[r] This corresponds to an assumed strong-interaction range of 1 fm.

[s] The masses of π, η, and $\rho(770)$ in Eq. (26) are set to $m_\pi = 139\,\mathrm{MeV}/c^2$, $m_\eta = 547\,\mathrm{MeV}/c^2$, and $m_\rho = 770\,\mathrm{MeV}/c^2$.

[t] In order to simplify notation, we omit the subscript j for these parameters.

fixed to $1\,\mathrm{GeV}/c^2$ and $0.5\,\mathrm{GeV}/c^2$, respectively. The quasi-two-body breakup momentum for the decay $X^- \to \xi^0\pi^-$ is represented by $\tilde{q}_{\xi\pi}(m_{3\pi})$. However, we cannot use Eq. (26) to calculate this quantity because $q_{\xi\pi}(m_{3\pi})$ becomes imaginary for $m_{3\pi} < m_\pi + m_\xi$. We therefore construct an approximation, $\tilde{q}_{\xi\pi}(m_{3\pi})$, to the two-body breakup momentum, which is valid also below the quasi-two-body threshold and takes into account the finite width of the isobar ξ^0,[u]

$$\tilde{q}_{\xi\pi}(m_{3\pi}) \equiv q_{\xi\pi}(m_\mathrm{norm})\,\frac{I_{aa}(m_{3\pi})}{I_{aa}(m_\mathrm{norm})}\,\frac{m_{3\pi}}{m_\mathrm{norm}}. \tag{28}$$

Here, $\tilde{q}_{\xi\pi}$ is normalized such that it is equal to the value of $q_{\xi\pi}$ at $m_\mathrm{norm} = 2.4\,\mathrm{GeV}/c^2$.[v] The decay phase-space volume I_{aa} of wave a is calculated according to Eq. (6).

For partial waves with small relative intensities $\leq 2.4\,\%$, we simplify the parametrization in Eq. (27) to

$$\mathcal{D}_j^\mathrm{NR}(m_{3\pi}; b = 0, c_0, c_1 = 0, c_2 = 0) = e^{-c_0\,\tilde{q}^2_{\xi\pi}(m_{3\pi})}. \tag{29}$$

This reduces the number of free parameters and increases the fit stability. The only exception is the spin-exotic $1^{-+}1^+\rho(770)\pi P$ wave because of its dominant nonresonant contribution.

3 Parametrization of the production probability

At high energies, hadronic scattering reactions are dominated by t-channel Pomeron ($\mathbb{P}$) exchange. In earlier measurements of inclusive diffractive reactions of the type $p + p \to X^+ + p$ at the CERN ISR [56], the differential cross section $\mathrm{d}^2\sigma/\,\mathrm{d}m_X^2\,\mathrm{d}t$ was observed to fall approximately as s/m_X^2, with $\sqrt{s}$ being the center-of-mass energy of the reaction and m_X the invariant mass of the produced system X^+. This behavior is described by Regge theory [57, 58],

$$\frac{\mathrm{d}^2\sigma}{\mathrm{d}m_X^2\,\mathrm{d}t} = g^\mathbb{P}_{pp}(t)\,\sigma^\mathrm{tot}_{\mathbb{P}p}(m_X^2, t)\,\left[\frac{s}{m_X^2}\right]^{2\alpha_\mathbb{P}(t)-1}, \tag{30}$$

where $g^\mathbb{P}_{pp}$ is the t-dependent proton-proton-Pomeron coupling and $\sigma^\mathrm{tot}_{\mathbb{P}p}(m_X^2, t)$ is the total Pomeron-proton cross section. The Regge trajectory of the Pomeron is $\alpha_\mathbb{P}(t) = \alpha_0 + \alpha'\,t$, which yields the $\mathrm{d}^2\sigma/\,\mathrm{d}m_X^2\,\mathrm{d}t \propto s/m_X^2$ behavior for $\alpha_0 = 1$ and $\alpha' = 0$.

In Ref. [59], a phenomenological Regge framework was developed to describe exclusive central-production reactions of the type $p + p \to p + X^0 + p$ in terms of double-Pomeron exchange. In these calculations, the cross section is proportional to the so-called "Pomeron flux" factor

$$F_{\mathbb{P}p}(x_\mathbb{P}, t) \propto \frac{e^{-b_\mathbb{P}\,|t|}}{x_\mathbb{P}^{2\alpha_\mathbb{P}(t)-1}} \tag{31}$$

using the approximate relation $m_X^2/s \approx x_\mathbb{P}$ with $x_\mathbb{P}$ being the longitudinal proton-momentum fraction carried by the Pomeron in the center-of-mass frame of the reaction. The slope parameter of the Pomeron exchange is $b_\mathbb{P}$. Equation (31) can be interpreted as the probability for Pomeron emission by the proton, which in the limit of $\alpha_0 = 1$ and $\alpha' = 0$ is proportional to $1/x_\mathbb{P}$ and therefore similar to the probability of photon emission in the case of bremsstrahlung. Assuming

[u] We start from the ansatz that the two-body phase-space volume $\varphi_2 \propto q_{\xi\pi}/m_{3\pi}$ approximates the three-body phase-space volume I_{aa} well at large values of $m_{3\pi}$ because the effects from the finite width of the ξ^0 and from the barrier factors become negligible. For lower values of $m_{3\pi}$, these effects are taken into account by defining an "effective" two-body breakup momentum via $I_{aa} \propto \tilde{q}_{\xi\pi}/m_{3\pi}$.

[v] The value of m_norm was somewhat arbitrarily chosen to lie above the maximum of the fit range of $2.3\,\mathrm{GeV}/c^2$ (see Table 2) and low enough so that the decay phase-space volume $I_{aa}(m_\mathrm{norm})$ can be calculated reliably.

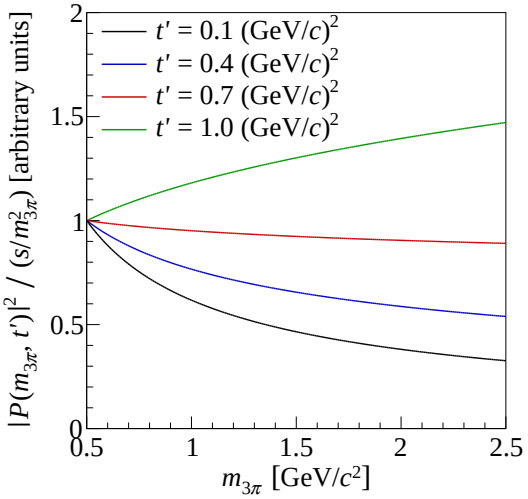

FIG. 3: Deviation of the $m_{3\pi}$ dependence of the 3π production probability $\left|\mathcal{P}(m_{3\pi}, t')\right|^2$, as given by Eq. (32), from the $s/m_{3\pi}^2$ dependence for various t' values. The curves are normalized to 1 at $m_{3\pi} = 0.5\,(\mathrm{GeV}/c)^2$.

that Eq. (31) is universal, it can be used to model various diffractive processes in terms of single-Pomeron exchange [60]. We follow this approach and have chosen the 3π production probability in Eq. (20) to be proportional to the probability of Pomeron emission by the target proton:

$$\left|\mathcal{P}(m_{3\pi}, t')\right|^2 \equiv \frac{1}{x_{\mathbb{P}}^{2\alpha_{\mathbb{P}}(t')-1}} = \left[\frac{s}{m_{3\pi}^2}\right]^{2\alpha_{\mathbb{P}}(t')-1} . \tag{32}$$

Here, $m_{3\pi}$ takes the role of m_X and we have made the approximation $t' \approx -t$ thereby neglecting $|t|_{\min}$, so that $\alpha_{\mathbb{P}}(t') = \alpha_0 - \alpha' t'$. The normalization and the explicitly t'-dependent factor $e^{-b_{\mathbb{P}}\, t'}$ in Eq. (31) are both absorbed into the coupling amplitudes $\mathcal{C}_a^2(t')$ in Eq. (20). We use a value of $\alpha_0 = 1.2$, based on an analysis of data from the H1 experiment at HERA [61], while for the shrinkage parameter we use a value of $\alpha' = 0.26\,(\mathrm{GeV}/c)^{-2}$, which was obtained from a simultaneous fit to CDF (Fermilab) and ISR (CERN) data [62].[w] Figure 3 shows the deviation of Eq. (32) from the $s/m_{3\pi}^2$ dependence in the analyzed kinematic range.

4 Discussion of the fit model

Our analysis focuses on 3π resonances with masses up to about $2\,\mathrm{GeV}/c^2$. The goal was to parametrize the data with a minimum number of resonances while at the same time covering an $m_{3\pi}$ range as large as possible. The employed $m_{3\pi}$ fit ranges are listed in Table 2. For most waves, the lower bound of the fit range is determined either by thresholds applied in the PWA (see Table IX in Appendix A of Ref. [30]) or by the phase-space opening. For some waves, the reduced phase-space volume at low $m_{3\pi}$ causes ambiguities in the solutions of the mass-independent analysis leading to unphysical structures. Such regions are excluded.[x] Seven of the 14 waves are described by the model up to masses of $2.3\,\mathrm{GeV}/c^2$. For the other waves, the model departs from the data already at lower masses. This could be due to higher-lying excited states above $2\,\mathrm{GeV}/c^2$ or due to increased nonresonant contributions. Motivations for the particular choice of the fit ranges will be discussed in more detail in Sec. VI.

[w] The result for α_0 in Ref. [61] is based on the α' value from Ref. [62]. The results of our resonance-model fit are not sensitive to the particular choice of the values for α_0 and α'.

[x] By limiting the fit ranges, 4.2 % of the summed intensities of all 14 waves are excluded from the fit.

Table 2: Fit model with 11 resonances to describe the elements of the spin-density matrix of the selected 14 partial waves from six J^{PC} sectors using Eq. (20). The relative intensities listed in the second column are evaluated as a sum over the 11 t' bins and are normalized to the total number of acceptance-corrected events [30]. The relative intensities do not include interference effects between the waves. The third column lists the resonances used to describe the waves. For most resonances, the total width is approximated by a constant [see Eq. (23)]. For the other resonances, the width parametrization is given in square brackets. The fourth column lists the parametrizations used for the nonresonant components, the last column the fit ranges (see Sec. IV B for details).

Partial wave	Relative intensity	Resonances	Nonresonant component Eq.	$m_{3\pi}$ fit range [GeV/c^2]
$0^{-+}0^+ f_0(980)\pi S$	2.4 %	$\pi(1800)$	(29)	1.20 to 2.30
$1^{++}0^+ \rho(770)\pi S$	32.7 %	$a_1(1260)$ [Eq. (24)], $a_1(1640)$	(27)	0.90 to 2.30
$1^{++}0^+ f_0(980)\pi P$	0.3 %	$a_1(1420)$	(29)	1.30 to 1.60
$1^{++}0^+ f_2(1270)\pi P$	0.4 %	$a_1(1260)$ [Eq. (24)], $a_1(1640)$	(29)	1.40 to 2.10
$1^{-+}1^+ \rho(770)\pi P$	0.8 %	$\pi_1(1600)$	(27)	0.90 to 2.00
$2^{++}1^+ \rho(770)\pi D$	7.7 %	$a_2(1320)$ [Eq. (25)], $a_2(1700)$	(27)	0.90 to 2.00
$2^{++}2^+ \rho(770)\pi D$	0.3 %		(29)	1.00 to 2.00
$2^{++}1^+ f_2(1270)\pi P$	0.5 %		(29)	1.00 to 2.00
$2^{-+}0^+ \rho(770)\pi F$	2.2 %	$\pi_2(1670)$, $\pi_2(1880)$, $\pi_2(2005)$	(27)	1.20 to 2.10
$2^{-+}0^+ f_2(1270)\pi S$	6.7 %		(27)	1.40 to 2.30
$2^{-+}1^+ f_2(1270)\pi S$	0.9 %		(29)	1.40 to 2.30
$2^{-+}0^+ f_2(1270)\pi D$	0.9 %		(29)	1.60 to 2.30
$4^{++}1^+ \rho(770)\pi G$	0.8 %	$a_4(2040)$	(29)	1.25 to 2.30
$4^{++}1^+ f_2(1270)\pi F$	0.2 %		(29)	1.40 to 2.30
Intensity sum	56.8 %			

We summarize in Table 2 the 14-wave fit model. In total, the model has 722 free real-valued parameters, to be determined by the fit: 22 resonance shape parameters, 29 shape parameters for the nonresonant components, 22 real-valued parameters for the branching amplitudes ${}_b\mathcal{B}_a^j$ [see Eq. (21)], and 649 real-valued parameters for the coupling amplitudes. The coupling amplitudes for the $a_1(1260)$ in the $1^{++}0^+\rho(770)\pi S$ wave are chosen to be real.

In the partial-wave decomposition (see Sec. III), resolution effects of the spectrometer in $m_{3\pi}$ and t' are not corrected, because the analysis is performed independently in $(m_{3\pi}, t')$ bins. Since the estimated resolution effects are small,[y] they are neglected in the resonance-model fit.

Although the fit model describes the data rather well (see Sec. VI), it has a number of potential caveats and limitations that are mainly rooted in its simplicity [63]. Breit-Wigner amplitudes are in general good approximations only for single narrow resonances. When using a constant-width parametrization [Eq. (23)], the resonance in addition has to be far above thresholds. The description of a set of resonances with the same quantum numbers as a sum of Breit-Wigner

[y] The 3π mass resolution varies between 5.4 MeV/c^2 at small $m_{3\pi}$ (in the range from 0.5 to 1.0 GeV/c^2) and 15.5 MeV/c^2 at large $m_{3\pi}$ (in the range from 2.0 to 2.5 GeV/c^2). The t' resolution as obtained from the reconstructed 3π final state ranges between 7×10^{-3} and 20×10^{-3} (GeV/c)^2 depending on the $m_{3\pi}$ and t' region. See Ref. [30] for details.

amplitudes may violate unitarity and is a good approximation only for well-separated resonances with little overlap. In particular for the $J^{PC} = 2^{-+}$ resonances, this condition is not well fulfilled. Also coupled-channel effects are not taken into account. All the above effects render the extracted Breit-Wigner parameters model and process dependent. An additional process and model dependence is introduced by the decomposition of the partial-wave amplitudes into resonant and nonresonant components, which is not unique. However, our results can be compared directly to previous analyses of diffractive three-pion production (see e.g., Ref. [17, 31, 46, 47]). The model assumption that the phase of the nonresonant amplitudes does not depend on $m_{3\pi}$ may not be well justified for cases where these amplitudes exhibit pronounced peaks in their intensity distribution. One may also remark that singularities in the scattering matrix that are not related to resonances might mimic Breit-Wigner resonances. A possible example is the $a_1(1420)$ [19], which could be the singularity of a triangle diagram [23, 26] (see also Sec. VI E).

Some of the potential issues mentioned above are expected to be mitigated by the fact that in our model most of the resonances are fitted in at least two decay modes. In addition, we combine in the fit the information of 11 t' bins while forcing the resonances to appear with the same parameters in each t' bin. By performing such a t'-resolved analysis, resonance parameters are constrained by the various production processes that may contribute with different strengths and phases to the reaction under study depending on the t' region.

Instead of Breit-Wigner parameters, one could attempt to extract the poles on the second Riemann sheet of the scattering amplitude, which correspond to resonances. The location of a resonance pole in the complex energy plane and its residue represent the universal resonance properties. However, the construction of coupled-channel models for the reaction $\pi^- + p \to \pi^-\pi^-\pi^+ + p_{\text{recoil}}$ that are consistent with the fundamental principles of unitarity and analyticity is a formidable task. In the past, quasi-two-body K-matrix approaches were applied to analyze 3π resonances in diffractive production (see e.g., Ref. [31, 45]). The extraction of resonance pole positions using an analytical model based on the principles of the relativistic S-matrix is currently under development [64, 65]. A first successful application of this model to the $\eta\pi$ D-wave extracted from COMPASS data yielded pole positions for the $a_2(1320)$ and $a_2(1700)$ [66]. In Sec. VI C 2 we compare those results to the ones from our analysis.

B Fit method

The free parameters of the model in Eq. (20), i.e., the set of coupling amplitudes $\mathcal{C}_a^j(t')$ and the set of shape parameters ζ_j of the wave components, are extracted by a fit to the spin-density matrix $\varrho_{ab}(m_{3\pi}, t')$ that was extracted in the mass-independent analysis (see Sec. III). In the resonance-model fit, the information of the Hermitian spin-density matrix is represented by a real-valued matrix $\Lambda_{ab}(m_{3\pi}, t')$ of the same dimension. The elements of this matrix are defined by the upper triangular part of ϱ_{ab}:

$$\Lambda_{ab}(m_{3\pi}, t') = \begin{cases} \text{Re}\left[\varrho_{ab}(m_{3\pi}, t')\right] & \text{for } a < b, \\ \text{Im}\left[\varrho_{ba}(m_{3\pi}, t')\right] & \text{for } a > b, \\ \varrho_{aa}(m_{3\pi}, t') = \left|\mathcal{T}_a(m_{3\pi}, t')\right|^2 & \text{for } a = b. \end{cases} \tag{33}$$

Hence the diagonal elements of $\Lambda_{ab}(m_{3\pi}, t')$ are the partial-wave intensities, the upper off-diagonal elements are the real parts of the interference terms, and the lower off-diagonal elements are the corresponding imaginary parts.

The deviation of the resonance model $\widehat{\Lambda}_{ab}$ from the matrix Λ_{ab}, which is extracted from data, is measured by summing up the squared Pearson's residuals [67] of all matrix elements for all $m_{3\pi}$

and t' bins [46]:

$$\chi^2 = \sum_{a,b}^{N_\text{waves}} \sum^{t' \text{ bins}} \sum^{(m_{3\pi} \text{ bins})_{ab}} \left[\frac{\Lambda_{ab}(m_{3\pi}, t') - \widehat{\Lambda}_{ab}(m_{3\pi}, t')}{\sigma_{ab}(m_{3\pi}, t')} \right]^2 . \tag{34}$$

Here, N_waves is the number of partial waves included in the fit model and $\sigma_{ab}(m_{3\pi}, t')$ is the statistical uncertainty of $\Lambda_{ab}(m_{3\pi}, t')$ as determined by the mass-independent analysis. The sum in Eq. (34) runs over all 11 t' bins and those $m_{3\pi}$ bins that lie within the fit ranges. The fit ranges for the intensity terms Λ_{aa} are listed in Table 2. The fit ranges for the off-diagonal interference terms Λ_{ab} are defined by the intersections of the fit ranges for the intensities of waves a and b. The values of the model parameters are determined by minimizing the χ^2 function using the MIGRAD algorithm of the MINUIT program [68].

Although we use the notation χ^2 in Eq. (34) for the quantity that is minimized in the resonance-model fit, it is important to note that the minimum of Eq. (34) does not follow a χ^2 distribution. Therefore, the expectation value of χ^2 is neither the number of degrees of freedom (n.d.f.) nor is its deviation from the n.d.f. an absolute measure for the goodness of the fit. The reason for this is that Eq. (34) does not take into account correlations among the spin-density matrix elements. Although the spin-density matrix elements from different $m_{3\pi}$ or t' bins are independent from each other, within an $(m_{3\pi}, t')$ bin, two kinds of correlations appear: (i) statistical correlations of the spin-density matrix elements and (ii) mathematical dependences caused by using a rank-1 spin-density matrix for the positive-reflectivity waves in the partial-wave decomposition (see Sec. III). The result of the mass-independent analysis in principle includes the covariance matrix of the extracted transition amplitudes $\mathcal{T}_a$. However, the propagation of this information to the covariance matrix for Λ_{ab} is not well-defined because the spin-density matrix has more free real-valued parameters than the set of transition amplitudes.[z] The rank-1 condition leads to analytical relations among the spin-density matrix elements for waves a, b, c, and d of the form

$$\varrho_{ab}\, \varrho_{cd} = \varrho_{ad}\, \varrho_{cb}. \tag{35}$$

We have performed studies using alternative formulations of χ^2 that take into account the statistical correlations and Eq. (35) (see Sec. C). For most parameters, the obtained results are similar to those obtained with Eq. (34) and the systematic effects are smaller than those from the other systematic studies (see Sec. V). Exceptions are discussed in Secs. D and VI. Given the limitations of our model in describing details of the data, the χ^2 formulation in Eq. (34) has practical advantages. The information from the 14 waves enters symmetrically; i.e., Eq. (34) does not require one to choose a reference wave as it is the case in the alternative χ^2 formulations. In addition, compared to the alternative χ^2 formulations, Eq. (34) effectively assigns more weight to the interference terms, which contain the phase information. This tends to improve the fit stability as imperfections in the description of the intensity distributions of some waves have less influence. A possible issue of neglecting the correlations of the spin-density matrix elements in Eq. (34) is that it may lead to biased estimates for the statistical uncertainties of the fit parameters. However, in our analysis this effect can be safely ignored because, due to the large data set, all uncertainties on physical parameters are dominated by systematic effects outweighing the statistical ones. For the above reasons, we use the χ^2 definition of Eq. (34) to determine the physical parameters.

The extraction of the resonance parameters using the fit model described in Sec. IV A is based on highly precise physical information obtained from the mass-independent analysis. The 722 free

[z] In each $(m_{3\pi}, t')$ bin, the resonance-model fit minimizes the distance to N^2_waves data points, which are the elements of $\Lambda_{ab}(m_{3\pi}, t')$. However, the transition amplitudes extracted in the mass-independent analysis with rank-1 spin-density matrix represent only $(2N_\text{waves} - 1)$ data points.

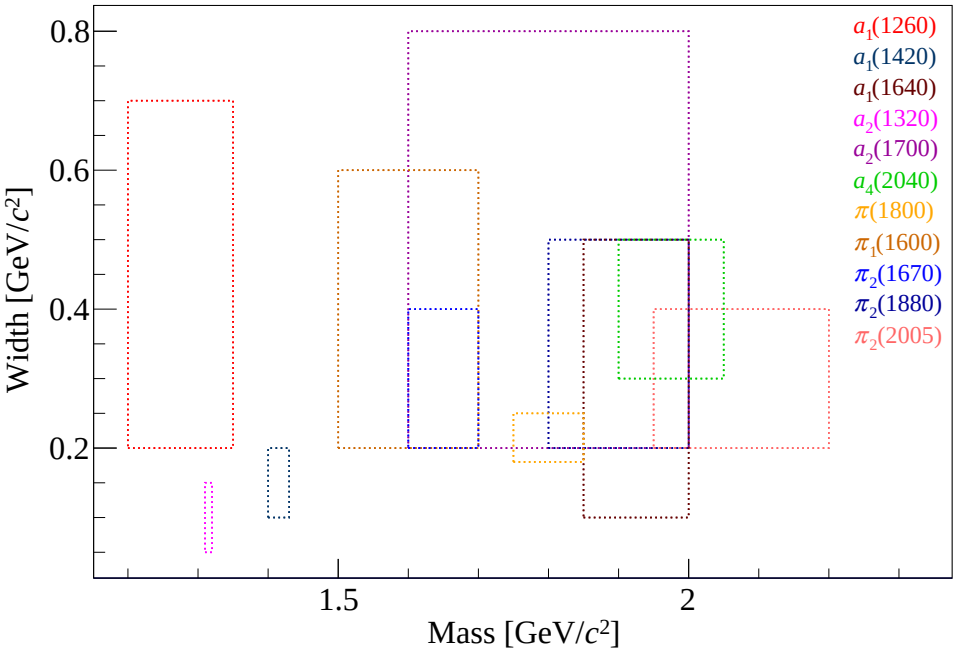

FIG. 4: The dotted boxes indicate the ranges of the uniform distributions that were used to randomly generate start values for the mass and width parameters of the resonances included in the fit model. Different colors encode different resonances.

parameters of the model are constrained by the matrix $\Lambda_{ab}(m_{3\pi}, t')$, which has 14×14 elements for each of the 100 $m_{3\pi}$ and 11 t' bins. Taking into account the chosen $m_{3\pi}$ fit ranges (see Table 2), this yields a total number of 76 505 data points that enter into the fit.

The fit model described in Sec. IV A is highly nonlinear in the shape parameters ζ_j of the wave components. Some of the model parameters are also strongly correlated. In addition, the employed parametrizations are only approximations or in the case of the nonresonant components purely empirical. Hence they often do not describe all details of our high-precision data. The resulting deviations between model and data lead to a multimodal behavior of the minimized χ^2 function. Therefore, the fit result may depend on the start values for the fit parameters. To avoid the fit being trapped in local χ^2 minima, we perform numerous fit attempts using different sets of start values for the shape parameters, which are randomly picked from uniform distributions. For the resonance parameters, conservatively wide ranges are chosen for these distributions based on previous measurements [10]. The ranges are shown as dotted rectangles in Fig. 4. For the shape parameters of the nonresonant components, we use wide uniform distributions to pick the start values as there is no prior knowledge. Details are discussed in Ref. [69]. The central values for the fit parameters are estimated by performing fits with 250 different sets of start values, which are shown as dots in Fig. 4. For the systematic studies discussed in Sec. V, we typically use 50 random sets of start values.

With the randomly chosen start values for the fit parameters, it is in general not possible to fit all 722 free parameters at once. Therefore, a multistaged approach is used, where first only a subset of the parameters is left free, while the others are kept fixed. The parameter values found in this first stage are then used as start values for the next fit stages, in which in addition some of the previously fixed parameters are freed. In the last fit stage, all 722 model parameters are left free. Since also the order, in which the parameters are released during the fit, may influence the fit result, we perform for each set of start values four different schemes of releasing the fit parameters

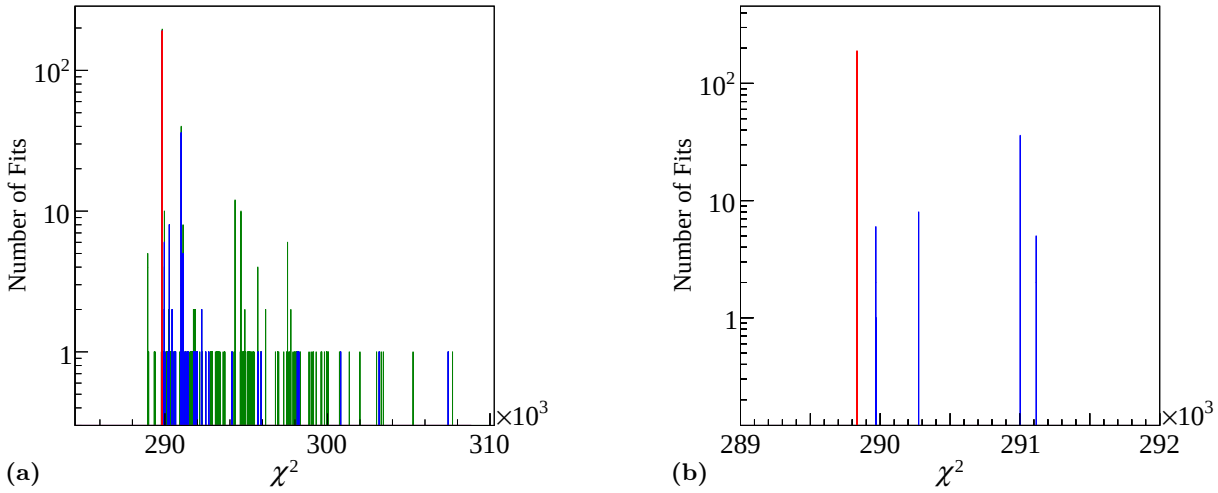

FIG. 5: (a) Distribution of the χ^2 values of the 832 fits that converged out of the 1000 fit attempts. The selected physical solution (see text) is shown in red. Additional solutions that are considered physical are shown in blue and unphysical solutions in green. (b) Corresponding distribution after removing all unphysical solutions. Note the narrower χ^2 range.

(see Ref. [69] for details). Using this procedure, the central values of the model parameters are estimated based on a total of 1000 fit attempts performed using the 250 independent randomly chosen sets of start values.

Figure 5(a) shows the frequency distribution of the χ^2 values from the 1000 fit attempts in narrow bins of 0.1 units of χ^2. We assume that fits falling into the same χ^2 bin correspond to identical solutions. In order to remove unphysical solutions from this set of solutions, we apply a series of selection criteria. Most of these criteria aim at rejecting solutions, where components of the resonance model are misused to compensate for imperfections in the model. The fit ranges listed in Table 2 were chosen such that they cover the peak regions of the resonances included in our model. Therefore, solutions are rejected if the mass value of any of the resonance components lies outside of the respective fit ranges[aa] (see Table 2). Solutions are also rejected if any of the resonance width values lie at the border of the allowed parameter range from 40 to 1000 MeV/c^2. Furthermore, solutions are rejected if a component that represents an excited resonance is misused by the fit to describe a lower-lying state and vice versa. Such solutions are clearly unphysical. For example, in some unphysical solutions the $a_1(1260)$ and $a_1(1640)$ components become wide and have nearly identical masses to better describe the dominant peak in the intensity distribution of the $1^{++}0^+\rho(770)\pi S$ wave. The above condition removes in particular all 17 solutions, which have a lower χ^2 than the selected physical solution [the latter one is shown in red in Fig. 5(a)]. In the last step, we remove solutions that are found only once.[ab] More details can be found in Refs. [69, 70].

The fit method described above is computationally expensive, but it avoids constraining the range of parameter values in the fit, while at the same time it allows us to use wide ranges for the random choice of the start values.

For 252 out of the total of 1000 fit attempts, the χ^2 minimization procedure converged and the

[aa] An exception is made for the $a_1(1260)$ component in the $1^{++}0^+ f_2(1270)\pi P$ wave.

[ab] With this step, we remove in particular solutions, where the fitting algorithm was trapped in shallow local minima. It is worth stressing that all solutions removed by this criterion have a larger χ^2 than the selected physical solution.

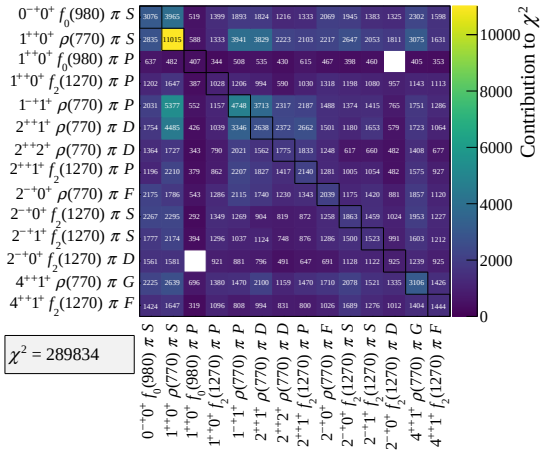

FIG. 6: Contributions from the intensities and interference terms to the χ^2 in Eq. (34) summed over the $m_{3\pi}$ and t' bins. The two cells for the interference term of the $1^{++}0^+ f_0(980)\pi P$ and $2^{-+}0^+ f_2(1270)\pi D$ waves are empty because the fit ranges for these two waves do not overlap (see Table 2).

resulting solution passed the selection criteria. The χ^2 distribution of those solutions is shown in Fig. 5(b). The solution with the lowest χ^2 of 289 834 is shown in red and is found 190 times. In addition, Fig. 5(b) shows four physical solutions with slightly larger χ^2 values. For all four solutions, the parameter values lie within the estimated systematic uncertainties (see Sec. V). The solution with the lowest χ^2, which is also the most frequently found solution, is called *main solution* in the remaining text. It is interesting to disentangle the contributions from the intensities and interference terms to the χ^2 in Eq. (34). This is visualized for the main solution in Fig. 6 in the form of a matrix, which shows the χ^2 contributions (summed over the $m_{3\pi}$ and t' bins) from the elements of the matrix $\Lambda_{ab}(m_{3\pi}, t')$ defined in Eq. (33). The diagonal elements in Fig. 6 show the χ^2 contributions from the intensity distributions of each partial wave, the off-diagonal elements the χ^2 contributions from the real (upper triangle) and imaginary parts (lower triangle) of the interference terms between the waves. The intensity distribution of the $1^{++}0^+\rho(770)\pi S$ wave gives by far the largest contribution to the χ^2. Also the χ^2 contributions of some of its interference terms are large. The reason for this is that the model is not able to describe all details of this partial-wave amplitude within the extremely small statistical uncertainties, which are a consequence of the large relative intensity of the $1^{++}0^+\rho(770)\pi S$ wave of 32.7 % and the large data set. Due to the dominant contribution of the $1^{++}0^+\rho(770)\pi S$ amplitude to the χ^2, the parameters of resonances in other waves are sensitive to the parametrizations used for the 1^{++} waves (see Secs. D and V).

C Extraction of t' spectra of wave components

Performing the partial-wave analysis in bins of t' not only helps to better disentangle resonant and nonresonant contributions via their different t' dependences but also allows us to determine the t' dependence of each wave component in the resonance model. Since the analysis is performed on the amplitude level, we can extract the t' dependence of the intensity, i.e., the t' spectrum, of each wave component and the t' dependence of the relative phases of the coupling amplitudes $\mathcal{C}_a^j(t')$ of the components. The latter is discussed in more detail in Sec. VII.

Starting from Eq. (19), we can write the model $\widehat{\mathcal{T}}_a$ for the transition amplitude of wave a as

$$\widehat{\mathcal{T}}_a(m_{3\pi}, t') = \sum_{j \,\in\, \mathbb{S}_a} \widehat{\mathcal{T}}_a^j(m_{3\pi}, t'). \tag{36}$$

Here, $\widehat{\mathcal{T}}_a^j$ is the transition amplitude for component j in this wave and given by

$$\widehat{\mathcal{T}}_a^j(m_{3\pi}, t') \equiv \sqrt{I_{aa}(m_{3\pi})}\,\sqrt{m_{3\pi}}\,\mathcal{P}(m_{3\pi}, t')\,\mathcal{C}_a^j(t')\,\mathcal{D}_j(m_{3\pi}, t'; \zeta_j). \tag{37}$$

With the above, the partial-wave intensity reads

$$\begin{aligned}\left|\widehat{\mathcal{T}}_a(m_{3\pi}, t')\right|^2 = &\sum_{j\,\in\,\mathbb{S}_a} \overbrace{I_{aa}(m_{3\pi})\,m_{3\pi}\left|\mathcal{P}(m_{3\pi}, t')\right|^2\left|\mathcal{C}_a^j(t')\right|^2\left|\mathcal{D}_j(m_{3\pi}, t'; \zeta_j)\right|^2}^{\text{Intensity of wave component } j} \\ &+ \sum_{j<k\,\in\,\mathbb{S}_a} I_{aa}(m_{3\pi})\,m_{3\pi}\left|\mathcal{P}(m_{3\pi}, t')\right|^2 \underbrace{2\,\mathrm{Re}\left[\mathcal{C}_a^j(t')\,\mathcal{D}_j(m_{3\pi}, t'; \zeta_j)\,\mathcal{C}_a^{k*}(t')\,\mathcal{D}_k^*(m_{3\pi}, t'; \zeta_k)\right]}_{\text{Overlap of wave components } j \text{ and } k}.\end{aligned} \tag{38}$$

Due to the chosen normalization of the transition amplitudes via Eq. (12), the partial-wave intensity in Eq. (38) corresponds to the expected number of events in wave a. Using the same reasoning as for Eq. (15), we interpret the terms

$$\left|\widehat{\mathcal{T}}_a^j(m_{3\pi}, t')\right|^2 = I_{aa}(m_{3\pi})\,m_{3\pi}\left|\mathcal{P}(m_{3\pi}, t')\right|^2\left|\mathcal{C}_a^j(t')\right|^2\left|\mathcal{D}_j(m_{3\pi}, t'; \zeta_j)\right|^2 \equiv \frac{\mathrm{d}N_a^j}{\mathrm{d}m_{3\pi}\,\mathrm{d}t'} \tag{39}$$

as the expected number of events N_a^j in component j in wave a in the $(m_{3\pi}, t')$ bin. Integrating Eq. (39) over $m_{3\pi}$ gives the t'-dependent yield, i.e., the t' spectrum $\mathcal{I}_a^j(t') \equiv \mathrm{d}N_a^j/\,\mathrm{d}t'$ of wave component j in wave a. To account for the nonequidistant t' binning, we normalize in each t' bin the intensity to the respective bin width $\Delta t'$:

$$\mathcal{I}_a^j(t') = \frac{1}{\Delta t'}\left|\mathcal{C}_a^j(t')\right|^2 \int\limits_{m_{\min}}^{m_{\max}} \mathrm{d}m_{3\pi}\, I_{aa}(m_{3\pi})\,m_{3\pi}\left|\mathcal{P}(m_{3\pi}, t')\right|^2\left|\mathcal{D}_j(m_{3\pi}, t'; \zeta_j)\right|^2. \tag{40}$$

The model for the nonresonant amplitudes is valid only within the applied fit ranges in $m_{3\pi}$. Therefore, we use the fit ranges from Table 2 as the $m_{3\pi}$ integration range in Eq. (40) for all wave components.

As an example, we show in Fig. 7(a) the t' spectrum of the $\pi_2(1880)$ component in the $2^{-+}\,0^+\rho(770)\pi F$ wave. In each t' bin, the black horizontal line indicates the central value of the intensity $\mathcal{I}_a^j(t')$ of the wave component as determined by Eq. (40). The horizontal extent of the line indicates the width of the t' bin. The statistical uncertainty is represented by the height of the gray box around the central value. It is calculated from the statistical uncertainties of the resonance-model parameters using Monte Carlo error propagation. For many wave components, the statistical uncertainties are very small and barely visible in the diagrams.

The intensities of most wave components fall approximately exponentially with increasing t'. This is consistent with Regge theory, which at high energies describes the scattering process as Pomeron exchange between the beam pion and target proton. For waves with spin projection $M \neq 0$, the exponential behavior is modified by an additional $(t')^{|M|}$ factor, which is given by the forward limit of the Wigner D-functions [71] and suppresses the intensity at small t' [see for example Fig. 7(b)]. We therefore parametrize the t' spectra by the model

$$\widehat{\mathcal{I}}_a^j(t') = \frac{\mathrm{d}\widehat{N}_a^j}{\mathrm{d}t'} = A_a^j \cdot \left(t'\right)^{|M|} \cdot e^{-b_a^j\,t'} \tag{41}$$

with the real-valued amplitude parameter A_a^j and the slope parameter b_a^j for component j in wave a as free parameters. The red curves in Fig. 7 show the result of a χ^2 fit of Eq. (41) to the

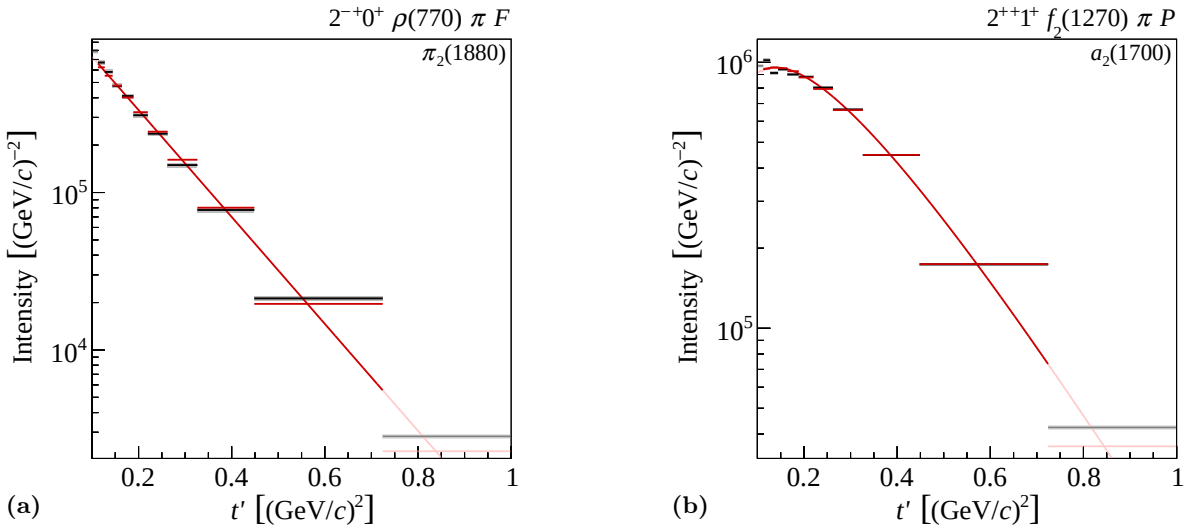

FIG. 7: Examples for t' spectra of wave components extracted according to Eq. (40). The black horizontal lines indicate the central values, and the gray boxes the statistical uncertainties (see text for details). (a) $\pi_2(1880)$ component in the $2^{-+}0^{+}\rho(770)\pi F$ wave; (b) $a_2(1700)$ component in the $2^{++}1^{+}f_2(1270)\pi P$ wave. The red curves and lines show the result of a fit of Eq. (41) to the data (see text for details).

data. In the formulation of the χ^2, the model function is integrated over each t' bin (red horizontal lines) and compared to the data (black horizontal lines). For most wave components, the simple model in Eq. (41) holds only approximately and in a limited t' range. Therefore, we exclude the two extremal t' bins and fit the data in the reduced range $0.113 < t' < 0.724\,(\mathrm{GeV}/c)^2$. For some wave components, narrower fit ranges are used (see Table 6 in Sec. VI). The t' bins excluded from the fit and the extrapolations of the model curve are shown in lighter colors.

Special cases are resonance components, for which the coupling amplitudes in different waves are constrained via Eq. (21). This constrains the t' dependence of the coupling amplitudes $\mathcal{C}_a^j(t')$ in the different waves to be the same up to complex-valued proportionality constants, i.e., the branching amplitudes ${}_b\mathcal{B}_a^j$. Although the dynamic amplitude $\mathcal{D}_j$ for a resonance component is independent of t', the t' spectra of the resonance component in the different waves can be slightly different even in this case. This is caused by the $I_{aa}(m_{3\pi})\left|\mathcal{P}(m_{3\pi},t')\right|^2$ term in the integrand in Eq. (40) as the function $I_{aa}(m_{3\pi})$ is different for different waves. In addition, the statistical uncertainties of the extracted intensities $\mathcal{I}_a^j(t')$ are different in the different waves. Therefore, the slope parameters of resonances in different waves, which are extracted using Eq. (41), may be slightly different even though the coupling amplitudes are related by Eq. (21).

D Extraction of branching-fraction ratios

In order to extract the branching-fraction ratios of resonances that appear in more than one decay channel, we calculate the yields $\mathcal{N}_a^j(t')$ of resonance component j in the corresponding waves. To this end, we integrate the resonance intensity in a given t' bin over $m_{3\pi}$:

$$\mathcal{N}_a^j(t') = \left|\mathcal{C}_a^j(t')\right|^2 \int_{m_{\mathrm{min}}}^{m_{\mathrm{max}}} \mathrm{d}m_{3\pi}\, I_{aa}(m_{3\pi})\, m_{3\pi} \left|\mathcal{D}_j^{\mathrm{R}}(m_{3\pi};\zeta_j^{\mathrm{R}})\right|^2 . \tag{42}$$

This expression corresponds to Eq. (40) with the production probability $\left|\mathcal{P}(m_{3\pi}, t')\right|^2$ set to unity[ac] and without the division by the t' bin width. The branching-fraction ratio for resonance component j is defined as the ratio of the t'-summed yields in the two waves a and b:

$$B^j_{ab} \equiv \frac{\sum\limits_{t' \text{ bins}} \mathcal{N}^j_a(t')}{\sum\limits_{t' \text{ bins}} \mathcal{N}^j_b(t')}. \tag{43}$$

It is important to note that due to the phase-space factor $I_{aa}(m_{3\pi})$ in Eq. (42), $\mathcal{N}^j_{a,b}(t')$ and therefore also B^j_{ab} depend on the chosen $m_{3\pi}$ integration limits. We use $m_{\min} = 0.5\,\text{GeV}/c^2$ and $m_{\max} = 2.5\,\text{GeV}/c^2$ for all resonances in all waves. This mass range is much wider than the width of any of the resonances.

V Systematic studies

The physical parameters obtained from the resonance-model fit, i.e., the resonance parameters, the branching-fraction ratios, and the t' slope parameters of the wave components, are subject to systematic uncertainties related to our fit model and fitting method (see Sec. IV). In order to estimate these uncertainties, we performed a large variety of studies. In each study, an aspect of the analysis is modified and the result is compared to our main result. In addition to studies that test the stability of the fit result, we performed studies to evaluate the evidence for selected resonance signals. These studies are discussed in Secs. D and VI.

Due to the multimodal nature of the χ^2 function (see Sec. IV B), the effects observed in the various systematic studies are statistically not always independent of one another. In fact, for some studies the systematic effects are correlated in a highly nonlinear way. Because of the complexity of the resonance-model fits and their high computational cost, it is not possible to estimate the correlations between the various systematic studies. We therefore estimate the systematic uncertainty intervals using the minimum and maximum values of the physical parameters observed in the performed studies. The uncertainties estimated with this approach do in general not represent Gaussian uncertainties. Unless stated otherwise in Secs. D and VI, all systematic studies discussed below are included in the estimation of the uncertainty intervals for the extracted parameters. The obtained systematic uncertainties are found to be at least 1 order of magnitude larger than the statistical uncertainties. Hence we quote in Sec. VI only the systematic uncertainties and omit statistical uncertainties.

In this section, we describe only the most important studies that either define the systematic uncertainties of some resonance parameters or illustrate interesting effects. We will discuss in Secs. D and VI the effects of these studies on the resonance and t' slope parameters in detail. For easier reference, the studies are labeled by uppercase letters.

Study (A): In this study, the influence of background contaminations from kaon diffraction, kaon pairs in the final state, central-production reactions, and nonexclusive events in the selected data sample on the fit result is studied. To this end, the analysis is performed on a data sample, in which (i) the information from the particle-identification detectors for the beam (CEDARs) and the final-state particles (RICH) was not used, (ii) the rejection of central-production events was not applied, and (iii) the requirements of exactly one recoil proton detected in the RPD and of transverse momentum balance were not applied in the event selection (see Sec. II). Possible

[ac] Equation (42) does not include the production probability because the branching-fraction ratio is a property of the resonance decay only. Therefore, the yields have arbitrary units and are not normalized to number of events.

Table 3: List of studies performed on smaller wave sets, in which some of the 14 waves that are used in the main fit (see Table 2) are omitted.

Study	Omitted waves
(B)	All four 2^{-+} waves
(C)	$1^{++}0^{+}\rho(770)\pi S$ and $1^{++}0^{+}f_2(1270)\pi P$
(D)	All two 4^{++} waves
(E)	$2^{++}1^{+}\rho(770)\pi D$
(F)	$2^{++}2^{+}\rho(770)\pi D$
(G)	$2^{++}1^{+}f_2(1270)\pi P$
(H)	$2^{++}2^{+}\rho(770)\pi D$ and $2^{++}1^{+}f_2(1270)\pi P$
(I)	$2^{++}1^{+}\rho(770)\pi D$ and $2^{++}1^{+}f_2(1270)\pi P$
(J)	$2^{++}1^{+}\rho(770)\pi D$ and $2^{++}2^{+}\rho(770)\pi D$
(K)	All three 2^{++} waves

Table 4: Borders of the eight nonequidistant t' bins used for Study (L). The intervals are chosen such that each bin contains approximately 5.8×10^6 events.

Bin	1	2	3	4	5	6	7	8	
t' $[(\mathrm{GeV}/c)^2]$	0.100	0.116	0.136	0.159	0.188	0.227	0.285	0.395	1.000

background contributions are expected to be enhanced in this data sample, which is 76.2 % larger than that used for the main analysis.

Studies (B) through (K): The selection of the 14 waves that enter the resonance-model fit (see Table 2) is to some extent subjective. In addition, the fit model has difficulties describing details of some partial-wave amplitudes. This in particular is true for the intensity distribution of the $1^{++}0^{+}\rho(770)\pi S$ wave, which is the most dominant wave in the data. We therefore investigate in Studies (B) through (K) how various waves influence the fit result, by omitting single waves or combinations of waves from the fit. The various studies are listed in Table 3.

Study (L): We investigate the impact of the t' binning by applying a coarser t' binning to the data using only eight bins, which are given in Table 4.

Study (M): The impact of the assumption that the t' dependence of resonance amplitudes is the same in partial waves with the same $J^{PC}\,M^{\varepsilon}$ quantum numbers but different decay modes is investigated in this study. To this end, we performed a resonance-model fit without the constraint in Eq. (21), so that the t' dependence of the resonance amplitudes can be chosen freely by the fit in all partial waves. This model has 942 free parameters in comparison to the 722 free parameters of the main fit. Despite the largely increased number of free parameters, the minimum χ^2 value decreases only by a factor of 0.93 with respect to the main fit. This shows that for many resonances the constraint in Eq. (21) is consistent with the data. Study (M) plays a special role in the determination of the systematic uncertainties of the branching-fraction ratios that are calculated using Eq. (43). For a true resonance, the branching-fraction ratio is expected to be independent of t'. We include the values found in the individual t' bins in the estimation of the uncertainty intervals for the branching-fraction ratios.

Study (N): As described in Sec. IV A, we use a purely phenomenological parametrization for the nonresonant contributions [see Eq. (27)]. The choice of this parametrization may impact the

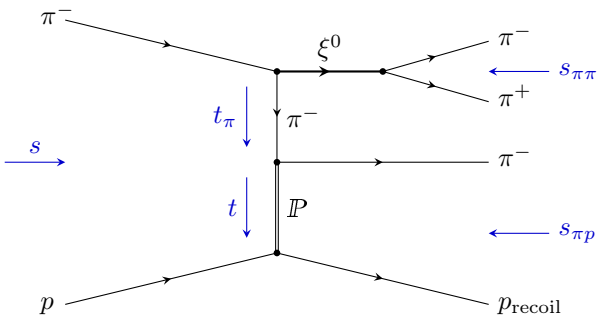

FIG. 8: Example for a nonresonant production process for the 3π final state as proposed by Deck [43]. In this process, the beam pion dissociates into the isobar ξ^0 and the bachelor π^-, followed by diffractive scattering of one of these beam fragments (typically the π^-, as shown here) off the target proton.

fit result, in particular for waves with significant nonresonant contributions. Although, we cannot uniquely identify the underlying physics processes, Deck-like processes [43] are believed to play a major role. Several models exist for the Deck process. An example is shown in Fig. 8. Using the Deck model in Eq. (B1), which is discussed in Sec. B, we generated 10^8 Monte Carlo events and performed a mass-independent analysis using the same model with 88 waves as for the real data. In Study (N), we replace the parametrizations of the nonresonant amplitudes [see Eqs. (27) and (29)] by the square root of the intensity distributions of the Deck Monte Carlo data in each partial wave. As in the main fit, the phases of these partial-wave projections of the Deck amplitude are assumed to be independent of $m_{3\pi}$. In Study (N), the fit model has 693 free parameters in comparison to the 722 free parameters of the main fit. With respect to the main fit, the minimum χ^2 value increases by a factor of 1.42. In order to find out which partial-wave amplitudes are described differently, we decompose the χ^2 difference between the study and the main fit into contributions from the elements of the matrix $\Lambda_{ab}(m_{3\pi}, t')$ defined in Eq. (33). This is visualized in Fig. 9 in the same way as in Fig. 6. The diagonal elements show the contributions to the χ^2 difference from the intensity distributions of each partial wave, the off-diagonal elements the contributions from the real (upper triangle) and imaginary parts (lower triangle) of the interference terms between the waves. Figure 9 shows that the largest contribution to the χ^2 increase in Study (N) comes from the $1^{++}0^+\rho(770)\pi S$ amplitude. Study (N) is particularly relevant for the interpretation of the resonance signals in the 1^{++} and 1^{-+} waves (see Secs. VI E 1 and VI F 1).

Studies (O) and (P): As explained in Sec. IV B, the minimum value of the χ^2 function that is determined by the resonance-model fit does not follow a χ^2 distribution because Eq. (34) does not take into account the correlations of the spin-density matrix elements. In order to test the potential bias introduced by this, we constructed two possible χ^2 functions that take into account these correlations (see Sec. C). In Study (O), we use the χ^2 formulation in Eq. (C5) with Eqs. (C1) to (C3), which is based on a single row of the spin-density matrix. In Study (P), we use Eq. (C5) with Eq. (C7), which directly compares the modeled and measured transition amplitudes. The differences between the resonance parameters estimated in Studies (O) and (P) are small compared to the systematic uncertainties. Comparing the two studies with the main solution, large effects are only observed for the resonances in the 1^{++} and 1^{-+} waves. They are discussed in Secs. VI E 1 and VI F 1.

Study (Q): The model we employ for the diffractive-production probability $|\mathcal{P}(m_{3\pi}, t')|^2$ in Eqs. (20) and (32) also influences the fit result. In order to estimate the systematic effect, we performed a study, in which this factor was set to unity. With respect to the main fit, the minimum χ^2 value increased by a factor of 1.01 while the number of free parameters remained unchanged. This shows that both models describe the data on average equally well. For most

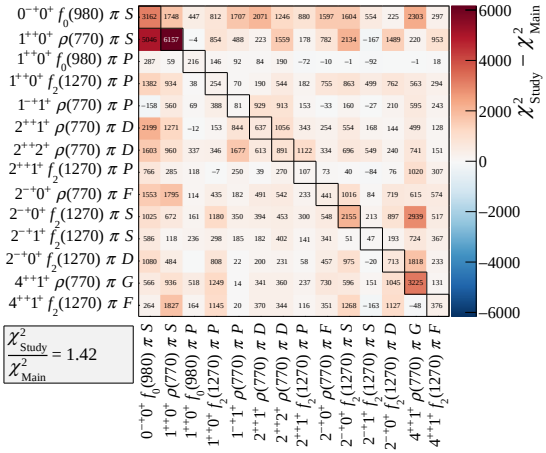

FIG. 9: Decomposition of the χ^2 difference between the main fit and the fit, in which the parametrization of the nonresonant amplitude was replaced by the square root of the intensity distribution of the partial-wave projections of Deck Monte Carlo data [Study (N)]. The χ^2 difference is visualized in the form of a matrix, which shows the contributions (summed over the $m_{3\pi}$ and t' bins) from the intensities and interference terms to the χ^2 difference. Positive values (red colors) indicate that the data are described less well in the study. The rare negative values (blue colors) indicate that the data are described better in the study.

of the resonance parameters the effects observed in Study (Q) are small. Exceptions are the $a_1(1640)$ (see Sec. D 2), the $\pi(1800)$ (see Sec. D 1), and the π_2 resonances (see Sec. D 5).

Studies (R) and (S): We also studied the effect of the range parameter q_R of the Blatt-Weisskopf factors in the decay $X^- \to \xi^0\pi^-$ (vertex 1 in Fig. 2). These factors appear explicitly in Eq. (25) and implicitly in the phase-space integrals I_{aa} in Eqs. (19) and (28). In Study (R) we set q_R to 267 MeV/c and in Study (S) to 155 MeV/c corresponding to assumed strong-interaction ranges of 0.75 fm and 1.29 fm, respectively. Most resonance parameters change only slightly in both studies. Exceptions are the a_2 resonances (see Sec. D 4), the $\pi_1(1600)$ (see Sec. D 3), and the $a_4(2040)$ (see Sec. D 6).

Integrating the model function in Eq. (34) over the $m_{3\pi}$ bins instead of taking the function values at the mass bin centers does not significantly influence the resonance parameters.

VI Results on resonance parameters and t' spectra of wave components

In this section, we describe and discuss the results of the resonance-model fit grouped by the J^{PC} quantum numbers of the resonances. The subsections are ordered by increasing complexity of the results. We start with the J^{PC} sectors that contain the clearest resonance signals that are well described by our model and later discuss the more complicated cases, where several resonances with the same J^{PC} quantum numbers appear. In the last Sec. VI F, we discuss the resonance content of the spin-exotic $J^{PC} = 1^{-+}$ wave. The extracted Breit-Wigner resonance parameters and their systematic uncertainties are listed in Table 5 and are compared to the PDG averages as listed in Ref. [10]. The positions of the resonance poles of the Breit-Wigner amplitudes in the complex energy plane are discussed in Sec. A. The t' slope parameters of the resonant and nonresonant wave components, determined by fitting the extracted t' spectra using Eq. (41) (see Sec. IV C), are listed in Table 6. In the presentation of the results, we restrict ourselves to figures that illustrate the typical quality of the fit or certain aspects of the analysis. The full fit result can be found in the supplemental material in Secs. E and F together with additional information

required to perform the resonance-model fit. The data required to perform the resonance-model fit are provided in computer-readable format at [35].

Table 5: Resonance parameters with systematic uncertainties as extracted in this analysis. The statistical uncertainties are at least an order of magnitude smaller than the systematic ones and are hence omitted. For comparison, the PDG averages are listed [10]. For the $a_2(1320)$, we quote the PDG average for the 3π decay mode. For the two entries marked with a " * " no PDG average exists. The $a_1(1420)$ is listed as "omitted from summary table" and the quoted mass and width values were estimated in an earlier COMPASS analysis based on the same data set that is used here but with only three waves in the resonance-model fit [19]. The $\pi_2(2005)$ is listed as a "further state" and we quote for comparison the parameters measured by the BNL E852 experiment [72] with the statistical and systematic uncertainties added in quadrature.

(a) a_J-like resonances

		$a_1(1260)$	$a_1(1420)$ (Sec. VI E)	$a_1(1640)$	$a_2(1320)$	$a_2(1700)$ (Sec. VI C)	$a_4(2040)$ (Sec. VI B)
COMPASS	Mass [MeV/c^2]	$1299\,^{+12}_{-28}$	$1411\,^{+4}_{-5}$	$1700\,^{+35}_{-130}$	$1314.5\,^{+4.0}_{-3.3}$	$1681\,^{+22}_{-35}$	$1935\,^{+11}_{-13}$
	Width [MeV/c^2]	380 ± 80	$161\,^{+11}_{-14}$	$510\,^{+170}_{-90}$	$106.6\,^{+3.4}_{-7.0}$	$436\,^{+20}_{-16}$	$333\,^{+16}_{-21}$
PDG	Mass [MeV/c^2]	1230 ± 40	$1414\,^{+15}_{-13}$	1647 ± 22	$1319.0\,^{+1.0}_{-1.3}$	1732 ± 16	$1995\,^{+10}_{-8}$
	Width [MeV/c^2]	250 to 600	$153\,^{+8}_{-23}$ *	254 ± 27	$105.0\,^{+1.6}_{-1.9}$	194 ± 40	$257\,^{+25}_{-23}$

(b) π_J-like resonances

		$\pi(1800)$ (Sec. VI A)	$\pi_1(1600)$ (Sec. VI F)	$\pi_2(1670)$	$\pi_2(1880)$ (Sec. VI D)	$\pi_2(2005)$
COMPASS	Mass [MeV/c^2]	$1804\,^{+6}_{-9}$	$1600\,^{+110}_{-60}$	$1642\,^{+12}_{-1}$	$1847\,^{+20}_{-3}$	$1962\,^{+17}_{-29}$
	Width [MeV/c^2]	$220\,^{+8}_{-11}$	$580\,^{+100}_{-230}$	$311\,^{+12}_{-23}$	$246\,^{+33}_{-28}$	$371\,^{+16}_{-120}$
PDG	Mass [MeV/c^2]	1812 ± 12	$1662\,^{+8}_{-9}$	1672.2 ± 3.0	1895 ± 16	1974 ± 84
	Width [MeV/c^2]	208 ± 12	241 ± 40	$260 \quad \pm 9$	235 ± 34	341 ± 152 *

Table 6: The t' slope parameters b_a^j in units of $(\mathrm{GeV}/c)^{-2}$ extracted by fitting Eq. (41) to the t' spectra of the wave components. The quoted uncertainties are of systematic origin. Statistical uncertainties are at least an order of magnitude smaller than the systematic ones and are hence omitted. For most wave components, the fits are performed in the range $0.113 < t' < 0.724\,(\mathrm{GeV}/c)^2$. Reduced fit ranges are given in the footnotes. Cases where the model is not able to describe the t' spectrum are marked by a dagger ("†"). Partial waves, for which the t' dependence of the resonance amplitudes is connected via Eq. (21), are marked with a star ("*"). Slight differences of the extracted slope-parameter values for the resonances in these waves originate from differences in the decay phase-space volumes and in the statistical uncertainties (see Sec. IV C).

(a) 0^{-+} Waves (Sec. VI A)

Wave	$\pi(1800)$	Nonresonant
$0^{-+}0^{+}f_0(980)\pi S$	$8.8\,^{+0.7}_{-0.3}$	$26\,^{+6\,[\mathrm{ad}]}_{-5}$

(b) 1^{++} Waves (Sec. VI E)

Wave		$a_1(1260)$	$a_1(1420)$	$a_1(1640)$	Nonresonant
$1^{++}0^{+}\rho(770)\pi S$	*	$11.8\,^{+0.9}_{-4.2}$	—	$7.7\,^{+6.2}_{-0.4}$	$12.5\,^{+2.1}_{-1.5}$
$1^{++}0^{+}f_0(980)\pi P$		—	$9.5\,^{+0.6}_{-1.0}$	—	$11.8\,^{+0.8}_{-1.2}$
$1^{++}0^{+}f_2(1270)\pi P$	*	11 ± 4	—	$7.6\,^{+1.6}_{-0.5}$	$11.2\,^{+2.7}_{-2.2}$

(c) 1^{-+} Waves (Sec. VI F)

Wave	$\pi_1(1600)$	Nonresonant
$1^{-+}1^{+}\rho(770)\pi P$	†	$19.1\,^{+1.4\,[\mathrm{ae}]}_{-4.7}$

(d) 2^{++} Waves (Sec. VI C)

Wave		$a_2(1320)$	$a_2(1700)$	Nonresonant
$2^{++}1^{+}\rho(770)\pi D$	*	7.9 ± 0.5	$7.3\,^{+2.4}_{-0.9}$	$13.6\,^{+0.4}_{-1.8}$
$2^{++}2^{+}\rho(770)\pi D$		$9.0\,^{+1.2}_{-0.7}$	†	$8.1\,^{+1.6}_{-0.5}$
$2^{++}1^{+}f_2(1270)\pi P$	*	$7.8\,^{+0.6}_{-0.5}$	$7.2\,^{+1.1}_{-0.8}$	†

(e) 2^{-+} Waves (Sec. VI D)

Wave		$\pi_2(1670)$	$\pi_2(1880)$	$\pi_2(2005)$	Nonresonant
$2^{-+}0^{+}\rho(770)\pi F$	*	$8.5\,^{+0.9}_{-0.5}$	$7.8\,^{+0.5}_{-0.9}$	$6.8\,^{+0.4}_{-3.9}$	†
$2^{-+}0^{+}f_2(1270)\pi S$	*	$8.5\,^{+0.9}_{-0.5}$	$7.8\,^{+7.5}_{-0.9}$	$6.7\,^{+0.4}_{-1.3}$	†
$2^{-+}1^{+}f_2(1270)\pi S$		†	†	$7.1\,^{+3.5}_{-2.6}$	$6.9\,^{+1.1}_{-1.9}$
$2^{-+}0^{+}f_2(1270)\pi D$	*	$8.4\,^{+0.8}_{-1.7}$	$7.8\,^{+0.5}_{-0.9}$	$6.7\,^{+0.4}_{-1.3}$	$12\,^{+6}_{-2}$

(f) 4^{++} Waves (Sec. VI B)

Wave		$a_4(2040)$	Nonresonant
$4^{++}1^{+}\rho(770)\pi G$	*	$9.2\,^{+0.8}_{-0.5}$	14 ± 4
$4^{++}1^{+}f_2(1270)\pi F$	*	$9.2\,^{+0.8}_{-0.5}$	$14.5\,^{+1.8}_{-3.7}$

[ad] Fit range $0.113 < t' < 0.326\,(\mathrm{GeV}/c)^2$
[ae] Fit range $0.113 < t' < 0.449\,(\mathrm{GeV}/c)^2$.

A $J^{PC} = 0^{-+}$ resonances

1 *Results on* 0^{-+} *resonances*

The only $J^{PC} = 0^{-+}$ wave included in the resonance-model fit is the $0^{-+}0^{+}f_0(980)\pi S$ wave. It contributes 2.4 % to the total intensity in the mass range from 0.5 to 2.5 GeV/c^2. The intensity distribution of this wave is shown in Figs. 10(a), 10(d), and 10(g) for three t' bins. Except in the highest t' bin, the intensity distributions exhibit a clear peak of the $\pi(1800)$ resonance at $m_{3\pi} \approx 1.8\,\text{GeV}/c^2$ with a shoulder toward lower masses. The picture changes dramatically in the highest t' bin, where the intensity at the $\pi(1800)$ peak position is close to zero and hence the low-mass shoulder dominates the spectrum. Figure 10 also shows, as an example, the $m_{3\pi}$ dependence of the relative phases of the 0^{-+} wave with respect to the $1^{++}0^{+}\rho(770)\pi S$ and the $2^{-+}1^{+}f_2(1270)\pi S$ waves. Clearly rising phase motions are observed in the 1.8 GeV/c^2 mass region.

The data are well described by the fit model (red curves in Fig. 10), which contains two 0^{-+} components: a Breit-Wigner resonance for the $\pi(1800)$ (blue curves) and a nonresonant component (green curves). The extrapolations of these curves below and above the fitted mass range of $1.2 < m_{3\pi} < 2.3\,\text{GeV}/c^2$ are shown in lighter colors in Fig. 10. The $\pi(1800)$ is parametrized using Eqs. (22) and (23), the nonresonant component using Eq. (29) (see Table 2). In our fit model, the nonresonant contribution is attributed to the low-mass shoulder. At low values of t', it interferes constructively with the resonance at the $\pi(1800)$ peak position. At higher values of t', the interference of the two components is destructive at the peak position due to a sign flip of the coupling amplitude of the nonresonant component at $t' \approx 0.3\,(\text{GeV}/c)^2$ (see discussion in Sec. VII). In the highest t' bin, the destructive interference of the two components is complete and leads to a dip in the intensity distribution around the $\pi(1800)$ mass. The remaining low-mass shoulder is completely described by the nonresonant component. In the intensity distributions, the model exhibits some disagreement with the observed peak shape and does not reproduce the high-mass shoulder in the two highest t' bins.

The strong variation of the intensity of the 0^{-+} wave with t' originates from the very different t' dependences of the amplitudes of the two 0^{-+} wave components. Figure 11 shows the t' spectra for both components as determined using Eq. (40) together with the results of fits using Eq. (41). While the intensity of the $\pi(1800)$ component exhibits an approximately exponential behavior with slope parameter $8.8\,^{+0.7}_{-0.3}\,(\text{sys.})\,(\text{GeV}/c)^{-2}$, the intensity of the nonresonant component first drops steeply with $b = 26\,^{+6}_{-5}\,(\text{sys.})\,(\text{GeV}/c)^{-2}$ at low values of t', before it starts to rise again with t', forming a dip at $t' \approx 0.3\,(\text{GeV}/c)^2$.

The 0^{-+} wave exhibits clearly rising phases with respect to the $1^{++}0^{+}\rho(770)\pi S$ wave in the $\pi(1800)$ region (see central column of Fig. 10). At low t', the relative phase decreases at about 1.3 GeV/c^2 due to the $a_1(1260)$ and rises at about 1.8 GeV/c^2 due to the $\pi(1800)$. At higher values of t', the decrease is less pronounced and the relative phase rises steeply starting at 1.5 GeV/c^2. This is explained in our fit model by a sign change of the coupling amplitude of the nonresonant 0^{-+} component, which dominates the low-mass region, leading to an additional rise of the total phase of the 0^{-+} amplitude. The extremely rapid phase motion at 1.8 GeV/c^2 in the highest t' bin is a direct consequence of the nearly vanishing intensity at this mass. Since the phase is defined with respect to the origin of the complex plane, its value changes rapidly by $\pm 180°$ if the amplitude passes close to the origin [73]. We observe a similar t' dependence of the phase motions with respect to other waves. As an example, we show in the right column of Fig. 10 the phase motions with respect to the $2^{-+}1^{+}f_2(1270)\pi S$ wave. Here, the phase drop in the lowest t' bin, which appears at about 1.6 GeV/c^2, is caused by the $\pi_2(1670)$. Within the fit ranges, the model describes all relative phases of the 0^{-+} wave well in all t' bins.

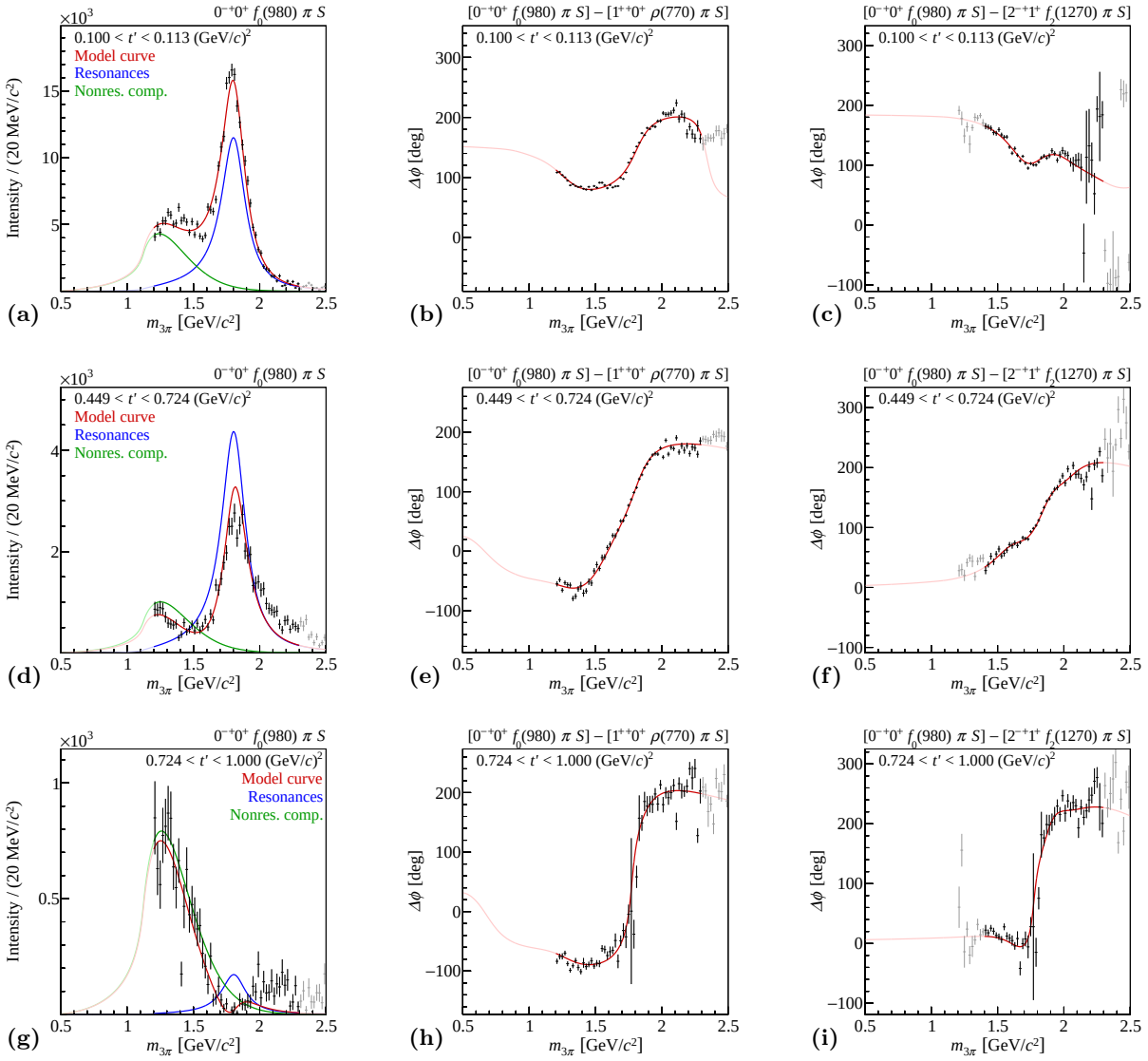

FIG. 10: The $0^{-+}0^{+}f_0(980)\pi S$ partial-wave amplitude in three t' bins (rows): (left column) intensity distributions; (central column) phase motions with respect to the $1^{++}0^{+}\rho(770)\pi S$ wave; (right column) phase motions with respect to the $2^{-+}1^{+}f_2(1270)\pi S$ wave. The data points are taken from Ref. [30] and represent the so-called mass-independent analysis (see Sec. III). The red curve represents the full model (see Table 2), which is the coherent sum of the wave components. The other curves represent the wave components: $\pi(1800)$ resonance (blue curves), nonresonant contribution (green curves). The extrapolations of the model and the wave components beyond the fit range are shown in lighter colors.

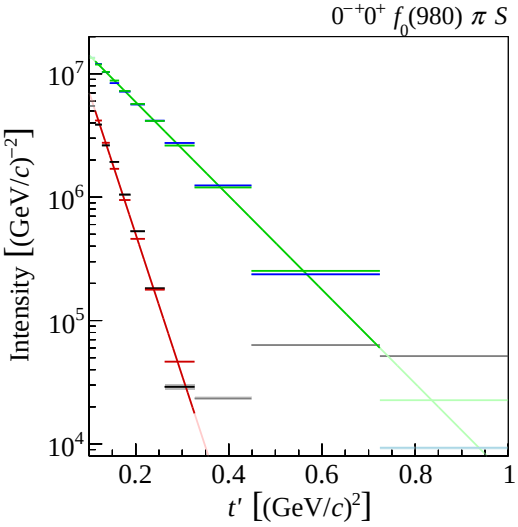

FIG. 11: Similar to Fig. 7, but showing the t' spectra of the two $J^{PC} = 0^{-+}$ wave components as given by Eq. (40): the $\pi(1800)$ component is shown as blue lines (central values) and light blue boxes (statistical uncertainties; not visible for most bins), the nonresonant component is shown as black lines and gray boxes as in Fig. 7. The red and green curves and horizontal lines represent fits using Eq. (41).

From the fit, we obtain the Breit-Wigner resonance parameters $m_{\pi(1800)} = 1804\,^{+6}_{-9}\,(\text{sys.})\,\text{MeV}/c^2$ and $\Gamma_{\pi(1800)} = 220\,^{+8}_{-11}\,(\text{sys.})\,\text{MeV}/c^2$. The $\pi(1800)$ resonance parameters are rather insensitive to changes of the fit model discussed in Sec. V. The estimated systematic uncertainties are therefore the smallest of all π_J-like resonances in the model. More details on the results of the systematic studies are discussed in Sec. D 1. It is worth mentioning that in the study, in which the fit range was narrowed to $1.6 < m_{3\pi} < 2.3\,\text{GeV}/c^2$, the nonresonant component is practically vanishing. This demonstrates that indeed most of the peak structure arises from the $\pi(1800)$.

2 Discussion of results on 0^{-+} resonances

Although the $\pi(1800)$ in principle has been well known for more than three decades, its resonance parameters are not well determined. In particular the $\pi(1800)$ mass values extracted by previous experiments show a large spread and fall into two clusters [10]: one with central values around $1780\,\text{MeV}/c^2$ and the other around $1860\,\text{MeV}/c^2$. Our result for the $\pi(1800)$ mass of $m_{\pi(1800)} = 1804\,^{+6}_{-9}\,(\text{sys.})\,\text{MeV}/c^2$ falls between these two clusters and is in good agreement with the PDG world average of $m_{\pi(1800)} = 1812 \pm 12\,\text{MeV}/c^2$ [10]. This is also true for the $\pi(1800)$ width, for which the PDG average is $\Gamma_{\pi(1800)} = 208 \pm 12\,\text{MeV}/c^2$ compared to our value of $\Gamma_{\pi(1800)} = 220\,^{+8}_{-11}\,(\text{sys.})\,\text{MeV}/c^2$. Our measurement of the $\pi(1800)$ parameters is the most precise and accurate so far. It is also consistent within uncertainties with a previous COMPASS measurement using a lead target [17].

In the $0^{-+}0^{+}[\pi\pi]_S\pi S$ wave, we observe a peak that is similar in shape and position to the $\pi(1800)$ peak in the $0^{-+}0^{+}f_0(980)\pi S$ wave [see Figs. 24 and 25(b) in Ref. [30]]. Although the $[\pi\pi]_S\pi$ wave was not included in the resonance model fit for reasons discussed below, the observed similarity of the peaks suggests that the $\pi(1800)$ resonance parameters would be similar in this wave.

The $\pi(1800)$ is the second radial excitation of the pion. Its lighter partner state is the $\pi(1300)$. This state has been observed in the $\rho(770)\pi$ and $[\pi\pi]_S\pi$ final states, as well as in $\gamma\gamma$ production [10]. The parameters of the $\pi(1300)$ are only poorly known. The world averages estimated by the PDG are $m_{\pi(1300)} = 1300 \pm 100\,\text{MeV}/c^2$ and $\Gamma_{\pi(1300)} = 200$ to $600\,\text{MeV}/c^2$ [10]. Also the coupling of the $\pi(1300)$ to the $[\pi\pi]_S\pi$ final state is controversial. The Obelix Collaboration claims that the

coupling is 2.2 ± 0.4 times stronger than for the $\rho(770)\pi$ final state and extracts a resonance mass of $m_{\pi(1300)} = 1200 \pm 40\,\mathrm{MeV}/c^2$ [74]. The Crystal Barrel Collaboration, however, sets an upper limit for the coupling to the $[\pi\pi]_S\pi$ decay channel of 0.15 times the coupling to $\rho(770)\pi$ [75] and quotes a mass of $m_{\pi(1300)} = 1375 \pm 40\,\mathrm{MeV}/c^2$. The two experiments also disagree on the value of the $\pi(1300)$ width. In our data, we observe an unusually strong t' dependence of the intensity of the $0^{-+}0^+[\pi\pi]_S\pi S$ wave in the $1.3\,\mathrm{GeV}/c^2$ region [see Figs. 24 and 35(a) in Ref. [30]], which is similar to that of the nonresonant component in the $0^{-+}0^+f_0(980)\pi S$ wave (see Fig. 11). In addition, the intensity in this mass region is strongly dependent on the PWA model employed for the mass-independent analysis. We therefore did not include the $0^{-+}0^+[\pi\pi]_S\pi S$ wave in the resonance-model fit.

Since the intensity spectra of the $0^{-+}0^+f_0(980)\pi S$ wave show a significant shoulder at $m_{3\pi} \approx 1.3\,\mathrm{GeV}/c^2$, we tried an alternative description of this partial-wave amplitude using a $\pi(1300)$ resonance component instead of the nonresonant component. This model describes the data less well than the main fit and does not yield meaningful $\pi(1300)$ resonance parameters.[af] If we include in another study a nonresonant component, the minimum χ^2 value decreases by a factor of 0.97 with respect to the main fit.[ag] In the solution with the lowest χ^2, the $\pi(1300)$ is found with a mass and width of about $1630\,\mathrm{MeV}/c^2$ and $380\,\mathrm{MeV}/c^2$, respectively. While the width value is compatible with previous measurements, the mass value is clearly not.[ah] Moreover, the $0^{-+}0^+f_0(980)\pi S$ wave does not show any phase rise in the $1.3\,\mathrm{GeV}/c^2$ mass region. Within our model, we therefore conclude that the data do not support a $\pi(1300)$ signal in the $f_0(980)\pi$ decay mode. This conclusion is consistent with the fact that so far no observation of such a $\pi(1300)$ decay has been claimed.

Heavier excited pion states with masses around 2070 and $2360\,\mathrm{MeV}/c^2$ were reported by the authors of Ref. [76]. We do not see clear resonance signals of heavy pions in the mass range from 2000 to $2500\,\mathrm{MeV}/c^2$ in the $0^{-+}0^+f_0(980)\pi S$ wave.

B $J^{PC} = 4^{++}$ resonances

1 Results on 4^{++} resonances

We include two $J^{PC} = 4^{++}$ waves, $4^{++}1^+\rho(770)\pi G$ and $4^{++}1^+f_2(1270)\pi F$, in the resonance-model fit. Both have small intensities and contribute 0.8 % and 0.2 %, respectively, to the total intensity in the mass range from 0.5 to $2.5\,\mathrm{GeV}/c^2$. The intensity distributions of the two waves are shown for the lowest t' bin in Figs. 12(a) and 12(e). In both waves, a clear peak around $1.9\,\mathrm{GeV}/c^2$ is observed. The shape of the intensity distributions depends only weakly on t'. The $4^{++}1^+f_2(1270)\pi F$ wave exhibits a slight shoulder at high masses. In the $4^{++}1^+\rho(770)\pi G$ wave, this shoulder is more pronounced, and in addition a low-mass shoulder is visible. In both waves, these features are most pronounced at low t' and vanish in the highest t' bin. Figure 12 also shows, as an example, the $m_{3\pi}$ dependence of the relative phases of the 4^{++} waves with respect to the $1^{++}0^+\rho(770)\pi S$ and $1^{++}0^+f_2(1270)\pi P$ waves in the lowest t' bin. Clearly rising phases are observed in the $1.9\,\mathrm{GeV}/c^2$ mass region. In addition, Fig. 12(b) shows the relative phase between the two 4^{++} waves. The approximately constant phase indicates that there is a common dominant resonance in the two waves.

Our model contains one $J^{PC} = 4^{++}$ resonance, the $a_4(2040)$, which is the only confirmed isovector state with these quantum numbers [10]. The $a_4(2040)$ is parametrized using Eqs. (22) and (23), the nonresonant components using Eq. (29) (see Table 2). The data are well described within the

[af] In the solutions with the lowest χ^2 values, the $\pi(1300)$ mass is found at the lower parameter limit of $1\,\mathrm{GeV}/c^2$.

[ag] Compared to the 722 free parameters of the main fit, this fit has 746 free parameters.

[ah] Only local minima with significantly larger χ^2 values yield $\pi(1300)$ masses of about $1270\,\mathrm{MeV}/c^2$ that are compatible with previous measurements.

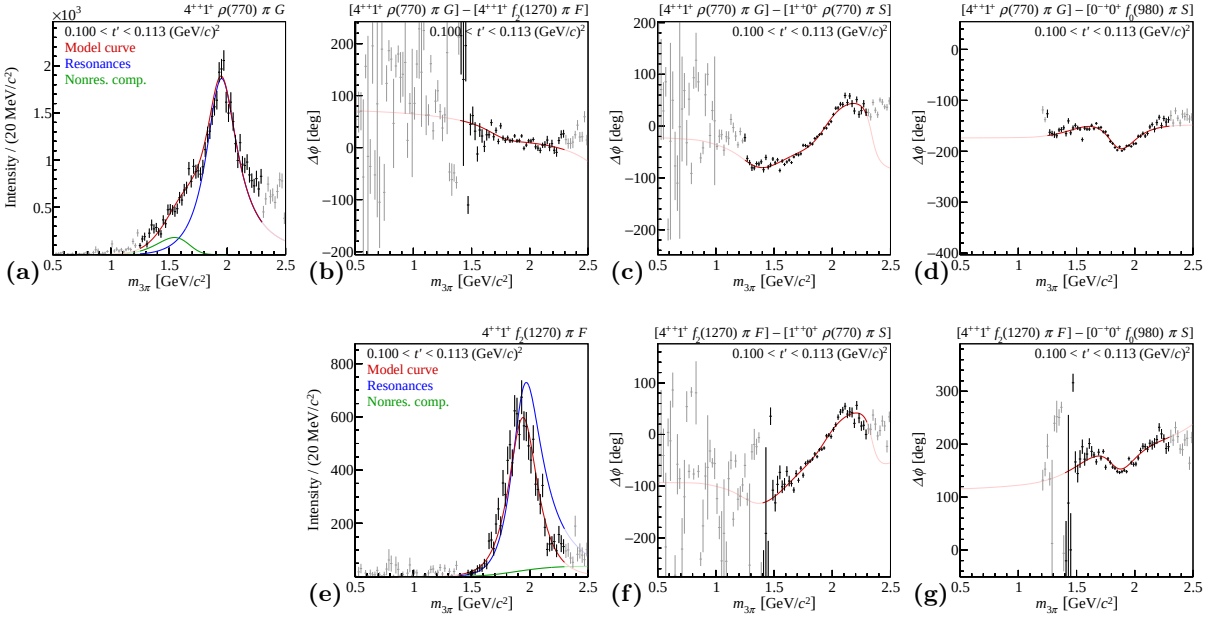

FIG. 12: Amplitudes of the two $J^{PC} = 4^{++}$ waves in the lowest t' bin. (a) through (d): intensity distribution and relative phases for the $4^{++}1^{+}\rho(770)\pi G$ wave. (e) through (g): intensity distribution and relative phases for the $4^{++}1^{+}f_2(1270)\pi F$ wave. The model and the wave components are represented as in Fig. 10, except that here the blue curve represents the $a_4(2040)$.

fit range, which for the $f_2(1270)\pi F$ wave is $1.4 < m_{3\pi} < 2.3\,\text{GeV}/c^2$. The low-mass tail of the $\rho(770)\pi G$ wave allows us to extend the fit range for this wave down to $1.25\,\text{GeV}/c^2$. In our fit model, the nonresonant components are small in both 4^{++} waves. Their contribution decreases with increasing t' and almost vanishes at higher values of t'. The nonresonant components interfere destructively with the high-mass tail of the $a_4(2040)$ in the $f_2(1270)\pi F$ wave and constructively with the low-mass tail of the $a_4(2040)$ in the $\rho(770)\pi G$ wave. The model is not able to reproduce the high-mass shoulder in the intensity distributions of the $\rho(770)\pi G$ wave at low t'.

The two 4^{++} waves exhibit clearly rising phases in the $1.9\,\text{GeV}/c^2$ mass region, e.g., with respect to the $1^{++}0^{+}\rho(770)\pi S$ wave, as shown in Figs. 12(c) and 12(f). This rise is observed for all t' bins. Its magnitude is slightly smaller for the $4^{++}1^{+}\rho(770)\pi G$ wave. The phase variations with respect to the $0^{-+}0^{+}f_0(980)\pi S$ wave exhibit a more complex pattern. The phase drop around $1.8\,\text{GeV}/c^2$ due to a stronger $\pi(1800)$ signal in the $0^{-+}0^{+}f_0(980)\pi S$ wave is compensated by the phase motion of the $a_4(2040)$ leading to a rising phase around $1.9\,\text{GeV}/c^2$ [see Figs. 12(d) and 12(g)]. The magnitude of these phase motions decreases with t'.

The relative phase between the two 4^{++} partial-wave amplitudes shows only little variation over the fitted mass region. Together with the phase motions discussed in the previous paragraph, this demonstrates that the two waves are dominated by resonances and that they have the same resonance content. The residual slight rise of the phase between the $f_2(1270)\pi F$ and $\rho(770)\pi G$ waves is caused by differences in the small nonresonant components.

We extract the Breit-Wigner parameters of the $a_4(2040)$ and find $m_{a_4(2040)} = 1935\,^{+11}_{-13}\,(\text{sys.})\,\text{MeV}/c^2$ and $\Gamma_{a_4(2040)} = 333\,^{+16}_{-21}\,(\text{sys.})\,\text{MeV}/c^2$. The $a_4(2040)$ resonance parameters are rather insensitive to the systematic studies (see Secs. D 6 and V).

The t' spectra of the 4^{++} wave components are shown in Fig. 13 together with the results of fits using Eq. (41). In our model, the t' dependence of the amplitudes of the $a_4(2040)$ components in the two waves is constrained by Eq. (21). The fit finds a relative phase of the branching

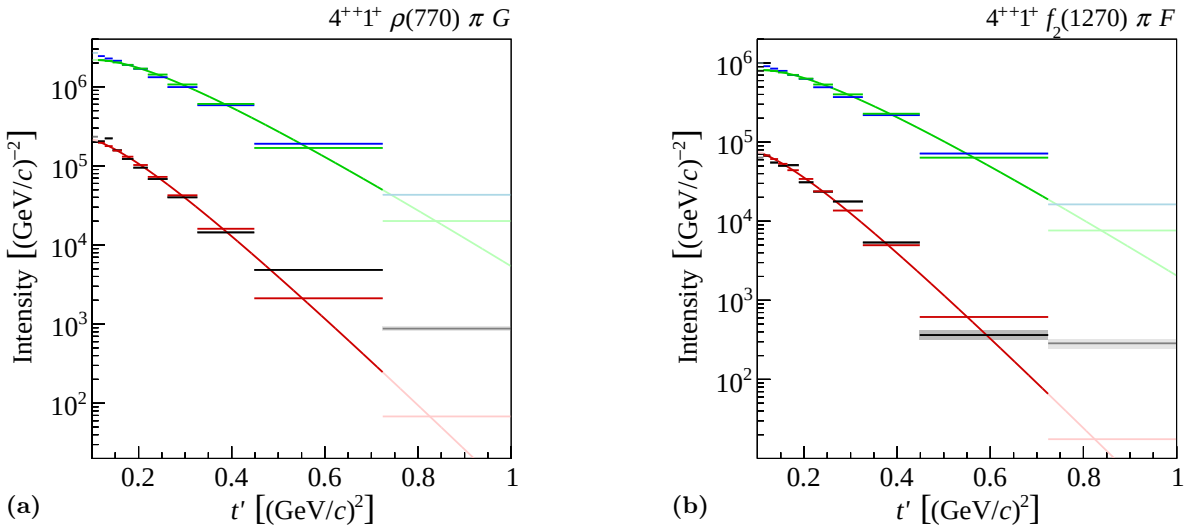

FIG. 13: Similar to Fig. 11, but showing the t' spectra of (a) the $4^{++}1^{+}\rho(770)\pi G$ and (b) the $4^{++}1^{+}$ $f_2(1270)\pi F$ wave components as given by Eq. (40): the $a_4(2040)$ component is shown as blue lines and light blue boxes, and the nonresonant components as black lines and gray boxes. The red and green curves and horizontal lines represent fits using Eq. (41).

amplitudes close to 0° for the $a_4(2040)$ components in the two waves (see Sec. VII). The slope parameters of the t' spectra of the $a_4(2040)$ component in the two waves have practically identical values of $9.2\,^{+0.8}_{-0.5}\,(\mathrm{sys.})\,(\mathrm{GeV}/c)^{-2}$. For both t' spectra, the model curve undershoots the data at small values of t'. This could indicate that in this t' range our resonance model overestimates the $a_4(2040)$ yields in both waves. The nonresonant contributions have steeper falling t' spectra with almost identical slope parameters of $14 \pm 4\,(\mathrm{sys.})\,(\mathrm{GeV}/c)^{-2}$ for the $\rho(770)\pi G$ wave and $14.5\,^{+1.8}_{-3.7}\,(\mathrm{sys.})\,(\mathrm{GeV}/c)^{-2}$ for the $f_2(1270)\pi F$ wave. It is worth noting that, if we do not constrain the $a_4(2040)$ coupling amplitudes via Eq. (21) and thus allow them to have different t' dependence [Study (M); see Sec. V], we obtain $a_4(2040)$ resonance and slope parameters that are consistent within the systematic uncertainties. Also the relative phase of approximately 0° between the $\rho(770)\pi G$ and $f_2(1270)\pi F$ decay modes is recovered. This confirms the assumptions contained in Eq. (21).

From the $a_4(2040)$ yields in the two analyzed decay branches we derive the ratio of branching fractions according to Eq. (43):

$$B^{a_4}_{\rho\pi G, f_2\pi F} = \frac{\mathrm{BF}\left[a_4(2040)^- \to \rho(770)^0\pi^- \to \pi^-\pi^-\pi^+\right]}{\mathrm{BF}\left[a_4(2040)^- \to f_2(1270)\pi^- \to \pi^-\pi^-\pi^+\right]} = 2.5\,^{+0.5}_{-0.3}\,(\mathrm{sys.}). \tag{44}$$

Taking into account the unobserved decays $a_4^- \to \rho^-\pi^0$ and $a_4^- \to f_2\pi^-$ to the $\pi^-\pi^0\pi^0$ final state and assuming isospin symmetry, this value increases by a factor of 4/3:

$$B^{a_4,\mathrm{iso}}_{\rho\pi G, f_2\pi F} = \frac{\mathrm{BF}\left[a_4(2040)^- \to \rho(770)\pi \to 3\pi\right]}{\mathrm{BF}\left[a_4(2040)^- \to f_2(1270)\pi \to 3\pi\right]} = 3.3\,^{+0.7}_{-0.4}\,(\mathrm{sys.}). \tag{45}$$

The isospin factor needs to be corrected for self-interference effects. Unlike the $\rho(770)\pi$ channel, the $f_2(1270)\pi$ channel is affected by different Bose symmetrizations in the $\pi^-\pi^-\pi^+$ and $\pi^-\pi^0\pi^0$ final states. In addition, the branching fraction of the $f_2(1270)$ into 2π of $84.2\,^{+2.9}_{-0.9}\,\%$ [10] needs to be included. Taking both effects into account, the isospin factor 4/3 should be replaced by

$1.19\,^{+0.04}_{-0.02}$[ai] leading to the corrected ratio

$$B^{a_4,\mathrm{corr}}_{\rho\pi G, f_2\pi F} = \frac{\mathrm{BF}\left[a_4(2040)^- \to \rho(770)\pi\right]}{\mathrm{BF}\left[a_4(2040)^- \to f_2(1270)\pi\right]} = 2.9\,^{+0.6}_{-0.4}. \tag{46}$$

2 Discussion of results on 4^{++} resonances

The PDG world averages for mass and width of the $a_4(2040)$ are $m_{a_4(2040)} = 1995\,^{+10}_{-8}\,\mathrm{MeV}/c^2$ and $\Gamma_{a_4(2040)} = 257\,^{+25}_{-23}\,\mathrm{MeV}/c^2$ [10]. Our measurement of the $a_4(2040)$ parameters of $m_{a_4(2040)} = 1935\,^{+11}_{-13}\,(\mathrm{sys.})\,\mathrm{MeV}/c^2$ and $\Gamma_{a_4(2040)} = 333\,^{+16}_{-21}\,(\mathrm{sys.})\,\mathrm{MeV}/c^2$ is the most accurate and precise so far, but we find the $a_4(2040)$ mass to be $60\,\mathrm{MeV}/c^2$ smaller and the width $76\,\mathrm{MeV}/c^2$ larger than the world average. We agree with our two previous analyses: the one based on the measurement of the $\pi^-\pi^-\pi^+$ final state diffractively produced on a solid lead target [17], and the other based on the measurement of the $\eta\pi$ and $\eta'\pi$ final states diffractively produced on a liquid-hydrogen target [52]. Also, the results on diffractively produced $\pi^-\pi^-\pi^+$ by the BNL E852 experiment [47] and $\omega\pi^-\pi^0$ by the VES experiment [77] are in good agreement with our results.

Our measurement of the $a_4(2040)$ width is especially at variance with the value of $\Gamma_{a_4(2040)} = 180 \pm 30\,\mathrm{MeV}/c^2$ obtained by the authors of Ref. [76]. They analyzed $3\pi^0$, $\eta\pi^0$, and $\eta'\pi^0$ final states produced in $\bar{p}p$ annihilations. They used a model with two 4^{++} resonances below $2.5\,\mathrm{GeV}/c^2$ and claimed an excited a_4 state with a mass of $2255 \pm 40\,\mathrm{MeV}/c^2$ and a width of $330\,^{+110}_{-50}\,\mathrm{MeV}/c^2$. In the two analyzed waves, we do not see clear resonance signals of heavier a_4 resonances in the mass range from 2000 to $2500\,\mathrm{MeV}/c^2$.

The measured value of $2.5\,^{+0.5}_{-0.3}\,(\mathrm{sys.})$ of the branching-fraction ratio $B^{a_4}_{\rho\pi G, f_2\pi F}$ in Eq. (44) is larger than the value $1.1 \pm 0.2\,(\mathrm{stat.}) \pm 0.2\,(\mathrm{sys.})$ that was reported by the BNL E852 experiment in a study of the same channel at $18\,\mathrm{GeV}/c$ beam momentum [47]. Taking into account the unobserved $\pi^-\pi^0\pi^0$ decay mode and the $f_2(1270)$ branching fraction into 2π, the present result of $2.9\,^{+0.6}_{-0.4}$ for $B^{a_4,\mathrm{corr}}_{\rho\pi G, f_2\pi F}$ in Eq. (46) agrees with the value of 3.3 predicted by the $^3P_0$ decay model [78]. In this model, the strong decay of a $q\bar{q}$ state to the $(q\bar{q}')\,(q'\bar{q})$ exit channel proceeds via production of a $q'\bar{q}'$ pair with vacuum quantum numbers, $J^{PC} = 0^{++}$. Note that the $a_4(2040)$ width predicted by this model is a factor of 2 smaller than our measured value of $\Gamma_{a_4(2040)}$.

C $J^{PC} = 2^{++}$ resonances

1 Results on 2^{++} resonances

We include three $J^{PC} = 2^{++}$ waves in the resonance-model fit: $2^{++}1^+\rho(770)\pi D$, $2^{++}2^+\rho(770)\pi D$, and $2^{++}1^+ f_2(1270)\pi P$. The $2^{++}1^+\rho(770)\pi D$ wave has the third largest intensity of the 88 waves in the mass-independent analysis (see Sec. III) and contributes 7.7 % to the total intensity in the mass range from 0.5 to $2.5\,\mathrm{GeV}/c^2$. The two other 2^{++} waves contribute 0.3 % and 0.8 % to the total intensity, respectively. The intensity distributions of the three waves are shown in Figs. 14(a), 14(e), and 14(h) for the lowest t' bin and in Figs. 15(a), 15(e), and 15(h) for the highest t' bin.

All three waves exhibit a clear peak around $1.3\,\mathrm{GeV}/c^2$. The intensity distributions of the two $\rho(770)\pi D$ waves are dominated by this peak. The peak shape is nearly independent of t'. At low t', the $\rho(770)\pi D$ wave with $M = 1$ exhibits a dip in the intensity distribution at about $1.8\,\mathrm{GeV}/c^2$ [see Fig. 16(a)]. With increasing t', this dip moves toward higher masses and becomes shallower until it disappears in the two highest t' bins [see Figs. 16(b) and 16(c)]. A much stronger variation of the shape of the intensity distribution with increasing t' is observed for the $f_2(1270)\pi P$ wave.

[ai] We only take into account the uncertainty of the $f_2(1270) \to 2\pi$ branching fraction.

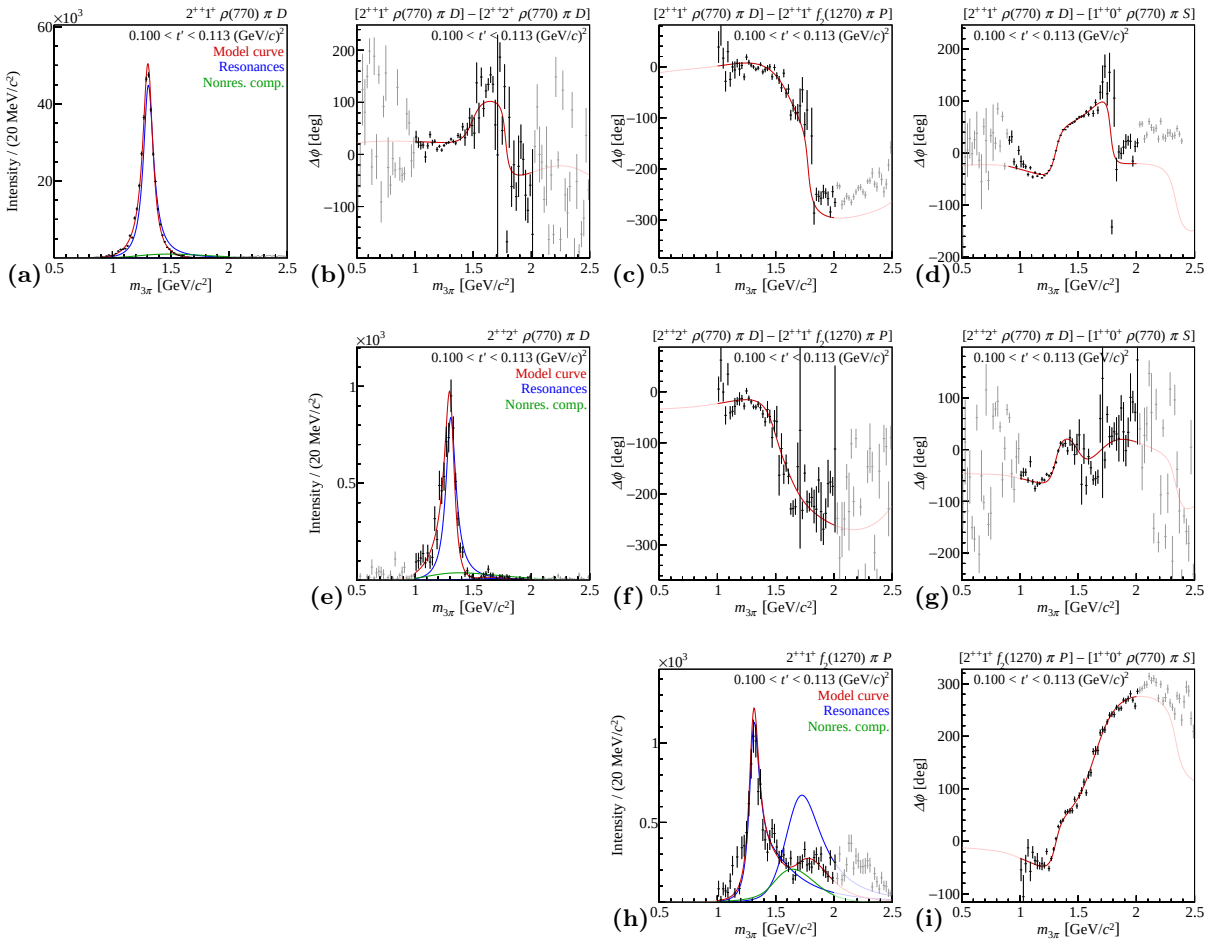

FIG. 14: Amplitudes of the three $J^{PC} = 2^{++}$ waves in the lowest t' bin. (a) through (d): Intensity distribution and relative phases for the $2^{++}1^{+}\rho(770)\pi D$ wave. (e) through (g): Intensity distribution and relative phases for the $2^{++}2^{+}\rho(770)\pi D$ wave. (h) and (i): Intensity distribution and relative phase for the $2^{++}1^{+}f_2(1270)\pi P$ wave. The model and the wave components are represented as in Fig. 10, except that here the blue curves represent the $a_2(1320)$ and the $a_2(1700)$.

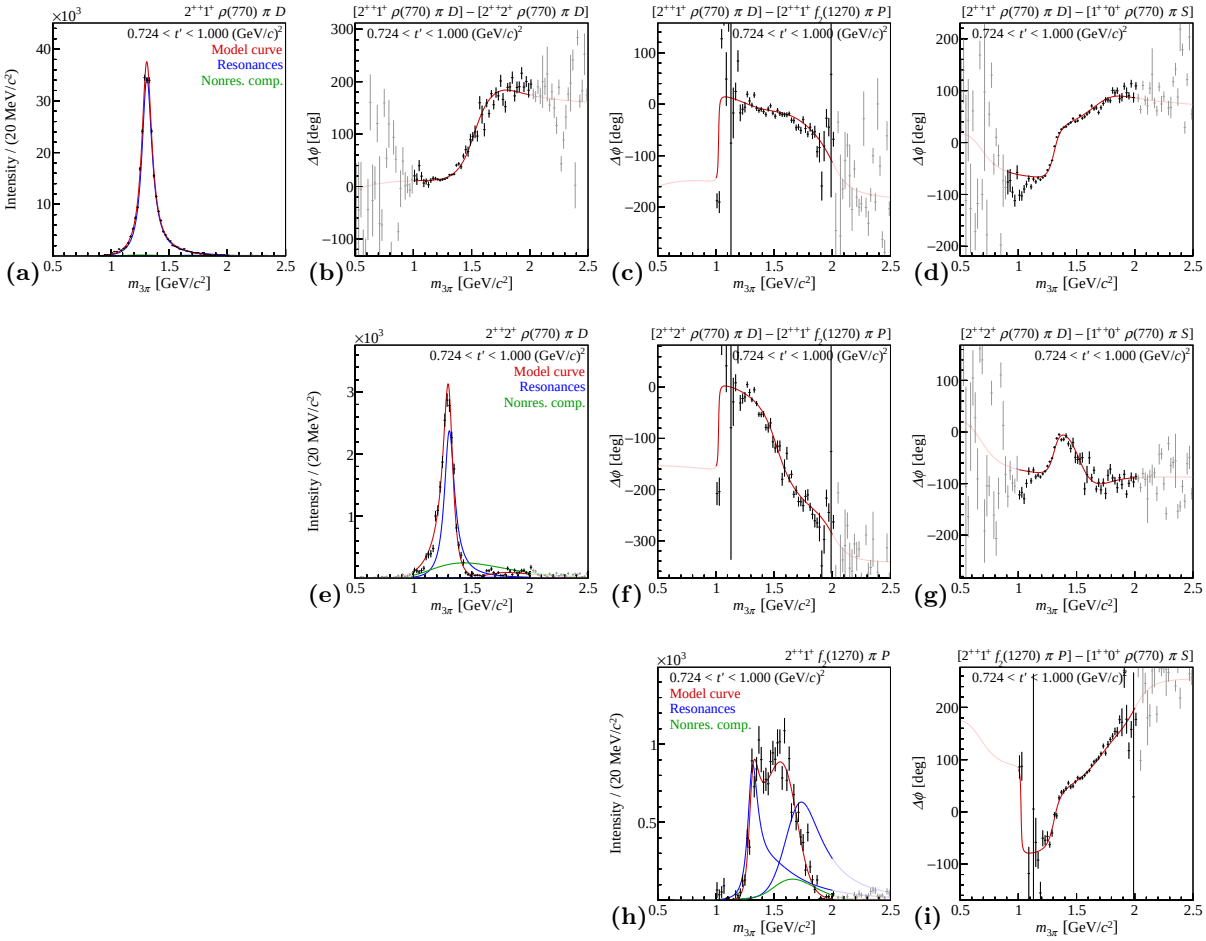

FIG. 15: Similar to Fig. 14 but for the highest t' bin.

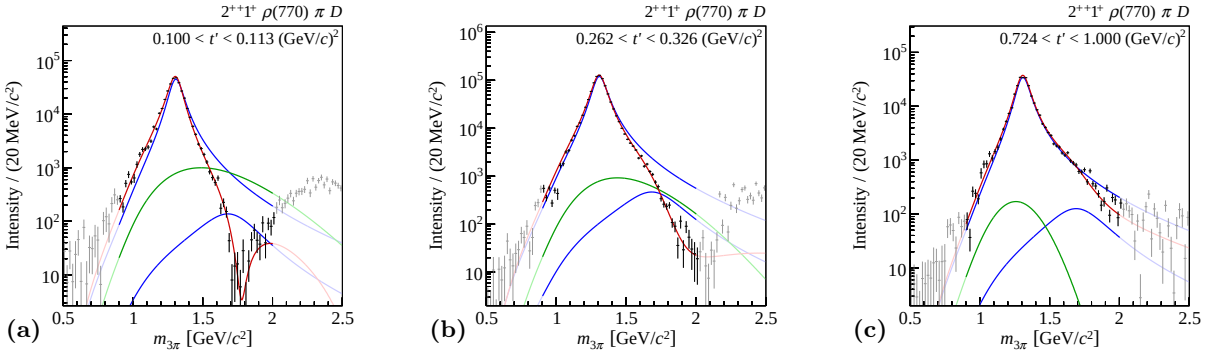

FIG. 16: Intensity distributions of the $2^{++}1^{+}\rho(770)\pi D$ wave for three t' bins shown in logarithmic scale. The model and the wave components are represented as in Fig. 14.

In addition to the peak at $1.3\,\mathrm{GeV}/c^2$, this wave exhibits a shoulder at about $1.6\,\mathrm{GeV}/c^2$, which is absent at low t' and increases with increasing t', and a high-mass tail that becomes weaker with increasing t'.

The right columns of Figs. 14 and 15 show the $m_{3\pi}$ dependence of the relative phases of the 2^{++} waves with respect to the $1^{++}0^{+}\rho(770)\pi S$ wave. Clearly rising phases are observed in the $1.3\,\mathrm{GeV}/c^2$ mass region in all t' bins. Figures 14 and 15 also show the relative phases between the three 2^{++} waves. Here, a more complex pattern is observed that points to different relative contributions of the components in these waves.

In our model, the three $J^{PC} = 2^{++}$ waves are described using two resonances, $a_2(1320)$ and $a_2(1700)$. The $a_2(1320)$ is parametrized using Eqs. (22) and (25), the $a_2(1700)$ using Eqs. (22) and (23), and the nonresonant components using Eq. (27) for the $2^{++}1^{+}\rho(770)\pi D$ wave and Eq. (29) for the other two 2^{++} waves (see Table 2).

Taking into account the high precision of the data in particular for the $2^{++}1^{+}\rho(770)\pi D$ wave, the model describes the data well within the fit range, which is $0.9 < m_{3\pi} < 2.0\,\mathrm{GeV}/c^2$ for the $2^{++}1^{+}\rho(770)\pi D$ wave and $1.0 < m_{3\pi} < 2.0\,\mathrm{GeV}/c^2$ for the other two waves. The two $\rho(770)\pi D$ waves are dominated by the $a_2(1320)$ with only small contributions from the $a_2(1700)$. This is strikingly different in the $f_2(1270)\pi P$ wave, in which the $a_2(1700)$ has an intensity comparable to that of the $a_2(1320)$ and the relative $a_2(1700)$ intensity grows with increasing t'. In our fit model, the nonresonant components behave differently in the three 2^{++} waves. Compared to the dominant $a_2(1320)$ peak, the nonresonant component in the $2^{++}1^{+}\rho(770)\pi D$ wave is small and vanishes nearly completely in the highest t' bin. The corresponding wave with $M = 2$ exhibits a larger nonresonant contribution relative to the $a_2(1320)$, which slightly increases with increasing t'. We find the largest nonresonant contribution with respect to the $a_2(1320)$ peak in the $2^{++}1^{+}$ $f_2(1270)\pi P$ wave. The relative nonresonant intensity, which grows slightly with increasing t', is concentrated mostly in the $a_2(1700)$ region and—as in the other two 2^{++} waves—is small in the $a_2(1320)$ peak region.

In the $a_2(1320)$ region, interference effects of the wave components are small in all three waves. The largest effect is a slight asymmetric distortion of the $a_2(1320)$ peak in the $2^{++}2^{+}\rho(770)\pi D$ wave due to interference of the $a_2(1320)$ with the nonresonant component. This is different for the $a_2(1700)$ region. In the $2^{++}1^{+}\rho(770)\pi D$ wave, a complicated interplay between $a_2(1320)$, $a_2(1700)$, and the nonresonant contribution becomes apparent. At low t', destructive interference causes the intensity to drop by 4 orders of magnitude from the $a_2(1320)$ peak down to the dip at about $1.8\,\mathrm{GeV}/c^2$. In the two highest t' bins, the nonresonant contribution practically vanishes in the $a_2(1700)$ region and the interference pattern changes so that the dip in the high-mass

region disappears. This distinct interference pattern helps the fit to separate the small $a_2(1700)$ contribution despite the presence of the dominant $a_2(1320)$. In the $2^{++}1^+ f_2(1270)\pi P$ wave, the high-mass shoulder is described by a relatively large $a_2(1700)$ contribution. At high t', the rather sharp drop of this shoulder around $1.8\,\mathrm{GeV}/c^2$ [see Fig. 15(h)] is described by the interference of all three wave components.

Although the fit model describes the intensity distributions in general well, it falls short in some regions. In the dominant $2^{++}1^+\rho(770)\pi D$ wave, it does not reproduce well the high-mass tail, which is most pronounced at low t' [see e.g., Fig. 16(a)]. Also, the extrapolation of the fit model above $2.0\,\mathrm{GeV}/c^2$, which is the upper limit of the fit range, disagrees with the data. We observe a similar behavior also in the $2^{++}1^+ f_2(1270)\pi P$ wave [see e.g., Fig. 14(h)]. In this wave, the model in addition undershoots the low-mass tail below $1.2\,\mathrm{GeV}/c^2$, which is, however, mainly defined by the opening of the $f_2(1270)\pi$ phase space.

The interpretation of the structures in the intensity distributions in terms of resonances is supported by the relative phases with respect to selected waves. The $2^{++}1^+\rho(770)\pi D$ wave exhibits rapidly rising phases with respect to the $1^{++}0^+\rho(770)\pi S$ wave in the $1.3\,\mathrm{GeV}/c^2$ region, which are caused by the $a_2(1320)$, and slower rising phases in the $1.6\,\mathrm{GeV}/c^2$ region [see Figs. 14(d) and 15(d)]. Both features depend only weakly on t'. The dominant $a_2(1320)$ leads to approximately constant phases relative to the other 2^{++} waves in the region between 1.0 and $1.4\,\mathrm{GeV}/c^2$ [see Figs. 14(b), 14(c), 15(b), and 15(c)]. The extremely rapidly decreasing phases around $1.8\,\mathrm{GeV}/c^2$ in Figs. 14(b) to 14(d) are connected to the dip in the intensity distribution of the $2^{++}1^+$ $\rho(770)\pi D$ wave. At this dip, the partial-wave amplitude becomes nearly zero due to destructive interference. This behavior of the phases is analogous to the one observed in the $0^{-+}0^+ f_0(980)$ πS wave [see Sec. VI A 1 and Figs. 10(h) and 10(i)]. As the dip in the intensity distributions, the phase drop disappears toward higher t'. At large values of t', the phase of the $2^{++}1^+\rho(770)\pi D$ wave with respect to the $2^{++}1^+ f_2(1270)\pi P$ wave becomes approximately constant [see Fig. 15(c)], consistent with the $a_2(1700)$ appearing in both waves. The phases of the $2^{++}2^+\rho(770)\pi D$ wave with respect to the $1^{++}0^+\rho(770)\pi S$ wave also exhibit the rapid rise in the $1.3\,\mathrm{GeV}/c^2$ region due to the $a_2(1320)$. It is followed by a drop of the phase toward the $1.7\,\mathrm{GeV}/c^2$ region. The missing rising phase from the $a_2(1700)$ is consistent with the small intensity of this component in this wave. The phase motion changes only slightly with t'. The phase with respect to the other two 2^{++} waves are approximately constant around the $a_2(1320)$. The phase relative to the $2^{++}1^+$ $f_2(1270)\pi P$ wave falls by more than 180° above about $1.4\,\mathrm{GeV}/c^2$. This drop is approximately independent of t' and covers the mass region of the $a_2(1700)$.[aj] The phases of the $2^{++}1^+ f_2(1270)$ πP wave with respect to the $1^{++}0^+\rho(770)\pi S$ wave exhibit two consecutive phase rises due to $a_2(1320)$ and $a_2(1700)$. Unlike the intensity distributions of this wave, the phase motions do not change drastically with t'.

From the fit, we extract the following $a_2(1320)$ Breit-Wigner resonance parameters: $m_{a_2(1320)} = 1314.5\,^{+4.0}_{-3.3}\,(\mathrm{sys.})\,\mathrm{MeV}/c^2$ and $\Gamma_{a_2(1320)} = 106.6\,^{+3.4}_{-7.0}\,(\mathrm{sys.})\,\mathrm{MeV}/c^2$. Due to the large intensity of the $a_2(1320)$, its small width, and the small contributions from the nonresonant components in the $1.3\,\mathrm{GeV}/c^2$ region, the systematic uncertainties of the $a_2(1320)$ resonance parameters are the smallest of all resonances in the model (see Sec. D 4).

The extracted Breit-Wigner resonance parameters for the $a_2(1700)$ are $m_{a_2(1700)} = 1681\,^{+22}_{-35}\,(\mathrm{sys.})\,\mathrm{MeV}/c^2$ and $\Gamma_{a_2(1700)} = 436\,^{+20}_{-16}\,(\mathrm{sys.})\,\mathrm{MeV}/c^2$. They are mainly determined by the $2^{++}1^+ f_2(1270)\pi P$ wave. Since the $a_2(1700)$ signal is much smaller than that of the $a_2(1320)$, the $a_2(1700)$ parameters have much larger systematic uncertainties. The $a_2(1700)$ parameters are sensitive to the parametrization of the nonresonant component and to the value of the range parameter q_R in the

[aj] A similar behavior is observed for the $a_1(1640)$ in the $1^{++}0^+ f_2(1270)\pi P$ wave (see Sec. VI E 2).

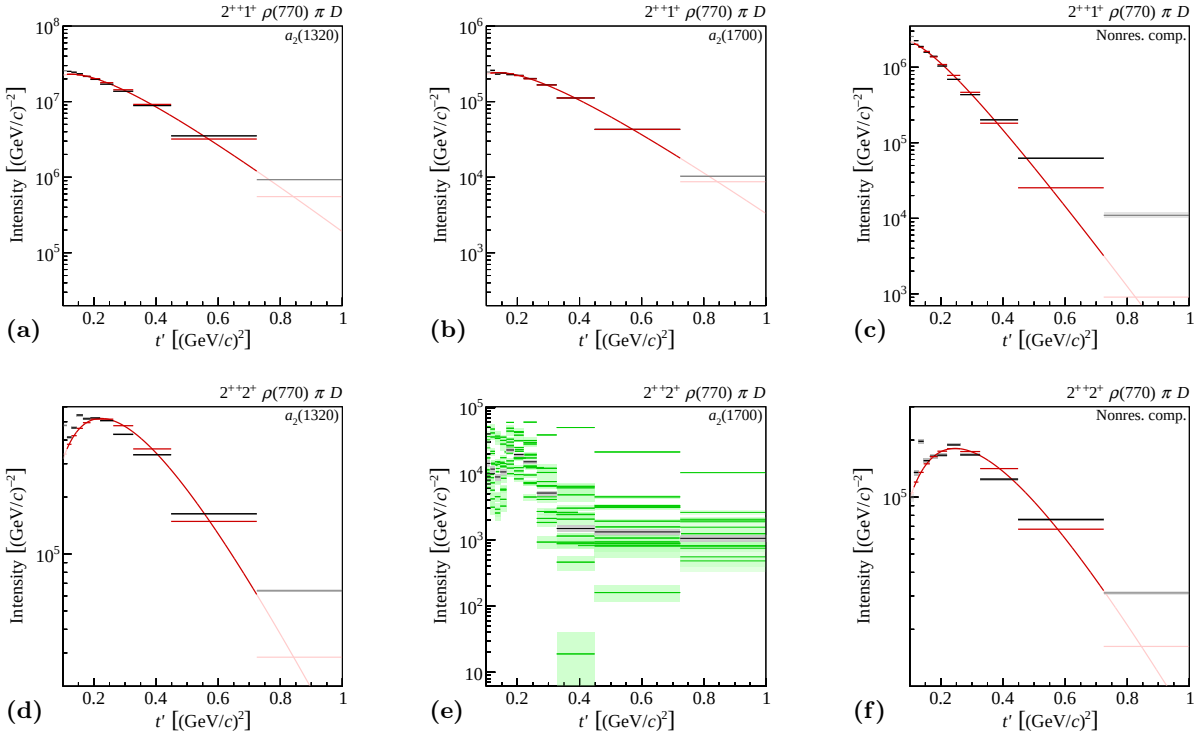

FIG. 17: Similar to Fig. 7 but showing the t' spectra of the components in the $2^{++}\rho(770)\pi D$ waves with (upper row) $M^{\varepsilon} = 1^+$ and (lower row) $M^{\varepsilon} = 2^+$ as given by Eq. (40): (left) $a_2(1320)$ component, (center) $a_2(1700)$ component, and (right) nonresonant components. The red curves and horizontal lines represent fits using Eq. (41). (e) shows in addition to the $a_2(1700)$ t' spectrum from the main fit (black/gray) the t' spectra obtained in the various systematic studies (central values shown in green, statistical uncertainties in light green).

Blatt-Weisskopf factors (see Sec. D 4).

The t' dependence of the intensities of the resonant and nonresonant 2^{++} wave components is shown in Figs. 17 and 18 together with the results of fits using Eq. (41). The coupling amplitudes of the resonance components in the two 2^{++} waves with $M^{\varepsilon} = 1^+$ are constrained by Eq. (21). Therefore, the extracted values of the slope parameters are nearly identical: the $a_2(1320)$ slope parameter has a value of $7.9 \pm 0.5\,(\text{sys.})\,(\text{GeV}/c)^{-2}$ in the $\rho(770)\pi D$ wave with $M = 1$ and of $7.8\,^{+0.6}_{-0.5}\,(\text{sys.})\,(\text{GeV}/c)^{-2}$ in the $f_2(1270)\pi P$ wave (see Table 6). Similar to the 1^{++} and 2^{-+} sectors (see Secs. VI D 1 and VI E 1, respectively), the slope parameter of the higher-mass state, here the $a_2(1700)$, is smaller. It has a value of $7.3\,^{+2.4}_{-0.9}\,(\text{sys.})\,(\text{GeV}/c)^{-2}$ in the $\rho(770)\pi D$ wave with $M = 1$ and $7.2\,^{+1.1}_{-0.8}\,(\text{sys.})\,(\text{GeV}/c)^{-2}$ in the $f_2(1270)\pi P$ wave. If we do not constrain the coupling amplitudes of the resonance components via Eq. (21) [Study (M); see Sec. V], the above slope values remain essentially unchanged. The only exception is the $a_2(1700)$ in the $\rho(770)\pi P$ wave, the slope of which becomes about $2\,(\text{GeV}/c)^{-2}$ steeper.

As in other waves, we observe that the t' spectra of the nonresonant components in the 2^{++} $1^+\rho(770)\pi D$ and $2^{++}1^+ f_2(1270)\pi P$ waves are distinctly different from those of the resonances. In particular in the $\rho(770)\pi D$ wave with $M = 1$, the nonresonant component exhibits a much steeper t' spectrum with a slope parameter value of $13.6\,^{+0.4}_{-1.8}\,(\text{sys.})\,(\text{GeV}/c)^{-2}$. The nonresonant t' spectrum in the $f_2(1270)\pi P$ wave is sensitive to changes of the fit model discussed in Sec. V (see Fig. 18). It is not well described by the model, Eq. (41). The $(t')^{|M|}$ factor in the model induces a downturn toward lower t', which is inconsistent with the data. From the above, we

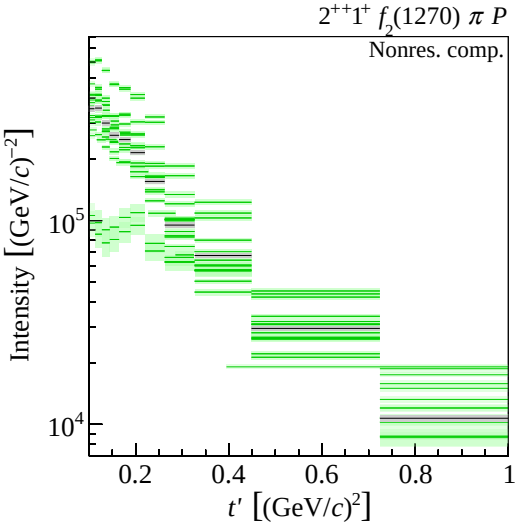

FIG. 18: Similar to Fig. 17(e), but showing the t' spectrum of the nonresonant component in the $2^{++}1^{+}$ $f_2(1270)\pi P$ wave as given by Eq. (40).

conclude that the nonresonant component in this wave seems to have too much freedom. We also cannot exclude that it is distorted by leakage into the small $f_2(1270)\pi P$ wave at the stage of the mass-independent analysis.

In the fit model, the t' dependence of the coupling amplitudes of the resonant components in the $2^{++}2^{+}\rho(770)\pi D$ wave is not constrained by Eq. (21) and is therefore determined independently of the other two 2^{++} waves. In the $M = 2$ wave, we observe slope parameters for the $a_2(1320)$ and the nonresonant contribution of $9.0\,^{+1.2}_{-0.7}\,(\text{sys.})\,(\text{GeV}/c)^{-2}$ and $8.1\,^{+1.6}_{-0.5}\,(\text{sys.})\,(\text{GeV}/c)^{-2}$, respectively. The value for the $a_2(1320)$ is slightly larger than in the other two 2^{++} waves, while the one for the nonresonant component is significantly smaller. Both effects are not understood at present and illustrate the limitations of our model. The t' spectrum of the $a_2(1700)$ in the $M = 2$ wave differs strongly from the t' spectra in the other two waves [see Fig. 17(e)]. It has a rather peculiar shape: after an initial rise with increasing t', the intensity drops sharply with t' until about $0.3\,(\text{GeV}/c)^2$ and then levels off. The fit function in Eq. (41) is not able to describe these data. The t' spectrum is sensitive to changes of the fit model discussed in Sec. V. We therefore conclude that with our model the $a_2(1700)$ signal in the $M = 2$ wave is too small in order to reliably extract $a_2(1700)$ yields, although it helps to constrain the $a_2(1700)$ parameters.

We extract the branching-fraction ratio for the decays of the $a_2(1320)$ into the $\rho(770)\pi D$ and $f_2(1270)\pi P$ decay modes with $M = 1$, where the latter one is a subthreshold decay. Using Eq. (43) we get

$$B^{a_2}_{\rho\pi D, f_2\pi P} = \frac{\text{BF}\big[a_2(1320)^- \to \rho(770)^0\pi^- \to \pi^-\pi^-\pi^+\big]}{\text{BF}\big[a_2(1320)^- \to f_2(1270)\pi^- \to \pi^-\pi^-\pi^+\big]} = 17.6\,^{+1.1}_{-2.6}\,(\text{sys.}). \tag{47}$$

This is the first measurement of this quantity. As for the $a_4(2040)$ (see Sec. VI B 1), this ratio increases by a factor of 4/3 when we take into account the unobserved decays $a_2^- \to \rho^-\pi^0$ and $a_2^- \to f_2\pi^-$ to the $\pi^-\pi^0\pi^0$ final state and assume isospin symmetry. Hence

$$B^{a_2,\text{iso}}_{\rho\pi D, f_2\pi P} = \frac{\text{BF}\big[a_2(1320)^- \to \rho(770)\pi \to 3\pi\big]}{\text{BF}\big[a_2(1320)^- \to f_2(1270)\pi \to 3\pi\big]} = 23.5\,^{+1.5}_{-3.5}\,(\text{sys.}). \tag{48}$$

Taking into account the branching fraction of the $f_2(1270)$ to 2π and the effect of the different Bose symmetrizations in the $\pi^-\pi^-\pi^+$ and $\pi^-\pi^0\pi^0$ final states, the isospin factor 4/3 should be

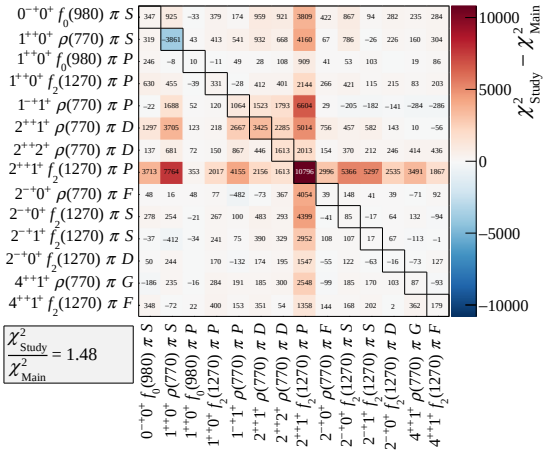

FIG. 19: Similar to Fig. 9, but for the study, in which the $a_2(1700)$ component was omitted from the fit model.

replaced by $0.936\,^{+0.032}_{-0.010}$[ak] yielding the corrected branching-fraction ratio

$$B^{a_2,\text{corr}}_{\rho\pi D, f_2\pi P} = \frac{\text{BF}\left[a_2(1320)^- \to \rho(770)\pi\right]}{\text{BF}\left[a_2(1320)^- \to f_2(1270)\pi\right]} = 16.5\,^{+1.2}_{-2.4}. \tag{49}$$

2 *Discussion of results on* 2^{++} *resonances*

From our analysis, we conclude that we observe two resonances with $J^{PC} = 2^{++}$. The $a_2(1320)$ appears as a clear peak in all three 2^{++} waves, whereas the $a_2(1700)$ shows up most prominently in the $f_2(1270)\pi P$ wave and is seen to couple only weakly to $\rho(770)\pi D$. In order to study the significance of the extracted $a_2(1700)$ signal, we performed a fit, in which the $a_2(1700)$ component was removed from the fit model. Compared to the main fit, this fit has a minimum χ^2 value that is larger by a factor of 1.48.[al] Figure 19 shows the contributions from the spin-density matrix elements to the χ^2 difference between this and the main fit. As expected, the largest contribution to the observed χ^2 increase comes from the $2^{++}1^+ f_2(1270)\pi P$ wave intensity and from its interferences. This shows that most of the support for the $a_2(1700)$ component comes from the $2^{++}1^+ f_2(1270)\pi P$ wave, which is consistent with the observation that the $a_2(1700)$ signal is small in the two $\rho(770)\pi D$ waves. Figure 20 shows that the $2^{++}1^+ f_2(1270)\pi P$ wave cannot be described without the $a_2(1700)$. The model without the $a_2(1700)$ that is represented by the dashed red curve is in particular unable to describe the shoulder at about $1.6\,\text{GeV}/c^2$ in the intensity distribution.

We clearly observe the production of $a_2(1320)$ with $M = 2$. This is consistent with the peak observed in the $M = 2$ D-wave of the $\pi^-\eta$ final state [see Fig. 3(g) in Ref. [52]]. Also the intensity ratio of the $M = 1$ and $M = 2$ waves at the $a_2(1320)$ peak position is similar for the two final states. In the present analysis, we have studied in detail the t' dependence of the $a_2(1320)$ component in the $\rho(770)\pi D$ waves with $M = 1$ and $M = 2$. Despite the different functional dependence due to the $(t')^{|M|}$ factor in Eq. (41), the extracted slope parameters have similar values. In addition, the relative phase of the coupling amplitudes of the $a_2(1320)$ in the two waves exhibits only a weak t' dependence and departs from zero by no more than 20° (see Sec. VII). All this points to the same production mechanism and shows that Pomeron exchange can transfer helicity 2 to the produced state.

[ak] We only take into account the uncertainty of the $f_2(1270) \to 2\pi$ branching fraction.

[al] Compared to the 722 free parameters of the main fit, this fit has 674 free parameters.

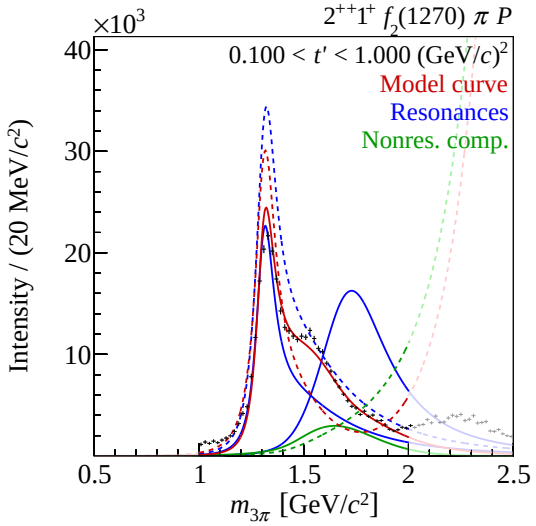

FIG. 20: t'-summed intensity of the $2^{++}1^{+}f_2(1270)\pi P$ wave with the result of the main fit (continuous curves) and of the fit, in which the $a_2(1700)$ component was removed from the fit model (dashed curves). The model and the wave components are represented as in Fig. 14.

The PDG quotes world averages for the $a_2(1320)$ parameters of $m_{a_2(1320)} = 1319.0\,^{+1.0}_{-1.3}\,\mathrm{MeV}/c^2$ and $\Gamma_{a_2(1320)} = 105\,^{+1.6}_{-1.9}\,\mathrm{MeV}/c^2$ [10] for the 3π decay mode. While our estimate of $m_{a_2(1320)} = 1314.5\,^{+4.0}_{-3.3}\,(\mathrm{sys.})\,\mathrm{MeV}/c^2$ is $4.5\,\mathrm{MeV}/c^2$ lower, our width value of $\Gamma_{a_2(1320)} = 106.6\,^{+3.4}_{-7.0}\,(\mathrm{sys.})\,\mathrm{MeV}/c^2$ agrees well with the PDG average. Our present $a_2(1320)$ parameters agree with the results of our two previous analyses: the one based on the measurement of the $\pi^-\pi^-\pi^+$ final state diffractively produced on a solid lead target [17], and the other based on the measurement of the $\eta\pi$ and $\eta'\pi$ final states diffractively produced on a liquid-hydrogen target [52]. The finite resolution in $m_{3\pi}$, which is neglected in our analysis, is estimated to affect the width by less than $1\,\mathrm{MeV}/c^2$. Our values for the slope parameter of the $a_2(1320)$ in the $\rho(770)\pi D$ and $f_2(1270)\pi P$ waves with $M = 1$ are in good agreement with the value of $7.3 \pm 0.1\,(\mathrm{GeV}/c)^{-2}$ measured by ACCMOR [31].

The $a_2(1700)$ is listed by the PDG as "omitted from summary table" with world averages for mass and width of $m_{a_2(1700)} = 1732 \pm 16\,\mathrm{MeV}/c^2$ and $\Gamma_{a_2(1700)} = 194 \pm 40\,\mathrm{MeV}/c^2$ [10]. Our result of $m_{a_2(1700)} = 1681\,^{+22}_{-35}\,(\mathrm{sys.})\,\mathrm{MeV}/c^2$ is consistent with the world average, but our width value of $\Gamma_{a_2(1700)} = 436\,^{+20}_{-16}\,(\mathrm{sys.})\,\mathrm{MeV}/c^2$ is $242\,\mathrm{MeV}/c^2$ larger. Our width estimate is especially in disagreement with the result of the Belle experiment, which measured an enhancement in the invariant mass spectrum of K^+K^- pairs produced in two-photon collisions [79] with a width of only $151 \pm 22\,(\mathrm{stat.}) \pm 24\,(\mathrm{sys.})\,\mathrm{MeV}/c^2$. The PDG assigns this measurement to the $a_2(1700)$ and includes it in the world average. It is interesting to compare our results with an analysis of the $\eta\pi$ D-wave intensity using an analytical model based on the principles of the relativistic S-matrix [66]. The analysis is based on the partial-wave decomposition of COMPASS data from Ref. [52]. The extracted $a_2(1320)$ pole parameters from Ref. [66] are consistent with the values of our Breit-Wigner parameters. The same is true for the $a_2(1700)$ mass, but the $a_2(1700)$ width of $280 \pm 10\,(\mathrm{stat.}) \pm 70\,(\mathrm{sys.})\,\mathrm{MeV}/c^2$ that is found in Ref. [66] appears to be lower than our value. This is a hint that our simplifying model assumptions may cause an overestimation of the $a_2(1700)$ width.

We observe that the $a_2(1700)$ predominantly decays into $f_2(1270)\pi P$ and less into $\rho(770)\pi D$. This finding is difficult to reconcile with the dominance of the $\rho(770)\pi$ over the $f_2(1270)\pi$ decay mode observed by the L3 experiment in an analysis of the $\pi^+\pi^-\pi^0$ final state produced in two-photon collisions [80]. At the current stage of the analysis we do not make a quantitative statement

on the $a_2(1700)$ branching fractions because the $a_2(1700)$ region in the two $\rho(770)\pi D$ waves is dominated by the $a_2(1320)$ high-mass tail and the nonresonant components.

A number of observations of potential higher excited a_2 states are listed by the PDG as "further states" [10]: $a_2(1950)$ [76], $a_2(1990)$ [72, 80], $a_2(2030)$ [76], $a_2(2175)$ [76], and $a_2(2255)$ [81]. We do not see clear resonance signals of heavy a_2 states above the $a_2(1700)$ in the analyzed waves.

D $J^{PC} = 2^{-+}$ resonances

1 *Results on 2^{-+} resonances*

We include four waves with $J^{PC} = 2^{-+}$ in the resonance-model fit. The $2^{-+}0^+\rho(770)\pi F$ and $2^{-+}0^+ f_2(1270)\pi S$ waves have relatively large intensities and contribute 2.2 % and 6.7 % to the total intensity, respectively. The $2^{-+}1^+ f_2(1270)\pi S$ and $2^{-+}0^+ f_2(1270)\pi D$ waves have smaller intensities and each contributes 0.9 % to the total intensity. Figure 21 shows the intensity distributions of the four waves for the lowest and the highest t' bins (first and third rows, respectively).

The intensities of the $\rho(770)\pi F$ wave and of the two $f_2(1270)\pi S$ waves exhibit a clear peak at $1.65\,\mathrm{GeV}/c^2$, which dominates in particular the $f_2(1270)\pi S$ waves. The position of this peak does not depend strongly on t'. The $\rho(770)\pi F$ wave has an additional high-mass shoulder at $1.9\,\mathrm{GeV}/c^2$, which becomes a dominant peak in the highest t' bin. The $f_2(1270)\pi S$ wave with $M = 0$ has a smaller high-mass shoulder at about $2.05\,\mathrm{GeV}/c^2$, which also grows relative to the $1.65\,\mathrm{GeV}/c^2$ peak with increasing t'. This shoulder is absent in the $f_2(1270)\pi S$ wave with $M = 1$. The $f_2(1270)\pi D$ wave has no structure at $1.65\,\mathrm{GeV}/c^2$. Instead, it exhibits a dominant peak at $1.8\,\mathrm{GeV}/c^2$ and a slight high-mass shoulder at $2.05\,\mathrm{GeV}/c^2$, which becomes more pronounced toward higher t'. The position of the peak is independent of t'.

The $2^{-+}0^+\rho(770)\pi F$ wave and the two $2^{-+} f_2(1270)\pi S$ waves exhibit clearly rising phases with respect to the $1^{++}0^+\rho(770)\pi S$ wave in the region of the $1.65\,\mathrm{GeV}/c^2$ peak (see second and fourth rows in Fig. 21). At low t', the phases of the $2^{-+}0^+\rho(770)\pi F$ and $2^{-+}1^+ f_2(1270)\pi S$ waves continue to rise in the $1.9\,\mathrm{GeV}/c^2$ region [see Figs. 21(e) and 21(g)]. The phase motion of the $2^{-+}0^+\rho(770)\pi F$ wave is approximately independent of t', whereas the phase of the $2^{-+}1^+ f_2(1270)\pi S$ wave flattens out at about $1.9\,\mathrm{GeV}/c^2$ at higher t', making the phase motion of this wave similar to that of the corresponding $M = 0$ wave. The phase motion of the $2^{-+}0^+ f_2(1270)\pi D$ wave with respect to the $1^{++}0^+\rho(770)\pi S$ wave exhibits a rapid rise in the region of the $1.8\,\mathrm{GeV}/c^2$ peak and a slower rise in the region of the $2.05\,\mathrm{GeV}/c^2$ shoulder. The amplitude of the phase motion decreases with increasing t'.

The fit model contains three resonances, $\pi_2(1670)$, $\pi_2(1880)$, and $\pi_2(2005)$, to describe the four $J^{PC} = 2^{-+}$ waves. The resonances are parametrized using Eqs. (22) and (23), the nonresonant components using Eq. (27) for the $2^{-+}0^+ f_2(1270)\pi S$ and $2^{-+}0^+\rho(770)\pi F$ waves and Eq. (29) for the other two 2^{-+} waves (see Table 2). The $\rho(770)\pi F$ wave is fit in the range from 1.2 to $2.1\,\mathrm{GeV}/c^2$, the two $f_2(1270)\pi S$ waves from 1.4 to $2.3\,\mathrm{GeV}/c^2$, and the $f_2(1270)\pi D$ wave from 1.6 to $2.3\,\mathrm{GeV}/c^2$.

The $\rho(770)\pi F$ wave and the two $f_2(1270)\pi S$ waves are dominated by the $\pi_2(1670)$. In the $\rho(770)\pi F$ wave, the nonresonant component is small compared to the $\pi_2(1670)$ component. Only in the two highest t' bins does it have a larger intensity. The contributions from the nonresonant components are larger in the two $f_2(1270)\pi S$ waves. These waves also show a stronger interference of the wave components in the $\pi_2(1670)$ region, in particular at lower t'. In the $\rho(770)\pi F$ wave and the two $f_2(1270)\pi S$ waves, the intensities of the two excited π_2 components are comparable to those of the nonresonant components or even smaller. In the $f_2(1270)\pi S$ wave with $M = 0$, the $\pi_2(1880)$ component is practically vanishing. The excited π_2 components show different

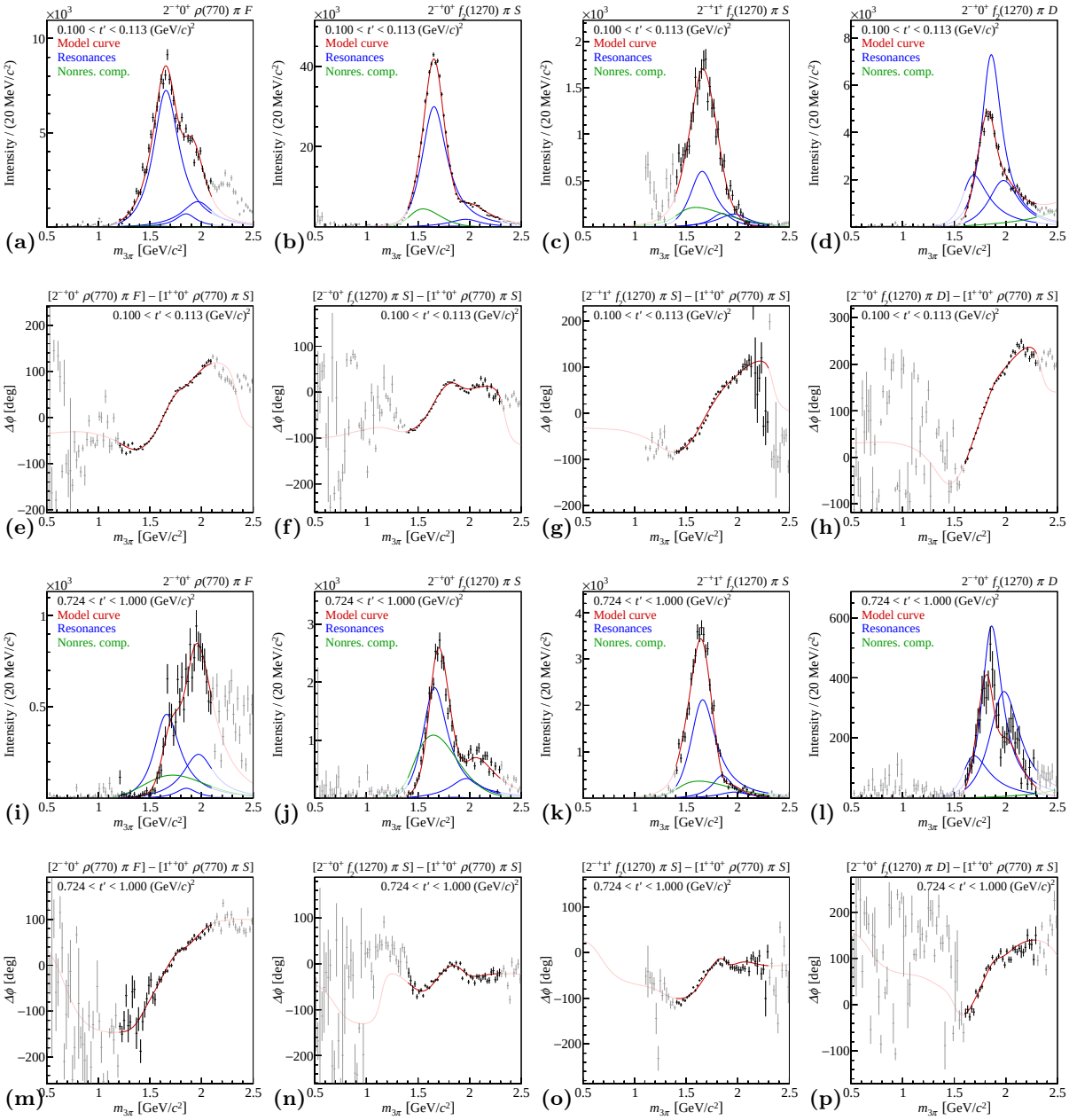

FIG. 21: Amplitudes of the four $J^{PC} = 2^{-+}$ waves: (first column) $2^{-+}0^{+}\rho(770)\pi F$ wave, (second column) $2^{-+}0^{+}f_2(1270)\pi S$ wave, (third column) $2^{-+}1^{+}f_2(1270)\pi S$ wave, and (fourth column) $2^{-+}0^{+}f_2(1270)$ πD wave. (first and third rows) Intensity distributions in the lowest and highest t' bins, respectively. (second and fourth rows) Phases relative to the $1^{++}0^{+}\rho(770)\pi S$ wave in the lowest and highest t' bins, respectively. The model and the wave components are represented as in Fig. 10, except that here the blue curves represent the $\pi_2(1670)$, the $\pi_2(1880)$, and the $\pi_2(2005)$.

interference patterns. In the $\rho(770)\pi F$ wave, significant constructive interference of the wave components describes the high-mass shoulder at $1.9\,\mathrm{GeV}/c^2$. In the $f_2(1270)\pi S$ wave with $M = 0$ these interference effects are much smaller, whereas in the $f_2(1270)\pi S$ wave with $M = 1$ the components interfere destructively leading to a steeper drop of the intensity in the $1.8\,\mathrm{GeV}/c^2$ region at larger t'.

The composition of the $f_2(1270)\pi D$ wave is strikingly different. In this wave, all three resonance components play a significant role, with the $\pi_2(1880)$ being the dominant one that destructively interferes with the other components. At lower values of t', the $\pi_2(1670)$ and the $\pi_2(2005)$ appear with similar intensities. In the two highest t' bins, the $\pi_2(2005)$ component becomes larger. The contribution from the nonresonant component is small.

Within the fit ranges, the fit model describes the intensity distributions in general well. This is in particular true for the two $f_2(1270)\pi S$ waves. The fit model does not reproduce the details of the high-mass shoulder at $2.05\,\mathrm{GeV}/c^2$ in the $f_2(1270)\pi D$ wave. In this wave, also the extrapolation of the fit model above the fit range of $2.3\,\mathrm{GeV}/c^2$ deviates from the data, in particular at lower t'. In the $\rho(770)\pi F$ wave, the fit model does not reproduce details of the peak at $1.65\,\mathrm{GeV}/c^2$ and of the shoulder at $1.9\,\mathrm{GeV}/c^2$. The extrapolation of the fit model above the fit range of $2.1\,\mathrm{GeV}/c^2$ deviates from the data.

The dominance of the $\pi_2(1670)$ in the $\rho(770)\pi F$ wave and in the two $f_2(1270)\pi S$ waves is supported by the clearly rising phases of these waves with respect to the $1^{++}0^+\rho(770)\pi S$ wave (see Fig. 21). It is also consistent with the approximately constant relative phases among these three 2^{-+} waves in the $1.6\,\mathrm{GeV}/c^2$ region at low t' (see Fig. 22). Above the $\pi_2(1670)$ region, the similar relative strengths of $\pi_2(1880)$ and $\pi_2(2005)$ in the $2^{-+}0^+\rho(770)\pi F$ and $2^{-+}1^+ f_2(1270)\pi S$ waves lead to only small variations of their relative phase. The $2^{-+}0^+\rho(770)\pi F$ and $2^{-+}1^+ f_2(1270)\pi S$ waves exhibit more pronounced phase motions in the $1.9\,\mathrm{GeV}/c^2$ region with respect to the $2^{-+}0^+ f_2(1270)\pi S$ wave because of the vanishing $\pi_2(1880)$ component in the latter wave. The interference pattern of the three 2^{-+} waves changes toward higher t' mainly because of the changing composition of the $2^{-+}0^+\rho(770)\pi F$ wave (see Fig. 23). The phase of the $2^{-+}0^+ f_2(1270)\pi D$ wave with respect to the $1^{++}0^+\rho(770)\pi S$ wave rises in the $1.8\,\mathrm{GeV}/c^2$ region and, less rapidly, in the $2.0\,\mathrm{GeV}/c^2$ region. This phase motion is caused by $\pi_2(1880)$ and $\pi_2(2005)$ and is connected to the phases of the coupling amplitudes of the two heavier π_2, which are close to 180° relative to the $\pi_2(1670)$ in this wave (see Sec. VII). With respect to the other three 2^{-+} waves, the $f_2(1270)\pi D$ wave shows similar phase motions. This is consistent with the large contributions from $\pi_2(1880)$ and $\pi_2(2005)$ in this wave compared to the $\pi_2(1670)$ component.

Within the fit range, the model is able to describe well most of the phase motions. Some details in the high-mass regions are not reproduced. Often, the high-mass extrapolations of the fit model deviate from the data (see e.g., Fig. 22 and the second row of Fig. 21). In some cases, this is also true for the extrapolations below the low-mass limits of the fit ranges (see e.g., Fig. 22). However, in many of these cases the intensities of the waves are small.

The extracted resonance parameters for $\pi_2(1670)$, $\pi_2(1880)$, and $\pi_2(2005)$ are

$$
\begin{aligned}
m_{\pi_2(1670)} &= 1642\,{}^{+12}_{-1}\,(\mathrm{sys.})\,\mathrm{MeV}/c^2,\\
\Gamma_{\pi_2(1670)} &= 311\,{}^{+12}_{-23}\,(\mathrm{sys.})\,\mathrm{MeV}/c^2,\\
m_{\pi_2(1880)} &= 1847\,{}^{+20}_{-3}\,(\mathrm{sys.})\,\mathrm{MeV}/c^2,\\
\Gamma_{\pi_2(1880)} &= 246\,{}^{+33}_{-28}\,(\mathrm{sys.})\,\mathrm{MeV}/c^2,\\
m_{\pi_2(2005)} &= 1962\,{}^{+17}_{-29}\,(\mathrm{sys.})\,\mathrm{MeV}/c^2, \text{ and}\\
\Gamma_{\pi_2(2005)} &= 371\,{}^{+16}_{-120}\,(\mathrm{sys.})\,\mathrm{MeV}/c^2.
\end{aligned}
$$

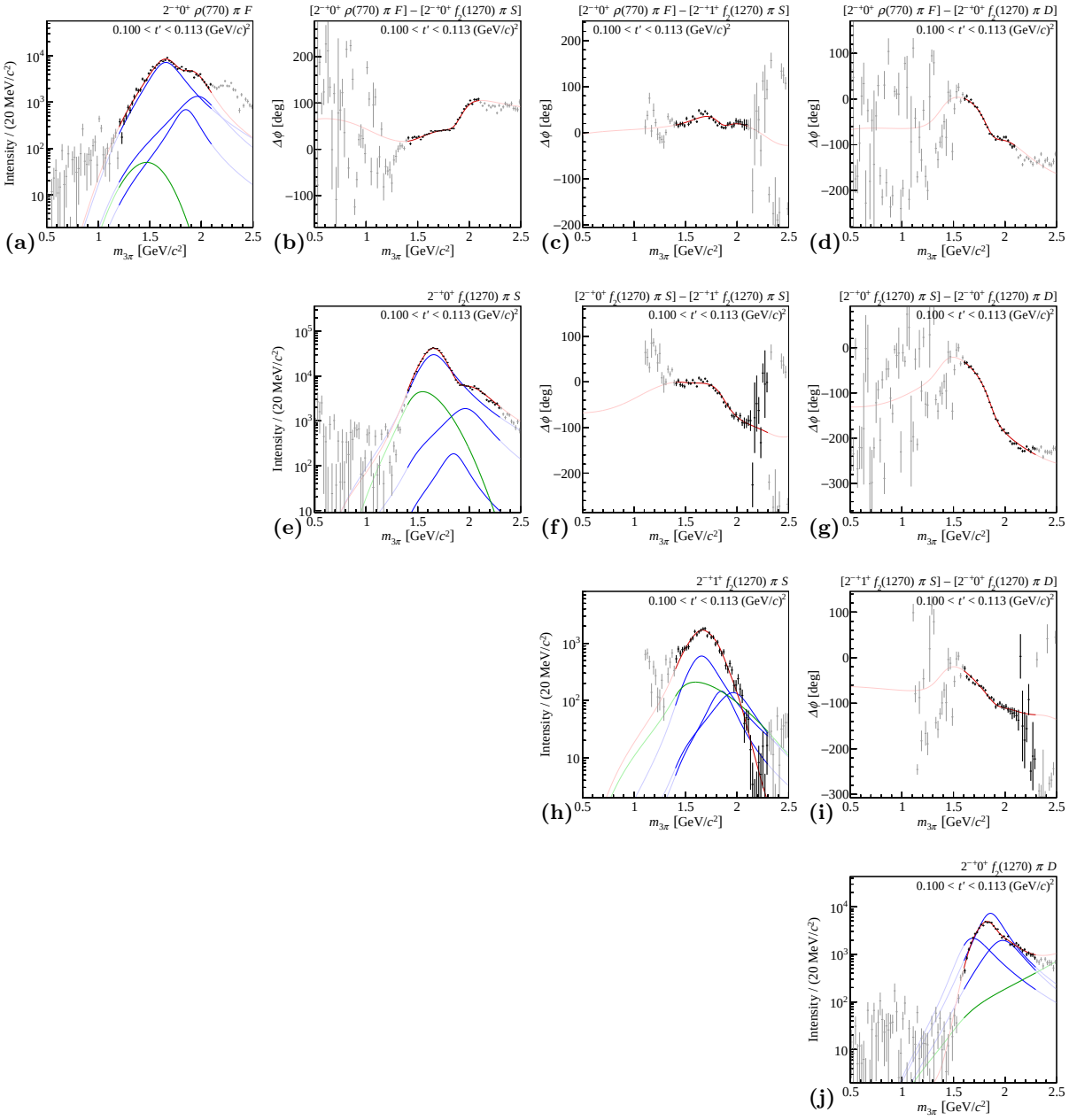

FIG. 22: Amplitudes of the four $J^{PC} = 2^{-+}$ waves in the lowest t' bin. (a) through (d): Intensity distribution and relative phases for the $2^{-+}0^+\rho(770)\pi F$ wave. (e) through (g): Intensity distribution and relative phases for the $2^{-+}0^+f_2(1270)\pi S$ wave. (h) and (i): Intensity distribution and relative phase for the $2^{-+}1^+f_2(1270)\pi S$ wave. (j): Intensity distribution for the $2^{-+}0^+f_2(1270)\pi D$ wave. The model and the wave components are represented as in Fig. 21.

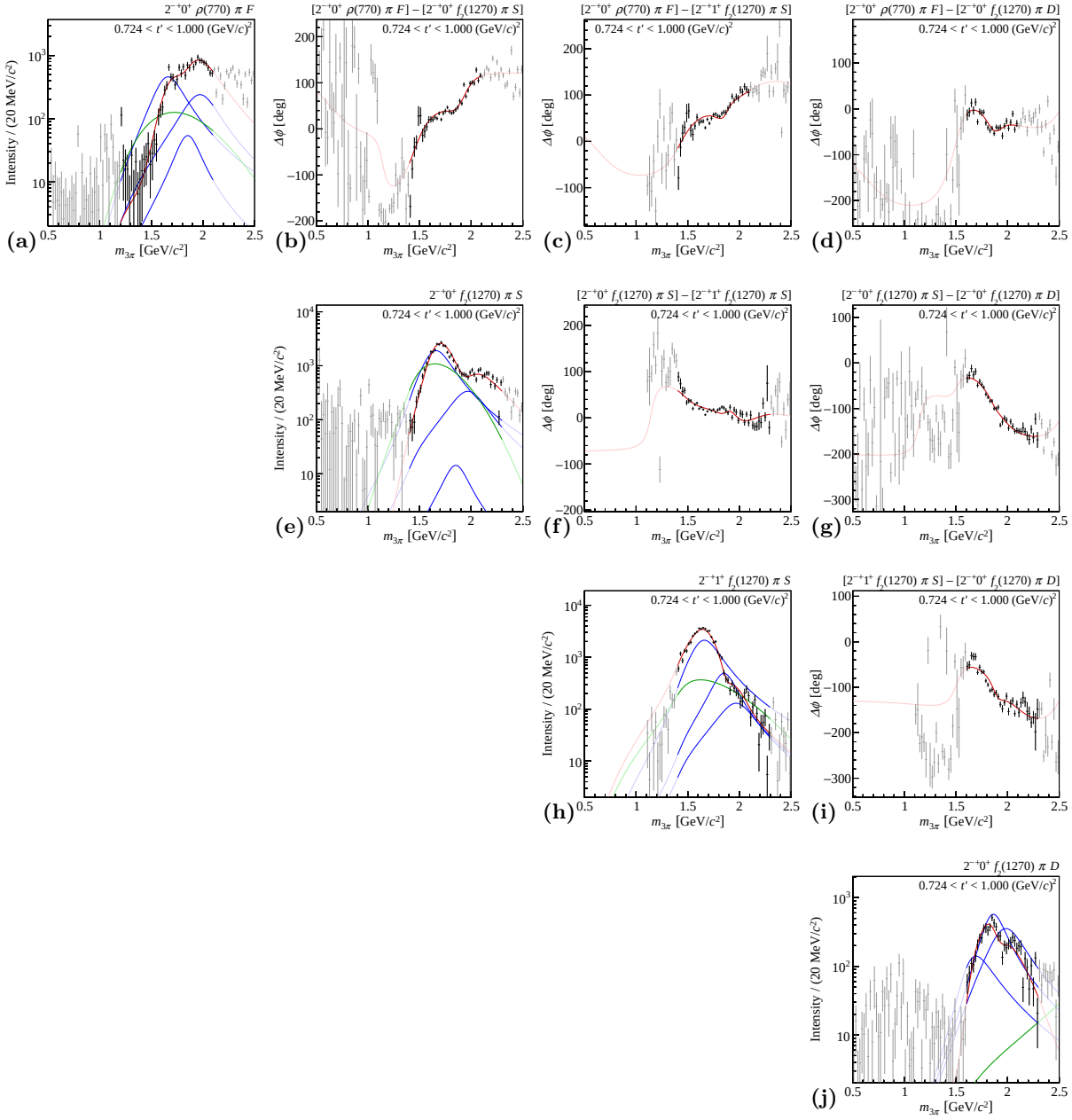

FIG. 23: Similar to Fig. 22 but for the highest t' bin.

Hence in the 2^{-+} sector, the model assumption of well-separated resonances with little overlap is not well fulfilled. Although constrained by the amplitudes of four waves, the 2^{-+} resonance parameters exhibit a larger sensitivity to changes of the fit model discussed in Sec. V. They therefore have larger systematic uncertainties than, for example, the parameters of the $\pi(1800)$. In addition, some of the systematic uncertainty intervals are highly asymmetric. The parameters of the three 2^{-+} resonances are correlated in a complicated way and depend, among other things, on the set of waves included in the fit. Also the number of background events in the selected data sample influences the resonance parameters. The parameters of $\pi_2(1880)$ and $\pi_2(2005)$ are in addition sensitive to the number of t' bins. This underlines the importance of using a fine-grained t' binning in order to capture the evolution of the 2^{-+} amplitudes with t'. The 2^{-+} resonance parameters exhibit an exceptionally large sensitivity to the $m_{3\pi}$ and t' dependences of the production probability $|\mathcal{P}(m_{3\pi}, t')|^2$ in Eqs. (20) and (32). The widths of $\pi_2(1670)$ and $\pi_2(1880)$ are also affected by the interference of the 2^{-+} waves with the low-mass part of the 0^{-+} $0^+ f_0(980)\pi S$ wave. More details on the results of the systematic studies can be found in Sec. D 5.

Figures 24 and 25 show the t' dependence of the intensities of the resonant and nonresonant 2^{-+} wave components together with the results of fits using Eq. (41). In our fit model, the coupling amplitudes of the resonance components in the three 2^{-+} waves with $M = 0$ are constrained by Eq. (21). The t' spectra of the resonance components are well described by the exponential model in Eq. (41). The extracted values of the slope parameters for $\pi_2(1670)$, $\pi_2(1880)$, and $\pi_2(2005)$ are approximately $8.5\,(\mathrm{GeV}/c)^{-2}$, $7.8\,(\mathrm{GeV}/c)^{-2}$, and $6.7\,(\mathrm{GeV}/c)^{-2}$, respectively [see Table 6 for details], which are typical values for resonances. As for the 1^{++} and 2^{++} resonances, the slope parameter decreases with increasing mass of the resonance. This flattening of the t' slope with increasing $m_{3\pi}$ was also observed in the t' spectra before partial-wave decomposition (see e.g., Fig. 31 in Ref. [30]). The three-component Deck model [58, 82, 83] may explain this behavior. The relative enhancement of higher-mass states at larger values of t' helps to better disentangle the various resonance components.

In the fit model, the t' dependence of the coupling amplitudes of the resonant components in the $2^{-+}1^+ f_2(1270)\pi S$ wave is not constrained by Eq. (21). Due to the relative smallness of this wave, the intensities of the wave components are extracted less reliably. Equation (41) does not describe well the t' spectra of the wave components. This is in particular true for the $\pi_2(1670)$ and $\pi_2(1880)$. Hence only a rough comparison of the slope parameters is possible. The slope parameter values for $\pi_2(1880)$ and $\pi_2(2005)$ are compatible with those found in the other three 2^{-+} waves. However, the slope of the $\pi_2(1670)$ t' spectrum is significantly smaller with $b = 5.0\,(\mathrm{GeV}/c)^{-2}$. This effect is not understood but it is consistent with the shallower t' slope of the intensity of this wave in the $\pi_2(1670)$ mass region (see Table VI in Ref. [30]).

Compared to the other J^{PC} sectors, where we observe in general a steeper t' slope for the nonresonant components than for the resonances, the nonresonant components in the 2^{-+} sector behave somewhat irregularly. The only exception is the nonresonant component in the $f_2(1270)\pi D$ wave. Its t' spectrum is well described by the exponential in Eq. (41) and has a slope of $12\,^{+6}_{-2}\,(\mathrm{sys.})\,(\mathrm{GeV}/c)^{-2}$, which is considerably steeper than the slopes of the π_2 resonances [see Fig. 25(b)]. The t' spectrum of the nonresonant component in the $f_2(1270)\pi S$ wave with $M = 1$ has a shallower slope of $6.9\,^{+1.1}_{-1.9}\,(\mathrm{sys.})\,(\mathrm{GeV}/c)^{-2}$ that is comparable to those of the π_2 resonances [see Fig. 24(h)]. However, at low t' the data deviate from the fit model. Also for the nonresonant component in the $f_2(1270)\pi S$ wave with $M = 0$, the model deviates from the data at low t' [see Fig. 24(d)]. Equation (41) cannot reproduce the step at $t' \approx 0.16\,(\mathrm{GeV}/c)^2$. The extracted value of $5.1\,(\mathrm{GeV}/c)^{-2}$ for the slope parameter is smaller than that for the π_2 resonances, but is not well defined. The nonresonant component in the $\rho(770)\pi F$ wave exhibits a complicated t' spectrum [see Fig. 25(a)]. It has a narrow dip at about $0.16\,(\mathrm{GeV}/c)^2$ at the same location where

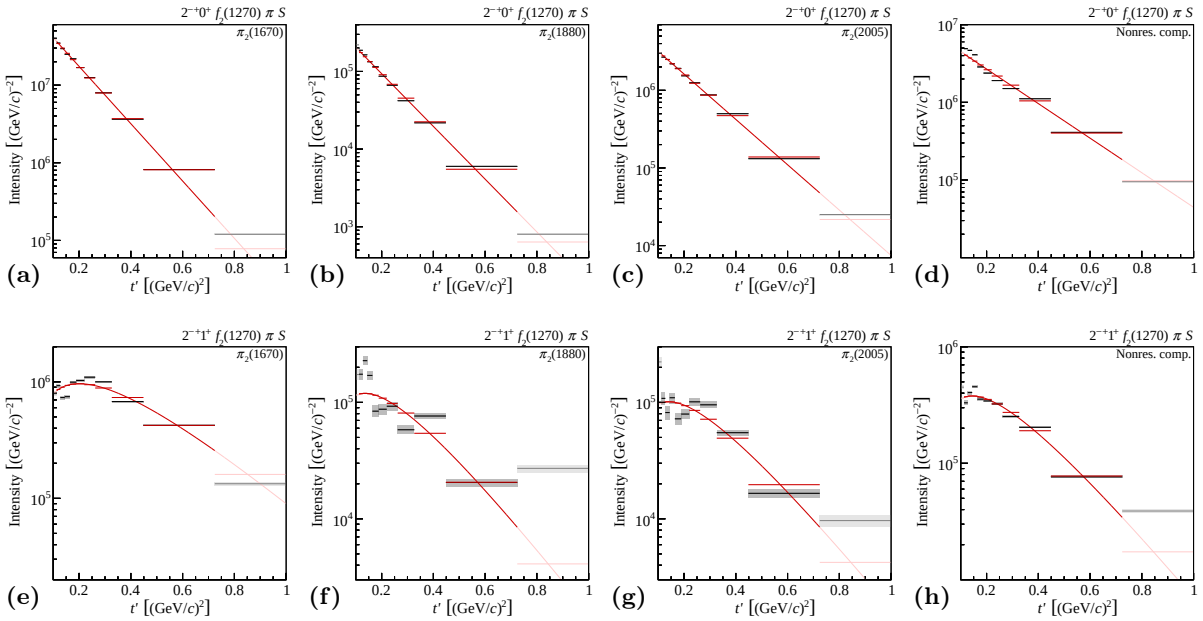

FIG. 24: Similar to Fig. 7, but showing the t' spectra of the components in the two $2^{-+}f_2(1270)\pi S$ waves as given by Eq. (40): (top row) $M^\varepsilon = 0^+$ wave and (bottom row) $M^\varepsilon = 1^+$ wave; (first column) $\pi_2(1670)$ component, (second column) $\pi_2(1880)$ component, (third column) $\pi_2(2005)$ component, and (fourth column) nonresonant components. The red curves and horizontal lines represent fits using Eq. (41).

we observe a step in the t' spectrum of the nonresonant component in the $2^{-+}0^+f_2(1270)\pi S$ wave. Equation (41) cannot describe such a distribution. The complicated shape of the t' spectrum may be an artifact caused by forcing the same t' dependence of the resonances in the $M = 0$ waves via Eq. (21). However, if we leave the t' dependence of all resonance components free [see discussion of Study (M) below], the dip at low t' remains. Since at low t' the nonresonant component is much smaller than any of the three resonance components, its intensity is less well determined and more sensitive to systematic effects. Monte Carlo studies of a model for the Deck effect (see Sec. B) have shown that the projection of this nonresonant amplitude into the $\rho(770)\pi F$ wave is vanishingly small so that the observed nonresonant intensity is presumably of different origin.

If we do not constrain the coupling amplitudes via Eq. (21) and thus allow the resonance components to have different t' dependences [Study (M); see Sec. V], the extracted t' spectra agree in general less with the simple model of Eq. (41). The components of the $2^{-+}1^+f_2(1270)\pi S$ and $2^{-+}0^+f_2(1270)\pi D$ waves show similar t' spectra with slope parameters that deviate by at most $2\,(\mathrm{GeV}/c)^{-2}$ from those of the main fit. This is also true for the $\pi_2(1670)$ component in the other two 2^{-+} waves, the $\pi_2(1880)$ component in the $2^{-+}0^+\rho(770)\pi F$ wave, and the $\pi_2(2005)$ component in the $2^{-+}0^+f_2(1270)\pi S$ wave. However, in the latter wave, the slope parameter of the $\pi_2(1880)$ becomes almost twice as large and thus inconsistent with the $\pi_2(1880)$ slope parameters in the other three waves. In the $\rho(770)\pi F$ wave, the $\pi_2(2005)$ t' spectrum changes drastically and becomes similar to the t' spectrum of the nonresonant component in the main fit. In turn, the t' spectrum of the nonresonant component becomes steeper. In addition to the t' spectra, also the resonance parameters of $\pi_2(1880)$ and $\pi_2(2005)$ change in Study (M). The $\pi_2(1880)$ becomes $29\,\mathrm{MeV}/c^2$ wider, whereas the $\pi_2(2005)$ becomes $75\,\mathrm{MeV}/c^2$ narrower. The results of this study indicate that without the constraint of Eq. (21), the relative intensities of the three π_2 states and the nonresonant components are not well constrained by the data. A possible reason for this behavior is that our approach to model the partial-wave amplitudes as a sum of Breit-Wigner amplitudes might not be a good approximation anymore because of the

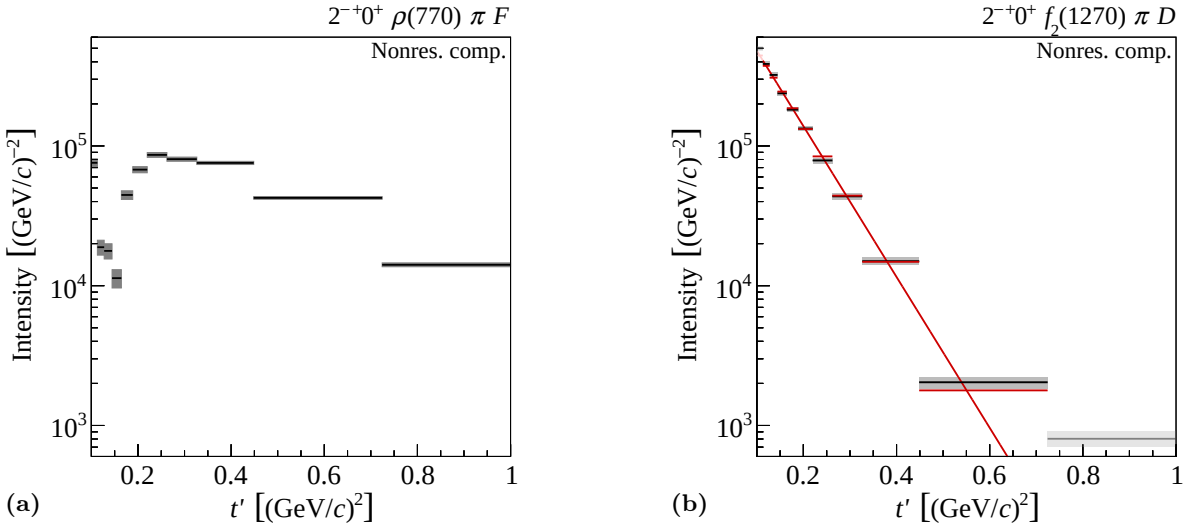

FIG. 25: Similar to Fig. 7, but showing the t' spectra of the nonresonant components (a) in the $2^{-+}0^{+}$ $\rho(770)\pi F$ wave and (b) in the $2^{-+}0^{+}f_2(1270)\pi D$ wave. The red curve and horizontal lines in (b) represent a fit using Eq. (41).

considerable overlap of the three π_2 resonances. Applying more advanced models is the topic of future research [64, 65].

2 Discussion of results on 2^{-+} resonances

We observe three distinct resonances with $J^{PC} = 2^{-+}$ in our data set, which are clearly identified owing to their different production characteristic and decay paths. The $\pi_2(1670)$ appears as a dominant peak with associated phase motion in the $\rho(770)\pi F$ and the two $f_2(1270)\pi S$ waves with $M^{\varepsilon} = 0^{+}$ and 1^{+}. The strongest signal for the $\pi_2(1880)$ appears in the $f_2(1270)\pi D$ wave in the form of a dominant peak with associated phase motion. The relative intensity of the $\pi_2(1880)$ in the other three 2^{-+} waves is small, which is in particular true for the $2^{-+}0^{+}f_2(1270)\pi S$ wave. The $\pi_2(2005)$ appears as high-mass shoulders in the $2^{-+}0^{+}\rho(770)\pi F$, $2^{-+}0^{+}f_2(1270)\pi S$, and $2^{-+}0^{+}f_2(1270)\pi D$ waves, which due to the shallower t' slope of the $\pi_2(2005)$ are more pronounced in the highest t' bin. In the $\rho(770)\pi F$ wave, this shoulder even turns into a clear peak at large t'. The $\pi_2(2005)$ contribution is significantly larger than that of the $\pi_2(1880)$ in the $\rho(770)\pi F$ wave and in the $f_2(1270)\pi S$ wave with $M = 0$. In the $f_2(1270)\pi S$ wave with $M = 1$, the two contributions are of comparable strength.

The parameters of the $\pi_2(1670)$ are well known. The PDG quotes world averages for its mass and width of $m_{\pi_2(1670)} = 1672.2 \pm 3.0\,\mathrm{MeV}/c^2$ and $\Gamma_{\pi_2(1670)} = 260 \pm 9\,\mathrm{MeV}/c^2$, respectively [10]. We find a mass of $m_{\pi_2(1670)} = 1642\,^{+12}_{-1}\,(\mathrm{sys.})\,\mathrm{MeV}/c^2$, which is smaller by $30\,\mathrm{MeV}/c^2$, and a width of $\Gamma_{\pi_2(1670)} = 311\,^{+12}_{-23}\,(\mathrm{sys.})\,\mathrm{MeV}/c^2$, which is larger by $51\,\mathrm{MeV}/c^2$. However, within uncertainties our result is consistent with our previous measurement of the $\pi^-\pi^-\pi^+$ final state diffractively produced on a solid lead target [17]. It is interesting to note that a study with a reduced set of only 11 waves, from which all 2^{-+} waves but the $2^{-+}0^{+}f_2(1270)\pi S$ wave have been removed, yields $\pi_2(1670)$ resonance parameters of $m_{\pi_2(1670)} = 1663\,\mathrm{MeV}/c^2$ and $\Gamma_{\pi_2(1670)} = 256\,\mathrm{MeV}/c^2$, which are close to the world average. In that fit, the $2^{-+}0^{+}f_2(1270)\pi S$ amplitude was described in a smaller mass range from 1.4 to $1.9\,\mathrm{GeV}/c^2$ using the $\pi_2(1670)$ as the only 2^{-+} resonance component.

The $\pi_2(1880)$ appears to be experimentally well established according to the PDG, although its measured mass and width values vary considerably. The PDG lists no observation for the

decay $\pi_2(1880) \to 3\pi$. The PDG world averages of the $\pi_2(1880)$ parameters are $m_{\pi_2(1880)} = 1895 \pm 16\,\mathrm{MeV}/c^2$ and $\Gamma_{\pi_2(1880)} = 235 \pm 34\,\mathrm{MeV}/c^2$ [10]. While we find a value for the $\pi_2(1880)$ width of $\Gamma_{\pi_2(1880)} = 246\,^{+33}_{-28}\,(\mathrm{sys.})\,\mathrm{MeV}/c^2$ that is compatible with the world average, our mass value of $m_{\pi_2(1880)} = 1847\,^{+20}_{-3}\,(\mathrm{sys.})\,\mathrm{MeV}/c^2$ is $48\,\mathrm{MeV}/c^2$ smaller. The four measurements listed by the PDG fall into two subsets. The first consists of two measurements with lower masses $m_{\pi_2(1880)} \leq 1880\,\mathrm{MeV}/c^2$ and smaller widths $\Gamma_{\pi_2(1880)} \leq 255\,\mathrm{MeV}/c^2$ [72, 84]. Our estimate of the $\pi_2(1880)$ parameters is within uncertainties compatible with these two measurements, although there is some disagreement with the extremely small width estimate of $146 \pm 17\,(\mathrm{stat.}) \pm 62\,(\mathrm{sys.})\,\mathrm{MeV}/c^2$ from Ref. [72]. The other two measurements with larger masses $m_{\pi_2(1880)} \geq 1929\,\mathrm{MeV}/c^2$ and larger widths $\Gamma_{\pi_2(1880)} \geq 306\,\mathrm{MeV}/c^2$ [85, 86] are better compatible with our estimates for the $\pi_2(2005)$ parameters.

The $\pi_2(2005)$ is listed by the PDG only as a "further state" with two observations [10]. It was claimed in an analysis by the BNL E852 experiment of the $\omega\pi^0\pi^-$ final state diffractively produced on a proton target [72] and in two analyses based on $p\bar{p}$ annihilation data from the Crystal Barrel experiment: a combined analysis of $3\pi^0$, $\pi^0\eta$, and $\pi^0\eta'$ final states [76] and an analysis of $\eta\eta\pi^0$ [81]. The mass range explored in $p\bar{p}$ annihilations in flight starts only around $1.95\,\mathrm{GeV}/c^2$ and thus covers only the high-mass part of the $\pi_2(2005)$ resonance. Within uncertainties, our estimate for the $\pi_2(2005)$ parameters, $m_{\pi_2(2005)} = 1962\,^{+17}_{-29}\,(\mathrm{sys.})\,\mathrm{MeV}/c^2$ and $\Gamma_{\pi_2(2005)} = 371\,^{+16}_{-120}\,(\mathrm{sys.})\,\mathrm{MeV}/c^2$, is compatible with either measurement.

In order to study the significance of the $\pi_2(2005)$ signal in our data, we have performed a systematic study, in which we omitted the $\pi_2(2005)$ from the fit model. The minimum χ^2 value found in this fit is 1.07 times larger than the one of the main fit.[am] Figure 26 shows the contributions from the spin-density matrix elements to the χ^2 difference between this and the main fit. Without the $\pi_2(2005)$, the model describes the 2^{-+} intensity distributions and interference terms less well, in particular for the $2^{-+}0^+ f_2(1270)\pi S$ and $2^{-+}0^+ f_2(1270)\pi D$ waves. Figure 27 shows that the high-mass shoulders cannot be reproduced well. Omitting the $\pi_2(2005)$ component also shifts some of the resonance parameters. On the one hand, the $\pi_2(1880)$ becomes $20\,\mathrm{MeV}/c^2$ lighter and $100\,\mathrm{MeV}/c^2$ wider, which would be contradictory to all previous measurements. On the other hand, the $\pi_2(1670)$ parameters move closer to the PDG world average.[an]

In addition to $\pi_2(1670)$, $\pi_2(1880)$, and $\pi_2(2005)$, the PDG lists the $\pi_2(2100)$ as "omitted from summary table" [10]. The PDG entry is based on two observations reported by the ACCMOR [31] and the VES experiments [45] in the diffractively produced $\pi^-\pi^-\pi^+$ final state. The $\pi_2(2100)$ thus requires further experimental confirmation. It is close in mass to the $\pi_2(2005)$, but has a much larger width of $625 \pm 50\,\mathrm{MeV}/c^2$. In the ACCMOR analysis, the intensity distributions of the $2^{-+}0^+[\pi\pi]_S\pi D$, $2^{-+}0^+\rho(770)\pi P$, $2^{-+}0^+ f_2(1270)\pi S$, and $2^{-+}0^+ f_2(1270)\pi D$ waves were fit together with selected relative phases of these waves using a model with two 2^{-+} resonances, $\pi_2(1670)$ and $\pi_2(2100)$, which was based on the K-matrix approach [31]. In this model, the dominant peak at $1.8\,\mathrm{GeV}/c^2$ in the $f_2(1270)\pi D$ wave is explained as a constructive interference of the two resonance components. The VES analysis is similar and confirms this finding [45]. It is worth noting that in both analyses rather high $\pi_2(1670)$ masses $\geq 1710\,\mathrm{MeV}/c^2$ are found. Our data exhibit similar features as the ACCMOR and VES data. In particular, considering the uncertainties it is likely that our $\pi_2(2005)$ signal corresponds to the $\pi_2(2100)$ measurements discussed above, although the width estimates differ significantly. The main difference of our analysis is that we include different waves in the resonance-model fit. We did not include the

[am] Compared to the 722 free parameters of the main fit, this fit has 672 free parameters.

[an] The $\pi_2(1670)$ becomes $17\,\mathrm{MeV}/c^2$ heavier and $20\,\mathrm{MeV}/c^2$ narrower. Large changes are also observed for the $a_1(1640)$, which becomes $42\,\mathrm{MeV}/c^2$ lighter and $82\,\mathrm{MeV}/c^2$ wider, and for the $\pi_1(1600)$, which becomes $51\,\mathrm{MeV}/c^2$ narrower.

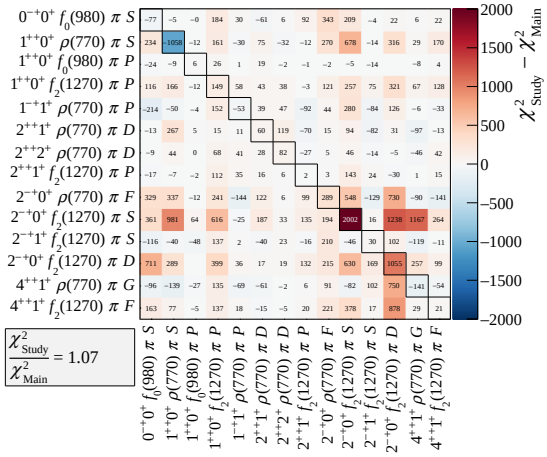

FIG. 26: Similar to Fig. 9, but for the study in which the $\pi_2(2005)$ resonance was omitted from the fit model.

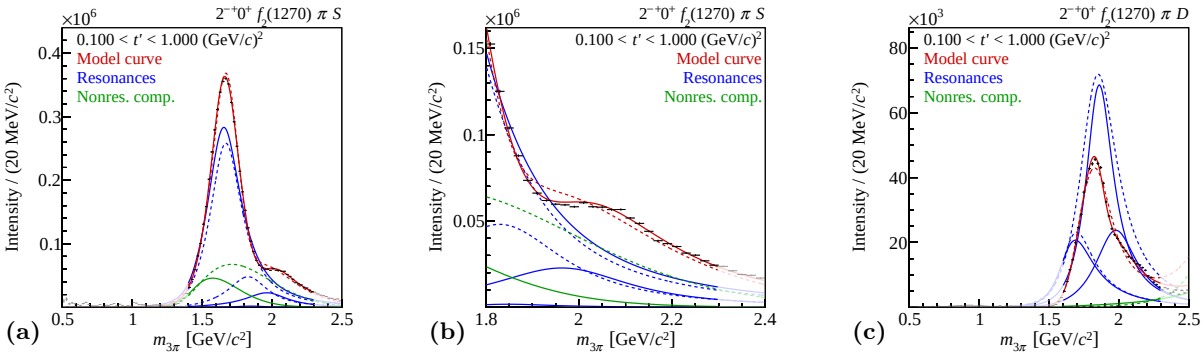

FIG. 27: t'-summed intensities of (a) the $2^{-+}0^{+}f_2(1270)\pi S$ wave and (c) the $2^{-+}0^{+}f_2(1270)\pi D$ wave with the result of the main fit (continuous curves) and of the fit in which the $\pi_2(2005)$ resonance was omitted from the fit model (dashed curves). The model and the wave components are represented as in Fig. 21. In (b), a zoomed view of the high-mass region in (a) is shown.

$\rho(770)\pi P$ wave because it exhibits a sizable and not well understood low-mass enhancement below the $\pi_2(1670)$ region [see Fig. 57(e) in Ref. [87]]. The $[\pi\pi]_S\pi D$ and $f_0(980)\pi D$ waves have complicated intensity distributions [see Figs. 25(c) and 25(d) in Ref. [30]]. At low $m_{3\pi}$, both partial-wave intensities are sensitive to the wave set that is used in the mass-independent analysis. They also may be affected by the particular parametrizations chosen for the $[\pi\pi]_S$ and $f_0(980)$ isobar amplitudes. A less model-dependent analysis, in which the amplitude of the $\pi^-\pi^+$ S-wave subsystem was extracted from the data instead of using a parametrization with fixed functional form, shows a clear correlation of a peak in the region of $m_{3\pi} = 1.9\,\mathrm{GeV}/c^2$, which is presumably the $\pi_2(1880)$, with a peak in the $f_0(980)$ region in the $\pi^-\pi^+$ mass spectrum [see Figs. 40 and 43(c) in Ref. [30]]. However, shape, position, and strength of the observed peak structure in the $\pi_2(1670)$ region depend strongly on t', which hints at large contributions from nonresonant components.

As discussed above, the four 2^{-+} waves selected for the resonance-model fit are not well described if we include only two 2^{-+} Breit-Wigner resonances in the model. In particular, we do not observe solutions similar to those found by ACCMOR or VES with a second resonance in the $2.1\,\mathrm{GeV}/c^2$ region. It is therefore unlikely that the $\pi_2(1880)$ signal is caused by a constructive interference of the other two resonances. It is also unlikely that the $\pi_2(1880)$ signal arises from an interference with a nonresonant component since the t' spectrum of the $\pi_2(1880)$ exhibits a resonancelike behavior [see Figs. 24(b) and 24(f)].

The PDG lists another potential higher excited π_2 state, the $\pi_2(2285)$, as a "further state" [10]. It was reported with the parameters $m_{\pi_2(2285)} = 2285 \pm 20\,(\mathrm{stat.}) \pm 25\,(\mathrm{sys.})\,\mathrm{MeV}/c^2$ and $\Gamma_{\pi_2(2285)} = 250 \pm 20\,(\mathrm{stat.}) \pm 25\,(\mathrm{sys.})\,\mathrm{MeV}/c^2$ by the authors of Ref. [88] in an analysis of the $\eta\pi^0\pi^0\pi^0$ final state produced in $p\bar{p}$ annihilations in flight, which was based on data from the Crystal Barrel experiment. Although we do not see clear resonance signals of heavy π_2 states in the mass range from 2200 to $2500\,\mathrm{MeV}/c^2$ in the analyzed waves, we cannot exclude that the observed deviations of the model from the data at high masses, in particular in the $2^{-+}0^+\rho(770)\pi F$ wave, are due to additional excited π_2 states.

The mass of the $\pi_2(1670)$ agrees well with the quark-model prediction for the π_2 ground state by Godfrey and Isgur [89]. The mass of the $\pi_2(2005)$ agrees with the prediction for the first radial excitation of the π_2. However, the $\pi_2(1880)$ does not fit into this picture. The interpretations of the $\pi_2(1880)$ are manifold. It has been interpreted as a supernumerous exotic meson with conventional quantum numbers. It has in particular been considered as a good candidate for a hybrid meson by the authors of Refs. [11, 84]. In contrast, Li and Zhou argue in Ref. [90] that the observed decay width of approximately $235\,\mathrm{MeV}/c^2$ is too large for a pure hybrid state, for which a smaller width of rather $100\,\mathrm{MeV}/c^2$ would be expected. In addition, the dominant decay into the $f_2(1270)\pi D$ wave and the small coupling to the $f_2(1270)\pi S$ wave that we observe in our data contradict the hybrid-meson interpretation based on model calculations for the decay of such objects performed by Page, Swanson, and Szczepaniak in Ref. [91], which predict the opposite behavior for a hybrid resonance. Li and Zhou argue that the $\pi_2(1880)$ decay pattern is more similar to model predictions for the first radial excitation of the conventional π_2 [90]. However, they do not exclude a possible small admixture of a hybrid state.

In an alternative approach, Dudek and Szczepaniak have proposed in Ref. [92] that the $1.65\,\mathrm{GeV}/c^2$ peak in the $f_2(1270)\pi S$ wave and the $1.8\,\mathrm{GeV}/c^2$ peak in the $f_2(1270)\pi D$ wave are caused by the same π_2 ground-state resonance. The seemingly different structures are caused by interference of this resonance with a type of nonresonant background originally proposed by Deck [43], which is much stronger in the $f_2(1270)\pi S$ wave. In order to explain the phase motions, this model requires a second π_2 resonance at a higher mass as in the ACCMOR and VES analyses discussed above. Their hypothesis may be tested by including the t' dependence and the population of the

M substates of the Deck amplitude.

E $J^{PC} = 1^{++}$ resonances

1 Results on 1^{++} resonances

The resonance-model fit includes three waves with $J^{PC} = 1^{++}$. The $1^{++}0^+\rho(770)\pi S$ wave is the most dominant wave in the 88-wave set with a relative intensity of 32.7 %. The $1^{++}0^+f_0(980)\pi P$ and $1^{++}0^+f_2(1270)\pi P$ waves are about 2 orders of magnitude less intense with relative intensities of 0.4 % and 0.3 %, respectively. The intensity distributions of the three 1^{++} waves, as shown in Figs. 28(a), 28(e), and 28(h) for the lowest t' bin and in Figs. 29(a), 29(e), and 29(h) for the highest t' bin, are surprisingly different.

The $1^{++}0^+\rho(770)\pi S$ intensity exhibits a broad peak around $1.2\,\mathrm{GeV}/c^2$, which changes its shape and shifts by about $140\,\mathrm{MeV}/c^2$ toward higher masses with increasing t' (see Fig. 30). This behavior suggests large contributions from nonresonant components in addition to the expected $a_1(1260)$ signal and underlines the importance of a t'-resolved analysis to better disentangle these components.

The $1^{++}0^+f_2(1270)\pi P$ intensity distribution exhibits a low-mass enhancement below threshold and a broad peak structure at about $1.8\,\mathrm{GeV}/c^2$ that disappears in the two highest t' bins. In addition, a weaker enhancement appears around $1.5\,\mathrm{GeV}/c^2$ at lower t'. A portion of the low-mass enhancement might originate from leakage within the 1^{++} sector at the stage of the partial-wave decomposition.[ao] This leakage is presumably induced by Deck-like nonresonant contributions. Monte Carlo simulations of a model for the Deck amplitude (see Sec. B) have shown that at low t', the shapes of the isobars are distorted, especially that of the $\rho(770)$. This might cause leakage into the $f_2(1270)\pi P$ wave, which has an intensity that is 2 orders of magnitude smaller than that of the $\rho(770)\pi S$ wave.

The most peculiar intensity distribution is observed for the $1^{++}0^+f_0(980)\pi P$ wave. It has a dominant narrow peak at approximately $1.45\,\mathrm{GeV}/c^2$ that disappears in the highest t' bin. In this mass region, large and rapid phase motions of the $f_0(980)\pi P$ wave are observed relative to the other two 1^{++} waves in all t' bins [see Figs. 28(b), 28(f), 29(b), and 29(f)]. This suggests that the $f_0(980)\pi P$ wave has a different resonance content. Similar phase motions are also observed with respect to other waves. As an example, Figs. 28(g) and 29(g) show the phases relative to the $4^{++}1^+\rho(770)\pi G$ wave, where the latter was discussed in Sec. VI B 1.

Also the relative phase between the $1^{++}0^+\rho(770)\pi S$ and $1^{++}0^+f_2(1270)\pi P$ waves changes substantially with $m_{3\pi}$ [see Figs. 28(c) and 29(c)], which suggests that the wave components contribute with different strengths to these two waves. At high t', this phase becomes approximately constant in the $a_1(1260)$ region and the phase motion in the $1.6\,\mathrm{GeV}/c^2$ region becomes shallower. In general, the $1^{++}0^+\rho(770)\pi S$ wave shows only slowly changing or approximately constant phases with respect to other waves in the $a_1(1260)$ mass region. As an example, Figs. 10(b), 10(e), and 10(h) in Sec. VI A 1 show the phase with respect to the $0^{-+}0^+f_0(980)\pi S$ wave. The dominant feature is a rising phase in the $1.8\,\mathrm{GeV}/c^2$ region due to the $\pi(1800)$. In a similar way, the phase with respect to the $4^{++}1^+\rho(770)\pi G$ wave is dominated by the $a_4(2040)$ [see Figs. 28(d) and 29(d)]. The $1^{++}0^+f_2(1270)\pi P$ wave shows phase motions in the $1.65\,\mathrm{GeV}/c^2$ region, for example with respect to the other two 1^{++} waves and the $4^{++}1^+\rho(770)\pi G$ wave [see Figs. 28(c), 28(f), 28(i), 29(c), and 29(f)]. In the highest t' bin, the phase with respect to the $4^{++}1^+\rho(770)\pi G$ wave becomes constant [see Fig. 29(i)].

[ao] This is supported by our finding that the low-mass enhancement in the intensity distribution of the $1^{++}0^+f_2(1270)\pi P$ wave changes significantly if a reduced set of 53 waves is used for the partial-wave decomposition (see Sec. IV F in Ref. [30]).

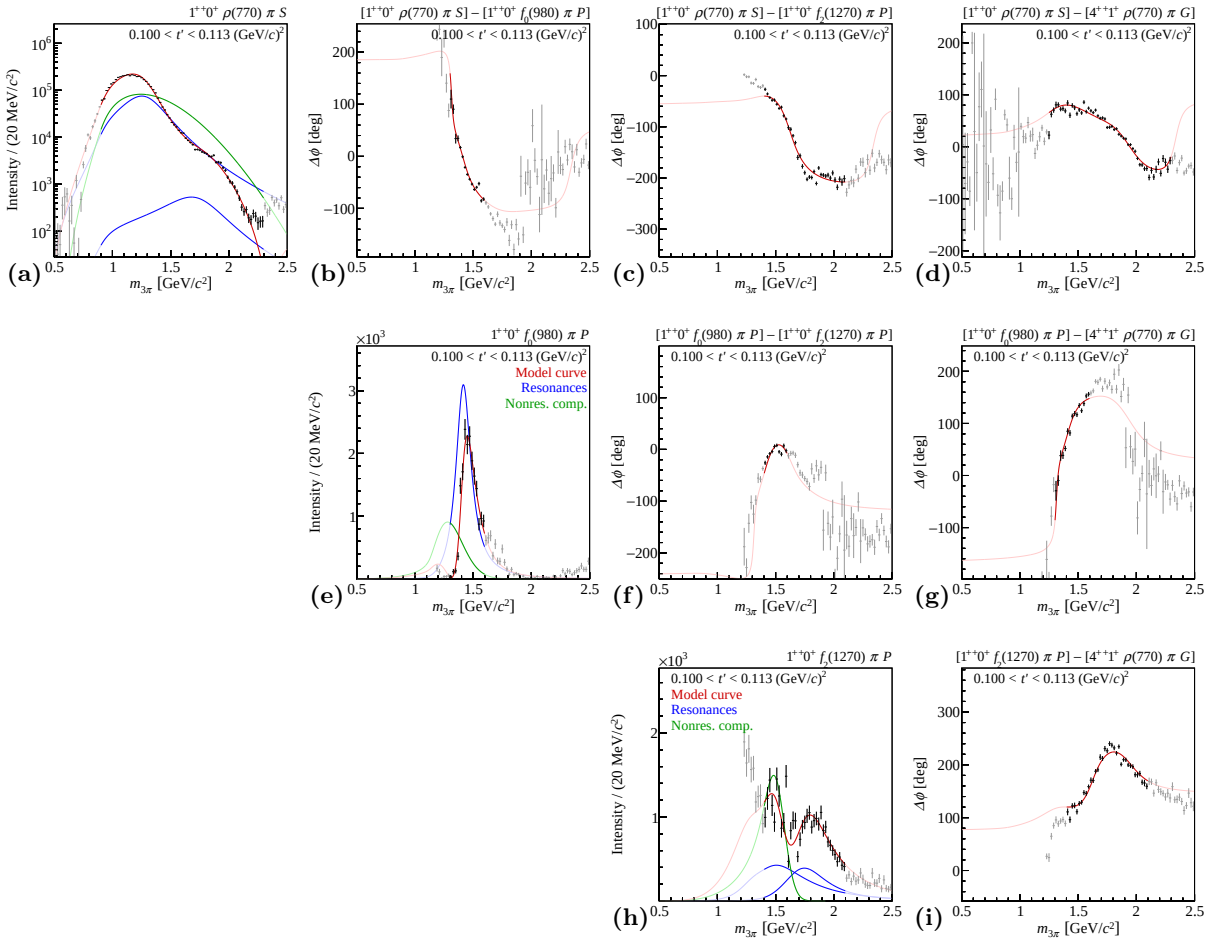

FIG. 28: Amplitudes of the three $J^{PC} = 1^{++}$ waves in the lowest t' bin. (a) through (d): Intensity distribution and relative phases for the $1^{++}0^{+}\rho(770)\pi S$ wave. Note that the intensity distribution in (a) is shown in logarithmic scale. (d) Corresponds to Fig. 12(c). (e) through (g): Intensity distribution and relative phases for the $1^{++}0^{+}f_0(980)\pi P$ wave. (h) and (i): Intensity distribution and relative phase for the $1^{++}0^{+}f_2(1270)\pi P$ wave. The model and the wave components are represented as in Fig. 10, except that in (a) and (h) the blue curves represent the $a_1(1260)$ and the $a_1(1640)$, whereas in (e) the blue curve represents the $a_1(1420)$.

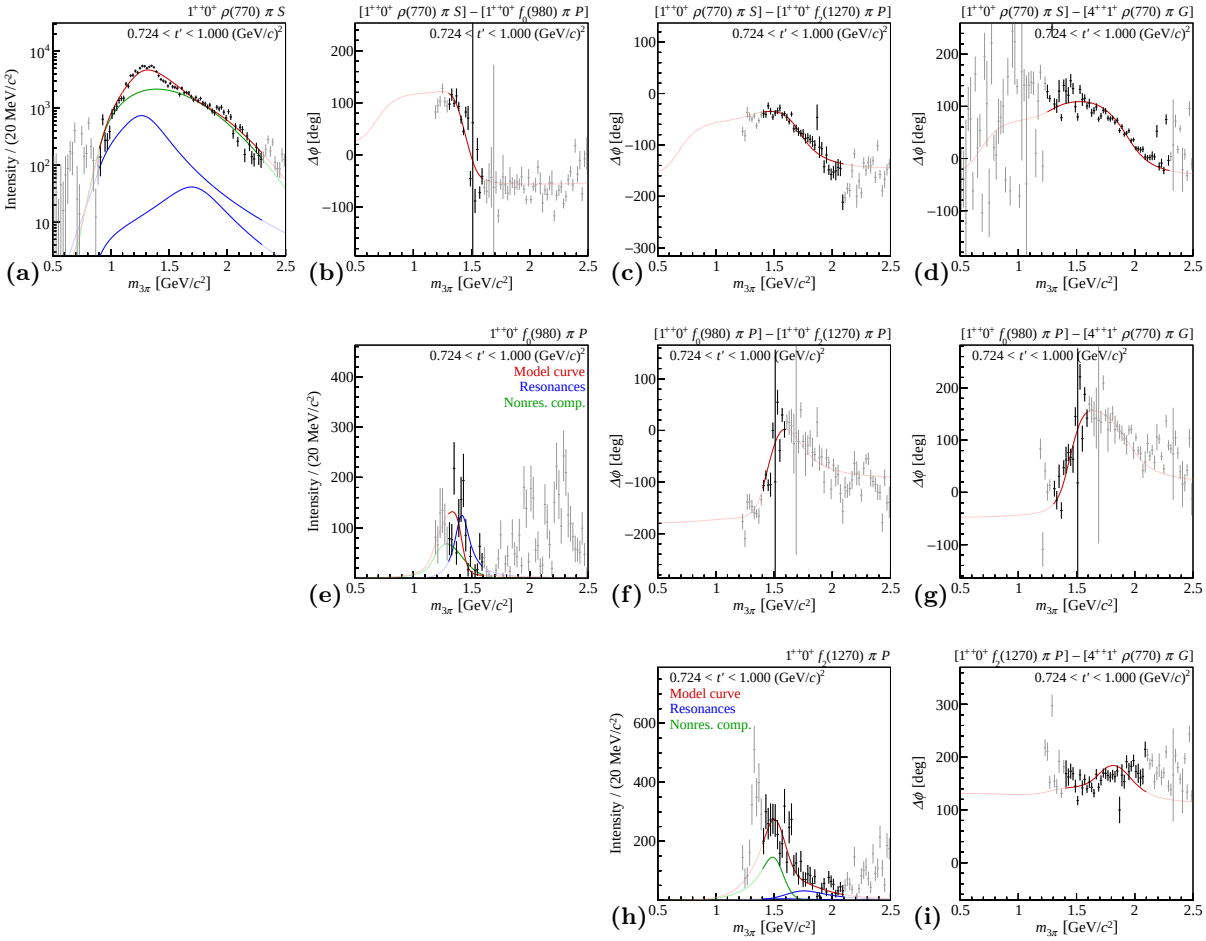

FIG. 29: Similar to Fig. 28 but for the highest t' bin.

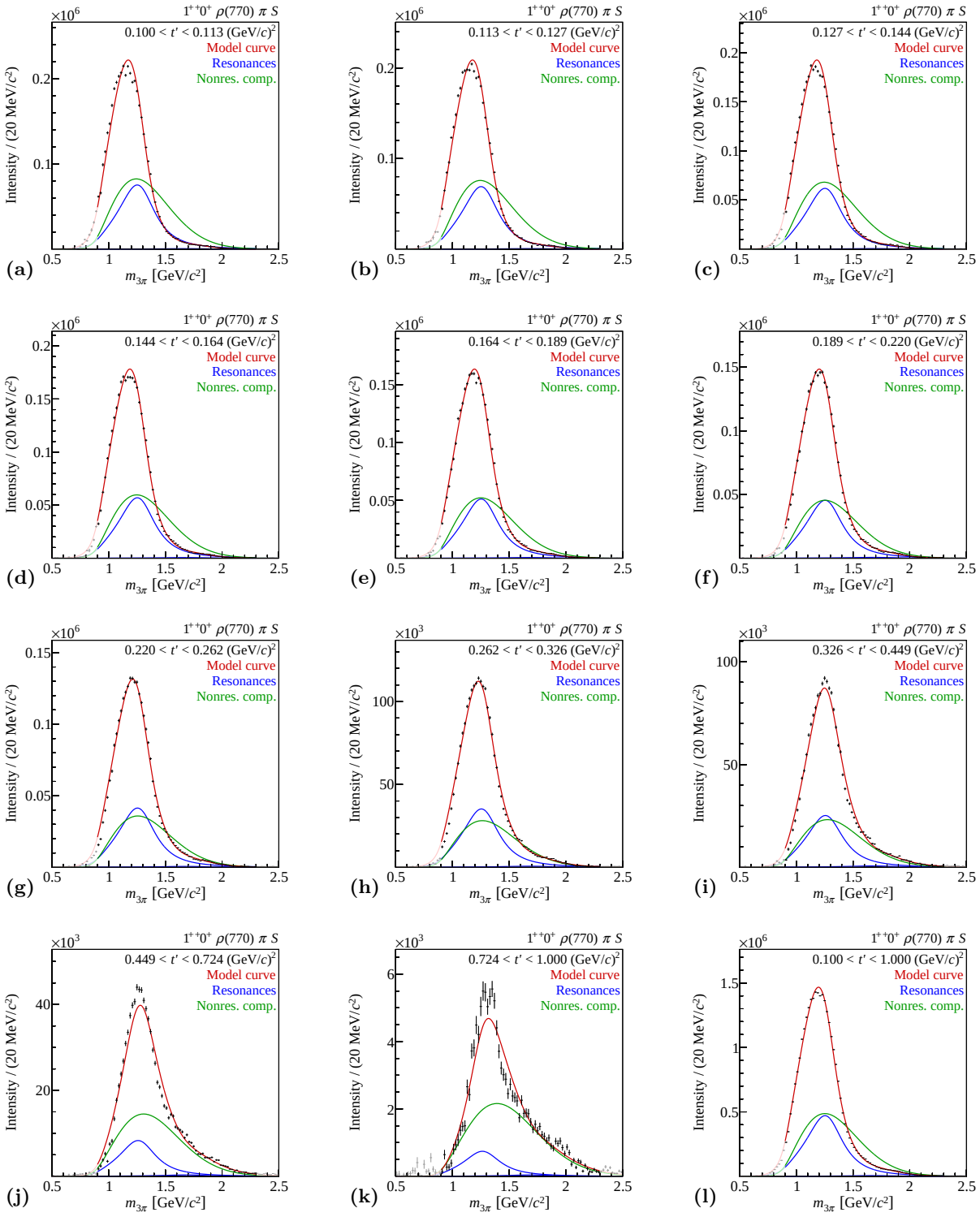

FIG. 30: (a) to (k): Intensity distributions of the $1^{++}0^{+}\rho(770)\pi S$ wave in the 11 t' bins. (l) The t'-summed intensity. The model and the wave components are represented as in Fig. 28. The contribution of the $a_1(1640)$ component is so small that it is barely visible in linear scale.

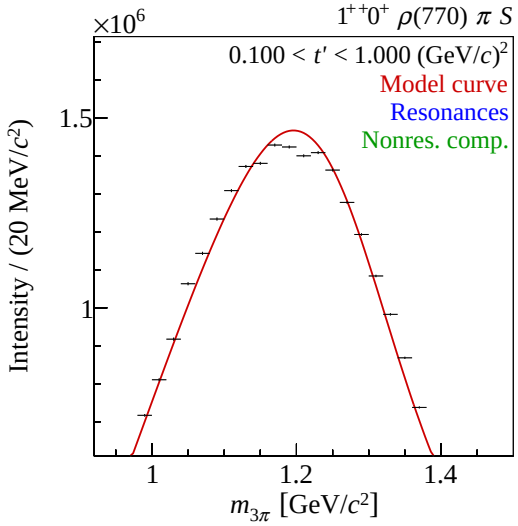

FIG. 31: Zoomed view of the t'-summed $1^{++}0^+\rho(770)\pi S$ intensity distribution in Fig. 30(l).

We model the three 1^{++} waves using three resonance components, $a_1(1260)$, $a_1(1420)$, and $a_1(1640)$. The $a_1(1260)$ and $a_1(1640)$ appear in both the $1^{++}0^+\rho(770)\pi S$ and $1^{++}0^+f_2(1270)\pi P$ waves, whereas the $1^{++}0^+f_0(980)\pi P$ wave is described using the $a_1(1420)$ as the only resonance component (see Table 2). The $a_1(1260)$ is parametrized by Eqs. (22) and (24), and the $a_1(1420)$ and $a_1(1640)$ by Eqs. (22) and (23). For the nonresonant component in the $\rho(770)\pi S$ wave we use Eq. (27), for those in the other two waves Eq. (29). The $\rho(770)\pi S$ wave is fit in the mass range from 0.9 to 2.3 GeV/c^2 and the $f_2(1270)\pi P$ wave from 1.4 to 2.1 GeV/c^2. For the $f_0(980)\pi P$ wave, a narrower fit range from 1.3 to 1.6 GeV/c^2 was chosen.[ap]

The employed model is in fair agreement with the data. In particular it is able to describe the change of the $\rho(770)\pi S$ intensity with t' in terms of a t'-dependent interference between the $a_1(1260)$ and the nonresonant component (see Fig. 30). The relative phase of the coupling amplitudes of the nonresonant component with respect to the $a_1(1260)$ changes from approximately 0° at low t' to +100° at high t' (see Fig. 53(a) in Sec. VII). Although the model reproduces the main features of the data, the extremely small statistical uncertainties of the $\rho(770)\pi S$ data points lead to significant disagreement of the model with the data in the $a_1(1260)$ region. The intensity distributions of the $\rho(770)\pi S$ wave and the real and imaginary parts of its interference terms in the 11 t' bins contribute together already about 25 % to the total χ^2 of the model [see Eq. (34)]. The model systematically deviates from the $\rho(770)\pi S$ intensity in the low- and high-mass flanks of the peak and also cannot well describe the tip of the peak (see Fig. 31). Some of the discontinuities in this mass region might be induced by the thresholds applied to some of the 88 waves used in the partial-wave decomposition (see Table IX in Appendix A of Ref. [30]). The deviations of the model from the $\rho(770)\pi S$ intensity increase with t'. In the two highest t' bins, the peak becomes significantly narrower, which the model is not able to reproduce [see Figs. 30(j) and 30(k)]. The model also does not reproduce smaller details in the high-mass region. The $a_1(1260)$ and the nonresonant component contribute with similar intensities to the $\rho(770)\pi S$ wave and interfere constructively in the $a_1(1260)$ region. In the low-t' region, the two components interfere destructively at higher masses. The contribution of the $a_1(1640)$ component to the $\rho(770)\pi S$ wave is approximately 2 orders of magnitude smaller than that of the $a_1(1260)$. It accounts for the small shoulder at 1.8 GeV/c^2.

The $a_1(1640)$ parameters are mainly determined by the $f_2(1270)\pi P$ wave. The model describes

[ap]Therefore, this wave has no overlap with the fit range of the $2^{-+}0^+f_2(1270)\pi D$ wave, which starts only at 1.6 GeV/c^2.

the low-mass enhancement of the $f_2(1270)\pi P$ intensity by a dominant nonresonant component that is sharply peaked in the $a_1(1260)$ region and a comparatively small $a_1(1260)$ component. The high-mass region of the $f_2(1270)\pi P$ intensity is dominated by a peak at about $1.8\,\mathrm{GeV}/c^2$ that is described well as the constructive interference of the $a_1(1260)$ and $a_1(1640)$ components. The peak disappears toward $t' = 1.0\,(\mathrm{GeV}/c)^2$ and so do the resonance components. The extrapolations of the model below and above the fit range undershoot the $f_2(1270)\pi P$ intensity at low and high $m_{3\pi}$ [see Figs. 28(h) and 29(h)].

The intensity distribution of the $f_0(980)\pi P$ wave is peculiar in that it shows a peak slightly above the $a_1(1260)$ but significantly narrower. The peak is well described by the third 1^{++} resonance in our model, the $a_1(1420)$. The $a_1(1420)$ interferes destructively with a smaller nonresonant component that peaks at about $1.3\,\mathrm{GeV}/c^2$. The model is not able to describe the high-mass tail, which grows with increasing t'. This is why the fit range was limited to below $1.6\,\mathrm{GeV}/c^2$.

Within the fit ranges, the model describes the relative phases of the 1^{++} waves better than the intensity distributions discussed above. In particular the rapid phase motion of the $1^{++}0^+f_0(980)\pi P$ with respect to other waves is well reproduced. This is also true for the phase motions of the $1^{++}0^+f_2(1270)\pi P$ wave in the $1.6\,\mathrm{GeV}/c^2$ region, which are caused by the $a_1(1640)$. A significant $a_1(1640)$ component in this wave is also consistent with the phase relative to the $2^{++}1^+f_2(1270)\pi P$ wave (see Fig. 32). The $a_2(1320)$ causes a decreasing phase in the $1.3\,\mathrm{GeV}/c^2$ region. At higher masses, the relative phase varies only slightly due to a compensation of the phase motions of $a_2(1700)$ and $a_1(1640)$. The phase of the $1^{++}0^+\rho(770)\pi S$ wave shows a completely different behavior [see Figs. 14(i) and 15(i)]. In addition to the rapid phase motion caused by the $a_2(1320)$, also the $a_2(1700)$ creates a clear phase motion that is not canceled by the $a_1(1640)$. Hence neither $a_1(1260)$ nor $a_1(1640)$ causes strong phase motions of the $1^{++}0^+\rho(770)\pi S$ wave. This is also true for the phases of this wave with respect to other waves [see e.g., Figs. 28(b) to 28(d) and 29(b) to 29(d)]. The behavior of the phases is consistent with the large nonresonant component over the full mass range and the weak signal of the $a_1(1640)$ compared to the $a_1(1260)$ ground state in the $\rho(770)\pi S$ wave. For many phases, the extrapolations of the model below and above the fit range follow approximately the data. Deviations appear in particular at low t'. For the phases of the $1^{++}0^+\rho(770)\pi S$ wave, the model extrapolations deviate from the data in the region above $2.3\,\mathrm{GeV}/c^2$ [see e.g., Figs. 28(c) and 28(d)]. For the phases of the $1^{++}0^+f_2(1270)\pi P$ wave, the model deviates typically at low masses [see e.g., Figs. 28(c) and 28(i)] where also the intensity distribution is not well reproduced.

Figure 33 shows the t' spectra of the 1^{++} wave components together with the results of fits using Eq. (41). The t' dependence of the amplitudes of $a_1(1260)$ and $a_1(1640)$ in the $1^{++}0^+\rho(770)\pi S$ and $1^{++}0^+f_2(1270)\pi P$ waves is constrained via Eq. (21). The t' dependence of the $a_1(1420)$ amplitude in the $1^{++}0^+f_0(980)\pi P$ wave is independently determined by the fit. The simple exponential model in Eq. (41) is in fair agreement with the t' spectra of all 1^{++} wave components. The extracted slope-parameter values for the $a_1(1260)$ are $11.8\,^{+0.9}_{-4.2}\,(\mathrm{sys.})\,(\mathrm{GeV}/c)^{-2}$ in the $\rho(770)\pi S$ wave and $11\,\pm 4\,(\mathrm{sys.})\,(\mathrm{GeV}/c)^{-2}$ in the $f_2(1270)\pi P$ wave. The $a_1(1260)$ has the steepest t' spectrum of all resonances in the model (see Table 6) although the uncertainty toward smaller slope values is considerable. The $a_1(1260)$ slope values agree within uncertainties with the slope values of the nonresonant components in all three 1^{++} waves. This is in contrast to most other waves, for which we typically observe steeper t' spectra for the nonresonant components. This might be a hint that the model is not able to completely separate the $a_1(1260)$ from the nonresonant components. As expected, the $a_1(1640)$ has a shallower t' spectrum with slope-parameter values close to $8\,(\mathrm{GeV}/c)^{-2}$. This value is similar to those of other resonances. In particular, it agrees with the slopes of the $a_2(1700)$, which has similar resonance parameters.

The t' spectrum of the $a_1(1420)$ in the $f_0(980)\pi P$ wave is consistent with the resonance inter-

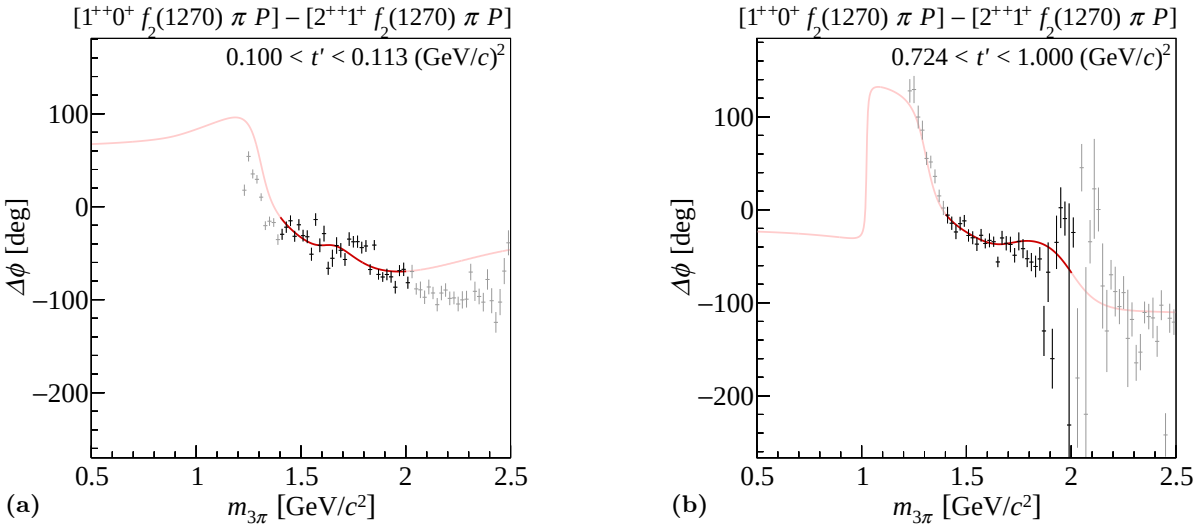

FIG. 32: Phase of the $1^{++}0^{+}f_2(1270)\pi P$ wave relative to the $2^{++}1^{+}f_2(1270)\pi P$ wave, (a) for the lowest t' bin and (b) for the highest t' bin. The model is represented as in Fig. 28.

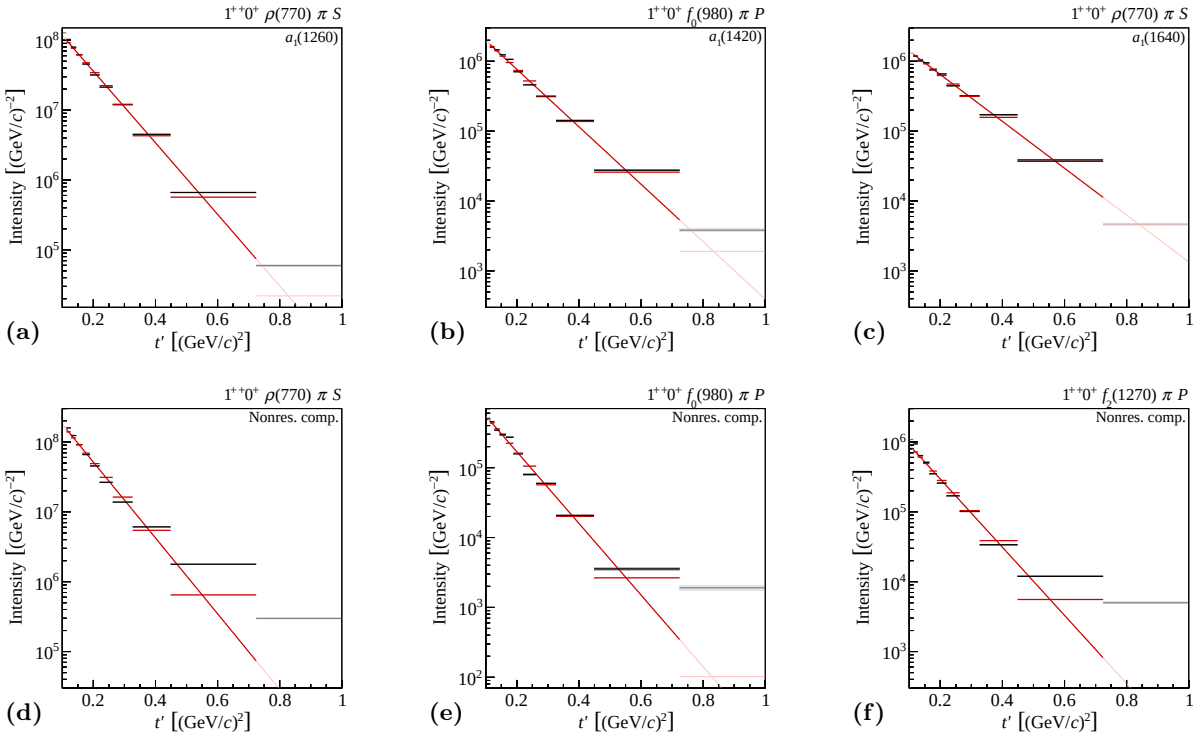

FIG. 33: Similar to Fig. 7, but showing the t' spectra of some of the components in the three 1^{++} waves as given by Eq. (40). The red curves and horizontal lines represent fits using Eq. (41).

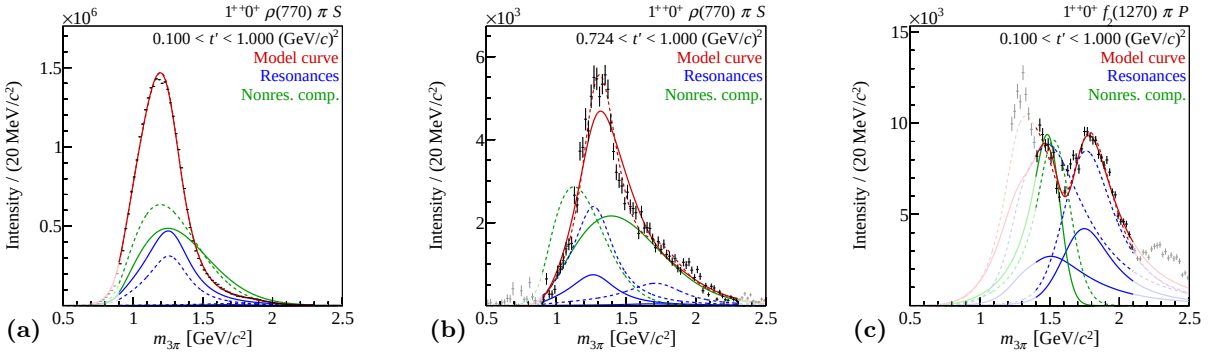

FIG. 34: (a) t'-summed intensity of the $1^{++}0^{+}\rho(770)\pi S$ wave. (b) Intensity of this wave in the highest t' bin. (c) t'-summed intensity of the $1^{++}0^{+}f_2(1270)\pi P$ wave. The result of the main fit is represented by the continuous curves. The fit, in which none of the coupling amplitudes of the resonance components was constrained via Eq. (21) [Study (M); see Sec. V], is represented by the dashed curves. The model and the wave components are represented as in Fig. 28.

pretation of this signal. The $a_1(1420)$ slope parameter has a value of $9.5\,^{+0.6}_{-1.0}\,(\text{sys.})\,(\text{GeV}/c)^{-2}$, which confirms the tendency that slopes decrease with increasing mass.

If none of the coupling amplitudes of the resonance components is constrained via Eq. (21) [Study (M); see Sec. V], the model has more freedom and can better describe the intensity distribution of the $\rho(770)\pi S$ wave at high t' [see Fig. 34(b)]. The $a_1(1260)$ resonance parameters change only slightly. However, the extracted $a_1(1260)$ slope parameters become inconsistent: $9.0\,(\text{GeV}/c)^{-2}$ in the $\rho(770)\pi S$ and $15\,(\text{GeV}/c)^{-2}$ in the $f_2(1270)\pi P$ wave. The slope of the $a_1(1640)$ increases to $14\,(\text{GeV}/c)^{-2}$ in the $\rho(770)\pi S$ wave but remains practically unchanged in the $f_2(1270)\pi P$ wave. This confirms that the $a_1(1640)$ resonance is well determined by the $f_2(1270)\pi P$ wave. The results of Study (M) also indicate that without the constraint of Eq. (21) the relative intensities of the two a_1 states and the nonresonant components are not well constrained by the data.

For the $a_1(1260)$, we extract the resonance parameters $m_{a_1(1260)} = 1299\,^{+12}_{-28}\,(\text{sys.})\,\text{MeV}/c^2$ and $\Gamma_{a_1(1260)} = 380 \pm 80\,(\text{sys.})\,\text{MeV}/c^2$. The extracted resonance parameters for the $a_1(1640)$ are $m_{a_1(1640)} = 1700\,^{+35}_{-130}\,(\text{sys.})\,\text{MeV}/c^2$ and $\Gamma_{a_1(1640)} = 510\,^{+170}_{-90}\,(\text{sys.})\,\text{MeV}/c^2$. Due to the dominance of the $a_1(1260)$ signal, the parameters of the $a_1(1640)$ are correlated with those of the $a_1(1260)$. The fit model does not describe well the $\rho(770)\pi S$ and $f_2(1270)\pi P$ intensities in some mass regions. This leads to a bimodal behavior of the fit with a second solution with a narrower $a_1(1260)$ and a wider and heavier $a_1(1640)$. In the main fit, this solution has a larger χ^2 but in some of the systematic studies (see Sec. V), the solution with the narrow $a_1(1260)$ is preferred. The parameters of $a_1(1260)$ and $a_1(1640)$ depend strongly on the interference of the 1^{++} and 2^{++} waves and therefore on the set of 2^{++} waves included in the fit. We also observe a large dependence of the parameters of $a_1(1260)$ and $a_1(1640)$ on the number of background events in the selected data sample. Studies (O) and (P) with alternative χ^2 formulations (see Sec. C) indicate that the model deviates more from the measured intensity distributions than from the phases of the 1^{++} waves. The results from the above mentioned systematic studies are discussed in more detail in Sec. D 2.

Since the $1^{++}0^{+}\rho(770)\pi S$ wave has a large nonresonant component, the fit result depends on the choice of the parametrization used for the nonresonant component. Also the strongly peaked shape of the nonresonant component at about $1.5\,\text{GeV}/c^2$ in the $1^{++}0^{+}f_2(1270)\pi P$ wave seems rather implausible. We therefore studied the dependence of the fit result on the parametrization used

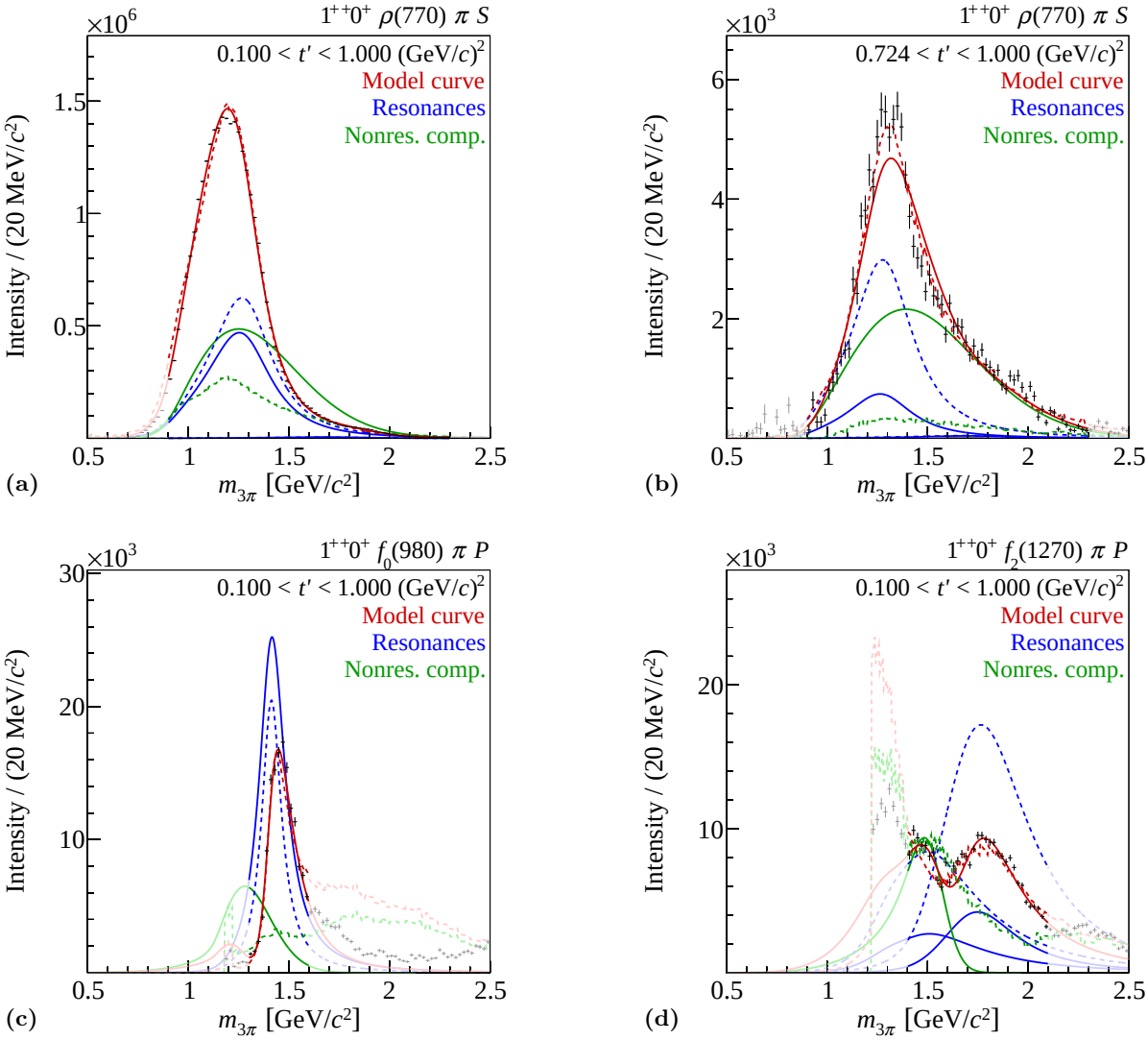

FIG. 35: (a) t'-summed intensity of the $1^{++}0^+\rho(770)\pi S$ wave. (b) Intensity of this wave in the highest t' bin. (c) and (d): The t'-summed intensity of the $1^{++}0^+f_0(980)\pi P$ and the $1^{++}0^+f_2(1270)\pi P$ wave, respectively. The result of the main fit is represented by the continuous curves. The fit, in which the parametrization of the nonresonant amplitude was replaced by the square root of the intensity distribution of the partial-wave decomposition of Deck Monte Carlo data [Study (N); see Sec. V], is represented by the dashed curves. The model and the wave components are represented as in Fig. 28.

for the nonresonant component. In Study (N), we replace the parametrization of the nonresonant amplitude by the square root of the intensity distribution of the partial-wave decomposition of Deck Monte Carlo data that were generated according to the model described in Sec. B. This model describes the measured $1^{++}0^+\rho(770)\pi S$ amplitude well [see Figs. 9, 35(a), and 35(b)]. The $\rho(770)\pi S$ intensity distribution in the high-t' region is described even better than in the main fit. The shape of the nonresonant component from the Deck model in the $\rho(770)\pi S$ wave is qualitatively similar to that obtained in the main fit. The $a_1(1260)$ parameters change only slightly but the yield of the $a_1(1260)$ component becomes larger and that of the nonresonant component smaller in particular at high t'. The model is also in fair agreement with the 1^{++} $0^+f_2(1270)\pi P$ intensity distribution [see Fig. 35(d)], although the shape of the nonresonant component from the Deck model is drastically different from that used in the main fit. The $a_1(1640)$ width increases by 126 MeV/c^2 in Study (N).

Compared to the studies discussed above, the $a_1(1260)$ and $a_1(1640)$ parameters depend only weakly on the particular choice of the t' binning. This was verified in Study (L), in which the analysis was performed using only 8 t' bins.

From the fit, we extract $a_1(1420)$ resonance parameters of $m_{a_1(1420)} = 1411\,^{+4}_{-5}\,(\text{sys.})\,\text{MeV}/c^2$ and $\Gamma_{a_1(1420)} = 161\,^{+11}_{-14}\,(\text{sys.})\,\text{MeV}/c^2$. In spite of the smallness of the $a_1(1420)$ signal, its resonance parameters are found to be remarkably stable in the systematic studies described above, which results in small systematic uncertainties[aq] (see Sec. D 2 for details). This result supersedes our previous measurement of the $a_1(1420)$ parameters reported in Ref. [19], which was obtained using the same data set and the same analysis technique but with only three waves included in the resonance-model fit.

2 Discussion of results on 1^{++} resonances

We observe three $J^{PC} = 1^{++}$ resonances in our analysis. The $a_1(1260)$ appears in the $1^{++}0^+\,\rho(770)\pi S$ wave, which is the most dominant wave, together with a large contribution of the nonresonant component. The contribution of the $a_1(1260)$ to the $1^{++}0^+ f_2(1270)\pi P$ wave is not well determined, since the model does not describe well the data in the region below $1.5\,\text{GeV}/c^2$ because of the apparent leakage as pointed out in Sec. VI E 1 above. The $a_1(1640)$ appears clearly as a peak in the $f_2(1270)\pi P$ wave with associated phase motion but has only a small relative contribution to the $\rho(770)\pi S$ wave. In general, the description of the $\rho(770)\pi S$ and $f_2(1270)\pi P$ intensities appears to be difficult. The disagreement of the model with the data induces large systematic uncertainties. The $a_1(1420)$ is observed as a clear peak in the $1^{++}0^+ f_0(980)\pi P$ wave with associated phase motion (see Figs. 28 and 29). There is no clear signature for the presence of the $a_1(1420)$ in the other two 1^{++} waves.

In order to study the significance of the $a_1(1420)$ resonance we have removed it from the fit model, so that the $1^{++}0^+ f_0(980)\pi P$ wave is described by the nonresonant component only. This fit has a minimum χ^2 value that is 1.44 times larger than that of the main fit.[ar] Without the $a_1(1420)$, the model is not able to describe the $f_0(980)\pi P$ intensity and relative phases (red dashed curve in Fig. 36).

In order to check if the peak in the $f_0(980)\pi P$ wave could be a threshold effect of the $a_1(1260)$, we performed a fit, in which the $a_1(1420)$ component is replaced by the $a_1(1260)$ component, so that the latter appears in all three 1^{++} waves. The minimum χ^2 value of this fit is 1.09 times larger than that of the main fit.[as] Figure 37 shows the contributions from the spin-density matrix elements to the χ^2 difference between this and the main fit. The model with the $a_1(1260)$ in the $f_0(980)\pi P$ wave describes the peak in this wave less well [see Fig. 38(b)]. The model requires a larger nonresonant component and a more destructive interference. While the description of the peak in the $\rho(770)\pi S$ wave is slightly improved [see Fig. 38(a)], the interference term of this wave with the $2^{++}1^+\rho(770)\pi D$ wave is described less well [see Fig. 37]. The $a_1(1260)$ resonance parameters and the decomposition of the $1^{++}0^+\rho(770)\pi S$ wave in terms of its components change drastically. The $a_1(1260)$ becomes $85\,\text{MeV}/c^2$ heavier and $188\,\text{MeV}/c^2$ narrower so that its resonance parameters actually become close to those of the $a_1(1420)$ in the main fit [cf. continuous and dashed blue curves in Fig. 38(b)].[at] The $\rho(770)\pi S$ intensity is described nearly completely by the nonresonant component with only a small contribution from the $a_1(1260)$ [see Fig. 38(a)].

[aq] We excluded Study (N) in the determination of the systematic uncertainty of the $a_1(1420)$ parameters, because the shape of the intensity distribution of the Deck model in the $1^{++}0^+ f_0(980)\pi P$ wave contradicts the data [see Fig. 35(c)].

[ar] Compared to the 722 free parameters of the main fit, this fit has 698 free parameters.

[as] Compared to the 722 free parameters of the main fit, this fit has 700 free parameters.

[at] Also the parameters of the $a_1(1640)$ change. It becomes $85\,\text{MeV}/c^2$ heavier and $20\,\text{MeV}/c^2$ wider.

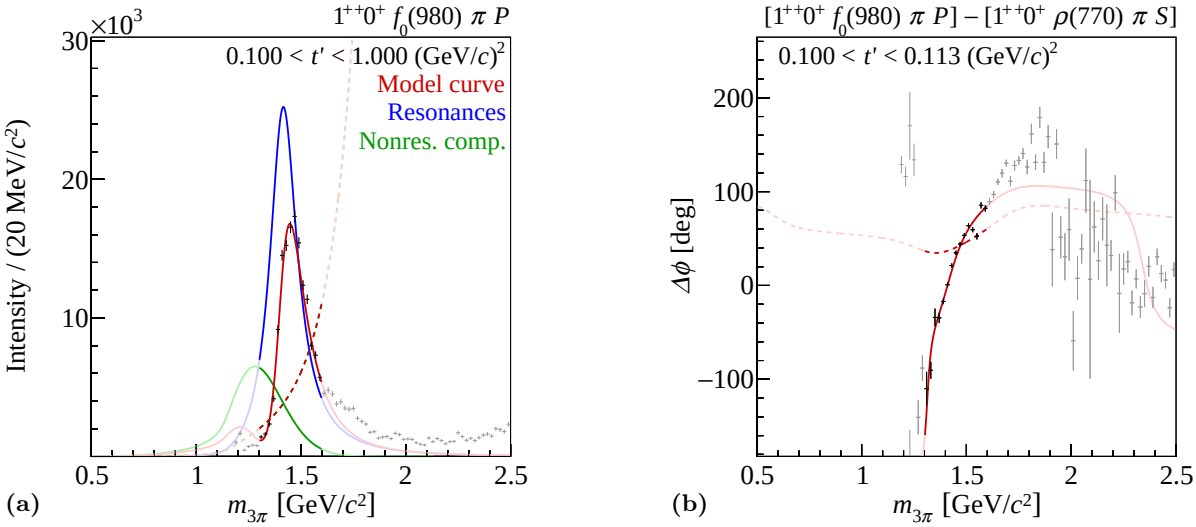

FIG. 36: (a) t'-summed intensity of the $1^{++}0^+ f_0(980)\pi P$ wave and (b) phase of this wave with respect to the $1^{++}0^+\rho(770)\pi S$ wave in the lowest t' bin. The result of the main fit is represented by the continuous curves. The fit, in which the $a_1(1420)$ component was removed from the model, is represented by the dashed curves. These curves correspond to the nonresonant component. The model and the wave components are represented as in Fig. 28.

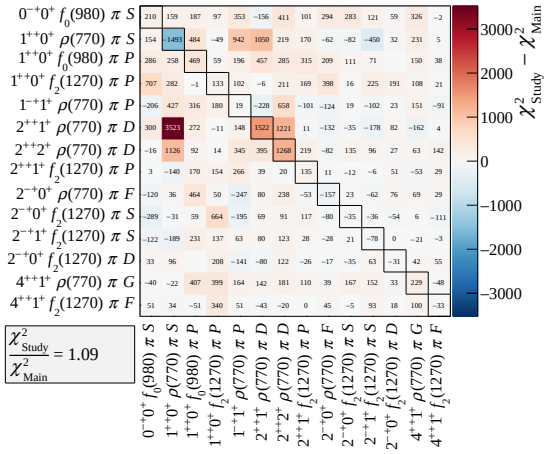

FIG. 37: Similar to Fig. 9, but for the study, in which the $a_1(1420)$ resonance in the $1^{++}0^+ f_0(980)\pi P$ wave was replaced by the $a_1(1260)$.

This interpretation of the $\rho(770)\pi S$ intensity seems implausible and would disagree with previous results on the $a_1(1260)$ (see discussion below). We therefore conclude that the peak in the $f_0(980)\pi P$ wave requires a resonance in our model, which is not the $a_1(1260)$.

We estimate the strength of a possible $a_1(1420)$ component in the other two 1^{++} waves by adding the $a_1(1420)$ component to the amplitudes of these waves. The minimum χ^2 of this fit is 0.96 times smaller than that of the main fit.[au] The largest contribution to this improvement in the description of the data comes from the intensity of the $\rho(770)\pi S$ wave (see Fig. 39). Adding the $a_1(1420)$ component to this wave improves the description of the peak in the $a_1(1260)$ region [see Fig. 40(a)]. Within the fit range, the description of the $f_2(1270)\pi P$ wave changes only slightly [see Fig. 40(b)]. However, the extrapolation of the model toward lower masses disagrees even

[au] Compared to the 722 free parameters of the main fit, this fit has 766 free parameters.

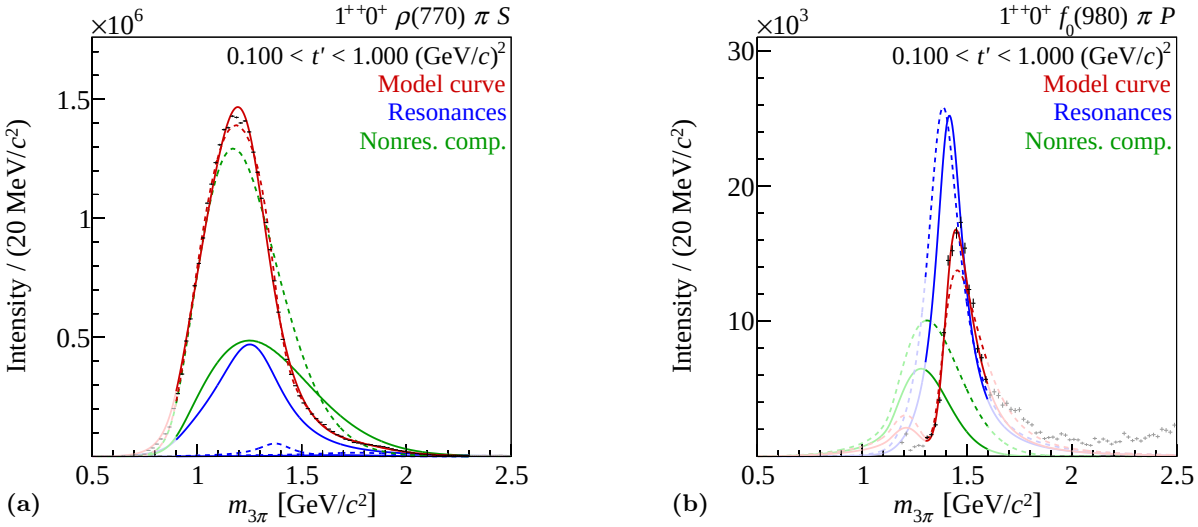

FIG. 38: t'-summed intensities of the $1^{++}0^+\rho(770)\pi S$ and the $1^{++}0^+f_0(980)\pi P$ wave. The result of the main fit is represented by the continuous curves. The fit, in which the $a_1(1420)$ resonance in the $1^{++}0^+$ $f_0(980)\pi P$ wave was replaced by the $a_1(1260)$, is represented by the dashed curves. The model and the wave components are represented as in Fig. 28.

more strongly with the data than in the main fit. The description of the $f_0(980)\pi P$ wave remains practically unchanged.[av] The relative contributions of the $a_1(1420)$ to the $f_2(1270)\pi P$ and in particular to the $\rho(770)\pi S$ wave are small. The coupling amplitudes of the $a_1(1420)$ in the three waves are not constrained by Eq. (21) and are therefore freely determined by the fit. The values of the $a_1(1420)$ slope parameters in the three waves differ significantly: in the $\rho(770)\pi S$ wave the slope is $6.7\,(\mathrm{GeV}/c)^{-2}$, in the $f_2(1270)\pi P$ wave it is $17.5\,(\mathrm{GeV}/c)^{-2}$, and in the $f_0(980)\pi P$ wave it is $9.5\,(\mathrm{GeV}/c)^{-2}$. The latter value is identical to the one from the main fit (see Table 6). The phase of the $a_1(1420)$ coupling amplitude in the $\rho(770)\pi S$ and the $f_2(1270)\pi P$ waves exhibits a stronger dependence on t' than that in the $f_0(980)\pi P$ wave. From the above, we conclude that we do not see convincing evidence for an $a_1(1420)$ component in the $\rho(770)\pi S$ or the $f_2(1270)\pi P$ wave, although we cannot rule out a small contribution.

In order to study the significance of the $a_1(1640)$ component, we performed a fit, in which we omitted the $a_1(1640)$ resonance from the fit model. The minimum χ^2 value of this fit is 1.13 times larger than that of the main fit.[aw] Figure 41 shows the contributions from the spin-density matrix elements to the χ^2 difference between this and the main fit. Without the $a_1(1640)$, the model describes less well in particular the intensity distributions of the $1^{++}0^+\rho(770)\pi S$ and 1^{++} $0^+f_2(1270)\pi P$ waves (see Fig. 42). The width of the $a_1(1260)$ becomes $47\,\mathrm{MeV}/c^2$ larger. From the above, we conclude that the $a_1(1640)$ component is necessary to describe the data but its parameters are not well determined.

Although the $a_1(1260)$ is a well-established resonance that has been observed in many experiments, its parameters are not well determined. Depending on the analyzed process and the employed parametrizations, the values of the $a_1(1260)$ parameters differ substantially [93]. The measurements listed by the PDG cover a wide range of mass values from $1041 \pm 13\,\mathrm{MeV}/c^2$ [94] up to $1331 \pm 10\,(\mathrm{stat.}) \pm 3\,(\mathrm{sys.})\,\mathrm{MeV}/c^2$ [95] and width values from $230 \pm 50\,\mathrm{MeV}/c^2$ [94]

[av] The $a_1(1420)$ parameters change only slightly. Its mass increases by $4\,\mathrm{MeV}/c^2$ and its width by $11\,\mathrm{MeV}/c^2$. In contrast, the parameters of the $a_1(1260)$ and $a_1(1640)$ change substantially. The $a_1(1260)$ becomes $27\,\mathrm{MeV}/c^2$ lighter and $75\,\mathrm{MeV}/c^2$ wider as compared to the main fit. The width of the $a_1(1640)$ decreases by $93\,\mathrm{MeV}/c^2$.

[aw] Compared to the 722 free parameters of the main fit, this fit has 696 free parameters.

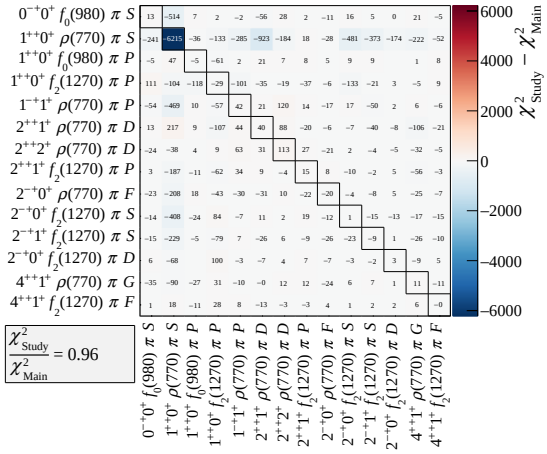

FIG. 39: Similar to Fig. 9, but for the study, in which the $a_1(1420)$ resonance was also included in the $1^{++}0^{+}\rho(770)\pi S$ and $1^{++}0^{+}f_2(1270)\pi P$ waves.

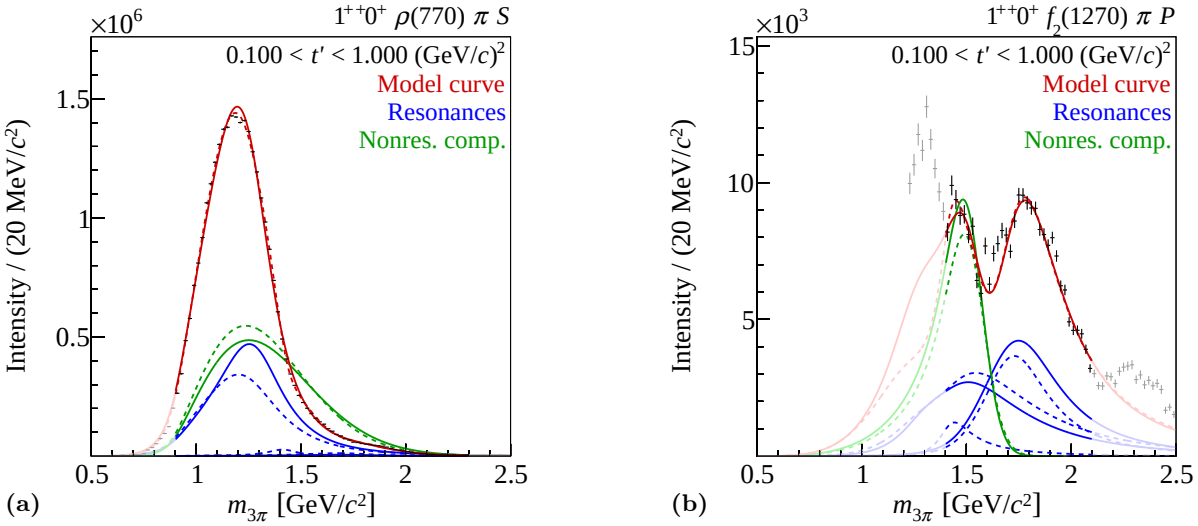

FIG. 40: t'-summed intensities of (a) the $1^{++}0^{+}\rho(770)\pi S$ wave and (b) the $1^{++}0^{+}f_2(1270)\pi P$ wave. The result of the main fit is represented by the continuous curves. The fit, in which the $a_1(1420)$ resonance is also included in the $1^{++}0^{+}\rho(770)\pi S$ and $1^{++}0^{+}f_2(1270)\pi P$ waves, is represented by the dashed curves. The model and the wave components are represented as in Fig. 28.

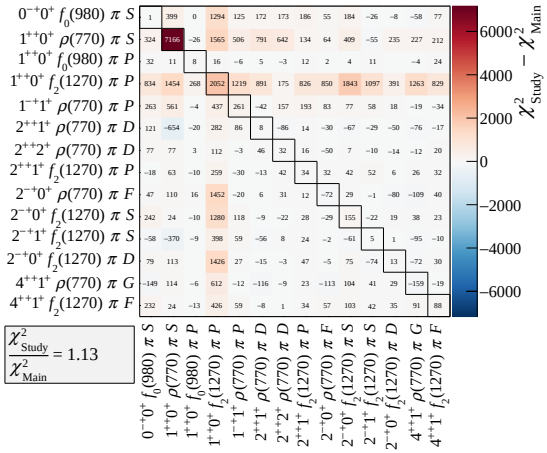

FIG. 41: Similar to Fig. 9, but for the study, in which the $a_1(1640)$ resonance was omitted from the fit model.

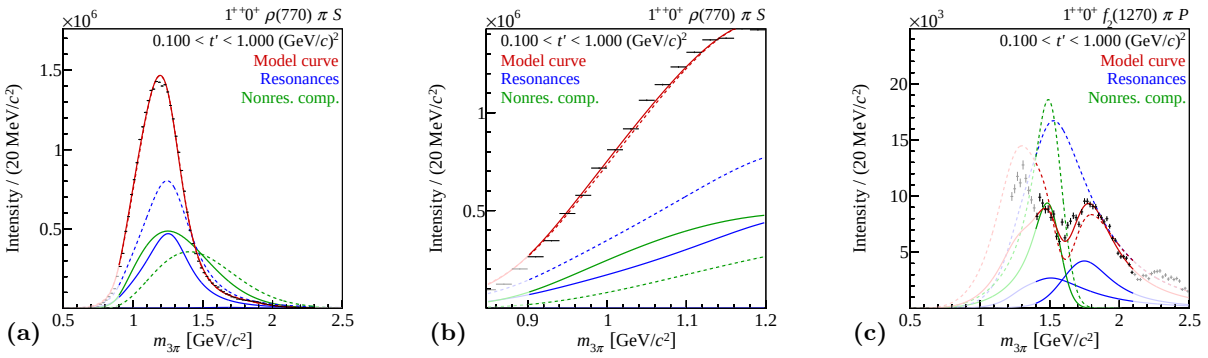

FIG. 42: t'-summed intensities of (a) the $1^{++}0^{+}\rho(770)\pi S$ wave and (c) the $1^{++}0^{+}f_2(1270)\pi P$ wave. In (b), a zoomed view of (a) is shown. The result of the main fit is represented by the continuous curves. The fit, in which the $a_1(1640)$ component was removed from the fit model, is represented by the dashed curves. The model and the wave components are represented as in Fig. 28.

up to 814 $\pm$ 36 (stat.) $\pm$ 13 (sys.) MeV/c^2 [95]. Due to the large spread of the measured parameter values, the PDG does not perform an average but provides only an estimate of $m_{a_1(1260)} = 1230 \pm 40\,\mathrm{MeV}/c^2$ and $\Gamma_{a_1(1260)} = 250$ to $600\,\mathrm{MeV}/c^2$ [10]. Our measured $a_1(1260)$ mass of $m_{a_1(1260)} = 1299\,^{+12}_{-28}\,(\mathrm{sys.})\,\mathrm{MeV}/c^2$ is larger than the PDG estimate but compatible within our large uncertainties. Our measured width of $\Gamma_{a_1(1260)} = 380 \pm 80\,(\mathrm{sys.})\,\mathrm{MeV}/c^2$ has large uncertainties and is close to the center of the range estimated by the PDG. Compared to our previous measurement of the $\pi^-\pi^-\pi^+$ final state diffractively produced on a solid lead target [17], the width agrees well but we obtain a larger mass that is in slight disagreement. However, since the lead-target data sample is approximately 2 orders of magnitude smaller, the analysis in Ref. [17] was performed by integrating over the t' range from 0.1 to 1.0 $(\mathrm{GeV}/c)^2$ and assuming a model for the t' dependence of the partial-wave amplitudes. Considering the unexpected t' dependence of the shape of the $1^{++}0^+\rho(770)\pi S$ intensity distribution as observed in Fig. 30, this might have been an inadequate approximation in former analyses and might explain the mass difference.

As already discussed in Ref. [19], the nature of the peculiar resonancelike $a_1(1420)$ signal, which is listed by the PDG as "omitted from summary table" [10], is still unclear and several interpretations were proposed. In Ref. [19] and in this analysis we have shown that it is consistent with a Breit-Wigner amplitude. Hence it could be the isospin partner to the $f_1(1420)$. Isovector $[n\,n]\,[\overline{n}\,\overline{n}]$ and $[n\,s]\,[\overline{n}\,\overline{s}]$ states with $n = u$ or d were predicted in the $1.4\,\mathrm{GeV}/c^2$ mass range in quark-model calculations that included tetraquark states [96]. The $a_1(1420)$ signal was also described as a two-quark-tetraquark mixed state [20] and as a tetraquark with mixed flavor symmetry [25]. In addition, calculations based on a soft-wall AdS/QCD approach predict a $[n\,\overline{s}]\,[s\,\overline{n}]$ tetraquark with a mass of $1414\,\mathrm{MeV}/c^2$ [27]. The authors of Ref. [97] studied the two-body decay rates for the modes $a_1(1420) \to f_0(980)\pi$ and $a_1(1420) \to K\overline{K}^*(892)$ for four-quark configurations using the covariant confined quark model. They found that a molecular configuration is preferred over a compact diquark-antidiquark state. However, other models were proposed that do not require an additional resonance. Basdevant and Berger proposed resonant rescattering corrections in the Deck process as an explanation [21,22], whereas the authors of Ref. [23] suggested an anomalous triangle singularity in the rescattering diagram for $a_1(1260) \to K\overline{K}^*(892) \to K\overline{K}\pi \to f_0(980)\pi$. The results of the latter calculation were confirmed in Ref. [26]. Preliminary studies show that the amplitude for the triangle diagram describes the data equally well as the Breit-Wigner model. In the case of a triangle singularity, the production rates of the $a_1(1420)$ would be completely determined by those of the $a_1(1260)$. Therefore, the slope parameters of the two peaks would be equal. Unfortunately, in our analysis the systematic uncertainties of the slope parameters are too large in order to draw any conclusion (see Table 6). Hence more detailed studies are still needed in order to distinguish between different models for the $a_1(1420)$.

The $a_1(1640)$ is listed by the PDG as "omitted from summary table" based on four measurements [47,98–100]. This state therefore requires further confirmation. The PDG world averages for the $a_1(1640)$ parameters are $m_{a_1(1640)} = 1647 \pm 22\,\mathrm{MeV}/c^2$ and $\Gamma_{a_1(1640)} = 254 \pm 27\,\mathrm{MeV}/c^2$ [10]. Compared to other waves, the agreement of our model with the $1^{++}0^+\rho(770)\pi S$ and 1^{++} $0^+ f_2(1270)\pi P$ intensities is worse and thus our measured $a_1(1640)$ parameters, $m_{a_1(1640)} = 1700\,^{+35}_{-130}\,(\mathrm{sys.})\,\mathrm{MeV}/c^2$ and $\Gamma_{a_1(1640)} = 510\,^{+170}_{-90}\,(\mathrm{sys.})\,\mathrm{MeV}/c^2$, have large systematic uncertainties. Our $a_1(1640)$ mass value is larger but within uncertainties compatible with the world average. However, our width value is significantly larger. As the study with the $a_1(1420)$ component in all three 1^{++} waves suggests (see discussion above), this discrepancy might be due to the disagreement between model and data in the mass region between $a_1(1260)$ and $a_1(1640)$ in the $\rho(770)\pi S$ and $f_2(1270)\pi P$ intensities. It might also be a consequence of not including any higher-lying a_1 states in the fit model.

The PDG [10] lists three further a_1 states: $a_1(1930)$ [76], $a_1(2095)$ [85], and $a_1(2270)$ [76]. Although we do not see clear resonance signals of heavy a_1 states in the mass range from 1900 to 2500 MeV/c^2 in the analyzed waves, we cannot exclude that some of the observed deviations of the model from the data at high masses are due to additional excited a_1 states that we do not take into account.

F $J^{PC} = 1^{-+}$ resonances

1 Results on 1^{-+} resonances

In addition to waves with ordinary $q\bar{q}$ quantum numbers, our analysis also includes the $1^{-+}1^+\rho(770)\pi P$ wave with an exotic J^{PC} combination. This wave contributes 0.8 % to the total intensity. Figure 43 shows the intensity distributions for all 11 t' bins. The shapes of these distributions exhibit a surprisingly strong dependence on t'. At low t', the intensity distribution is dominated by a broad structure that extends from about 1.0 to 1.7 GeV/c^2 with a maximum at approximately 1.2 GeV/c^2. With increasing t', the structure becomes narrower and the maximum moves to about 1.6 GeV/c^2. This behavior suggests large contributions from nonresonant processes in this wave. In the highest t' bin, a dip appears at 1.25 GeV/c^2 where the intensity nearly vanishes. At low t', a narrow enhancement appears at 1.1 GeV/c^2 on top of the broad structure. This enhancement is sensitive to details of the wave set that is used in the partial-wave decomposition and we therefore suspect it to be an artifact induced by imperfections in the PWA model.

Figure 44 shows selected phases of the $1^{-+}1^+\rho(770)\pi P$ wave with respect to other waves in the lowest and the highest t' bins (top and bottom rows, respectively). At low t', decreasing phases appear at masses that correspond to resonances in the other waves.[ax] In Figs. 44(a) and 44(d) slightly rising phases are observed in the 1.6 GeV/c^2 region. The phase with respect to the $2^{++}1^+\rho(770)\pi D$ wave is approximately constant between 1.4 and 1.6 GeV/c^2. Its rapid rise at 1.7 GeV/c^2 [see Fig. 44(b)] is induced by the nearly vanishing intensity of the $2^{++}1^+\rho(770)\pi D$ wave (see Sec. VI C 1). Compared to the intensity of the 1^{-+} wave, its phase motions with respect to most waves show less dependence on t' in the 1.6 GeV/c^2 region (see bottom row of Fig. 44). At high t', rapidly decreasing phases appear at 1.25 GeV/c^2 because of the nearly vanishing intensity of the 1^{-+} wave.[ay] It is worth noting that we do not observe any phase motions in the 1.1 GeV/c^2 region, where the narrow enhancement is observed in the intensity distribution. This supports interpretation of this structure as a model artifact.

We describe the $1^{-+}1^+\rho(770)\pi P$ amplitude by a spin-exotic $J^{PC} = 1^{-+}$ resonance, the $\pi_1(1600)$, and a nonresonant component. The $\pi_1(1600)$ is parametrized by Eqs. (22) and (23), the nonresonant component using Eq. (27) (see Table 2). The 1^{-+} wave is fit in the mass range from 0.9 to 2.0 GeV/c^2.

The model is in fair agreement with the intensity distributions. It reproduces in particular the strong t' dependence of the shape of the intensity distribution by a t'-dependent interference of the $\pi_1(1600)$ with the nonresonant component. The latter strongly changes shape, strength, and phase with t'. At low t', the intensity is dominated by the large nonresonant component, which interferes constructively with the $\pi_1(1600)$ at low masses. With increasing t', the strength of the nonresonant component decreases quickly so that the $\pi_1(1600)$ becomes the dominant component.

[ax] The slightly decreasing phase with respect to the $1^{++}0^+\rho(770)\pi S$ wave around 1.2 GeV/c^2 is caused by the $a_1(1260)$ [see Fig. 44(a) and Sec. VI E 1]. The rapidly decreasing phase with respect to the $2^{++}1^+\rho(770)\pi D$ wave around 1.3 GeV/c^2 is caused by the $a_2(1320)$ [see Fig. 44(b) and Sec. VI C 1]. The slightly decreasing phase with respect to the $2^{-+}0^+f_2(1270)\pi S$ wave around 1.7 GeV/c^2 is caused by the $\pi_2(1670)$ [see Fig. 44(c) and Sec. VI D 1]. The decreasing phase with respect to the $4^{++}1^+\rho(770)\pi G$ wave around 1.9 GeV/c^2 is caused by the $a_4(2040)$ [see Fig. 44(d) and Sec. VI B 1].

[ay] This is the same effect as seen in the $0^{-+}0^+f_0(980)\pi S$ wave; see Sec. VI A 1 and Figs. 10(h) and 10(i).

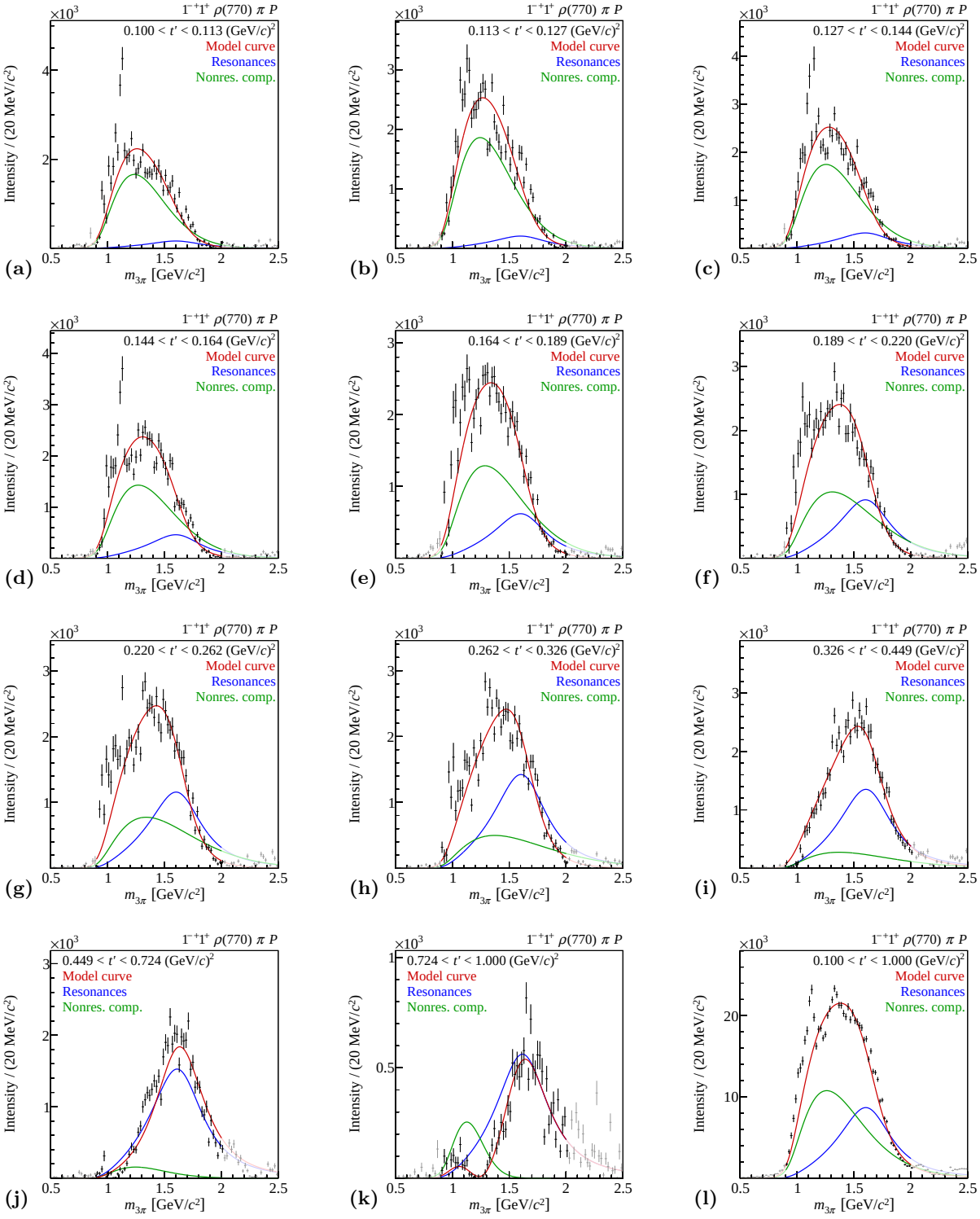

FIG. 43: (a) to (k): Intensity distribution of the $1^{-+}1^{+}\rho(770)\pi P$ wave in the 11 t' bins. (l) The t'-summed intensity. The model and the wave components are represented as in Fig. 10, except that the blue curve represents the $\pi_1(1600)$.

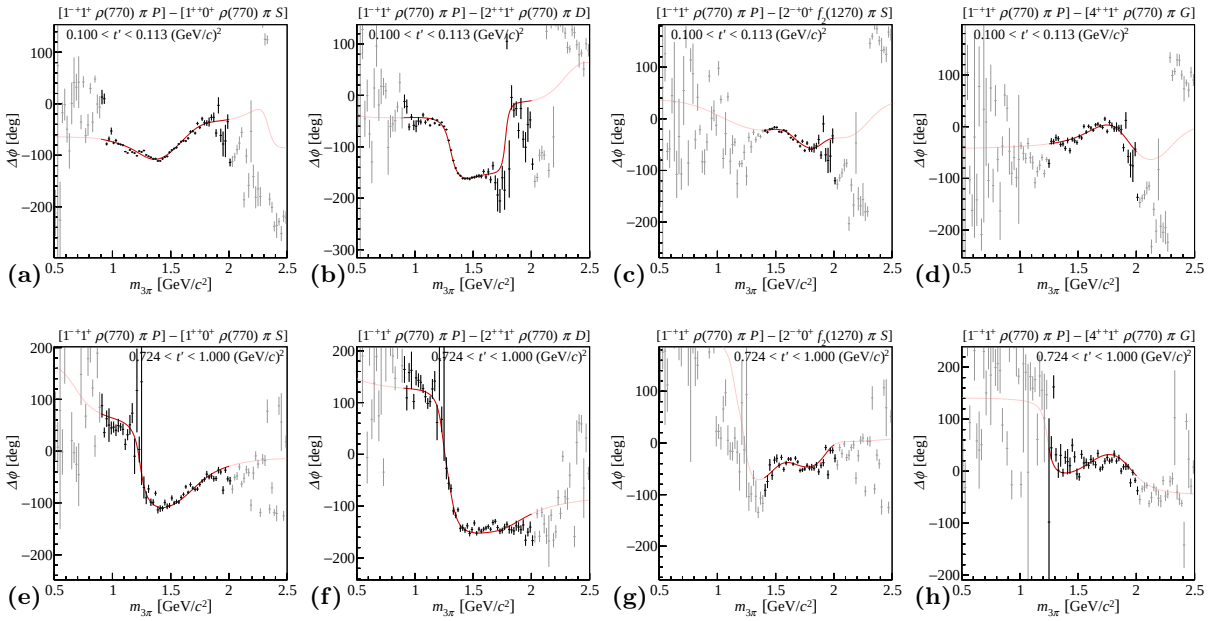

FIG. 44: Phase of the $1^{-+}1^{+}\rho(770)\pi P$ wave relative to (a) the $1^{++}0^{+}\rho(770)\pi S$, (b) the $2^{++}1^{+}\rho(770)\pi D$, (c) the $2^{-+}0^{+}f_2(1270)\pi S$, and (d) the $4^{++}1^{+}\rho(770)\pi G$ wave for the lowest t' bin. (e) through (h): The phases for the highest t' bin. The model is represented as in Fig. 43.

In the two highest t' bins, the nonresonant component is small or even vanishes in the $1.6\,\mathrm{GeV}/c^2$ region and the broad peak in the data is nearly entirely described by the $\pi_1(1600)$. The intensity dip at $1.25\,\mathrm{GeV}/c^2$ in the highest t' bin is reproduced by a destructive interference of the $\pi_1(1600)$ and the nonresonant component. However, the shape of the nonresonant component in the highest t' bin seems implausible since it is inconsistent with the continuous evolution with increasing t' (see the discussion of the Deck model below). At low t', the model does not describe well the low-mass part of the intensity distribution. In particular, the model cannot reproduce the presumably artificial narrow enhancement at $1.1\,\mathrm{GeV}/c^2$.

The model describes the phases of the 1^{-+} wave well within the fit range. The $\pi_1(1600)$ component causes only slight phase motions. This becomes particularly obvious in the nearly constant phase with respect to the $4^{++}1^{+}\rho(770)\pi G$ wave in the $1.6\,\mathrm{GeV}/c^2$ region [see Figs. 44(d) and 44(h)]. The 4^{++} wave contains no resonance in this mass range. For some waves, the model extrapolations to low or high masses deviate from the data [see e.g., Figs. 44(a) and 44(c)].

The strong t' dependence of the relative strength of the nonresonant and the $\pi_1(1600)$ components is shown in Fig. 45(a). For $t' \gtrsim 0.3\,(\mathrm{GeV}/c)^2$, the $\pi_1(1600)$ contribution dominates, whereas in the lowest t' bin the intensity of the nonresonant component, integrated over the fit range, is nearly an order of magnitude larger. The t' spectrum of the $\pi_1(1600)$ is not well described by the parametrization in Eq. (41). The model is not able to reproduce the downturn toward low t'. This may be a hint that, at low t', the fit is not able to separate the small $\pi_1(1600)$ component from the dominant nonresonant component due to an inappropriate description of the shape of the latter. This hypothesis is supported by the result of a study, in which the shape of the nonresonant component was determined from a Deck model (see discussion below). Limiting the fit range to the region $0.189 < t' < 0.724\,(\mathrm{GeV}/c)^2$, where the model is able to describe the data, yields a $\pi_1(1600)$ slope parameter of $7.3\,(\mathrm{GeV}/c)^{-2}$. This value lies in the range that is typical for resonances and is clearly much smaller than the slope value of the nonresonant component. The model in Eq. (41) is in fair agreement with the t' spectrum of the nonresonant component, which has a slope parameter value of $19.1\,^{+1.4}_{-4.7}\,(\mathrm{sys.})\,(\mathrm{GeV}/c)^{-2}$. This is the second largest slope

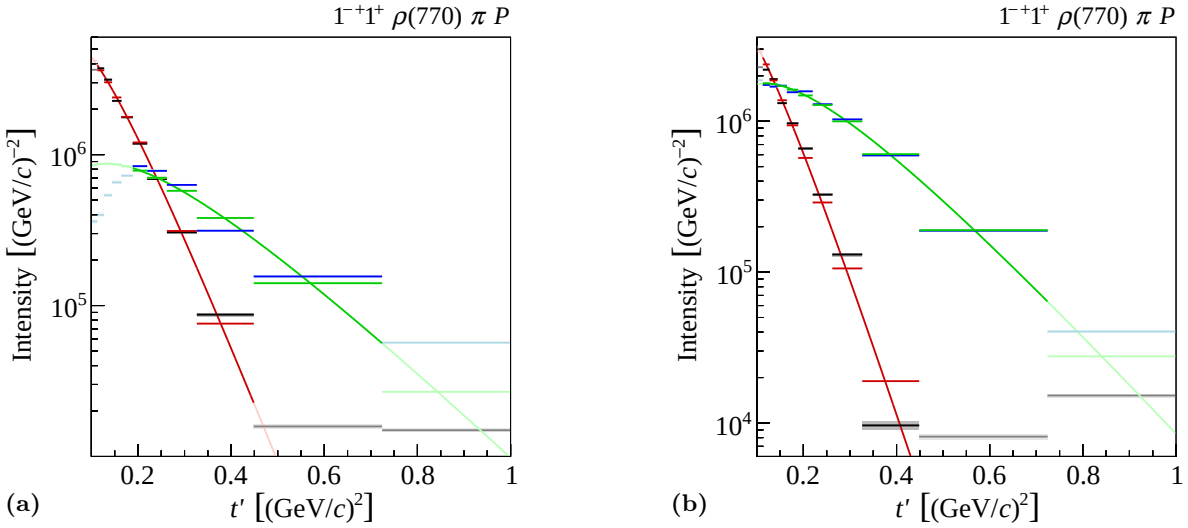

FIG. 45: Similar to Fig. 11, but showing the t' spectra of the two $J^{PC} = 1^{-+}$ wave components as given by Eq. (40): the $\pi_1(1600)$ component is shown as blue lines and light blue boxes, and the nonresonant component as black lines and gray boxes. The red and green curves and horizontal lines represent fits using Eq. (41). (a) The result of the main fit. (b) The result of a fit, in which the parametrization of the nonresonant amplitude was replaced by the square root of the intensity distribution of the partial-wave decomposition of Deck Monte Carlo data [Study (N); see Sec. V and Fig. 46].

value of all wave components in the fit.[az]

From the fit, we obtain the Breit-Wigner resonance parameters $m_{\pi_1(1600)} = 1600\,^{+110}_{-60}\,(\mathrm{sys.})\,\mathrm{MeV}/c^2$ and $\Gamma_{\pi_1(1600)} = 580\,^{+100}_{-230}\,(\mathrm{sys.})\,\mathrm{MeV}/c^2$. Since the 1^{-+} wave has a small intensity and is dominated by nonresonant contributions, the $\pi_1(1600)$ resonance parameters are sensitive to changes of the fit model discussed in Sec. V and hence have large systematic uncertainties. In the systematic studies, we observe a correlation of the $\pi_1(1600)$ parameters with the $a_1(1260)$, $a_1(1640)$, and $a_2(1700)$ parameters. We also observe that the $\pi_1(1600)$ parameters depend on the choice of the waves included in the fit. Studies (O) and (P) with alternative χ^2 formulations (see Sec. C) indicate that larger width values are preferred when less weight is given to the phase information in the χ^2 function. The $\pi_1(1600)$ parameters are also sensitive to the range parameter q_R in the Blatt-Weisskopf factors. More details on the results of these systematic studies are discussed in Sec. D 3.

Since the 1^{-+} wave is dominated by the nonresonant component, the fit result depends on the choice of the parametrization for the nonresonant component. In order to estimate this dependence, we performed Study (N), in which the parametrization of the nonresonant amplitude was replaced by the square root of the intensity distribution of the partial-wave decomposition of Deck Monte Carlo data generated according to the model described in Sec. B. This fit describes the 1^{-+} amplitude fairly well (see Figs. 9 and 46). The Deck model behaves qualitatively similar to the empirical parametrization used in the main fit, except in the highest t' bin, where the Deck model has a more plausible shape. The main difference with respect to the main fit is a larger $\pi_1(1600)$ yield at low t'. The resulting t' spectrum for the $\pi_1(1600)$ [see Fig. 45(b)] is much better described by the parametrization in Eq. (41) than the t' spectrum of the main fit [see Fig. 45(a)]. The slope value of $8.5\,(\mathrm{GeV}/c)^{-2}$ that is extracted using a fit range of $0.113 < t' < 0.742\,(\mathrm{GeV}/c)^2$ is in the range typical for resonances. Mass and width of the $\pi_1(1600)$ resonance

[az] Only the nonresonant component in the $0^{-+}0^{+}f_0(980)\pi S$ wave has an even steeper slope (see Table 6 and Sec. VI A 1).

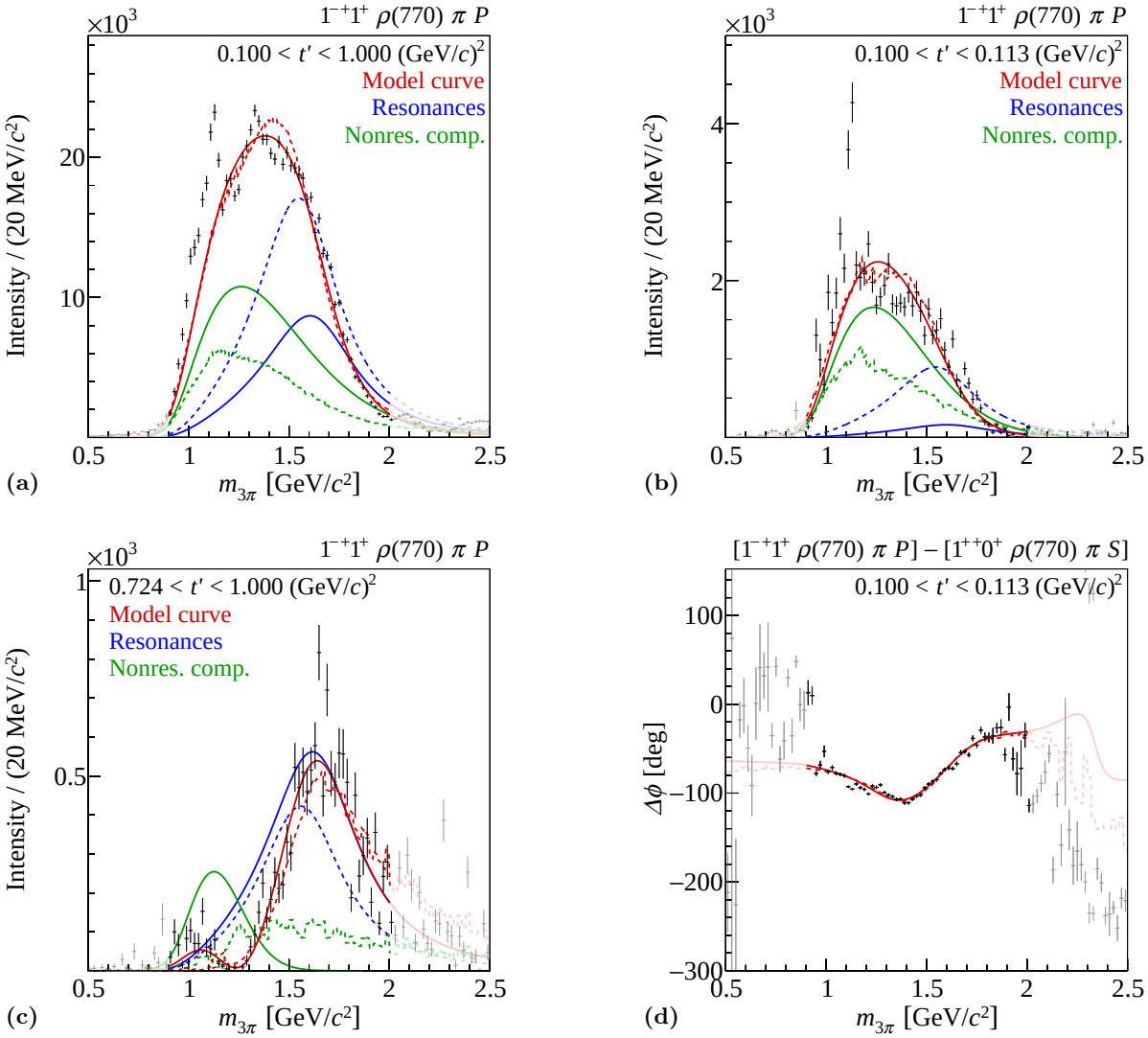

FIG. 46: (a) t'-summed intensity of the $1^{-+}1^{+}\rho(770)\pi P$ wave. (b) and (c): Intensity of this wave in the lowest and highest t' bins, respectively. (d) Phase of the 1^{-+} wave relative to the $1^{++}0^{+}\rho(770)\pi S$ wave in the highest t' bin. The result of the main fit is represented by the continuous curves. The fit, in which the parametrization of the nonresonant amplitude was replaced by the square root of the intensity distribution of the partial-wave decomposition of Deck Monte Carlo data [Study (N); see Sec. V], is represented by the dashed curves. The model and the wave components are represented as in Fig. 43.

decrease by $60\,\mathrm{MeV}/c^2$. Study (N) defines the lower boundary of the uncertainty interval for the $\pi_1(1600)$ mass.

In the related Study (A), we estimate the effect of an increased background contamination on the fit result by using weaker event-selection criteria. The t'-summed $\pi_1(1600)$ yield remains approximately unchanged while the strength of the nonresonant component increases.[ba]

Since at low t' the intensity distribution of the 1^{-+} wave exhibits presumably artificial structures in the low-mass region, we performed a study, in which the fit range for the 1^{-+} wave was limited to $1.4 < m_{3\pi} < 2.0\,\mathrm{GeV}/c^2$. In this study, the mass of the $\pi_1(1600)$ increases by $60\,\mathrm{MeV}/c^2$ but remains within the systematic uncertainty while the width remains unchanged. A similar result

[ba] However, the $\pi_1(1600)$ parameters change. It becomes $46\,\mathrm{MeV}/c^2$ heavier and $130\,\mathrm{MeV}/c^2$ narrower.

is obtained in Study (L), in which the analysis was performed using only eight t' bins, so that the subdivision of the analyzed t' range into 11 bins seems to be sufficient to capture the rapid change of the shape of the intensity distribution of the 1^{-+} wave with t'.

We obtain slightly changed values for mass and width, i.e., $m_{\pi_1(1600)} = 1650\,\mathrm{MeV}/c^2$ and $\Gamma_{\pi_1(1600)} = 560\,\mathrm{MeV}/c^2$, if we use a mass-dependent width for the parametrization of the $\pi_1(1600)$ analogous to Eq. (25) and assume that this width is saturated by the $\rho(770)\pi P$-wave decay mode.

2 Discussion of results on 1^{-+} resonances

The results of previous experiments on the existence of a $\pi_1(1600)$ signal in the 3π final state are contradictory. On the one hand, the BNL E852 experiment, which analyzed pion diffraction at $18\,\mathrm{GeV}/c$ beam momentum, claimed a $\pi_1(1600)$ signal in the $\rho(770)\pi$ decay mode [46, 47]. On the other hand, the authors of Ref. [41] concluded that the peak structure in the $1^{-+}1^+\rho(770)\pi P$ wave that was reported in Refs. [46, 47] was due to leakage caused by a too small wave set and that they do not observe a significant $\pi_1(1600)$ signal in the $\rho(770)\pi$ channel. This conclusion was based on a partial-wave analysis of a much larger 3π data set also from the BNL E852 experiment in the kinematic range $0.08 < t' < 0.53\,(\mathrm{GeV}/c)^2$ using an extended wave set. However, a $\pi_1(1600)$ signal was observed in a combined analysis of $\eta'\pi$, $b_1(1235)\pi$, and $\rho(770)\pi$ final states from pion diffraction at $36.6\,\mathrm{GeV}/c$ beam momentum by the VES experiment [101, 102]. No $\pi_1(1600)$ signal was found by the CLAS experiment in $\pi^-\pi^-\pi^+$ photoproduction [103, 104].

We have studied the significance of the $\pi_1(1600)$ signal by performing a fit, in which we omitted the $\pi_1(1600)$ component from the model. Hence in this fit, the $1^{-+}1^+\rho(770)\pi P$ wave is described solely by the nonresonant component. The minimum χ^2 value of this fit is 1.17 times larger than that of the main fit.[bb] Figure 47 shows the contributions from the spin-density matrix elements to the χ^2 difference between this and the main fit. In particular, the intensity of the 1^{-+} wave and its phase relative to the $1^{++}0^+\rho(770)\pi S$ wave are described less well by the model without the $\pi_1(1600)$ (see Fig. 48). The disagreement is largest in the two highest t' bins where the model cannot describe the data. However, at lower t' the nonresonant component is sufficient to describe the basic features of the data.[bc] Furthermore, we performed a fit with a model that describes the 1^{-+} amplitude using two independent coherent nonresonant contributions but no $\pi_1(1600)$. Also this fit does not yield a satisfactory description of the data. Based upon the items discussed above, we conclude that the significance of the $\pi_1(1600)$ signal is strongly t' dependent. At t' below about $0.5\,(\mathrm{GeV}/c)^2$, there is only weak evidence for the $\pi_1(1600)$. This is consistent with the nonobservation of the $\pi_1(1600)$ in the BNL E852 data in the kinematic range $t' < 0.53\,(\mathrm{GeV}/c)^2$ [41], as discussed above. However, our data show that a resonancelike signal is required to describe the data in the t' region above about $0.5\,(\mathrm{GeV}/c)^2$, which was not analyzed in Ref. [41].

The $\pi_1(1600)$ is considered by the PDG to be an established state. It was seen by the BNL E852 and VES experiments in diffractively produced $\eta'\pi$ [51, 105], $\eta\pi^+\pi^-\pi^-$ [85, 106], and $\omega\pi^-\pi^0$ [72, 106] final states. Evidence for the $\pi_1(1600)$ was also found in an analysis of $p\bar{p} \to \omega\pi^+\pi^-\pi^0$ Crystal Barrel data [100] and in $\chi_{c1} \to \eta'\pi^+\pi^-$ decays by the CLEO-c experiment [107].

[bb] Compared to the 722 free parameters of the main fit, this fit has 698 free parameters.

[bc] The omission of the $\pi_1(1600)$ also affects some of the resonance parameters in the fit. Most striking is the impact on the description of the intensity distribution of the $1^{++}0^+\rho(770)\pi S$ wave. Although this wave has a relative intensity that is about 40 times larger than that of the 1^{-+} wave and although the $a_1(1260)$ and the $\pi_1(1600)$ have a mass difference of about $300\,\mathrm{MeV}/c^2$, the $a_1(1260)$ becomes $56\,\mathrm{MeV}/c^2$ heavier and $78\,\mathrm{MeV}/c^2$ narrower if the $\pi_1(1600)$ is omitted from the model. Also the $a_1(1640)$ and $a_2(1700)$ parameters change substantially. The $a_1(1640)$ becomes $92\,\mathrm{MeV}/c^2$ heavier and $26\,\mathrm{MeV}/c^2$ wider; the $a_2(1700)$ becomes $28\,\mathrm{MeV}/c^2$ heavier and $60\,\mathrm{MeV}/c^2$ wider.

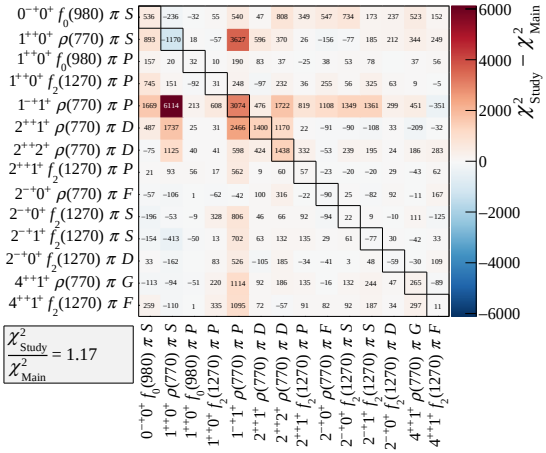

FIG. 47: Similar to Fig. 9, but for the study, in which the $\pi_1(1600)$ resonance was omitted from the fit model.

The PDG world averages for mass and width of the $\pi_1(1600)$ are $m_{\pi_1(1600)} = 1662\,^{+8}_{-9}\,\text{MeV}/c^2$ and $\Gamma_{\pi_1(1600)} = 241 \pm 40\,\text{MeV}/c^2$, respectively [10]. Our measured $\pi_1(1600)$ mass of $m_{\pi_1(1600)} = 1600\,^{+110}_{-60}\,(\text{sys.})\,\text{MeV}/c^2$ is consistent with the world average within the large systematic uncertainties; however, our measured $\pi_1(1600)$ width of $\Gamma_{\pi_1(1600)} = 580\,^{+100}_{-230}\,(\text{sys.})\,\text{MeV}/c^2$ is larger. This discrepancy is mainly due to the extremely small width value of $\Gamma_{\pi_1(1600)} = 185 \pm 25\,(\text{stat.}) \pm 28\,(\text{sys.})\,\text{MeV}/c^2$ quoted by the BNL E852 experiment for the $\omega\pi^-\pi^0$ final state [72]. The present width is also larger than our previously published one from an analysis of the same process on a solid-lead target [17]. Due to the approximately 2 orders of magnitude smaller data sample, the analysis in Ref. [17] was performed by integrating over the t' range from 0.1 to $1.0\,(\text{GeV}/c)^2$ and by assuming a model for the t' dependence of the partial-wave amplitudes. Therefore, the t' dependence of the shape of the $1^{-+}1^{+}\rho(770)\pi P$ amplitude was not taken into account. It is remarkable that in the lead-target data, the contribution of the nonresonant component is much smaller than that in the proton-target data so that the t'-integrated lead-target data resemble the high-t' region of the proton-target data.

The PDG summary table lists the $\pi_1(1400)$ as an additional $J^{PC} = 1^{-+}$ resonance. This state was observed by several experiments in the $\eta\pi$ final state [48, 108–114]. In the $\rho(770)\pi$ channel, it was only observed by the Obelix experiment [74]. We do not see any clear resonance signal below $1.5\,\text{GeV}/c^2$ in the $1^{-+}1^{+}\rho(770)\pi P$ wave. Aside from the presumably artificial narrow structure at $1.1\,\text{GeV}/c^2$, the description of the intensities and phases by our model leaves little room for a possible $\pi_1(1400)$ component in the $\rho(770)\pi P$ wave.

The BNL E852 experiment also reported a heavy spin-exotic state, i.e., the $\pi_1(2015)$, in the $f_1(1285)\pi$ [85] and $b_1(1235)\pi$ [72] decay modes. We do not see any clear resonance signal of a heavy π_1 state in the mass range from 1900 to $2500\,\text{MeV}/c^2$ in the $\rho(770)\pi P$ wave. However, we cannot exclude that some of the observed deviations of the model from the data at high masses are due to an additional excited π_1 state.

VII Results on t' dependence of relative phases of coupling amplitudes

As discussed in Sec. IV, our fit model in Eq. (20) contains coupling amplitudes $\mathcal{C}_a^j(t')$ for each wave component j in partial wave a, in addition to the shape parameters of the resonant and nonresonant components. The coupling amplitudes in the 11 t' bins are independent parameters of the model, which are determined by the fit. In order to reduce the number of these fit parameters,

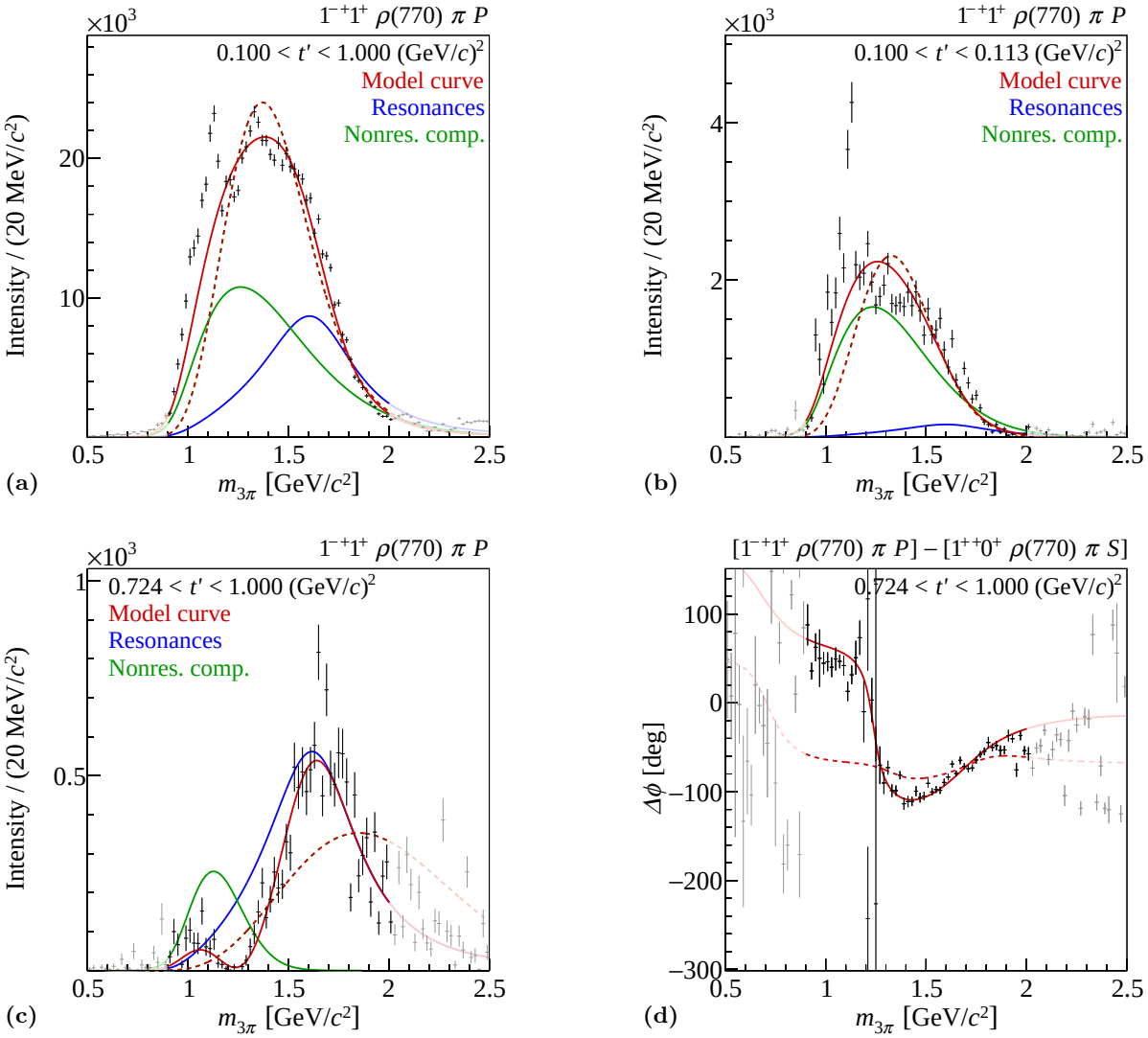

FIG. 48: (a) t'-summed Intensity of the $1^{-+}1^{+}\rho(770)\pi P$ wave. (b) and (c): intensity of this wave in the lowest and highest t' bins, respectively. (d) Phase of the 1^{-+} wave relative to the $1^{++}0^{+}\rho(770)\pi S$ wave in the highest t' bin. The result of the main fit is represented by the continuous curves. The fit, in which the $\pi_1(1600)$ resonance was omitted from the fit model, is represented by the dashed curves. These curves correspond to the nonresonant component. The model and the wave components are represented as in Fig. 43.

the coupling amplitudes of resonance components that appear in waves with the same $J^{PC}\,M^{\varepsilon}$ quantum numbers but different decay modes are constrained to have the same t' dependence via Eq. (21). In Sec. VI, we already discussed the t'-dependent yields of the resonant and nonresonant components as given by Eq. (40). Most of these t' spectra approximately follow the simple model in Eq. (41).

In this section, we discuss the t' dependence of the relative phases between the coupling amplitudes of wave component j in wave a and of wave component k in wave b,

$$\Delta\phi^{j,a;k,b}_{\text{coupl.}}(t') \equiv \arg\Big[\mathcal{C}^{j}_{a}(t')\,\mathcal{C}^{k*}_{b}(t')\Big]\,. \tag{50}$$

In the text below, we refer to these relative phases as *coupling phases*. Coupling amplitudes of the same resonance in different decay channels, which are constrained via Eq. (21), have t'-independent relative coupling phases that correspond to $\arg\left[{}_{b}\mathcal{B}^{j}_{a}\right]$.

As the coupling amplitude of a particular wave component is the product of the actual production amplitude of this wave component and the complex-valued couplings, $\alpha_{X\to\xi\pi}$ and $\alpha_{\xi\to\pi\pi}$, which appear in its decay via the isobar ξ^0 (see Sec. IV), the physical interpretation of the coupling phase is not straightforward. Assuming that a single production mechanism dominates, we would expect the coupling phases of resonances to be approximately independent of t'. These phases may be altered by effects from final-state interactions.

Our fit model assumes that resonances are described by Breit-Wigner amplitudes and that they have the same masses and widths in different waves and in all t' bins. In contrast, the shape of the nonresonant components can be adapted individually for each wave by the fit. For some waves, we allow the shape of the nonresonant component to change with t' (see Table 2). In addition, the fit has the freedom to choose the relative strengths and phases for the different components within a single wave and the relative strengths and phases between different waves. The imperfections in our model, in particular concerning the parametrization of the nonresonant components (see Sec. VI), might cause offsets in the relative phases, which may even be uncorrelated across t' bins. Considering these possible artifacts, we consider small phase differences up to 20° as insignificant for the physical interpretation.

The discussion of coupling phases will focus mostly on the resonance components. In Fig. 49, we show the t' dependence of the coupling phases of the 11 resonance components in the dominant wave of the respective J^{PC} sector relative to the $\pi_2(1670)$ in the $2^{-+}0^+ f_2(1270)\pi S$ wave. The dominant waves are characterized by a large contribution from the respective ground-state resonance, while the contributions from higher excited states are substantially smaller. Since the $a_1(1420)$ does not appear in the dominant 1^{++} wave, its coupling phase is shown for the $1^{++}0^+$ $f_0(980)\pi P$ wave. In Fig. 49, we have chosen the $\pi_2(1670)$ as the reference component because it turned out to be relatively stable in our systematic studies. The coupling phases of all resonances show a smooth variation as a function of t'. Since the model does not contain any assumptions on the t' behavior of the coupling phases, the observed continuous behavior is a nontrivial result, which supports our analysis model. We observe a similar behavior for the coupling phases of the nonresonant components, although the variation with t' is typically larger (see Figs. 50 to 55 in Secs. VII A and VII B below).

The coupling phases of the resonance components exhibit three striking features in their t' dependence: (i) for most resonances, we find for $t' \lesssim 0.3\,(\text{GeV}/c)^2$ a slow change of the coupling phases with t', whereas for $t' \gtrsim 0.3\,(\text{GeV}/c)^2$ the phases level off; (ii) with the exception of the $a_1(1420)$, the coupling phases of different states with the same J^{PC} show large relative offsets in the highest t' bin; and (iii) the coupling phases of the ground-state resonances do not deviate by more than ±60° from the phase of the $\pi_2(1670)$ in the highest t' bin. In particular the

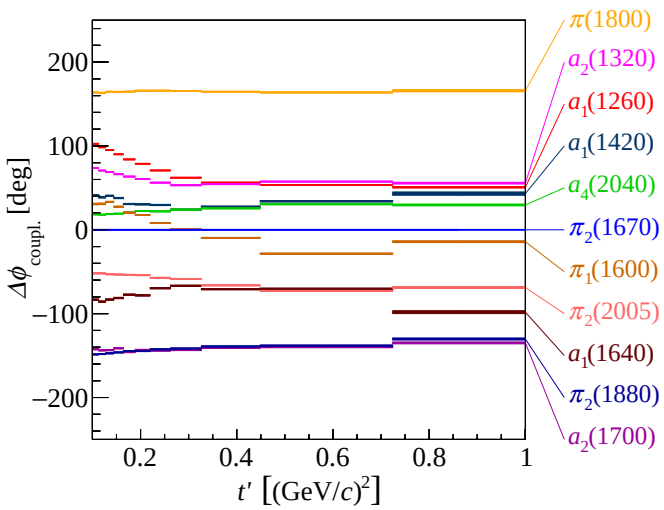

FIG. 49: t' dependence of the relative phases $\Delta\phi_{\text{coupl.}}$ of the coupling amplitudes [see Eq. (50)] of the 11 resonance components in the fit model with respect to the $\pi_2(1670)$. The coupling phases are shown for the dominant wave of the respective J^{PC} sector: $0^{-+}0^+f_0(980)\pi S$, $1^{++}0^+\rho(770)\pi S$, $1^{-+}1^+\rho(770)\pi P$, $2^{++}1^+\rho(770)\pi D$, $2^{-+}0^+f_2(1270)\pi S$, and $4^{++}1^+\rho(770)\pi G$. The only exception is the $a_1(1420)$, which appears only in the $1^{++}0^+f_0(980)\pi P$ wave. The width of the horizontal lines represents the statistical uncertainty. The systematic uncertainty is not shown.

nearly constant phases of all resonances for $t' \gtrsim 0.3\,(\text{GeV}/c)^2$ are remarkable and appear to be characteristic of resonances. This behavior is consistent with a common production mechanism for the resonances.

A Relative phases of the coupling amplitudes of the π_J resonances

The t' dependence of the coupling phases of the 2^{-+} wave components is shown in Fig. 50 relative to the $\pi_2(1670)$ in the $2^{-+}0^+f_2(1270)\pi S$ wave. The t' dependence of the coupling phases of the resonance components in the three 2^{-+} waves with $M = 0$ is constrained via Eq. (21). Therefore, in these waves the coupling phases of the resonances follow the same t' dependence but may have relative offsets, which correspond to the phase of the branching amplitudes ${}_b\mathcal{B}^j_a$. As for the resonance parameters and the t' spectra that were discussed in Secs. VI A to VI F, the uncertainties of the coupling phases are dominated by systematic effects; i.e., statistical uncertainties are negligible in comparison. The t' dependence of the coupling phases differs in the various systematic studies (see Sec. V). In order to illustrate the magnitude of the systematic effects at least qualitatively, we show in Fig. 50 for each wave component in addition to the continuous lines, which represent the result of the main fit, two sets of dashed lines. They represent the results of the two systematic studies that in the highest t' bin have the largest deviation from the coupling phase of the main fit. In order to guide the eye, the region between the two sets of dashed lines is shaded.[bd]

The coupling phase of the $\pi_2(1670)$ in the $f_2(1270)\pi S$ wave with $M = 0$ is zero by definition. The coupling phases of the $\pi_2(1670)$ in the $f_2(1270)\pi D$ wave and in the $f_2(1270)\pi S$ wave with $M = 1$ are similar and offset by less than $\pm 20°$ (see Fig. 50). The latter observation is remarkable because the coupling phase of the $\pi_2(1670)$ in the $f_2(1270)\pi S$ wave with $M = 1$ is not constrained via Eq. (21). In the $\rho(770)\pi F$ wave, the $\pi_2(1670)$ coupling amplitude shows a larger offset of about $+50°$.

[bd] Note that the shaded areas defined in this way cannot be interpreted as systematic uncertainties.

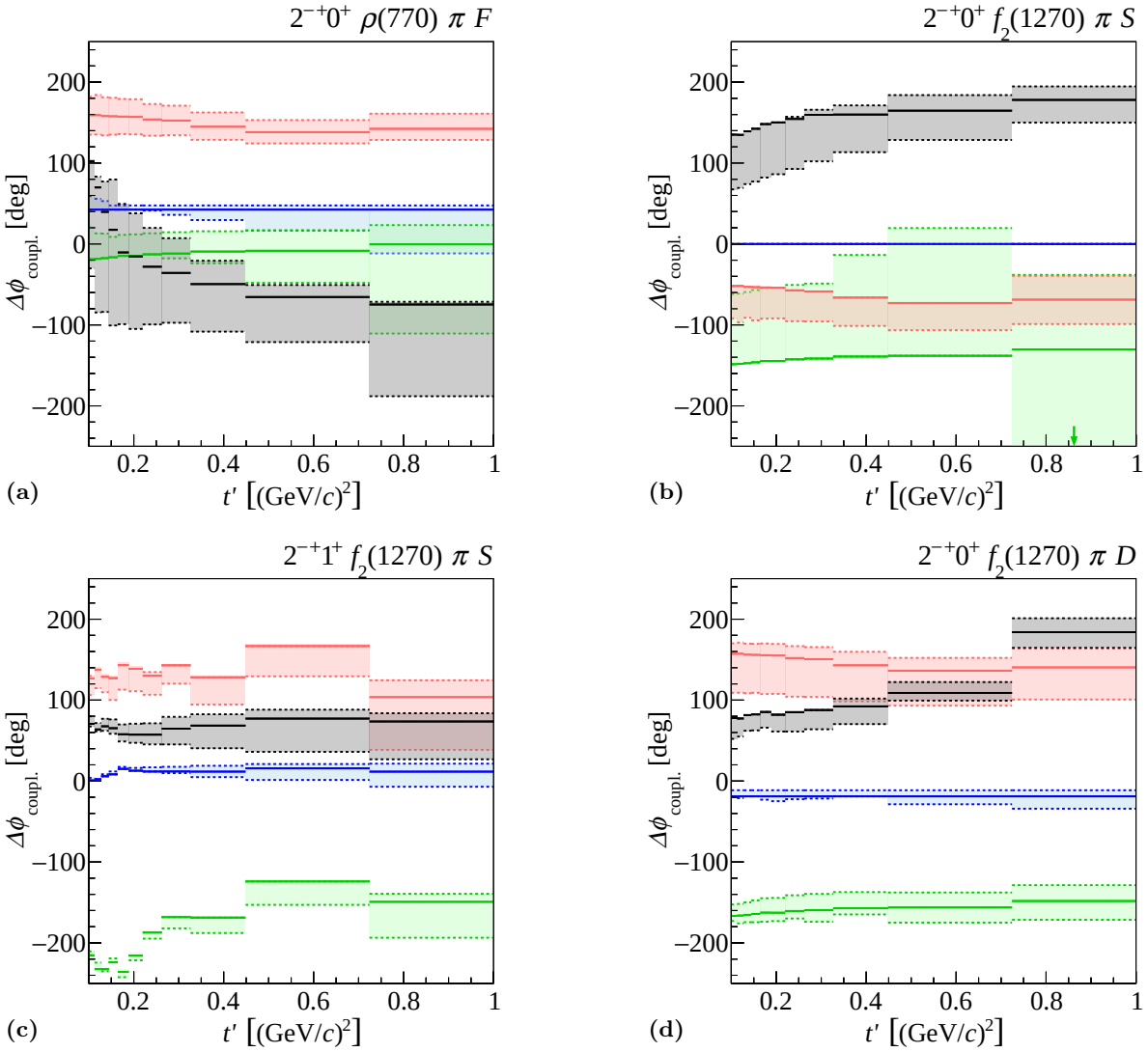

FIG. 50: t' dependence of the coupling phases of the wave components in (a) the $2^{-+}0^{+}\rho(770)\pi F$, (b) the $2^{-+}0^{+}f_2(1270)\pi S$, (c) the $2^{-+}1^{+}f_2(1270)\pi S$, and (d) the $2^{-+}0^{+}f_2(1270)\pi D$ wave. The coupling phases of the $\pi_2(1670)$ (blue lines), the $\pi_2(1880)$ (green lines), the $\pi_2(2005)$ (red lines), and the nonresonant components (black lines) are shown relative to the $\pi_2(1670)$ in the $2^{-+}0^{+}f_2(1270)\pi S$ wave. For each wave component, the magnitude of the effects observed in the systematic studies (see Sec. V) is illustrated qualitatively by two sets of dashed lines with shaded area in between (see text).

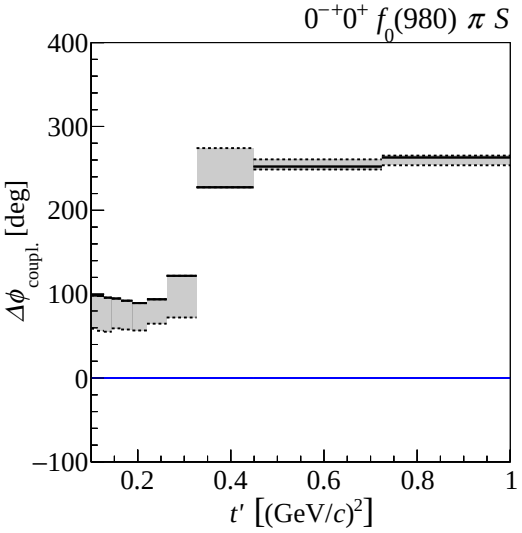

FIG. 51: Similar to Fig. 50 but for the wave components in the $0^{-+}0^{+}f_0(980)\pi S$ wave. The coupling phase of the nonresonant component (black lines) is shown relative to the $\pi(1800)$ (blue line).

The $\pi_2(1880)$ shows a coupling phase offset of about $-180°$[be] in the $f_2(1270)\pi D$ wave (see Fig. 50). In this wave, the $\pi_2(1880)$ is the dominant component. Therefore, the corresponding coupling phase is relatively stable with respect to the systematic studies. In contrast, the relative contribution of the $\pi_2(1880)$ to the other 2^{-+} waves is much smaller, which leads to larger variations of these coupling phases in the systematic studies. In the two $f_2(1270)\pi S$ waves, the coupling phase remains at an offset of about $-180°$. However, in the $\rho(770)\pi F$ wave the $\pi_2(1880)$ has a coupling phase of about $0°$.

The $\pi_2(2005)$ is best determined by the $\rho(770)\pi F$ wave and shows a phase offset of about $+150°$ (see Fig. 50). Similar offsets, although with larger systematic variations, are also observed in the $f_2(1270)\pi D$ wave and in the $f_2(1270)\pi S$ wave with $M = 1$. In contrast, the coupling phase in the $f_2(1270)\pi S$ wave with $M = 0$ is about $-90°$.

The t' dependence of the coupling phase of the $\pi(1800)$ follows that of the $\pi_2(1670)$ with an offset close to $+180°$ (see Fig. 49). The black lines in Fig. 51 show the coupling phase of the nonresonant component in the $0^{-+}0^{+}f_0(980)\pi S$ wave relative to the $\pi(1800)$. At low t', the nonresonant coupling phase is offset by about $+100°$. It then jumps by about $+150°$ at $t' \approx 0.3\,(\text{GeV}/c)^2$, thereby changing the sign of the coupling amplitude with respect to the $\pi(1800)$. At the same t' value, we observe a dip in the t' spectrum of the nonresonant component (see Fig. 11).

The coupling phase of the $\pi_1(1600)$ relative to the $\pi_2(1670)$ shows the most pronounced t' dependence of all resonances in Fig. 49 but stays within about $\pm 30°$ of the $\pi_2(1670)$ coupling phase. Qualitatively, the $\pi_1(1600)$ coupling phase behaves similar to that of the ground-state resonances. The coupling phase of the nonresonant component in the $1^{-+}1^{+}\rho(770)\pi P$ wave relative to the $\pi_1(1600)$ shows a strong t' dependence (see Fig. 52). Below $t' \approx 0.3\,(\text{GeV}/c)^2$, the coupling phase of the nonresonant component is approximately similar to the coupling phase of the $\pi_1(1600)$ with a negligible offset. In this t' region, the 1^{-+} wave is dominated by the nonresonant component (see Sec. VI F 1). Therefore, the $\pi_1(1600)$ is not well separated from the nonresonant component. Above $t' \approx 0.3\,(\text{GeV}/c)^2$, the coupling phase rises rapidly to about $+180°$. This rapid change of the interference pattern between the $\pi_1(1600)$ and the nonresonant component at high t' is needed for the model to describe the changing shape of the 1^{-+} intensity distribution. However, the variation of the coupling phase in the systematic studies is large as in

[be] This is, of course, mathematically equivalent to $+180°$.

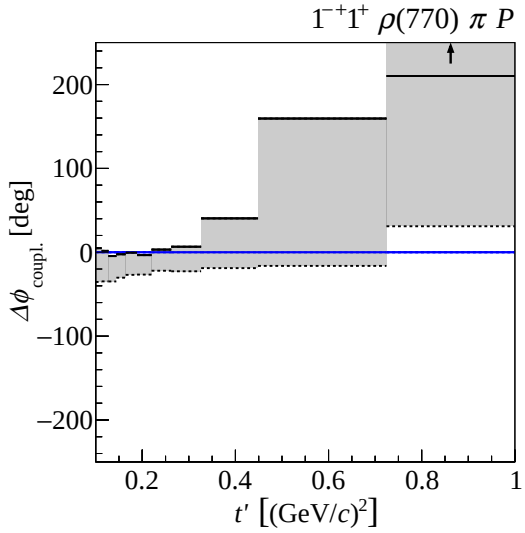

FIG. 52: Similar to Fig. 50 but for the wave components in the $1^{-+}1^{+}\rho(770)\pi P$ wave. The coupling phase of the nonresonant component (black lines) is shown relative to the $\pi_1(1600)$ (blue line).

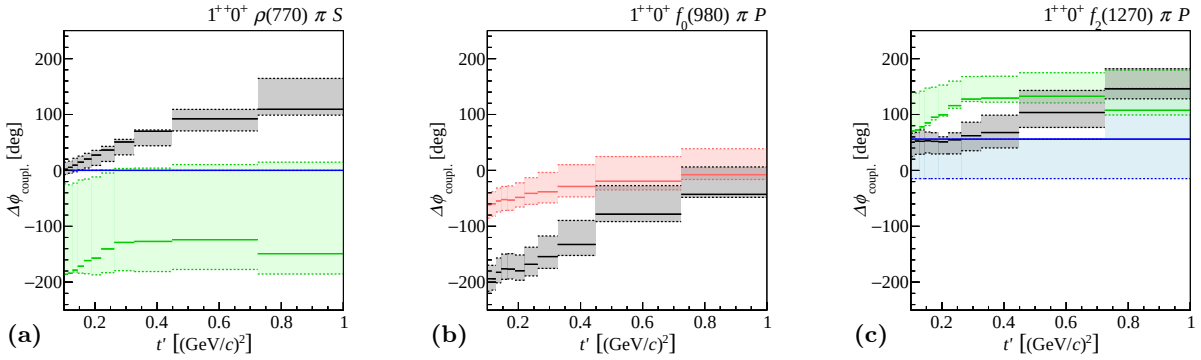

FIG. 53: Similar to Fig. 50 but for the wave components in (a) the $1^{++}0^{+}\rho(770)\pi S$, (b) the $1^{++}0^{+}$ $f_0(980)\pi P$, and (c) the $1^{++}0^{+}f_2(1270)\pi P$ wave. The coupling phases of the $a_1(1260)$ (blue lines), the $a_1(1420)$ (red lines), the $a_1(1640)$ (green lines), and the nonresonant components (black lines) are shown relative to the $a_1(1260)$ in the $1^{++}0^{+}\rho(770)\pi S$ wave.

the case of the $\pi_1(1600)$ resonance parameters.

B Relative phases of the coupling amplitudes of the a_J resonances

The coupling phase of the $a_1(1260)$ relative to the $\pi_2(1670)$ shows the largest variation with t' of all ground-state resonances in Fig. 49. It starts at $+100°$ at $t' = 0.1\,(\text{GeV}/c)^2$ and falls until $t' \approx 0.3\,(\text{GeV}/c)^2$, after which it levels off at about $+50°$. Figure 53 shows the coupling phases of the 1^{++} wave components relative to the $a_1(1260)$ in the $\rho(770)\pi S$ wave. The t' dependence of the coupling phases of the resonance components in the $\rho(770)\pi S$ and $f_2(1270)\pi P$ waves are constrained via Eq. (21). The phase offset between the coupling phases of the $a_1(1260)$ in these two waves is about $+50°$. However, the variation of the $a_1(1260)$ coupling phase in the $f_2(1270)\pi P$ wave in the systematic studies is large. In the $\rho(770)\pi S$ wave, the coupling phase of the nonresonant component rises by about $100°$ with respect to the $a_1(1260)$ over the analyzed t' range. This change of the interference pattern is needed for the model to describe the movement of the peak in the intensity distribution of the $\rho(770)\pi S$ wave with t'.

The $a_1(1640)$ coupling phase with respect to the $\pi_2(1670)$ is approximately independent of t'

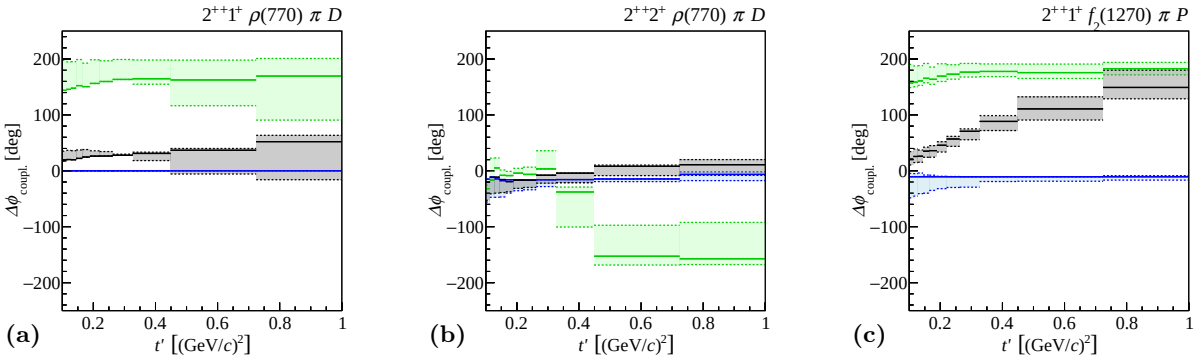

FIG. 54: Similar to Fig. 50 but for the wave components in (a) the $2^{++}1^{+}\rho(770)\pi D$, (b) the $2^{++}2^{+}\rho(770)\pi D$, and (c) the $2^{++}1^{+}f_2(1270)\pi P$ wave. The coupling phases of the $a_2(1320)$ (blue lines), the $a_2(1700)$ (green lines), and the nonresonant component (black lines) are shown relative to the $a_2(1320)$ in the $2^{++}1^{+}\rho(770)\pi D$ wave.

with an offset of about $-70°$ (see Fig. 49). Relative to the $a_1(1260)$, the coupling phases of the $a_1(1640)$ rise up to $t' \approx 0.3\,(\mathrm{GeV}/c)^2$ and then level off (see Fig. 53). As discussed in Sec. VI E 1, the parameters of the $a_1(1640)$ are mainly determined by the $f_2(1270)\pi P$ wave. This is also true for its coupling phase, which has a much smaller systematic variation in the $f_2(1270)\pi P$ wave. In this wave, the $a_1(1640)$ has a phase offset with respect to the $a_1(1260)$ of about $+130°$ at high t', whereas in the $\rho(770)\pi S$ wave, the phase offset is about $-130°$. However, the variation of the latter coupling phase in the systematic studies is large because the $a_1(1640)$ is only a small signal in the tail of the dominant $a_1(1260)$.

The $a_1(1420)$ has a nearly constant coupling phase relative to the $\pi_2(1670)$ with an offset of about $+40°$ (see Fig. 49). It therefore behaves qualitatively similar to the ground-state resonances. In our model, the $a_1(1420)$ appears only in the $f_0(980)\pi P$ wave. Its coupling phase relative to the $a_1(1260)$ is shown as red lines in Fig. 53(b). This phase rises from about $-60°$ at low t' to about $0°$ at high t' and thus changes more strongly than the one with respect to the $\pi_2(1670)$.

The $a_2(1320)$ is the narrowest resonance in our analysis. In the two $2^{++}\rho(770)\pi D$ waves, all other wave components are very small in the $1.3\,\mathrm{GeV}/c^2$ mass range. The coupling phase of the $a_2(1320)$ in the $\rho(770)\pi D$ wave with $M = 1$ relative to the $\pi_2(1670)$ shows a weak dependence on t' with an offset of about $+60°$ (see Fig. 49). Figure 54 shows the coupling phases of the 2^{++} wave components relative to the $a_2(1320)$ in the $\rho(770)\pi D$ wave with $M = 1$. The t' dependence of the coupling phases of the resonance components in the $\rho(770)\pi D$ wave with $M = 1$ and in the $f_2(1270)\pi P$ wave are constrained via Eq. (21). The phase offset of the $a_2(1320)$ in these two waves is close to zero, which confirms that we indeed see the $f_2(1270)\pi$ decay mode of the $a_2(1320)$. The coupling phases of the $a_2(1320)$ in the $\rho(770)\pi D$ wave with $M = 2$ is practically identical to that in the $\rho(770)\pi D$ wave with $M = 1$. This result is particularly remarkable since the $\rho(770)\pi D$ wave with $M = 2$ has a small relative intensity and the coupling phase of the $a_2(1320)$ component in this wave is not constrained via Eq. (21).

The coupling phase of the $a_2(1700)$ in the $\rho(770)\pi D$ wave with $M = 1$ has a nearly constant offset of $-140°$ with respect to the $\pi_2(1670)$ (see Fig. 49). Relative to the $a_2(1320)$, the coupling phase of the $a_2(1700)$ shows a similar behavior in the $\rho(770)\pi D$ wave with $M = 1$ and in the $f_2(1270)\pi P$ wave with a nearly constant offset of about $+180°$ (see Fig. 54). In the $2^{++}2^{+}\rho(770)\pi D$ wave, the coupling phase starts at $0°$ at low t' and decreases to $-180°$ at high t'. However, the $a_2(1700)$ signal is very small in this wave and therefore not extracted reliably (see Sec. VI C 1).

Compared to the other ground-state resonances in Fig. 49, the coupling phase of the $a_4(2040)$ is

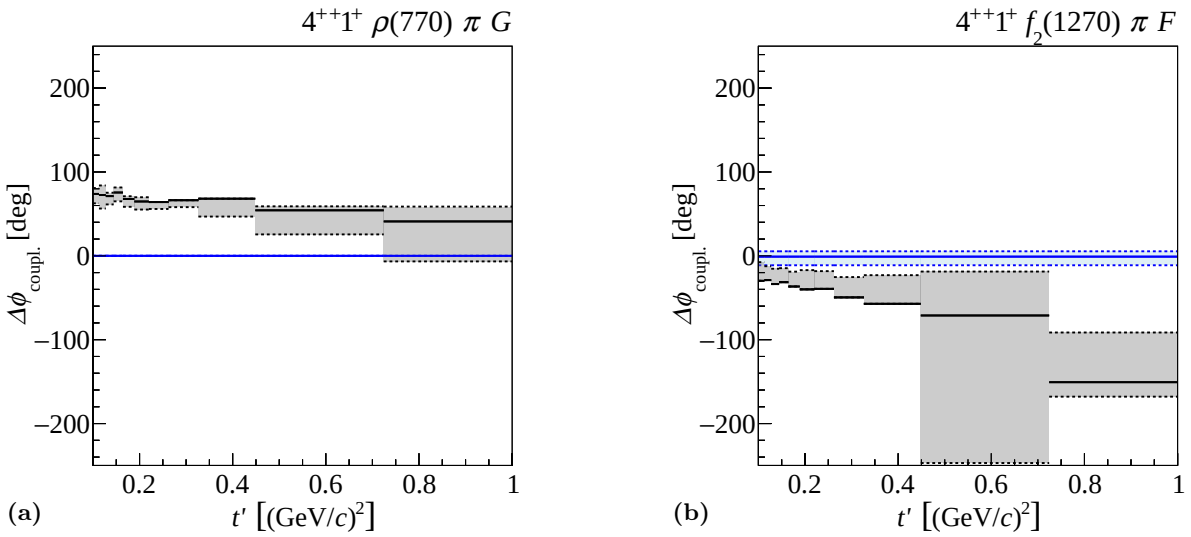

FIG. 55: Similar to Fig. 50 but for the wave components in (a) the $4^{++}1^{+}\rho(770)\pi G$ and (b) the $4^{++}1^{+}f_2(1270)\pi F$ wave. The coupling phases of the $a_4(2040)$ (blue lines) and the nonresonant component (black lines) are shown relative to the $a_4(2040)$ in the $4^{++}1^{+}\rho(770)\pi G$ wave.

closest to that of the $\pi_2(1670)$ with an offset of about $+30°$. Figure 55 shows the coupling phases of the 4^{++} wave components relative to the $a_4(2040)$ in the $\rho(770)\pi G$ wave. The t' dependence of the coupling phases of the $a_4(2040)$ in the $\rho(770)\pi G$ and $f_2(1270)\pi F$ waves are constrained via Eq. (21). The coupling phase offset of the $a_4(2040)$ in the $f_2(1270)\pi F$ wave is close to $0°$.

VIII Summary and conclusions

In this paper, we have presented the results of a fit of a Breit-Wigner resonance model to 14 selected partial-wave amplitudes with $J^{PC} = 0^{-+}$, 1^{++}, 2^{++}, 2^{-+}, 4^{++}, and spin-exotic 1^{-+} quantum numbers. The amplitudes result from a partial-wave analysis of 46×10^6 exclusive events of the diffractive reaction $\pi^- + p \to \pi^-\pi^-\pi^+ + p_{\text{recoil}}$ using a model with 88 partial waves [30].

We have measured the masses and widths of the a_J-like resonances: $a_1(1260)$, $a_1(1640)$, $a_2(1320)$, $a_2(1700)$, $a_4(2040)$, and of the resonancelike $a_1(1420)$ [see Fig. 56(a) and Table 5]; and those of the π_J-like resonances: $\pi(1800)$, $\pi_2(1670)$, $\pi_2(1880)$, $\pi_2(2005)$, and the spin-exotic $\pi_1(1600)$ [see Fig. 56(b) and Table 5].

The parameters of $a_1(1420)$, $a_2(1320)$, $a_4(2040)$, $\pi(1800)$, and $\pi_2(1670)$ are reliably extracted with comparatively small uncertainties. The consistency of the $a_1(1420)$ signal with a Breit-Wigner amplitude is confirmed. The $a_1(1420)$ parameter values are consistent with those from a simpler analysis of the same data in Ref. [19], but have smaller uncertainties. The $a_2(1320)$ and $\pi(1800)$ parameter values are consistent with previous measurements. The measured values of the $a_4(2040)$ mass and width are the most accurate so far. We find a lower $a_4(2040)$ mass and a larger width than some of the previous experiments.

We observe production of the $a_2(1320)$ with spin projection $M = 2$ along the beam axis. In order to describe the 2^{++} partial-wave amplitudes, the inclusion of an excited $a_2(1700)$ is necessary. It appears most strongly in the $2^{++}1^{+}f_2(1270)\pi P$ wave. The $a_2(1700)$ mass is consistent with previous measurements while the width is larger.

In order to describe the four 2^{-+} partial-wave amplitudes that are included in the fit, three resonances are needed, the $\pi_2(1670)$, the $\pi_2(1880)$, and the $\pi_2(2005)$. The latter one is not

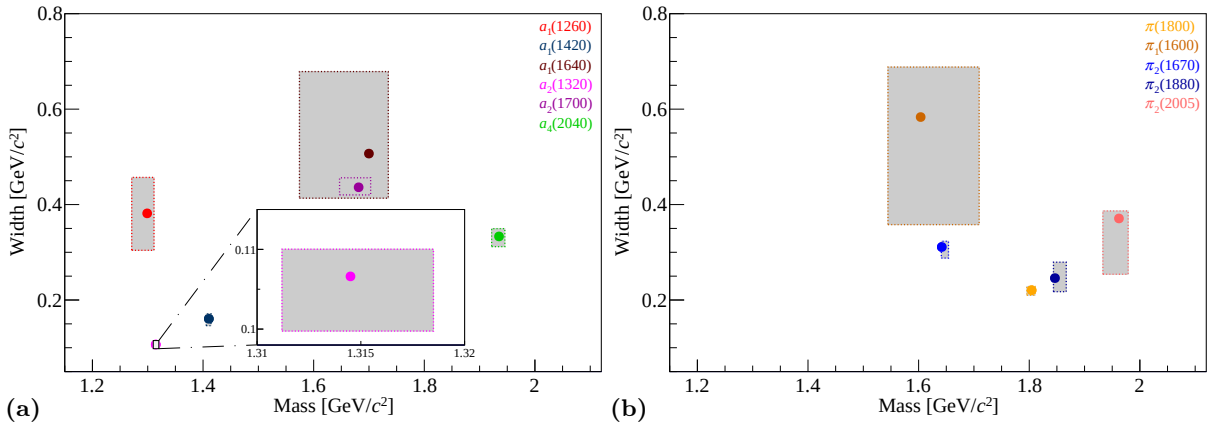

FIG. 56: Masses and widths of (a) a_J-like and (b) π_J-like resonances extracted in this analysis (points). The systematic uncertainties are represented by the boxes. The statistical uncertainties are at least an order of magnitude smaller than the systematic ones and are hence omitted. Different colors encode different resonances.

an established state. The measured $\pi_2(2005)$ parameter values are consistent with the two measurements by previous experiments. We find the $\pi_2(1670)$ to be lighter and broader than the world average. The $\pi_2(1880) \to 3\pi$ decay is observed for the first time. The measured $\pi_2(1880)$ width is consistent with the world average, and the mass is found to be smaller.

The $1^{++}0^+\rho(770)\pi S$ and $1^{-+}1^+\rho(770)\pi P$ partial-wave amplitudes are dominated by the nonresonant components and are difficult to describe. This is a main source of systematic uncertainty. The shape of the intensity distributions of both waves depends strongly on t'. By fitting the resonance model simultaneously in 11 t' bins, we achieve a better separation of the resonant and nonresonant components in these waves compared to previous analyses of diffractive-dissociation reactions. In both waves, the intensity of the nonresonant components behaves similar to a model for the Deck effect. The resonance model is not able to describe all details of the $a_1(1260)$ peak in the $1^{++}0^+$ $\rho(770)\pi S$ wave, which leads to comparatively large uncertainties for the $a_1(1260)$ parameters. The data require an excited $a_1(1640)$ state. However, because of the dominant $a_1(1260)$, the $a_1(1640)$ parameters are not well determined. The data also require a spin-exotic resonance, the $\pi_1(1600)$, in the $1^{-+}1^+\rho(770)\pi P$ wave. The t'-resolved analysis allows us to establish for the first time that a significant $\pi_1(1600)$ signal appears only for $t' \gtrsim 0.5\,(\mathrm{GeV}/c)^2$, whereas at low t' the intensity of the spin-exotic wave is saturated by Deck-like nonresonant contributions. The $\pi_1(1600)$ parameters have large uncertainties. The measured width is significantly larger than that observed in previous experiments including our own result from the data taken with a lead target, but it has a large systematic uncertainty toward smaller values.

The resonance yields are found to be much more sensitive to model assumptions than the resonance parameters. For the $a_2(1320)$ and $a_4(2040)$ the systematic uncertainties are small enough to extract their branching-fraction ratios for the decays into $\rho(770)\pi$ and $f_2(1270)\pi$. The branching-fraction ratio for the $a_4(2040)$ was measured to be $B^{a_4,\mathrm{corr}}_{\rho\pi G, f_2\pi F} = 2.9\,^{+0.6}_{-0.4}$. This value is corrected for the unobserved $\pi^-\pi^0\pi^0$ decay mode, the effects from self-interference, and the branching fraction of the $f_2(1270)$ into 2π. The measured value is in good agreement with predictions by the $^3P_0$ decay model. The corresponding branching-fraction ratio $B^{a_2,\mathrm{corr}}_{\rho\pi D, f_2\pi P} = 16.5\,^{+1.2}_{-2.4}$ for the $a_2(1320)$ was measured for the first time to our knowledge.

Since the resonance-model fit is performed simultaneously in 11 bins of t', the t' dependence of the amplitudes of the resonant and nonresonant wave components has been studied in unprecedented

detail. The t' dependence of the intensities of most of the resonance signals follows approximately the expected exponential behavior with slope parameters between about 7 to 9 $(\mathrm{GeV}/c)^{-2}$ (see Table 6). This is in particular true for the $a_1(1420)$. The $\pi_1(1600)$ exhibits an exponential t' spectrum only, if the Deck model is used to describe the nonresonant components. The slope parameters of the higher-mass states are found to be smaller than those of the ground states. In many waves, the slope of the nonresonant component is steeper than that of the resonances.

The t' dependence of the relative phases of the wave components was studied for the first time to our knowledge. Most resonances, including the $a_1(1420)$, are produced with a phase that is approximately independent of t', which is expected if the production mechanism is the same over the analyzed t' range. The production phase of the $\pi_1(1600)$ exhibits a stronger dependence on t'. In many waves the production phase of the nonresonant component exhibits a strong t' dependence, which is a hint that more than one production mechanism contributes.

A Pole positions

For those resonances that are described by the simple relativistic Breit-Wigner amplitude,

$$\mathcal{D}_j^{\mathrm{R}}(m_{3\pi}; m_j, \Gamma_j) = \frac{m_j\,\Gamma_j}{m_j^2 - m_{3\pi}^2 - i\,m_j\,\Gamma_j}$$

[see Eqs. (22) and (23) in Sec. IV A 1], we can calculate the pole positions in the complex energy plane. The pole position $s_{\mathrm{R},j}$ of the Breit-Wigner amplitude for resonance j is given by

$$s_{\mathrm{R},j} = m_j^2 - i\,m_j\,\Gamma_j. \tag{A1}$$

Traditionally, the pole position is related to the resonance mass $m_{\mathrm{R},j}$ and the total width $\Gamma_{\mathrm{R},j}$ by [63]

$$\sqrt{s_{\mathrm{R},j}} = m_{\mathrm{R},j} - i\,\frac{\Gamma_{\mathrm{R},j}}{2}. \tag{A2}$$

In Table 7, we compare the Breit-Wigner parameters m_j and Γ_j from Table 5 with the pole parameters $m_{\mathrm{R},j}$ and $\Gamma_{\mathrm{R},j}$. Except for the $a_2(1320)$, the listed pole parameters are estimated using Eqs. (A1) and (A2). The parametrization for the $a_2(1320)$ uses the mass-dependent width in Eq. (25). Therefore, Eq. (A1) does not hold and the $a_2(1320)$ pole position was estimated by numerical methods.[bf] The $a_1(1260)$ is an even more complicated case. In order to calculate its pole position, one would need to analytically continue the phase-space integral $I_{aa}(m_{3\pi})$ in Eq. (24) into the complex plane. We therefore omit the $a_1(1260)$ in Table 7.

The width values of the pole positions are nearly identical to the Breit-Wigner width values. For some resonances, the pole masses differ slightly from the Breit-Wigner masses. Interestingly the pole masses for the $a_2(1320)$ and $a_2(1700)$ are closer to the pole masses of $1307 \pm 1\,(\mathrm{stat.}) \pm 6\,(\mathrm{sys.})\,\mathrm{MeV}/c^2$ and $1720 \pm 10\,(\mathrm{stat.}) \pm 60\,(\mathrm{sys.})\,\mathrm{MeV}/c^2$, respectively, which were obtained in an analysis of the $\eta\pi$ D-wave intensity using an analytical model based on the principles of the relativistic S-matrix [66]. However, the discrepancy in the $a_2(1700)$ width remains (see Sec. VI C 2). The caveats of our simple Breit-Wigner model, which are discussed in Sec. IV A 4, also apply to the extracted pole parameters and may be the reason for this discrepancy.

[bf] The $a_2(1320)$ amplitude has additional poles that are caused by the phase-space terms in Eq. (25). However, these poles lie below $1\,\mathrm{GeV}/c^2$, far away from the $a_2(1320)$ pole.

Table 7: Breit-Wigner resonance parameters from Table 5 compared to pole parameters defined in Eq. (A2).

(a) a_J-like resonances

		$a_1(1420)$	$a_1(1640)$	$a_2(1320)$	$a_2(1700)$	$a_4(2040)$
		(Sec. VI E)		(Sec. VI C)		(Sec. VI B)
BW	Mass [MeV/c^2]	$1411\,^{+4}_{-5}$	$1700\,^{+35}_{-130}$	$1314.5\,^{+4.0}_{-3.3}$	$1681\,^{+22}_{-35}$	$1935\,^{+11}_{-13}$
	Width [MeV/c^2]	$161\,^{+11}_{-14}$	$510\,^{+170}_{-90}$	$106.6\,^{+3.4}_{-7.0}$	$436\,^{+20}_{-16}$	$333\,^{+16}_{-21}$
Pole	Mass [MeV/c^2]	1413	1718	1306.8	1695	1942
	Width [MeV/c^2]	160	501	105.2	433	332

(b) π_J-like resonances

		$\pi(1800)$	$\pi_1(1600)$	$\pi_2(1670)$	$\pi_2(1880)$	$\pi_2(2005)$
		(Sec. VI A)	(Sec. VI F)		(Sec. VI D)	
BW	Mass [MeV/c^2]	$1804\,^{+6}_{-9}$	$1600\,^{+110}_{-60}$	$1642\,^{+12}_{-1}$	$1847\,^{+20}_{-3}$	$1962\,^{+17}_{-29}$
	Width [MeV/c^2]	$220\,^{+8}_{-11}$	$580\,^{+100}_{-230}$	$311\,^{+12}_{-23}$	$246\,^{+33}_{-28}$	$371\,^{+16}_{-120}$
Pole	Mass [MeV/c^2]	1808	1629	1649	1851	1971
	Width [MeV/c^2]	220	574	310	245	369

B Deck model

To construct a model for the Deck process [43] (see also Fig. 8), we follow Ref. [31], where the Deck amplitude is described as a product of two vertex amplitudes and a pion propagator in the t channel:

$$\mathcal{A}(s_{\pi\pi}, s_{\pi p}, t_\pi, t) = \mathcal{A}_{\pi\pi}(s_{\pi\pi})\, \mathcal{A}_{\pi p}(s_{\pi p}, t)\, \frac{e^{-b_2\,(m_\pi^2 - t_\pi)}}{m_\pi^2 - t_\pi}. \tag{B1}$$

Here, t_π is the squared four-momentum of the exchanged pion. The amplitude $\mathcal{A}_{\pi\pi}$, which depends on the squared center-of-mass energy $s_{\pi\pi}$ of the $\pi^-\pi^+$ system, describes production, propagation, and decay of the isobar ξ^0. As a parametrization of $\mathcal{A}_{\pi\pi}$, we use the elastic $\pi\pi$ scattering amplitude from Ref. [115], which includes the dominant isobars used in our PWA model: $[\pi\pi]_S$, $\rho(770)$, $f_0(980)$, $f_2(1270)$, and $\rho_3(1690)$. The amplitude

$$\mathcal{A}_{\pi p}(s_{\pi p}, t) = i\, s_{\pi p}\, \sigma_{\pi p\to\pi p}\, e^{b_1\, t} \tag{B2}$$

describes the elastic scattering of pion and proton and depends on the squared center-of-mass energy $s_{\pi p}$ of the bachelor pion and the recoil proton and on the squared four-momentum t transferred to the target nucleon. We use a value of $\sigma_{\pi p\to\pi p} = 64\,\text{GeV}^{-2} = 25\,\text{mb}$ for the total $\pi^- p$ elastic scattering cross section and choose the slope parameter to be $b_1 = 8\,(\text{GeV}/c)^{-2}$. The description of the observed t dependence around $m_{3\pi} = 1\,\text{GeV}/c^2$ requires the additional exponential factor in Eq. (B1) with $b_2 = 0.45\,(\text{GeV}/c)^{-2}$.

C Alternative χ^2 formulations

The elements of a rank-1 spin-density matrix ϱ_{ab} are related by Eq. (35). Therefore, the full information from the mass-independent analysis is already contained in a single row (or column) of ϱ_{ab}. For a chosen reference wave with index r, the elements of the corresponding row vector $\varrho_{ra} = \mathcal{T}_r\, \mathcal{T}_a^*$ represent in total $(2N_\text{wave} - 1)$ independent real values. This corresponds to the number of independent real values of the N_wave transition amplitudes. The deviation of the model from the data is measured by the quantities

$$\Delta_a^\text{Re} = \text{Re}[\varrho_{ra}] - \text{Re}[\widehat{\varrho}_{ra}] \tag{C1}$$

and

$$\Delta_a^\text{Im} = \text{Im}[\varrho_{ra}] - \text{Im}[\widehat{\varrho}_{ra}] \tag{C2}$$

for $a \neq r$, and

$$\Delta_r = \varrho_{rr} - \widehat{\varrho}_{rr} \tag{C3}$$

for $a = r$. These deviations are collected into the $(2N_\text{wave} - 1)$-dimensional vector[bg]

$$\boldsymbol{\Delta} \equiv \big(\Delta_1^\text{Re}, \Delta_1^\text{Im}, \Delta_2^\text{Re}, \Delta_2^\text{Im}, \ldots, \Delta_{r-1}^\text{Im}, \Delta_r, \Delta_{r+1}^\text{Re}, \ldots, \Delta_{N_\text{wave}}^\text{Re}, \Delta_{N_\text{wave}}^\text{Im}\big). \tag{C4}$$

The total deviation of the model from the data is given by the sum of the squared Mahalanobis distances [116] over all $m_{3\pi}$ and t' bins:

$$\chi^2 = \sum_{i,j}^{2N_\text{wave}-1} \sum_{t'\ \text{bins}} \sum_{(m_{3\pi}\ \text{bins})_{ij}} \boldsymbol{\Delta}_i(m_{3\pi}, t')\, V_{ij}^{-1}(m_{3\pi}, t')\, \boldsymbol{\Delta}_j(m_{3\pi}, t'). \tag{C5}$$

[bg] Note that here the wave indices a and r represent both the quantum numbers of the waves as defined in Eq. (4) and the numerical index in the list of N_wave waves included in the resonance-model fit.

Here, i and j are the indices of the elements of $\boldsymbol{\Delta}$ and V_{ij} is the covariance matrix of the corresponding terms that appear in $\boldsymbol{\Delta}$. The matrix V_{ij} is calculated from the covariance matrix of the transition amplitudes using Gaussian error propagation.

In contrast to Eq. (34), the χ^2 formulation in Eq. (C5) requires choosing a reference wave. This wave needs to have significant intensity over the full analyzed mass range, which extends from 0.9 to 2.3 GeV/c^2. Also the model has to describe this wave over this mass range. In our analysis, only the $1^{++}0^+\rho(770)\pi S$ wave fulfills these criteria. In addition, Eq. (C5) is asymmetric with respect to the way the information of the partial waves enters. The transition amplitude of the reference wave enters in every term of the sum, whereas the transition amplitudes of the other waves enter each only in two interference terms per $(m_{3\pi}, t')$ bin. Furthermore, the transition amplitudes of the reference wave appear with a maximum power of 4, whereas the transition amplitudes of the other waves have a maximum power of 2. This is in contrast to Eq. (34), where the transition amplitudes of all waves enter in a symmetric way.

Another possible approach is to construct the χ^2 function from the differences of the modeled transition amplitudes and those obtained from real data. However, in order to fix the immeasurable global phase, this approach also requires a reference wave. The deviation of the model from the data is measured in terms of the rotated transition amplitudes

$$e^{i\varphi_r}\,\mathcal{T}_a^* = \frac{\mathcal{T}_r}{|\mathcal{T}_r|}\,\mathcal{T}_a^* \tag{C6}$$

The corresponding χ^2 function can be derived from Eqs. (C1) and (C2) using the substitution

$$\varrho_{ra} = \mathcal{T}_r\,\mathcal{T}_a^* \to \frac{\mathcal{T}_r}{|\mathcal{T}_r|}\,\mathcal{T}_a^* = \frac{\varrho_{ra}}{|\mathcal{T}_r|} \tag{C7}$$

The resulting χ^2 function is similar to Eq. (C5). The only difference is that each term of the sum now contains the phase of the reference wave instead of the full transition amplitude.

D Systematic uncertainties of resonance parameters

In this section, we discuss the results of selected systematic studies, in addition to the studies already covered in Sec. VI. We focus in particular on studies that yield the largest deviations of resonance parameters from those of the main fit and therefore define the systematic uncertainties. The systematic studies are explained in Sec. V.

1 Systematic uncertainties of the $\pi(1800)$ parameters

The $\pi(1800)$ parameters vary only slightly among the systematic studies. They are in particular only weakly sensitive to how well the nonresonant component describes the low-mass shoulder. Using the mass shapes of the nonresonant components from the partial-wave decomposition of a model for the Deck amplitude in Study (N), the fit is not able to reproduce the enhancement at 1.3 GeV/c^2 in the intensity distributions. Nevertheless, the $\pi(1800)$ width remains practically unchanged and the mass increases only slightly by 6 MeV/c^2, which defines the upper limit of the uncertainty interval for the $\pi(1800)$ mass.

A similar result is obtained in a study, in which the fit range for the 0^{-+} wave is narrowed to the $\pi(1800)$ peak region of $1.6 < m_{3\pi} < 2.3\,\text{GeV}/c^2$. In this study, the nonresonant component nearly vanishes and the width of the $\pi(1800)$ increases by only 8 MeV/c^2, which defines the upper limit of the uncertainty interval for the $\pi(1800)$ width.

The $\pi(1800)$ parameters also depend on the model for the production probability $|\mathcal{P}(m_{3\pi}, t')|^2$ in Eqs. (20) and (32). In Study (Q), in which $|\mathcal{P}(m_{3\pi}, t')|^2$ is set to unity, the $\pi(1800)$ mass

decreases by $9\,\mathrm{MeV}/c^2$ and the width by $11\,\mathrm{MeV}/c^2$, which both define the lower limits of the respective uncertainty intervals.

2 Systematic uncertainties of parameters of the $J^{PC} = 1^{++}$ resonances

The parameters of $a_1(1260)$ and $a_1(1640)$ depend strongly on the interference of the 1^{++} and 2^{++} waves. In Studies (E) through (K) (see Table 3), the solution with the narrow $a_1(1260)$ (see discussion in Sec. VI E 1) has the lowest χ^2. Study (I) defines the upper limit of the uncertainty interval for the $a_1(1260)$ mass and the lower limit of the uncertainty interval for the $a_1(1260)$ width. Study (J) defines the upper limit of the uncertainty interval for the $a_1(1640)$ mass.

A strong dependence of the parameters of $a_1(1260)$ and $a_1(1640)$ on the number of background events in the selected data sample is observed in Study (A). In this study, weaker event-selection criteria lead to an increased background. Study (A) defines the lower limit of the uncertainty interval for the $a_1(1260)$ mass. This study also defines the lower limit of the uncertainty interval for the $a_1(1640)$ mass and the upper limit of the uncertainty interval for the $a_1(1640)$ width.

The upper limit of the uncertainty interval for the $a_1(1260)$ width and the lower limit for the $a_1(1640)$ width are defined by the study, which included the $a_1(1420)$ resonance also in the $1^{++}0^+$ $\rho(770)\pi S$ and $1^{++}0^+ f_2(1270)\pi P$ waves (see discussion in Sec. VI E 2). This study and Study (A) discussed above are the only two studies that yield a significantly broader $a_1(1260)$.

In Studies (O) and (P), alternative χ^2 formulations (see Sec. C) are used that, compared to the main fit, give more relative weight to the intensity distributions than to the phases. As discussed in Sec. VI E 1, the model is not able to describe all details of the $1^{++}0^+\rho(770)\pi S$ intensity distributions and the resulting deviations of the model from the data give a large contribution to the χ^2. In both studies, the fit tries to compensate the deviations by using unphysical values for the $a_1(1260)$ and $a_1(1640)$ parameters[bh] [69]. Therefore, the results of Studies (O) and (P) are not considered for the systematic uncertainties of the $a_1(1260)$ and $a_1(1640)$ parameters.

In Study (Q), in which the production probability $|\mathcal{P}(m_{3\pi}, t')|^2$ in Eqs. (20) and (32) is set to unity, the $a_1(1260)$ parameters are only slightly affected but the $a_1(1640)$ width increases by $96\,\mathrm{MeV}/c^2$.

The parameters of the $a_1(1420)$ have significantly smaller systematic uncertainties than the other two 1^{++} resonances. The upper limits of the uncertainty intervals for the $a_1(1420)$ mass and width are defined by the study, in which the $a_1(1420)$ resonance is also included in the $1^{++}0^+$ $\rho(770)\pi S$ and $1^{++}0^+ f_2(1270)\pi P$ waves (see discussion in Sec. VI E 2). Study (A) defines the lower limit of the uncertainty interval for the $a_1(1420)$ mass, and Study (P) the one for the $a_1(1420)$ width.

3 Systematic uncertainties of the $\pi_1(1600)$ parameters

As discussed in Sec. VI F 1, the $\pi_1(1600)$ parameters depend on the description used for the nonresonant component. The lower limit of the uncertainty interval for the $\pi_1(1600)$ mass is defined by Study (N), in which a model for the Deck amplitude is used to determine the shape of the nonresonant contribution.

The $\pi_1(1600)$ parameters are also sensitive to the range parameter q_R in the Blatt-Weisskopf factors. In Study (R), in which q_R was set to $267\,\mathrm{MeV}/c$ corresponding to an assumed strong-interaction range of 0.75 fm, the $\pi_1(1600)$ mass increases by $110\,\mathrm{MeV}/c^2$ and the width decreases by $90\,\mathrm{MeV}/c^2$. This study defines the upper limit of the uncertainty interval for the $\pi_1(1600)$

[bh] Both resonances become approximately $600\,\mathrm{MeV}/c^2$ wide and have nearly identical masses around $1.35\,\mathrm{GeV}/c^2$.

mass. It is worth noting that increasing the interaction radius in Study (S) to 1.29 fm, which corresponds to $q_R = 155\,\mathrm{MeV}/c$, leaves the $\pi_1(1600)$ parameters practically unchanged.

A particularly large effect on the $\pi_1(1600)$ parameters is observed if the two $2^{++}\rho(770)\pi D$ waves are omitted from the fit [Study (J)]. In this study, the $\pi_1(1600)$ mass increases by $80\,\mathrm{MeV}/c^2$ and the width decreases by $230\,\mathrm{MeV}/c^2$.[bi] The latter defines the lower limit of the uncertainty interval for the $\pi_1(1600)$ width.

Studies (O) and (P) with alternative χ^2 formulations (see Sec. C) also influence the $\pi_1(1600)$ parameters. The mass decreases by $30\,\mathrm{MeV}/c^2$, and the width increases by $100\,\mathrm{MeV}/c^2$. The latter defines the upper limit of the uncertainty interval for the $\pi_1(1600)$ width. These studies show that larger width values are preferred when less weight is given to the phase information in the χ^2 function.[bj]

4 Systematic uncertainties of parameters of the $J^{PC} = 2^{++}$ resonances

As mentioned in Sec. VI C 1, the 2^{++} resonance parameters are sensitive to the parametrization of the nonresonant components. We investigated this, by determining the mass shape of the nonresonant component from the partial-wave decomposition of a model for the Deck amplitude [Study (N); see Sec. V]. In all three 2^{++} waves, the shape of the Deck intensity is distinctly different from that of the nonresonant components determined from data in the main fit. Study (N) defines the lower limits of the uncertainty intervals for the masses of $a_2(1320)$ and $a_2(1700)$.

The 2^{++} resonance parameters also depend on the choice of the wave set included in the fit. The $a_2(1320)$ parameters change only slightly if we omit the two dominant 1^{++} waves [Study (C)], the four 2^{-+} waves [Study (B)], or the two 4^{++} waves [Study (D)]. However, Study (I), in which only the low-intensity $2^{++}2^{+}\rho(770)\pi D$ wave was included in the fit, defines the upper limit of the uncertainty interval for the $a_2(1320)$ mass and also the lower limit for the $a_2(1320)$ width. The $a_2(1700)$ parameters do not depend strongly on the wave set used in the fit. The only exceptions are Studies (G), (H), and (I), in which the $2^{++}1^{+}f_2(1270)\pi P$ wave is omitted from the fit. If, for example, only the two $2^{++}\rho(770)\pi D$ waves are included in the fit [Study (G)], we observe a strong increase of the $a_2(1700)$ mass by $150\,\mathrm{MeV}/c^2$ and of the width by $41\,\mathrm{MeV}/c^2$. However, the two $\rho(770)\pi D$ waves are dominated by the $a_2(1320)$ and contain only very weak $a_2(1700)$ signals. Therefore, the $a_2(1700)$ parameters are not reliably determined in these three studies and they have been omitted from the determination of the systematic uncertainties.

Also the value of the range parameter q_R in the Blatt-Weisskopf factors influences the 2^{++} resonance parameters. Study (R), in which q_R was set to $267\,\mathrm{MeV}/c$ corresponding to an assumed strong-interaction range of 0.75 fm, defines the upper limits of the uncertainty intervals for the $a_2(1320)$ width and the $a_2(1700)$ mass. The lower limit of the uncertainty interval for the $a_2(1700)$ width is defined by Study (S), in which q_R was set to $155\,\mathrm{MeV}/c$, which corresponds to a range of 1.29 fm.

The upper limit of the uncertainty interval for the $a_2(1700)$ width is defined by Study (P), in which an alternative χ^2 formulation (see Sec. C) was used.

5 Systematic uncertainties of parameters of the $J^{PC} = 2^{-+}$ resonances

As discussed in Sec. VI D 1, the parameters of the π_2 resonances depend on the wave set. Study (D), in which the two 4^{++} waves are omitted from the fit, defines the lower limits of the uncertainty

[bi] In Study (J), also the $a_1(1260)$ becomes narrower and the $a_1(1640)$ heavier and wider (see Sec. VI E 1).

[bj] In Studies (O) and (P) also the parameters of the $a_1(1260)$ and the $a_1(1640)$ change significantly (see Sec. D 2) and the parameters of the $\pi_1(1600)$ are sensitive to these a_1 parameters.

intervals for the masses of $\pi_2(1670)$ and $\pi_2(1880)$. The omission of the $1^{++}0^+\rho(770)\pi S$ wave from the fit in Study (E) leads to the largest $\pi_2(2005)$ width.

Study (A), in which weaker event-selection criteria lead to an increased background, defines the lower limits of the uncertainty intervals for the widths of $\pi_2(1670)$ and $\pi_2(1880)$. The parameters of the $\pi_2(2005)$ are only weakly affected.

The parameters of $\pi_2(1880)$ and $\pi_2(2005)$ also depend on the number of t' bins. Study (L), in which the analysis was performed using only eight t' bins, defines the upper limit of the uncertainty interval for the $\pi_2(1880)$ mass and the lower limit for the $\pi_2(2005)$ mass. The parameters of the $\pi_2(1670)$ change only slightly.

The π_2 resonance parameters are exceptionally sensitive to the $m_{3\pi}$ and t' dependences of the production probability $|\mathcal{P}(m_{3\pi}, t')|^2$ in Eqs. (20) and (32). Study (Q), in which this factor was set to unity, defines the upper limits of the systematic uncertainty intervals for the $\pi_2(1670)$ mass and the $\pi_2(1880)$ width. It also defines the lower limit for the $\pi_2(2005)$ width.

Studies (O) and (P) with alternative χ^2 formulations (see Sec. C) leave the $\pi_2(1670)$ parameters virtually unchanged. The $\pi_2(1880)$ width increases by about $20\,\text{MeV}/c^2$. The strongest effect is observed for the $\pi_2(2005)$ parameters in Study (P), where the $\pi_2(2005)$ mass increases by $17\,\text{MeV}/c^2$, and the width decreases by $63\,\text{MeV}/c^2$. The former value defines the upper limit of the systematic uncertainty interval for the $\pi_2(2005)$ mass.

The interference of the 2^{-+} wave with the $0^{-+}0^+ f_0(980)\pi S$ wave affects the widths of the $\pi_2(1670)$ and the $\pi_2(1880)$. If the lower limit of the fit range in the 0^{-+} wave is increased from $1.2\,\text{GeV}/c^2$ to $1.6\,\text{GeV}/c^2$, the width of the $\pi_2(1670)$ increases by $12\,\text{MeV}/c^2$ and that of the $\pi_2(1880)$ by $32\,\text{MeV}/c^2$. The former value defines the upper limit of the systematic uncertainty interval for the $\pi_2(1670)$ width. The latter value is close to the upper limit for the $\pi_2(1880)$ width. The width of the $\pi_2(2005)$ decreases by $90\,\text{MeV}/c^2$.

When we use the mass shapes of the nonresonant components from the partial-wave decomposition of a model for the Deck amplitude in Study (N), the intensities and interference terms of all four 2^{-+} waves are described less well by the model (see Fig. 9). In this study, the fit finds smaller intensities for the nonresonant components. In contrast, the resonance components have larger intensities and exhibit a sizable destructive interference. We therefore conclude that the used Deck model does not describe well the nonresonant components in the 2^{-+} waves.

6 Systematic uncertainties of the $a_4(2040)$ parameters

The $a_4(2040)$ resonance parameters depend only weakly on the set of waves included in the fit. This is in particular true for Studies (K) and (B), in which we omitted the 2^{++} and 2^{-+} waves from the fit, respectively. In Study (C), in which the $1^{++}0^+\rho(770)\pi S$ and $1^{++}0^+ f_2(1270)\pi P$ waves are omitted, the $a_4(2040)$ width increases by $13\,\text{MeV}/c^2$.

Also the value of the range parameter q_R in the Blatt-Weisskopf factors influences the $a_4(2040)$ parameters. Study (R), in which q_R was set to $267\,\text{MeV}/c$ corresponding to an assumed strong-interaction range of 0.75 fm, defines the lower limits of the uncertainty intervals for the $a_4(2040)$ mass and width.

The upper limit of the uncertainty interval for the $a_4(2040)$ mass is defined by Study (A), in which weaker event-selection criteria lead to an increased background.

Study (N), in which the parametrization of the nonresonant amplitude was replaced by the square root of the intensity distribution of the partial-wave decomposition of Deck Monte Carlo data generated according to the model described in Sec. B, defines the upper limit of the uncertainty

interval for the $a_4(2040)$ width. While the shape of the Deck intensity in the $f_2(1270)\pi F$ wave is similar to that of the nonresonant component found in the main fit, it deviates in the $\rho(770)\pi G$ wave leading to a worse description of the data (see Fig. 9).

Acknowledgements

We have received many suggestions and input during a series of PWA workshops: a joint COMPASS-JLab-GSI Workshop on Physics and Methods in Meson Spectroscopy (Garching/2008), Workshops on Spectroscopy at COMPASS held 2009 and 2011 in Garching, and in the context of the ATHOS workshop series (Camogli/2012, Kloster Seeon/2013, Ashburn/2015, and Bad Honnef/2017). We are especially indebted to V. Mathieu, W. Ochs, J. Pelaez, M. Pennington, and A. Szczepaniak for their help and suggestions. S.U. Chung would like to thank the IAS at the TU München and together with D. Ryabchikov the Excellence Cluster "Universe" for supporting many visits to Munich during the past years.

We gratefully acknowledge the support of the CERN management and staff as well as the skills and efforts of the technicians of the collaborating institutions. This work is supported by MEYS (Czech Republic); "HadronPhysics3" Integrating Activity in FP7 (European Union); CEA, Laboratoire d'Excellence P2IO and ANR (France); BMBF, DFG cluster of excellence "Origin and Structure of the Universe", the DFG Collaborative Research Centre/Transregio 110, the computing facilities of the Computational Center for Particle and Astrophysics (C2PAP), IAS-TUM, and Humboldt Foundation (Germany); SAIL (CSR) (India); ISF (Israel); INFN (Italy); MEXT, JSPS, Daiko, and Yamada Foundations (Japan); NRF (Republic of Korea); NCN (Poland); FCT (Portugal).

References

[1] P. Abbon *et al.*, [COMPASS Collaboration], "The COMPASS setup for physics with hadron beams," *Nucl. Instrum. Methods Phys. Res., Sect. A* **779** (2015) 69–115, arXiv:1410.1797 [physics.ins-det].

[2] M. Battaglieri, [CLAS Collaboration], "Present and future of hadron spectroscopy at Jefferson Lab," *Int. J. Mod. Phys. E* **19** (2010) 837–843.

[3] H. Al Ghoul *et al.*, [GlueX Collaboration], "First Results from The GlueX Experiment," *AIP Conf. Proc.* **1735** (2016) 020001, arXiv:1512.03699 [nucl-ex].

[4] D. M. Asner *et al.*, "Physics at BES-III," *Int. J. Mod. Phys. A* **24** no. supp01, (2009) 1–794, arXiv:0809.1869 [hep-ex].

[5] A. J. Bevan *et al.*, [Belle and *BABAR* Collaborations], "The Physics of the B Factories," *Eur. Phys. J. C* **74** (2014) 3026, arXiv:1406.6311 [hep-ex].

[6] X. Feng, K. Jansen, and D. B. Renner, "Resonance parameters of the ρ meson from lattice QCD," *Phys. Rev. D* **83** (2011) 094505, arXiv:1011.5288 [hep-lat].

[7] D. J. Wilson, R. A. Briceno, J. J. Dudek, R. G. Edwards, and C. E. Thomas, "Coupled $\pi\pi, K\bar{K}$ scattering in P-wave and the ρ resonance from lattice QCD," *Phys. Rev. D* **92** (2015) 094502, arXiv:1507.02599 [hep-ph].

[8] S. Prelovsek, L. Leskovec, C. B. Lang, and D. Mohler, "$K\pi$ scattering and the K^* decay width from lattice QCD," *Phys. Rev. D* **88** (2013) 054508, arXiv:1307.0736 [hep-lat].

[9] D. J. Wilson, J. J. Dudek, R. G. Edwards, and C. E. Thomas, "Resonances in coupled πK, ηK scattering from lattice QCD," *Phys. Rev. D* **91** (2015) 054008, arXiv:1411.2004 [hep-ph].

[10] C. Patrignani *et al.*, [Particle Data Group], "Review of Particle Physics," *Chin. Phys. C* **40** (2016) 100001.

[11] E. Klempt and A. Zaitsev, "Glueballs, hybrids, multiquarks: Experimental facts versus QCD inspired concepts," *Phys. Rep.* **454** (2007) 1–202, arXiv:0708.4016 [hep-ph].

[12] V. Crede and C. A. Meyer, "The Experimental Status of Glueballs," *Prog. Part. Nucl. Phys.* **63** (2009) 74–116, arXiv:0812.0600 [hep-ex].

[13] W. Ochs, "The Status of Glueballs," *J. Phys. G* **40** (2013) 043001, arXiv:1301.5183 [hep-ph].

[14] C. A. Meyer and Y. V. Haarlem, "Status of exotic-quantum-number mesons," *Phys. Rev. C* **82** (2010) 025208, arXiv:1004.5516 [nucl-ex].

[15] C. A. Meyer and E. S. Swanson, "Hybrid Mesons," *Prog. Part. Nucl. Phys.* **82** (2015) 21–58, arXiv:1502.07276 [hep-ph].

[16] N. Brambilla, S. Eidelman, P. Foka, S. Gardner, A. S. Kronfeld, *et al.*, "QCD and strongly coupled gauge theories: challenges and perspectives," *Eur. Phys. J. C* **74** (2014) 2981, arXiv:1404.3723 [hep-ph].

[17] M. Alekseev *et al.*, [COMPASS Collaboration], "Observation of a $J^{PC} = 1^{-+}$ Exotic Resonance in Diffractive Dissociation of 190 GeV/c π^- into $\pi^-\pi^-\pi^+$," *Phys. Rev. Lett.* **104** (2010) 241803, arXiv:0910.5842 [hep-ex].

[18] C. Adolph *et al.*, [COMPASS Collaboration], "Measurement of radiative widths of $a_2(1320)$ and $\pi_2(1670)$," *Eur. Phys. J. A* **50** (2014) 79, arXiv:1403.2644 [hep-ex].

[19] C. Adolph *et al.*, [COMPASS Collaboration], "Observation of a New Narrow Axial-Vector Meson $a_1(1420)$," *Phys. Rev. Lett.* **115** (2015) 082001, arXiv:1501.05732 [hep-ex].

[20] Z.-G. Wang, "Light axial-vector tetraquark state candidate: $a_1(1420)$," arXiv:1401.1134 [hep-ph].

[21] J.-L. Basdevant and E. L. Berger, "The twofold emergence of the a_1 axial vector meson in high energy hadronic production," arXiv:1501.04643 [hep-ph].

[22] J.-L. Basdevant and E. L. Berger, "Peak Locations and Relative Phase of Different Decay Modes of the a_1 Axial Vector Resonance in Diffractive Production," *Phys. Rev. Lett.* **114** (2015) 192001, arXiv:1504.05955 [hep-ph].

[23] M. Mikhasenko, B. Ketzer, and A. Sarantsev, "Nature of the $a_1(1420)$," *Phys. Rev. D* **91** (2015) 094015, arXiv:1501.07023 [hep-ph].

[24] W. Wang and Z.-X. Zhao, "Production of a_1 in heavy meson decays," *Eur. Phys. J. C* **76** (2016) 59, arXiv:1511.06998 [hep-ph].

[25] H.-X. Chen, E.-L. Cui, W. Chen, T. G. Steele, X. Liu, and S.-L. Zhu, "$a_1(1420)$ resonance as a tetraquark state and its isospin partner," *Phys. Rev. D* **91** (2015) 094022, arXiv:1503.02597 [hep-ph].

[26] F. Aceti, L. R. Dai, and E. Oset, "$a_1(1420)$ peak as the $\pi f_0(980)$ decay mode of the $a_1(1260)$," *Phys. Rev. D* **94** (2016) 096015, arXiv:1606.06893 [hep-ph].

[27] T. Gutsche, V. E. Lyubovitskij, and I. Schmidt, "Tetraquarks in holographic QCD," *Phys. Rev. D* **96** (2017) 034030, arXiv:1706.07716 [hep-ph].

[28] X.-H. Liu, M. Oka, and Q. Zhao, "Searching for observable effects induced by anomalous triangle singularities," *Phys. Lett. B* **753** (2016) 297–302, arXiv:1507.01674 [hep-ph].

[29] F.-K. Guo, C. Hanhart, U.-G. Meißner, Q. Wang, Q. Zhao, and B.-S. Zou, "Hadronic molecules," *Rev. Mod. Phys.* **90** (2018) 015004, arXiv:1705.00141 [hep-ph].

[30] C. Adolph *et al.*, [COMPASS Collaboration], "Resonance production and $\pi\pi$ S-wave in $\pi^- + p \to \pi^-\pi^-\pi^+ + p_{\text{recoil}}$ at 190 GeV/c," *Phys. Rev. D* **95** (2017) 032004, arXiv:1509.00992 [hep-ex].

[31] C. Daum *et al.*, [ACCMOR Collaboration], "Diffractive production of 3π states at 63 and 94 GeV," *Nucl. Phys.* **B182** (1981) 269.

[32] D. V. Amelin *et al.*, [VES Collaboration], "Partial-wave analysis of the reaction $\pi^- p \to \pi^+\pi^-\pi^0 n$ at $p_{\pi^-} = 36$ GeV/c: Study of $a_2(1320)$ and $\omega_3(1670)$ mesons," *Z. Phys. C* **70** (1996) 71–76.

[33] J. Gunter *et al.*, [E852 Collaboration], "Partial wave analysis of the $\pi^0\pi^0$ system produced in $\pi^- p$ charge exchange collisions," *Phys. Rev. D* **64** (2001) 072003, arXiv:hep-ex/0001038 [hep-ex].

[34] C. W. Salgado and D. P. Weygand, "On the partial-wave analysis of mesonic resonances decaying to multiparticle final states produced by polarized photons," *Phys. Rep.* **537** (2014) 1–58, arXiv:1310.7498 [nucl-ex]. and references therein.

[35] See data tables in HEPData repository at http://www.hepdata.net/record/82958.

[36] F. Haas, *Two-Dimensional Partial-Wave Analysis of Exclusive 190 GeV $\pi^- p$ Scattering into the $\pi^-\pi^-\pi^+$ Final State at COMPASS (CERN)*. Ph.D. thesis, Technische Universität München, 2014. http://cds.cern.ch/record/1662589/. CERN-THESIS-2013-277.

[37] P. Abbon *et al.*, [COMPASS Collaboration], "The COMPASS experiment at CERN," *Nucl. Instrum. Methods Phys. Res., Sect. A* **577** (2007) 455–518, arXiv:0703049 [hep-ex].

[38] J. D. Jackson and D. R. Tovey, [Particle Data Group], "Kinematics," *Chin. Phys. C* **40** (2016) 560–564. http://pdg.lbl.gov/2016/reviews/rpp2016-rev-kinematics.pdf.

[39] D. Herndon, P. Söding, and R. J. Cashmore, "Generalized isobar model formalism," *Phys. Rev. D* **11** (1975) 3165.

[40] S. U. Chung and T. L. Trueman, "Positivity conditions on the spin density matrix: A simple parametrization," *Phys. Rev. D* **11** (1975) 633.

[41] A. R. Dzierba, R. Mitchell, E. Scott, M. R. Shepherd, P. Smith, M. Swat, *et al.*, "Partial wave analysis of the $\pi^-\pi^-\pi^+$ and $\pi^-\pi^0\pi^0$ systems and the search for a $J^{PC} = 1^{-+}$ meson," *Phys. Rev. D* **73** (2006) 072001, arXiv:hep-ex/0510068 [hep-ex].

[42] I. A. Kachaev *et al.*, [VES Collaboration], "Study of reaction $\pi^- A \to \pi^+\pi^-\pi^- A$ at VES setup," *AIP Conf. Proc.* **619** (2002) 577–581, arXiv:hep-ex/0111067 [hep-ex].

[43] R. T. Deck, "Kinematical Interpretation of the First π-ρ Resonance," *Phys. Rev. Lett.* **13** (1964) 169–173.

[44] R. J. Barlow, "Extended maximum likelihood," *Nucl. Instrum. Methods Phys. Res., Sect. A* **297** (1990) 496–506.

[45] D. V. Amelin *et al.*, [VES Collaboration], "Study of resonance production in diffractive reaction $\pi^- A \to \pi^+\pi^-\pi^- A$," *Phys. Lett. B* **356** (1995) 595–600.

[46] G. S. Adams *et al.*, [E852 Collaboration], "Observation of a New $J^{PC} = 1^{-+}$ Exotic State in the Reaction $\pi^- p \to \pi^+\pi^-\pi^- p$ at 18 GeV/c," *Phys. Rev. Lett.* **81** (1998) 5760–5763.

[47] S. U. Chung *et al.*, [E852 Collaboration], "Exotic and $q\overline{q}$ resonances in the $\pi^+\pi^-\pi^-$ system produced in $\pi^- p$ collisions at 18 GeV/c," *Phys. Rev. D* **65** (2002) 072001.

[48] S. U. Chung *et al.*, [E852 Collaboration], "Evidence for exotic $J^{PC} = 1^{-+}$ meson production in the reaction $\pi^- p \to \eta\pi^- p$ at 18 GeV/c," *Phys. Rev. D* **60** (1999) 092001, arXiv:hep-ex/9902003 [hep-ex].

[49] G. Breit and E. Wigner, "Capture of Slow Neutrons," *Phys. Rev.* **49** (1936) 519–531.

[50] M. G. Bowler, "The A_1 revisited," *Phys. Lett. B* **182** (1986) 400.

[51] G. M. Beladidze *et al.*, [VES Collaboration], "Study of $\pi^- N \to \eta\pi^- N$ and $\pi^- N \to \eta'\pi^- N$ reactions at 37 GeV/c," *Phys. Lett. B* **313** (1993) 276–282.

[52] C. Adolph *et al.*, [COMPASS Collaboration], "Odd and even partial waves of $\eta\pi^-$ and $\eta'\pi^-$ in $\pi^- p \to \eta^{(\prime)}\pi^- p$ at 191 GeV/c," *Phys. Lett. B* **740** (2015) 303–311, arXiv:1408.4286 [hep-ex].

[53] J. Blatt and V. Weisskopf, *Theoretical Nuclear Physics.* John Wiley & Sons, New York, 1952.

[54] F. von Hippel and C. Quigg, "Centrifugal-Barrier Effects in Resonance Partial Decay Widths, Shapes, and Production Amplitudes," *Phys. Rev. D* **5** (1972) 624–638.

[55] N. A. Törnqvist, "Understanding the scalar meson $q\overline{q}$ nonet," *Z. Phys. C* **68** (1995) 647–660, arXiv:hep-ph/9504372 [hep-ph].

[56] M. G. Albrow *et al.*, [CHLM Collaboration], "Inelastic Diffractive Scattering at the CERN ISR," *Nucl. Phys.* **B108** (1976) 1–29.

[57] P. D. B. Collins, *An Introduction to Regge Theory and High-Energy Physics.* Cambridge Monographs on Mathematical Physics. Cambridge University Press, Cambridge, UK, 1977.

[58] A. B. Kaidalov, "Diffractive Production Mechanisms," *Phys. Rep.* **50** (1979) 157–226.

[59] M. R. Ataian *et al.*, [EHS/NA22 Collaboration], "A study of double pomeron exchange in $\pi^+ p$ and $K^+ p$ interactions at 250 GeV/c," *Z. Phys. C* **50** (1991) 353–360.

[60] B. E. Cox and J. R. Forshaw, "POMWIG: HERWIG for diffractive interactions," *Comput. Phys. Commun.* **144** (2002) 104–110, arXiv:hep-ph/0010303 [hep-ph].

[61] C. Adloff *et al.*, [H1 Collaboration], "Inclusive measurement of diffractive deep inelastic ep scattering," *Z. Phys. C* **76** (1997) 613–629, arXiv:hep-ex/9708016 [hep-ex].

[62] F. Abe *et al.*, [CDF Collaboration], "Measurement of small angle $\bar{p}p$ elastic scattering at $\sqrt{s} = 546$ GeV and 1800 GeV," *Phys. Rev. D* **50** (1994) 5518–5534.

[63] D. Asner, C. Hanhart, and E. Klempt, [Particle Data Group], "Resonances," *Chin. Phys. C* **40** (2016) 565–569. http://pdg.lbl.gov/2016/reviews/rpp2016-rev-resonances.pdf.

[64] A. Jackura, M. Mikhasenko, and A. Szczepaniak, [JPAC Collaboration], "Amplitude analysis of resonant production in three pions," *EPJ Web Conf.* **130** (2016) 05008, arXiv:1610.04567 [hep-ph].

[65] M. Mikhasenko, A. Jackura, B. Ketzer, and A. Szczepaniak, [COMPASS and JPAC Collaborations], "Unitarity approach to the mass-dependent fit of 3π resonance production data from the COMPASS experiment," *EPJ Web Conf.* **137** (2017) 05017.

[66] A. Jackura *et al.*, [JPAC and COMPASS Collaborations], "New analysis of $\eta\pi$ tensor resonances measured at the COMPASS experiment," *Phys. Lett. B* **779** (2018) 464–472, arXiv:1707.02848 [hep-ph].

[67] K. Pearson, "On the criterion that a given system of deviations from the probable in the case of a correlated system of variables is such that it can be reasonably supposed to have arisen from random sampling," *Philosophical Magazine Series 5* **50** no. 302, (1900) 157–175.

[68] F. James and M. Roos, "Minuit: A System for Function Minimization and Analysis of the Parameter Errors and Correlations," *Comput. Phys. Commun.* **10** (1975) 343–367.

[69] S. Wallner, "Extraction of Resonance Parameters of Light Meson Resonances in the Charged Three-Pion Final State at the COMPASS Experiment (CERN)," Master's thesis, Technische Universität München, 2015. http://wwwcompass.cern.ch/compass/publications/theses/2015_dpl_wallner.pdf.

[70] S. Schmeing, "Resonance Extraction in Diffractive 3π Production using 190 GeV/c π^- at the COMPASS Experiment (CERN)," Master's thesis, Technische Universität München, 2014. http://wwwcompass.cern.ch/compass/publications/theses/2014_dpl_schmeing.pdf.

[71] M. L. Perl, *High Energy Hadron Physics.* Wiley-Interscience Publication. Wiley, 1974.

[72] M. Lu *et al.*, [E852 Collaboration], "Exotic Meson Decay to $\omega\pi^0\pi^-$," *Phys. Rev. Lett.* **94** (2005) 032002, arXiv:hep-ex/0405044 [hep-ex].

[73] A. N. Grigorenko, P. I. Nikitin, and A. V. Kabashin, "Phase jumps and interferometric surface plasmon resonance imaging," *Appl. Phys. Lett.* **75** no. 25, (1999) 3917–3919.

[74] P. Salvini *et al.*, [OBELIX Collaboration], "$\overline{p}p$ annihilation into four charged pions at rest and in flight," *Eur. Phys. J. C* **35** (2004) 21–33.

[75] A. Abele *et al.*, [Crystal Barrel Collaboration], "Study of f_0 decays into four neutral pions," *Eur. Phys. J. C* **19** (2001) 667–675.

[76] A. V. Anisovich, C. A. Baker, C. J. Batty, D. V. Bugg, V. A. Nikonov, *et al.*, "Partial wave analysis of $\overline{p}p$ annihilation channels in flight with $I = 1$, $C = +1$," *Phys. Lett. B* **517** (2001) 261–272, arXiv:1110.0278 [hep-ex].

[77] D. V. Amelin *et al.*, [VES Collaboration], "Investigation of the reaction $\pi^- + A \to \omega\pi^-\pi^0 + A^*$," *Phys. Atom. Nucl.* **62** (1999) 445–453. [Yad. Fiz. **62**, 487 (1999)].

[78] T. Barnes, F. E. Close, P. R. Page, and E. S. Swanson, "Higher quarkonia," *Phys. Rev. D* **55** (1997) 4157–4188, arXiv:hep-ph/9609339 [hep-ph].

[79] K. Abe *et al.*, [Belle Collaboration], "Measurement of K^+K^- production in two photon collisions in the resonant mass region," *Eur. Phys. J. C* **32** (2003) 323–336, arXiv:hep-ex/0309077 [hep-ex].

[80] V. A. Shchegelsky, A. V. Sarantsev, A. V. Anisovich, and M. P. Levchenko, "Partial wave analysis of $\pi^+\pi^-\pi^0$ production in two-photon collisions at LEP," *Eur. Phys. J. A* **27** (2006) 199–205.

[81] A. V. Anisovich, C. A. Baker, C. J. Batty, D. V. Bugg, V. A. Nikonov, *et al.*, "A partial wave analysis of $\overline{p}p \to \eta\eta\pi^0$," *Phys. Lett. B* **517** (2001) 273–281, arXiv:1109.6817 [hep-ex].

[82] G. Cohen-Tannoudji, A. Santoro, and M. Souza, "Duality and mass-slope correlation in diffractive dissociations," *Nucl. Phys.* **B125** (1977) 445–466.

[83] A. C. B. Antunes, A. F. S. Santoro, and M. H. G. Souza, "Systematic of the slope-mass correlations in diffractive dissociation reactions," *Rev. Bras. Fis.* **14** (1984) 397. http://lib-extopc.kek.jp/preprints/PDF/1985/8505/8505308.pdf.

[84] A. V. Anisovich, C. A. Baker, C. J. Batty, D. V. Bugg, V. A. Nikonov, *et al.*, "Study of $\overline{p}p \to \eta\eta\pi^0\pi^0$ in flight," *Phys. Lett. B* **500** (2001) 222–231, arXiv:1109.6433 [hep-ex].

[85] J. Kuhn *et al.*, [E852 Collaboration], "Exotic meson production in the $f_1(1285)\pi^-$ system observed in the reaction $\pi^-p \to \eta\pi^+\pi^-\pi^-p$ at 18 GeV/c," *Phys. Lett. B* **595** (2004) 109–117, arXiv:hep-ex/0401004 [hep-ex].

[86] P. Eugenio *et al.*, [E852 Collaboration], "Observation of the $\pi(1800)$ and $\pi_2(1880)$ mesons in $\eta\eta\pi^-$ decay," *Phys. Lett. B* **660** (2008) 466–470.

[87] C. Adolph *et al.*, [COMPASS Collaboration], "Resonance production and $\pi\pi$ S-wave in $\pi^- + p \to \pi^-\pi^-\pi^+ + p_{\text{recoil}}$ at 190 GeV/c—Supplemental Material," *Phys. Rev. D* **95** (2017) 032004, arXiv:1509.00992 [hep-ex]. http://link.aps.org/supplemental/10.1103/PhysRevD.95.032004.

[88] A. V. Anisovich, C. J. Batty, D. V. Bugg, V. A. Nikonov, and A. V. Sarantsev, "A fresh look at $\eta_2(1645)$, $\eta_2(1870)$, $\eta_2(2030)$ and $f_2(1910)$ in $\overline{p}p \to \eta\pi^0\pi^0\pi^0$," *Eur. Phys. J. C* **71** (2011) 1511, arXiv:1009.1781 [hep-ex].

[89] S. Godfrey and N. Isgur, "Mesons in a Relativized Quark Model with Chromodynamics," *Phys. Rev. D* **32** (1985) 189–231.

[90] D.-M. Li and S. Zhou, "Nature of the $\pi_2(1880)$," *Phys. Rev. D* **79** (2009) 014014, arXiv:0811.0918 [hep-ph].

[91] P. R. Page, E. S. Swanson, and A. P. Szczepaniak, "Hybrid meson decay phenomenology," *Phys. Rev. D* **59** (1999) 034016, arXiv:hep-ph/9808346 [hep-ph].

[92] J. Dudek and A. Szczepaniak, "The Deck effect in $\pi N \to \pi\pi\pi N$," *AIP Conf. Proc.* **814** (2006) 587–591.

[93] S. Eidelman, [Particle Data Group], "The $a_1(1260)$ and $a_1(1640)$," *J. Phys. G* **33** (2006) 575–576. http://pdg.lbl.gov/2006/listings/m010.pdf.

[94] P. Gavillet *et al.*, [Amsterdam-CERN-Nijmegen-Oxford Collaboration], "Backward production of a spin parity 1^+ $\rho\pi$ Enhancement at 1.04 GeV," *Phys. Lett. B* **69** (1977) 119.

[95] D. M. Asner *et al.*, [CLEO Collaboration], "Hadronic structure in the decay $\tau^- \to \nu_\tau \pi^- \pi^0 \pi^0$ and the sign of the tau-neutrino helicity," *Phys. Rev. D* **61** (1999) 012002, arXiv:hep-ex/9902022 [hep-ex].

[96] J. Vijande, A. Valcarce, F. Fernandez, and B. Silvestre-Brac, "Nature of the light scalar mesons," *Phys. Rev. D* **72** (2005) 034025, arXiv:hep-ph/0508142 [hep-ph].

[97] T. Gutsche, M. A. Ivanov, J. G. Körner, V. E. Lyubovitskij, and K. Xu, "Test of the multiquark structure of $a_1(1420)$ in strong two-body decays," *Phys. Rev. D* **96** (2017) 114004, arXiv:1710.02357 [hep-ph].

[98] G. Bellini *et al.*, "2^- resonances in the $\pi^+\pi^-\pi^-$ systems," *Yad. Fiz.* **41** (1985) 1223–1228. [Sov. J. Nucl. Phys. **41** (1985) 781].

[99] C. A. Baker *et al.*, "Evidence for a $J^{PC} = 1^{++}$ $I = 1$ meson at 1640 MeV," *Phys. Lett. B* **449** (1999) 114–121.

[100] C. A. Baker, C. J. Batty, K. Braune, D. V. Bugg, N. Dzhaoshvili, *et al.*, "Confirmation of $a_0(1450)$ and $\pi_1(1600)$ in $\overline{p}p \to \omega\pi^+\pi^-\pi^0$ at rest," *Phys. Lett. B* **563** (2003) 140–149.

[101] A. Zaitsev, [VES Collaboration], "Study of exotic resonances in diffractive reactions," *Nucl. Phys.* **A675** (2000) 155–160.

[102] Y. A. Khokhlov, [VES Collaboration], "Study of $X(1600)$ 1^{-+} hybrid," *Nucl. Phys.* **A663** (2000) 596–599.

[103] M. Nozar *et al.*, [CLAS Collaboration], "Search for the Photoexcitation of Exotic Mesons in the $\pi^+\pi^+\pi^-$ System," *Phys. Rev. Lett.* **102** (2009) 102002, arXiv:0805.4438 [hep-ex].

[104] P. Eugenio and C. Bookwalter, [CLAS Collaboration], "Search for exotic mesons in photoproduction at JLab CLAS," *AIP Conf. Proc.* **1560** (2013) 421–423.

[105] E. I. Ivanov *et al.*, [E852 Collaboration], "Observation of exotic meson production in the reaction $\pi^- p \to \eta'\pi^- p$ at 18 GeV/c," *Phys. Rev. Lett.* **86** (2001) 3977–3980, arXiv:hep-ex/0101058 [hep-ex].

[106] D. V. Amelin, Y. G. Gavrilov, Y. P. Gouz, V. A. Dorofeev, R. I. Dzhelyadin, *et al.*, [VES Collaboration], "Investigation of hybrid states in the VES experiment at the Institute for High Energy Physics (Protvino)," *Phys. Atom. Nucl.* **68** (2005) 359–371.

[107] G. S. Adams *et al.*, [CLEO Collaboration], "Amplitude analyses of the decays $\chi_{c1} \to \eta\pi^+\pi^-$ and $\chi_{c1} \to \eta'\pi^+\pi^-$," *Phys. Rev. D* **84** (2011) 112009, arXiv:1109.5843 [hep-ex].

[108] D. Alde *et al.*, "Evidence for a 1^{-+} Exotic Meson," *Phys. Lett. B* **205** (1988) 397.

[109] H. Aoyagi *et al.*, "Study of the $\eta\pi^-$ system in the $\pi^- p$ reaction at 6.3 GeV/c," *Phys. Lett. B* **314** (1993) 246–254.

[110] D. R. Thompson *et al.*, [E852 Collaboration], "Evidence for Exotic Meson Production in the Reaction $\pi^- p \to \eta\pi^- p$ at 18 GeV/c," *Phys. Rev. Lett.* **79** (1997) 1630–1633, arXiv:hep-ex/9705011 [hep-ex].

[111] G. S. Adams *et al.*, [E862 Collaboration], "Confirmation of the 1^{-+} meson exotics in the $\eta\pi^0$ system," *Phys. Lett. B* **657** (2007) 27–31, arXiv:hep-ex/0612062 [hep-ex].

[112] V. Dorofeev *et al.*, [VES Collaboration], "The $J^{PC} = 1^{-+}$ hunting season at VES," *AIP Conf. Proc.* **619** (2002) 143–154, arXiv:hep-ex/0110075 [hep-ex].

[113] A. Abele *et al.*, [Crystal Barrel Collaboration], "Exotic $\eta\pi$ state in $\overline{p}d$ annihilation at rest into $\pi^-\pi^0\eta p_{\mathrm{spectator}}$," *Phys. Lett. B* **423** (1998) 175–184.

[114] A. Abele *et al.*, [Crystal Barrel Collaboration], "Evidence for a $\pi\eta$-P-wave in $\overline{p}p$-annihilations at rest into $\pi^0\pi^0\eta$," *Phys. Lett. B* **446** (1999) 349–355.

[115] B. Hyams, C. Jones, P. Weilhammer, W. Blum, H. Dietl, *et al.*, "$\pi\pi$ Phase Shift Analysis from 600 to 1900 MeV," *Nucl. Phys.* **B64** (1973) 134–162.

[116] P. C. Mahalanobis, "On the generalised distance in statistics," *Proc. Natl. Inst. Sci., India* **2** no. 1, (1936) 49–55. http://insa.nic.in/writereaddata/UpLoadedFiles/PINSA/Vol02_1936_1_Art05.pdf.

Supplemental Material

In this supplemental material, we provide additional information necessary to repeat the analysis. In Sec. E, we present the full data set together with the result of the resonance-model fit. In Sec. F, we provide the decay phase-space integrals I_{aa} that enter Eqs. (19) and (20). The data required to perform the resonance-model fit are also provided in computer-readable format at [35].

E Spin-density matrices in t' bins

In this section, we present the used data from the partial-wave analysis presented in Ref. [30] together with the result of the resonance-model fit. The measured spin-density matrix elements of the 14 selected waves and the fit model are presented in terms of the partial-wave intensities and the relative phases between the partial waves, which are visualized in the form of a 14×14 upper-triangular matrix of graphs. The $m_{3\pi}$ dependence of the intensities is shown as diagonal elements. The $m_{3\pi}$ dependence of the relative phases is shown in the off-diagonal elements. A relative phase $\Delta\phi_{ab}$ between two waves is defined as the phase difference of partial wave a in the row and partial wave b in the column of the matrix: $\Delta\phi_{ab} \equiv \phi_a - \phi_b$. In order to be able to show all phases with a common axis, we plot instead $\Delta\phi_{ab} - \delta\phi_{ab}$. The phase offset $\delta\phi_{ab}$ is calculated as the arithmetic average of the minimum and maximum value of $\Delta\phi_{ab}$ in the respective fit range. For each phase motion, the value of $\delta\phi_{ab}$ is given in the corresponding graph in the matrix.

In each graph of the matrix, the data from the partial-wave analysis are shown by black crosses with horizontal lines that indicate the $m_{3\pi}$ bin width and vertical lines that indicate the statistical uncertainties. The data are overlaid by the red model curve. In each intensity distribution, also the resonances (blue curves) and the nonresonant component (green curve) are shown. All wave components interfere among each other so that in general the intensities of the wave components do not add up to the model curve. In each graph of the matrix, points outside the fit range are shown in gray. The extrapolations of the model curve and of the curves of the wave components outside the fit range are shown in lighter colors.

Due to the large size of the matrix, it is broken down into 10 submatrices labeled A through J. This is illustrated in Table 8. Each of the following Secs. E 1 to E 10 shows the corresponding submatrix in the 11 bins of the analyzed t' range from 0.1 to 1.0 $(\mathrm{GeV}/c)^2$.

Table 8: Subdivision scheme for the 14×14 matrix of graphs that represents the spin-density matrix. The $m_{3\pi}$ dependence of the partial-wave intensities are shown as diagonal elements, the $m_{3\pi}$ dependence of the relative phases as off-diagonal elements. The matrix is subdivided into 10 submatrices labeled A through J. Each submatrix is shown in all 11 t' bins in the corresponding Secs. E 1 to E 10.

$0^{-+}0^+f_0(980)\pi S$	$1^{++}0^+\rho(770)\pi S$	$1^{++}0^+f_0(980)\pi P$	$1^{++}0^+f_2(1270)\pi P$	$1^{-+}1^+\rho(770)\pi P$	$2^{++}1^+\rho(770)\pi D$	$2^{++}2^+\rho(770)\pi D$	$2^{++}1^+f_2(1270)\pi P$	$2^{-+}0^+\rho(770)\pi F$	$2^{-+}0^+f_2(1270)\pi S$	$2^{-+}1^+f_2(1270)\pi S$	$2^{-+}0^+f_2(1270)\pi D$	$4^{++}1^+\rho(770)\pi G$	$4^{++}1^+f_2(1270)\pi F$	
A	A	A	A	B	B	B	B	C	C	C	C	D	D	$0^{-+}0^+f_0(980)\pi S$
	A	A	A	B	B	B	B	C	C	C	C	D	D	$1^{++}0^+\rho(770)\pi S$
		A	A	B	B	B	B	C	C	C	C	D	D	$1^{++}0^+f_0(980)\pi P$
			A	B	B	B	B	C	C	C	C	D	D	$1^{++}0^+f_2(1270)\pi P$
				E	E	E	E	F	F	F	F	G	G	$1^{-+}1^+\rho(770)\pi P$
					E	E	E	F	F	F	F	G	G	$2^{++}1^+\rho(770)\pi D$
						E	E	F	F	F	F	G	G	$2^{++}2^+\rho(770)\pi D$
							E	F	F	F	F	G	G	$2^{++}1^+f_2(1270)\pi P$
								H	H	H	H	I	I	$2^{-+}0^+\rho(770)\pi F$
									H	H	H	I	I	$2^{-+}0^+f_2(1270)\pi S$
										H	H	I	I	$2^{-+}1^+f_2(1270)\pi S$
											H	I	I	$2^{-+}0^+f_2(1270)\pi D$
												J	J	$4^{++}1^+\rho(770)\pi G$
													J	$4^{++}1^+f_2(1270)\pi F$

1 Submatrix A

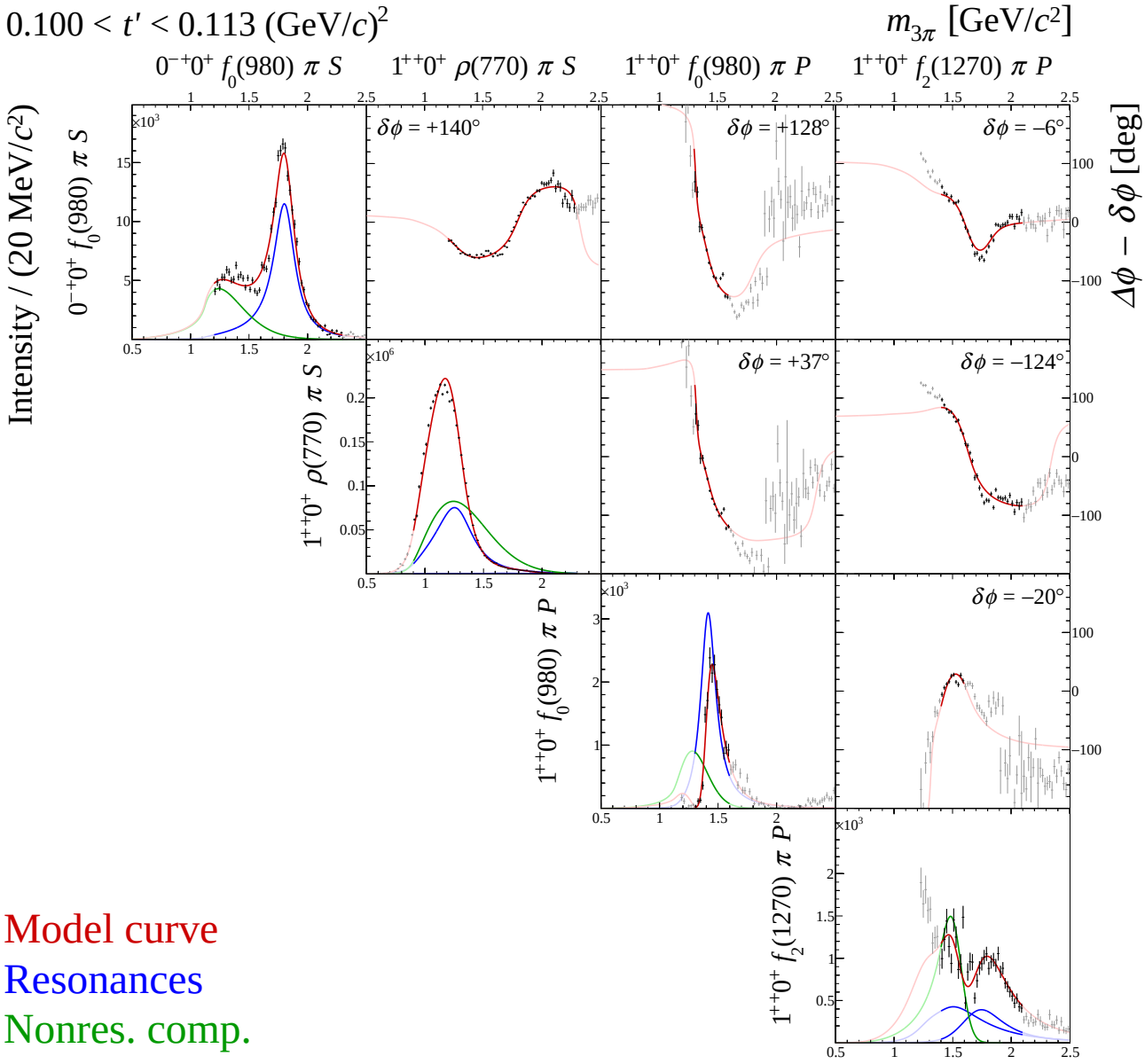

FIG. 57: Submatrix A of the 14 × 14 matrix of graphs that represents the spin-density matrix (see Table 8).

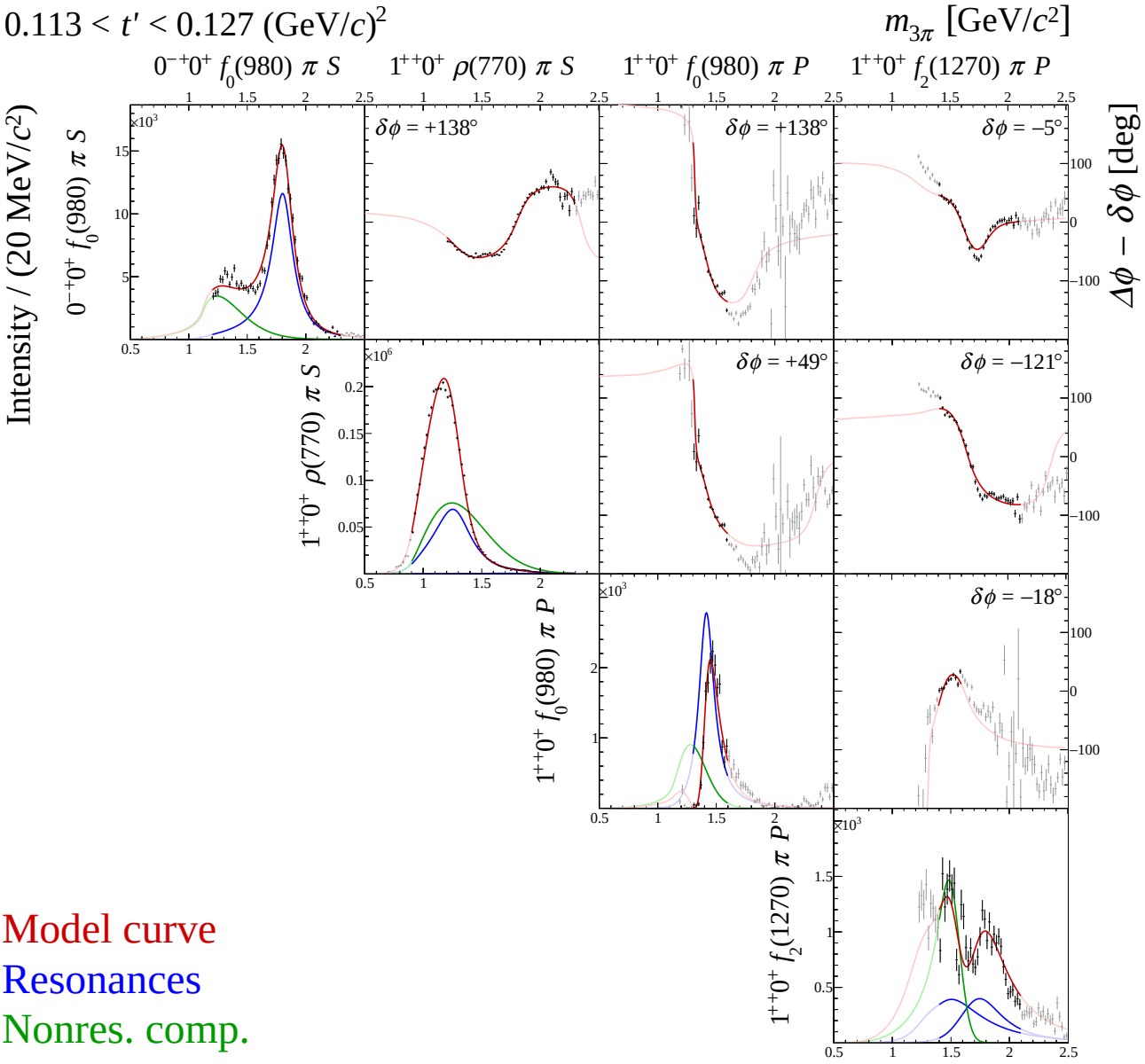

FIG. 58: Submatrix A of the 14 × 14 matrix of graphs that represents the spin-density matrix (see Table 8).

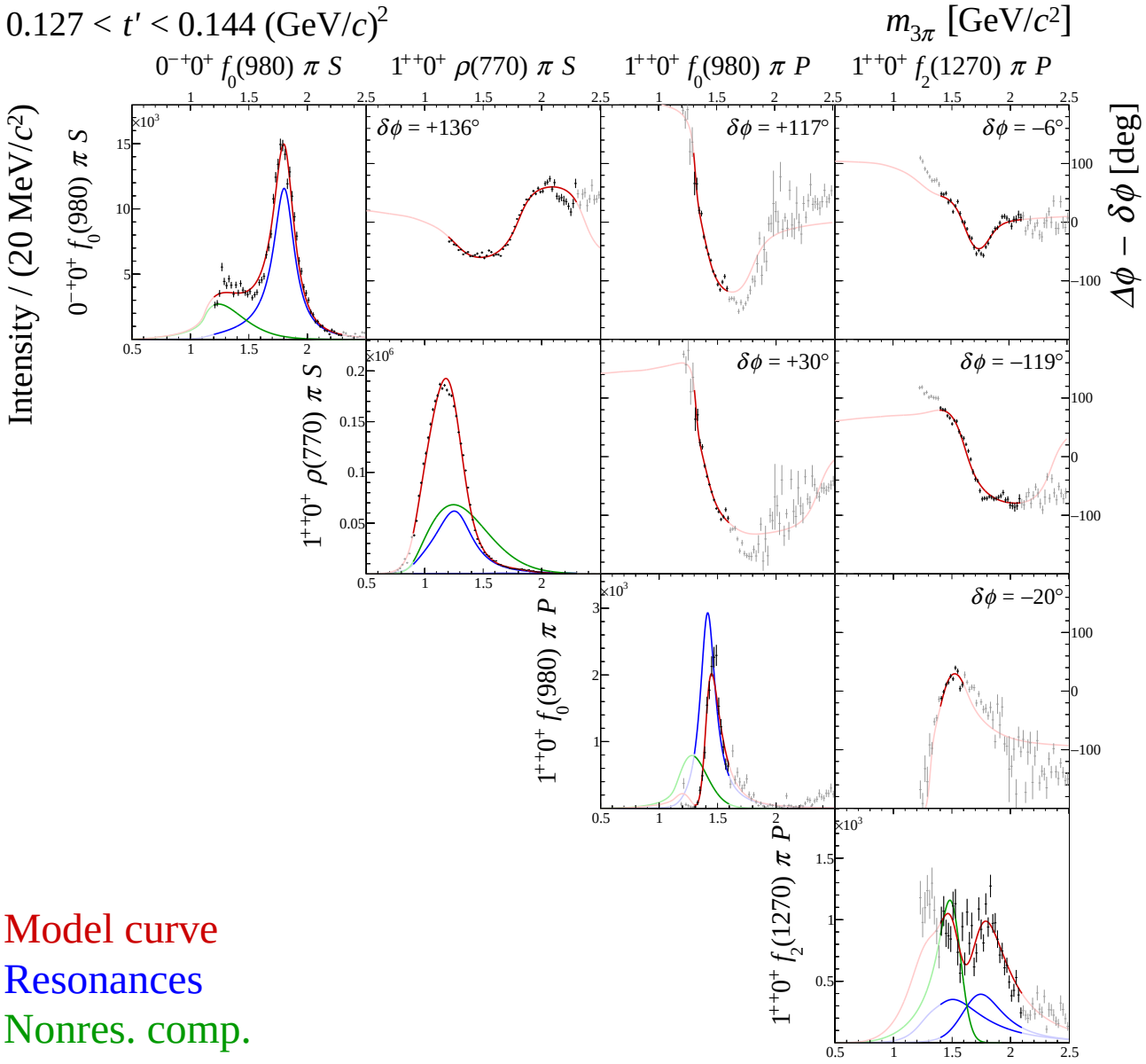

FIG. 59: Submatrix A of the 14 × 14 matrix of graphs that represents the spin-density matrix (see Table 8).

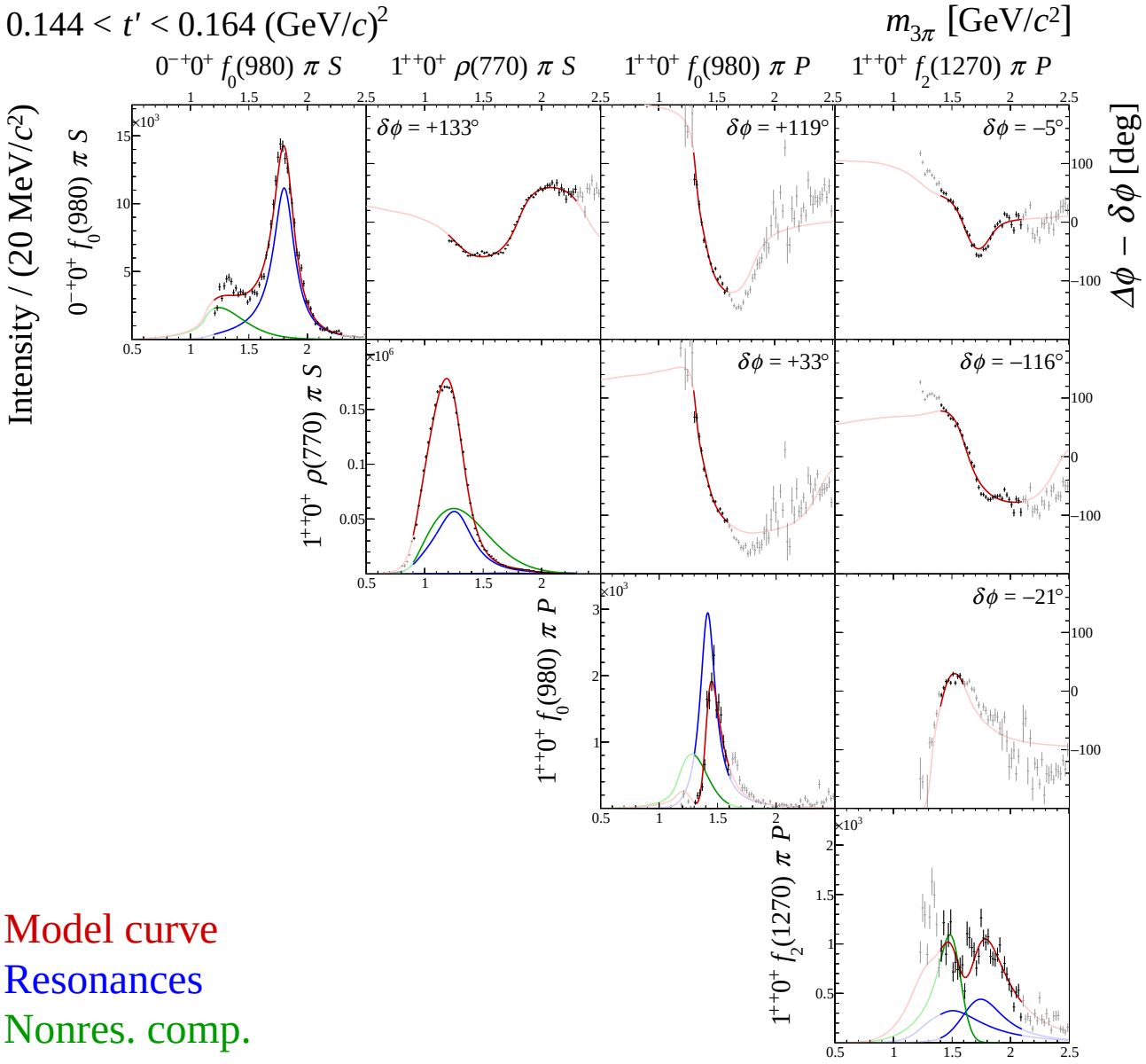

FIG. 60: Submatrix A of the 14 × 14 matrix of graphs that represents the spin-density matrix (see Table 8).

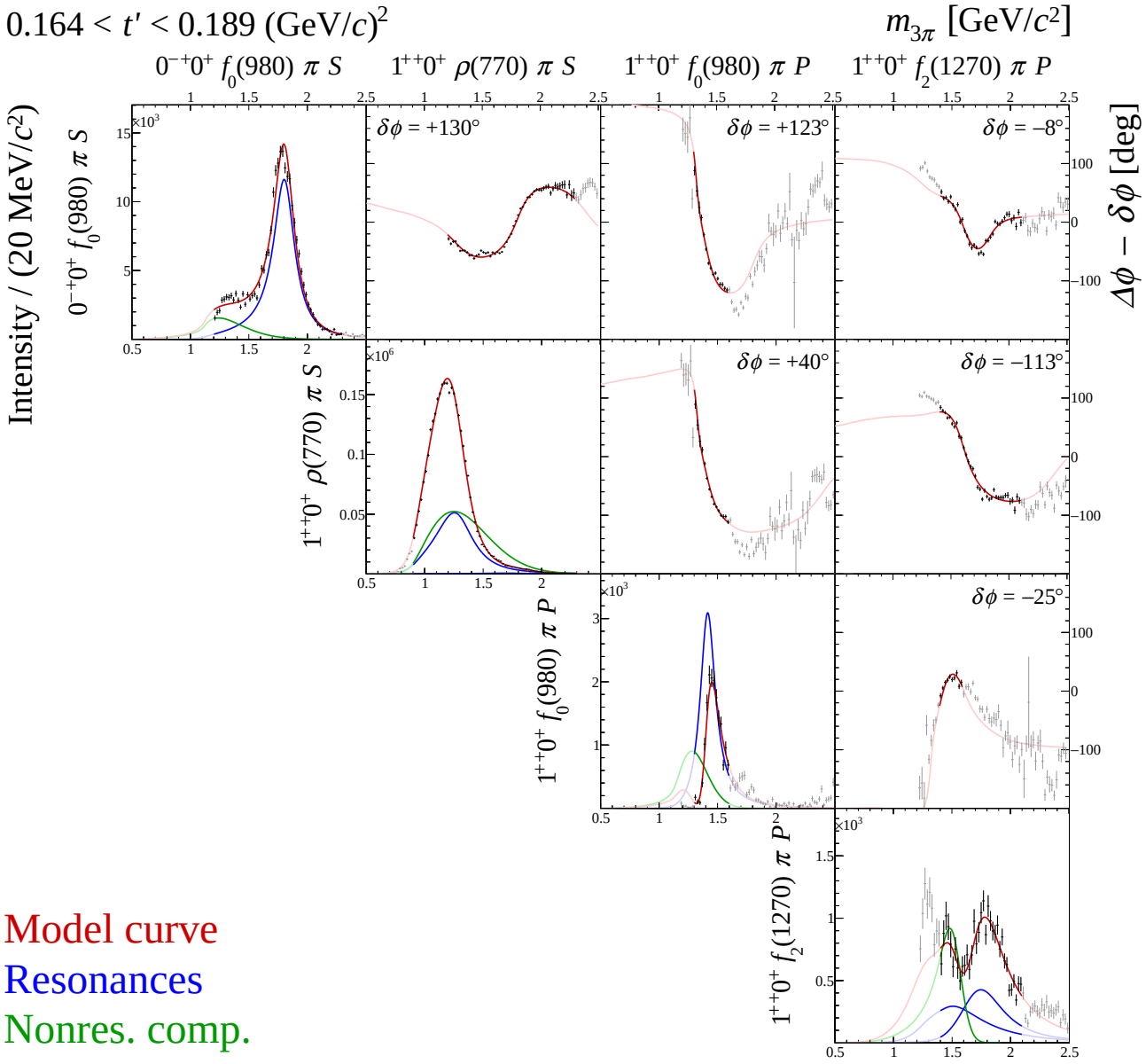

FIG. 61: Submatrix A of the 14 × 14 matrix of graphs that represents the spin-density matrix (see Table 8).

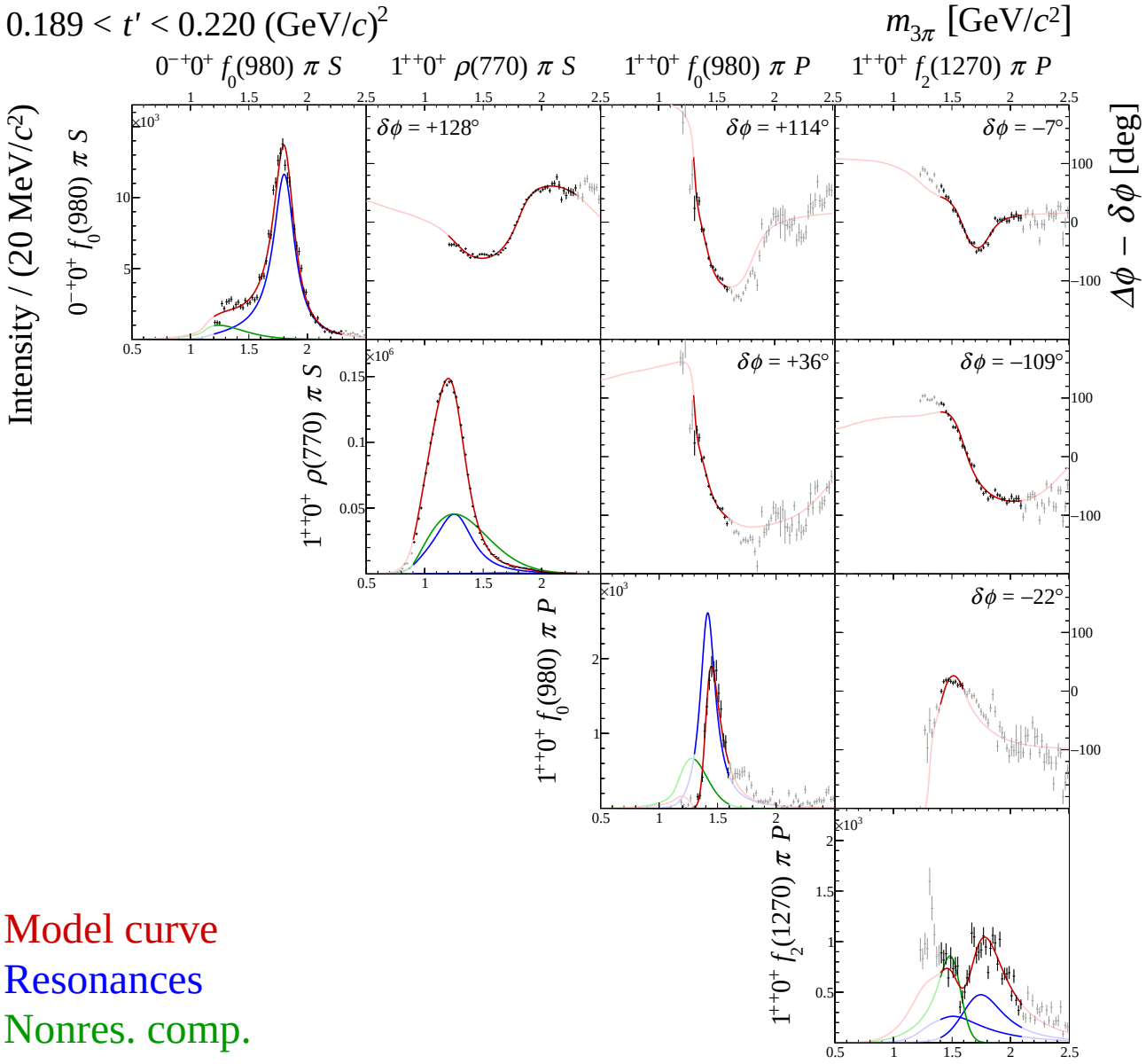

FIG. 62: Submatrix A of the 14 × 14 matrix of graphs that represents the spin-density matrix (see Table 8).

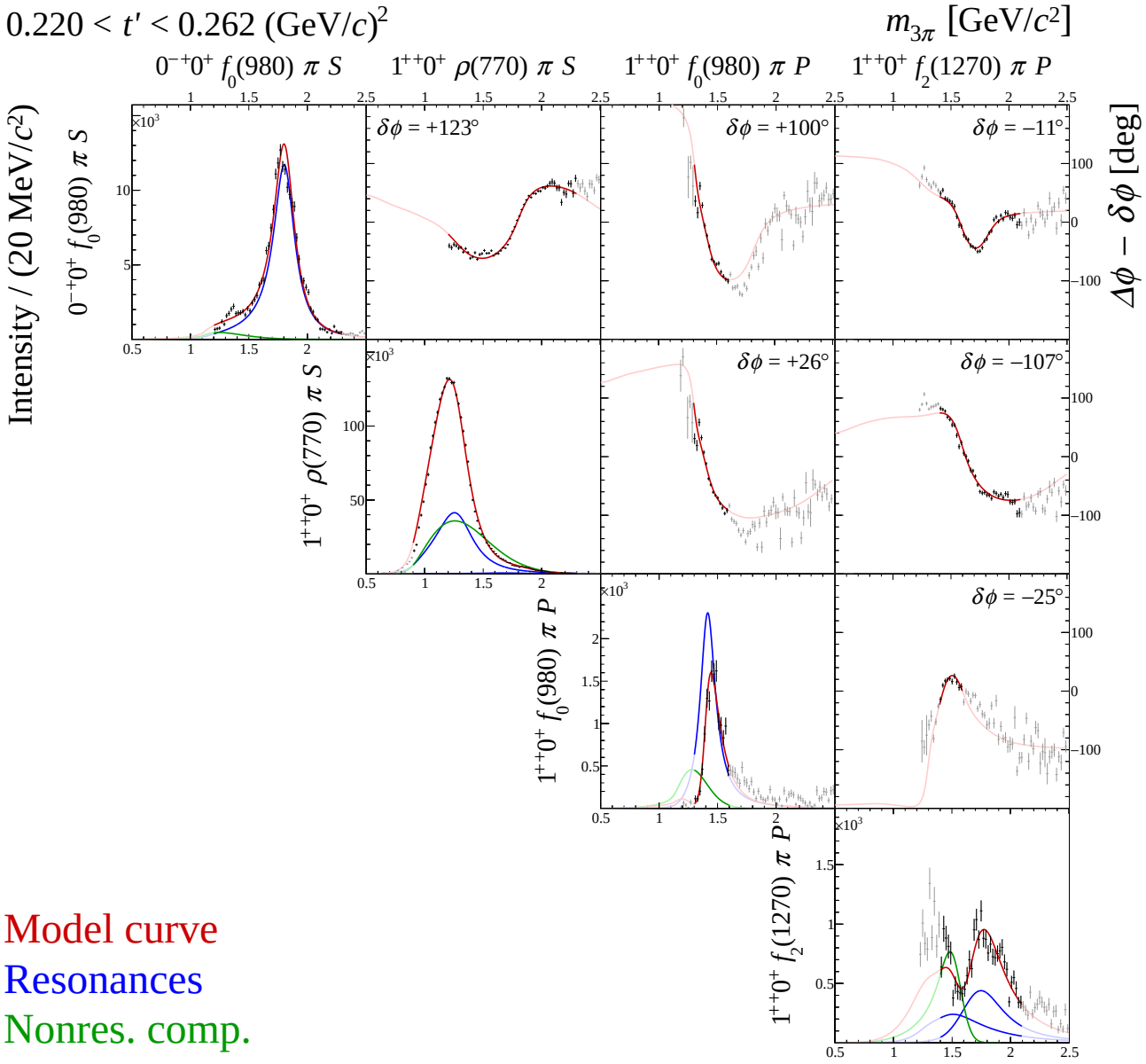

FIG. 63: Submatrix A of the 14 × 14 matrix of graphs that represents the spin-density matrix (see Table 8).

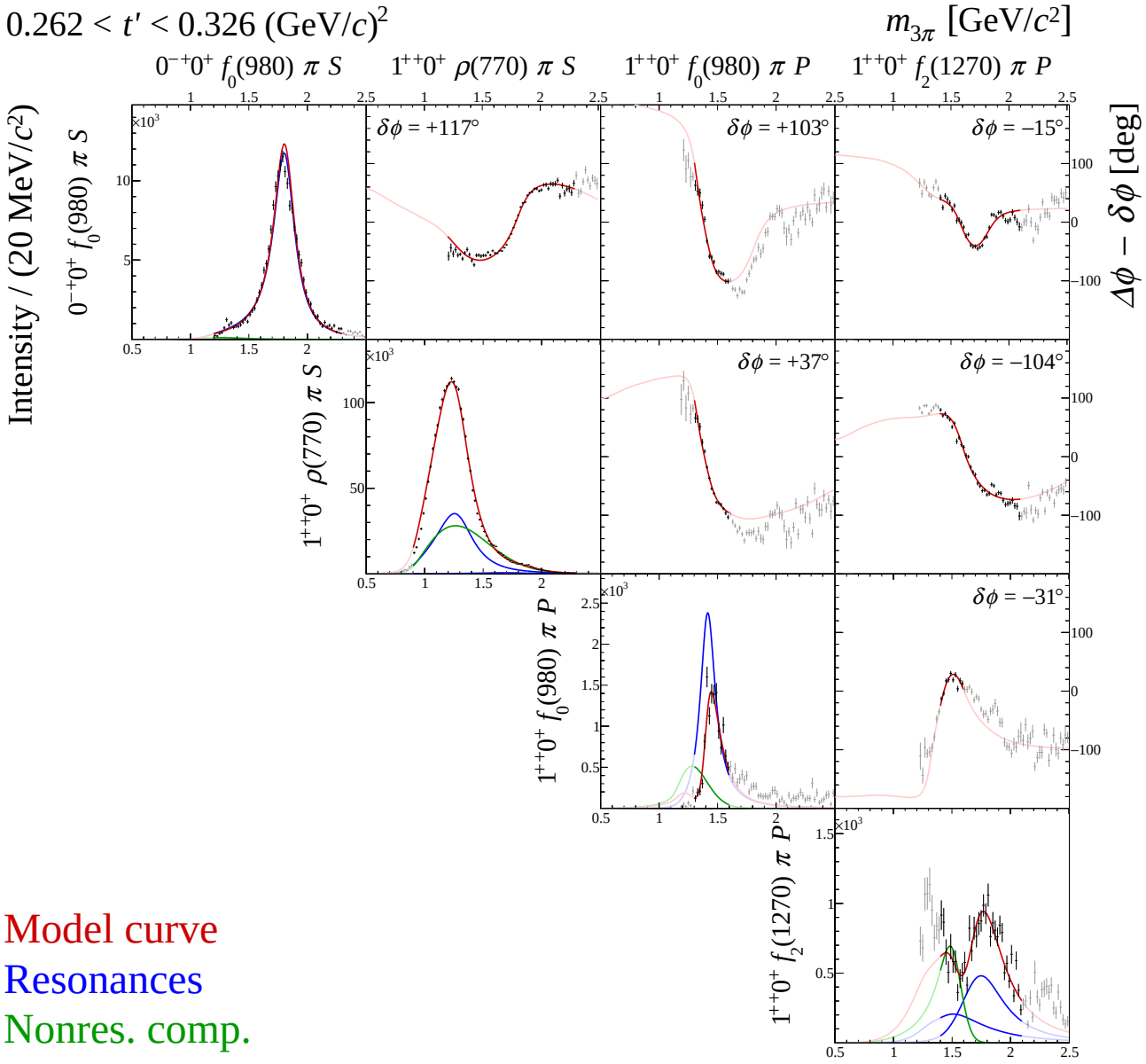

FIG. 64: Submatrix A of the 14 × 14 matrix of graphs that represents the spin-density matrix (see Table 8).

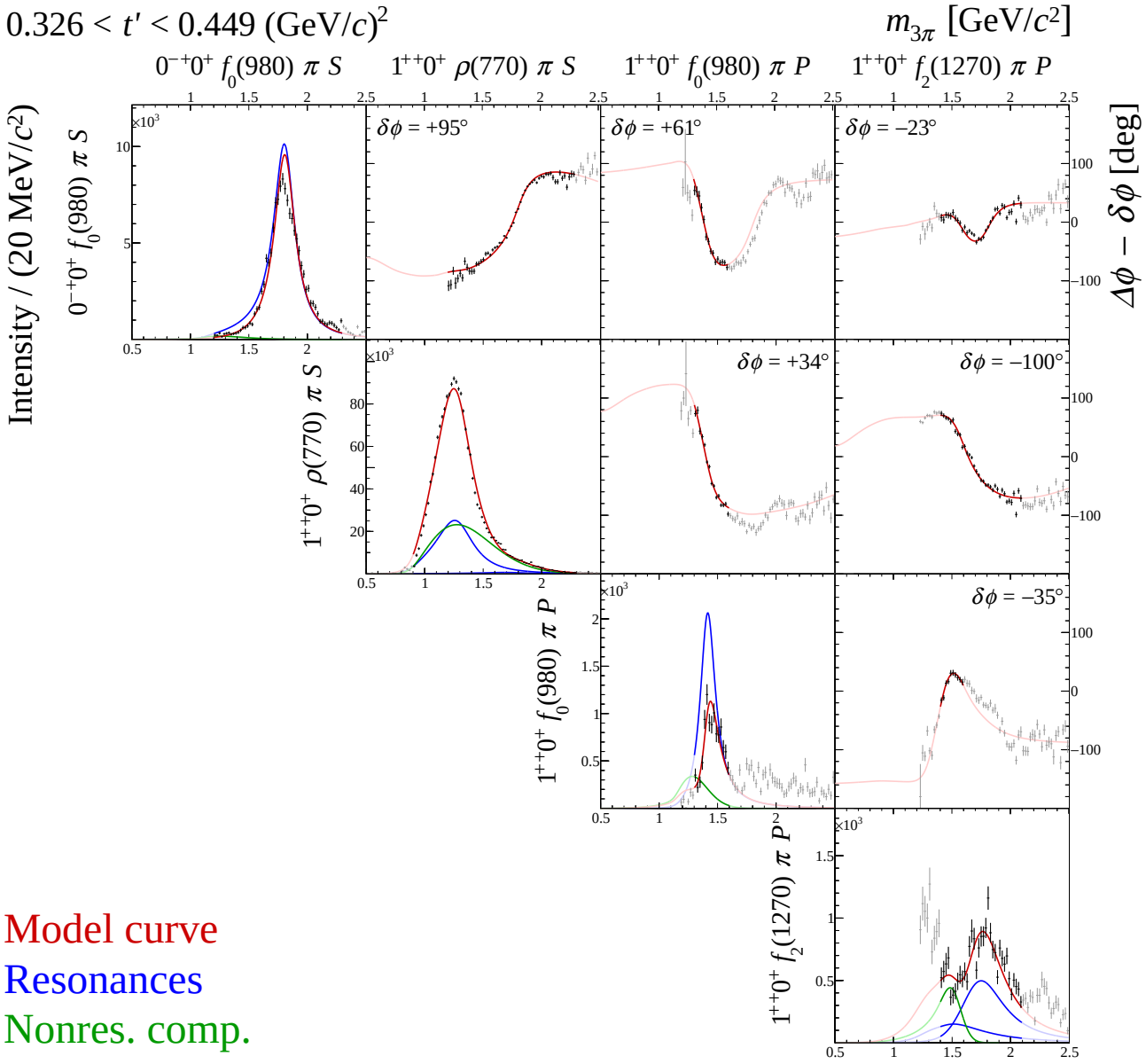

FIG. 65: Submatrix A of the 14 × 14 matrix of graphs that represents the spin-density matrix (see Table 8).

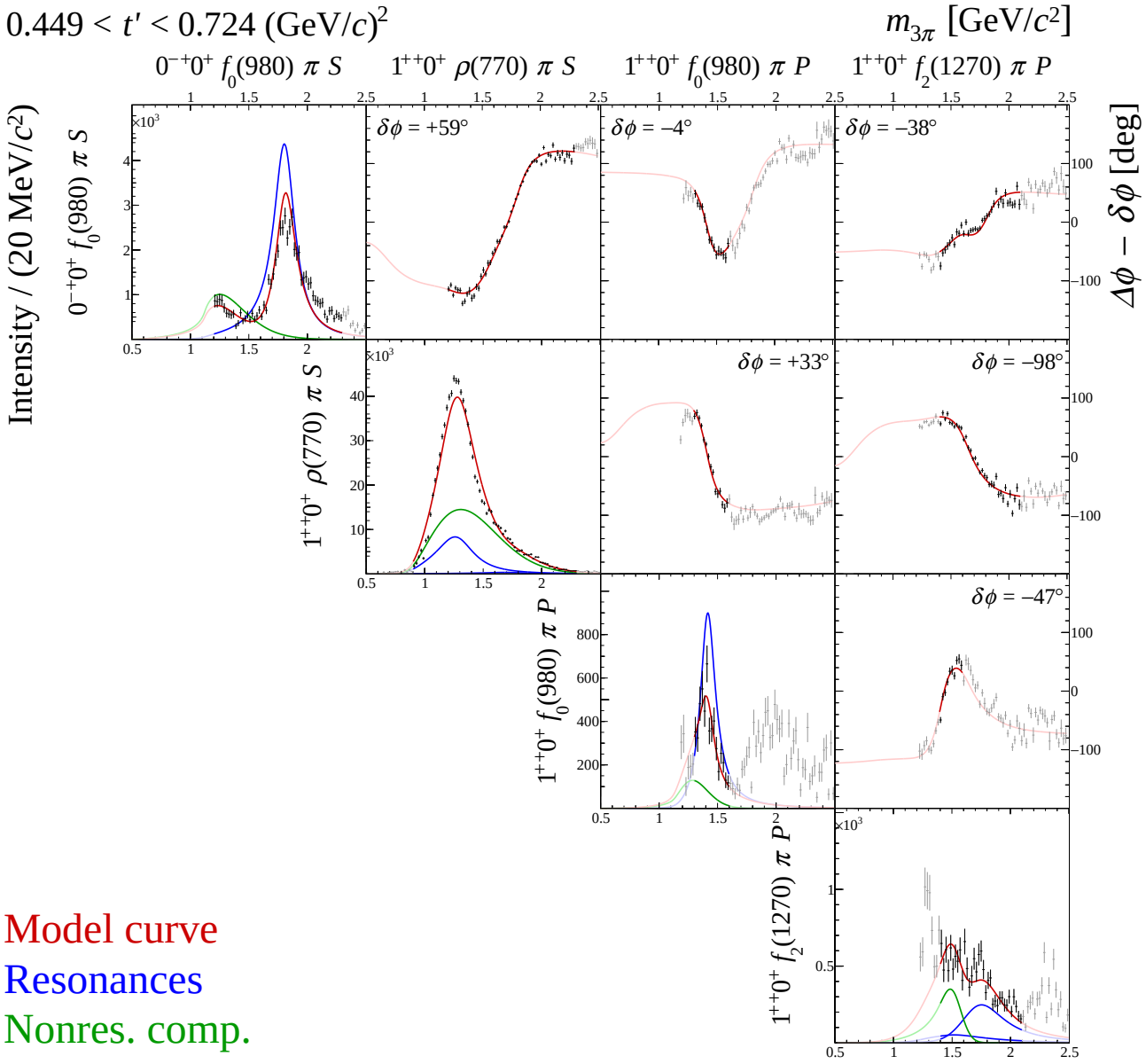

FIG. 66: Submatrix A of the 14 × 14 matrix of graphs that represents the spin-density matrix (see Table 8).

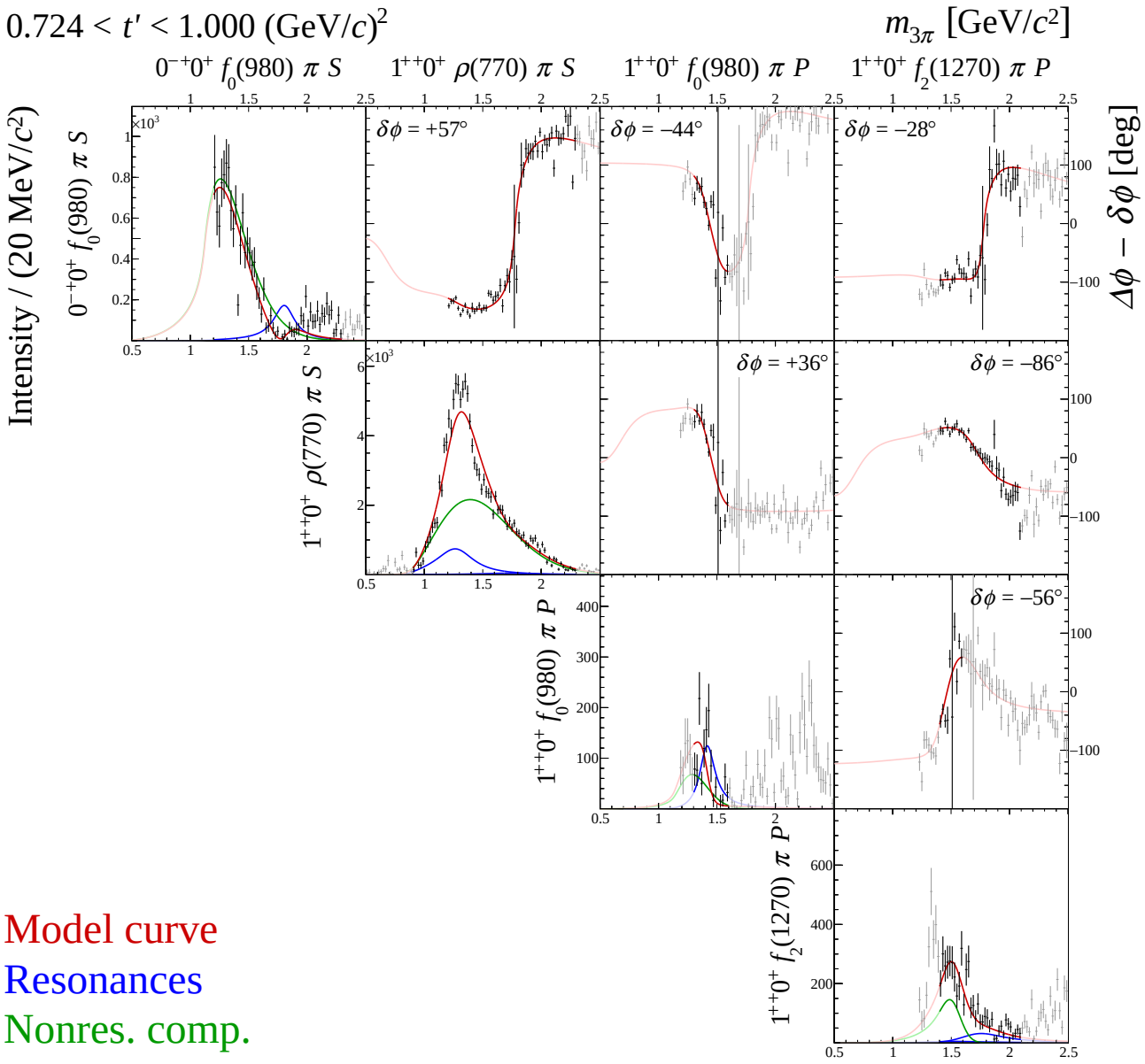

FIG. 67: Submatrix A of the 14 × 14 matrix of graphs that represents the spin-density matrix (see Table 8).

2 Submatrix B

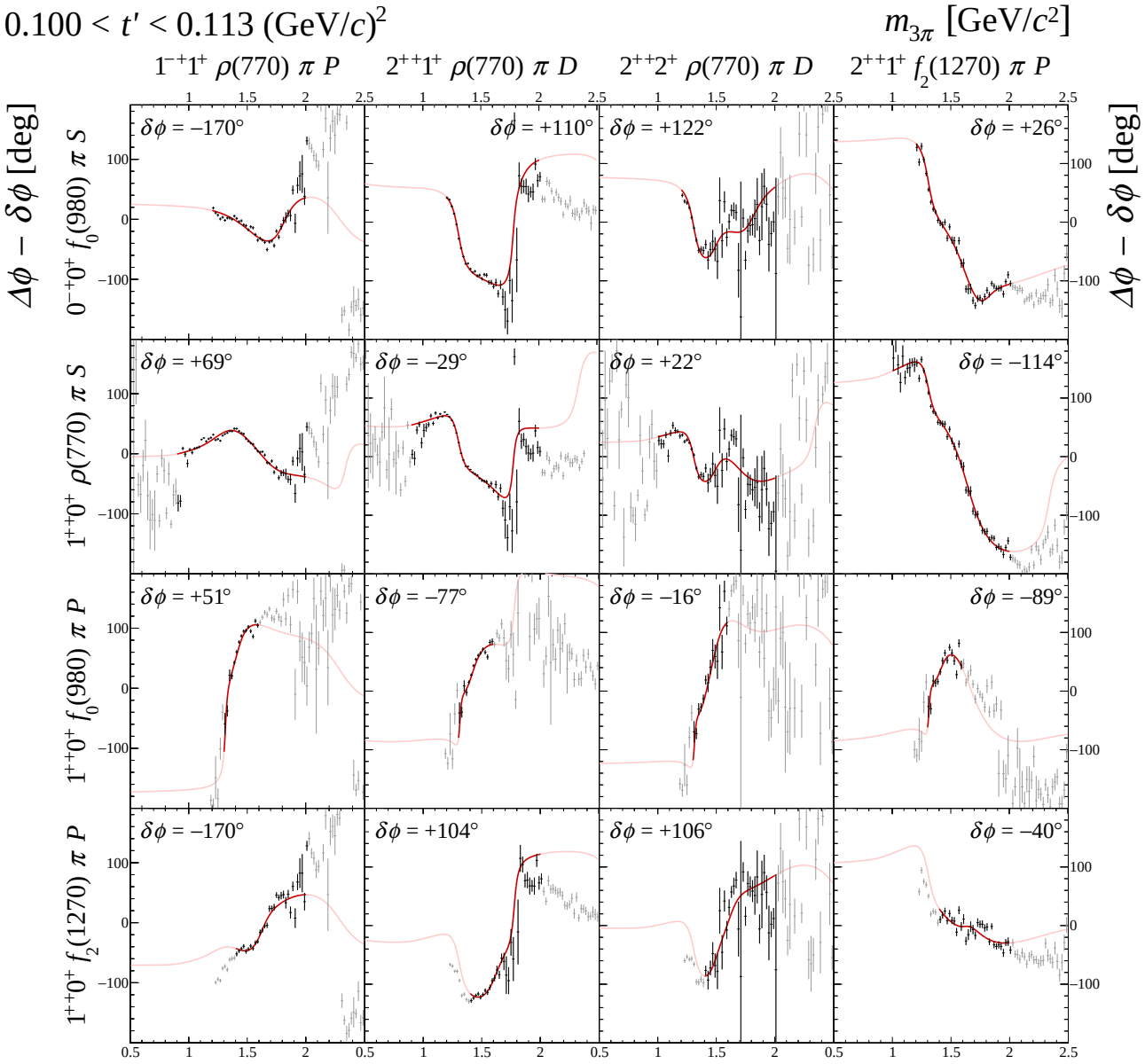

FIG. 68: Submatrix B of the 14 × 14 matrix of graphs that represents the spin-density matrix (see Table 8).

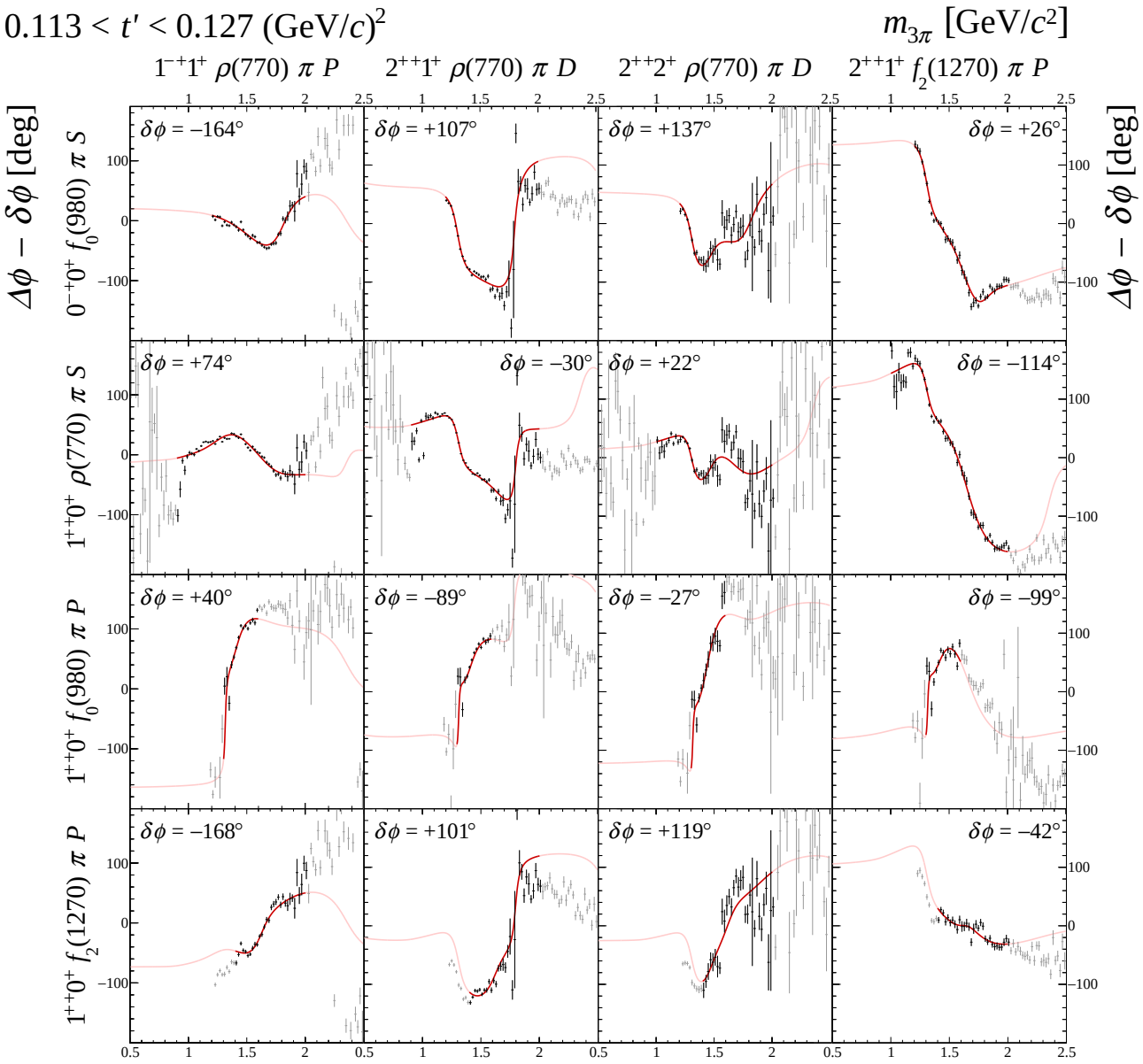

FIG. 69: Submatrix B of the 14 × 14 matrix of graphs that represents the spin-density matrix (see Table 8).

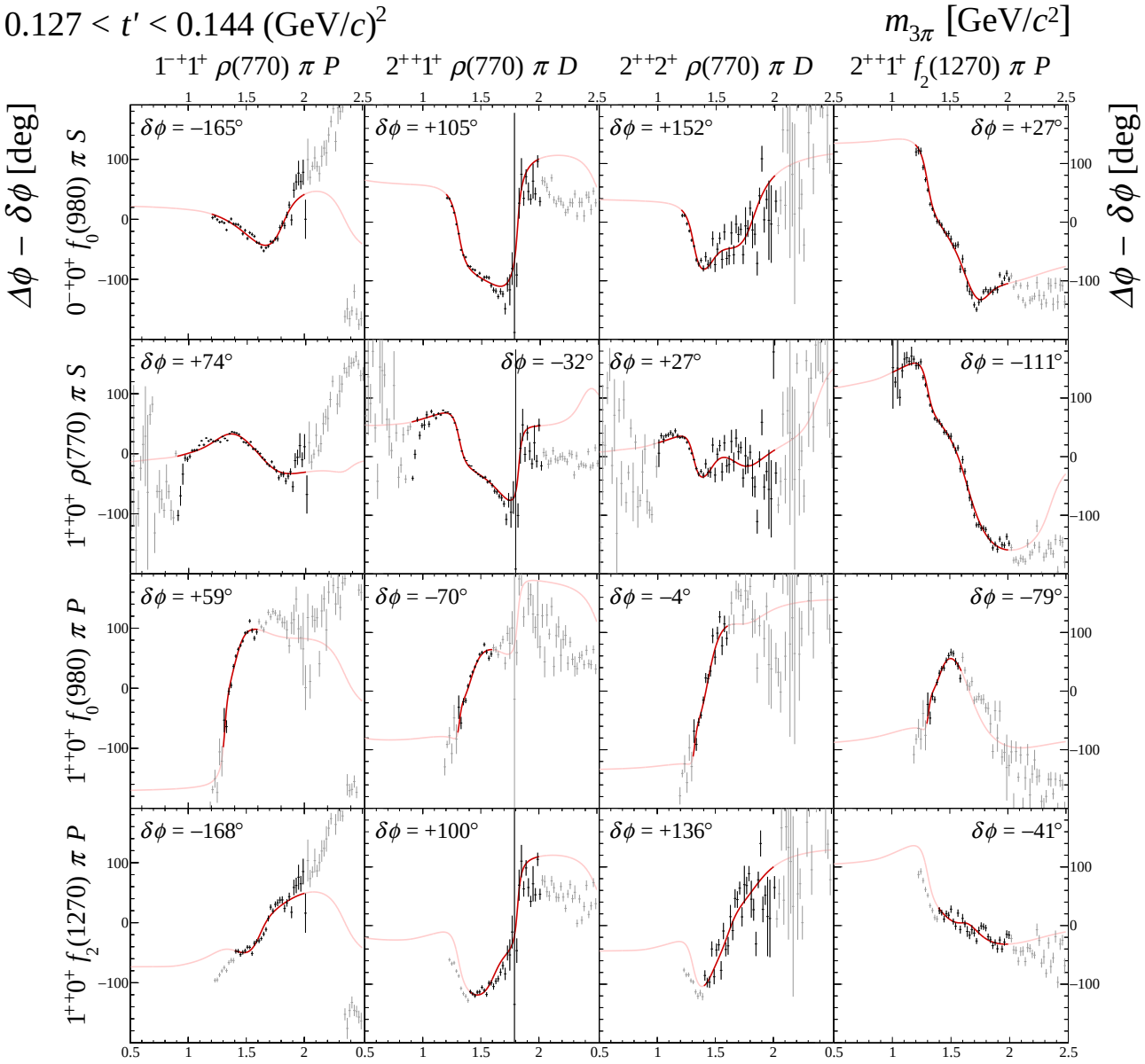

FIG. 70: Submatrix B of the 14 × 14 matrix of graphs that represents the spin-density matrix (see Table 8).

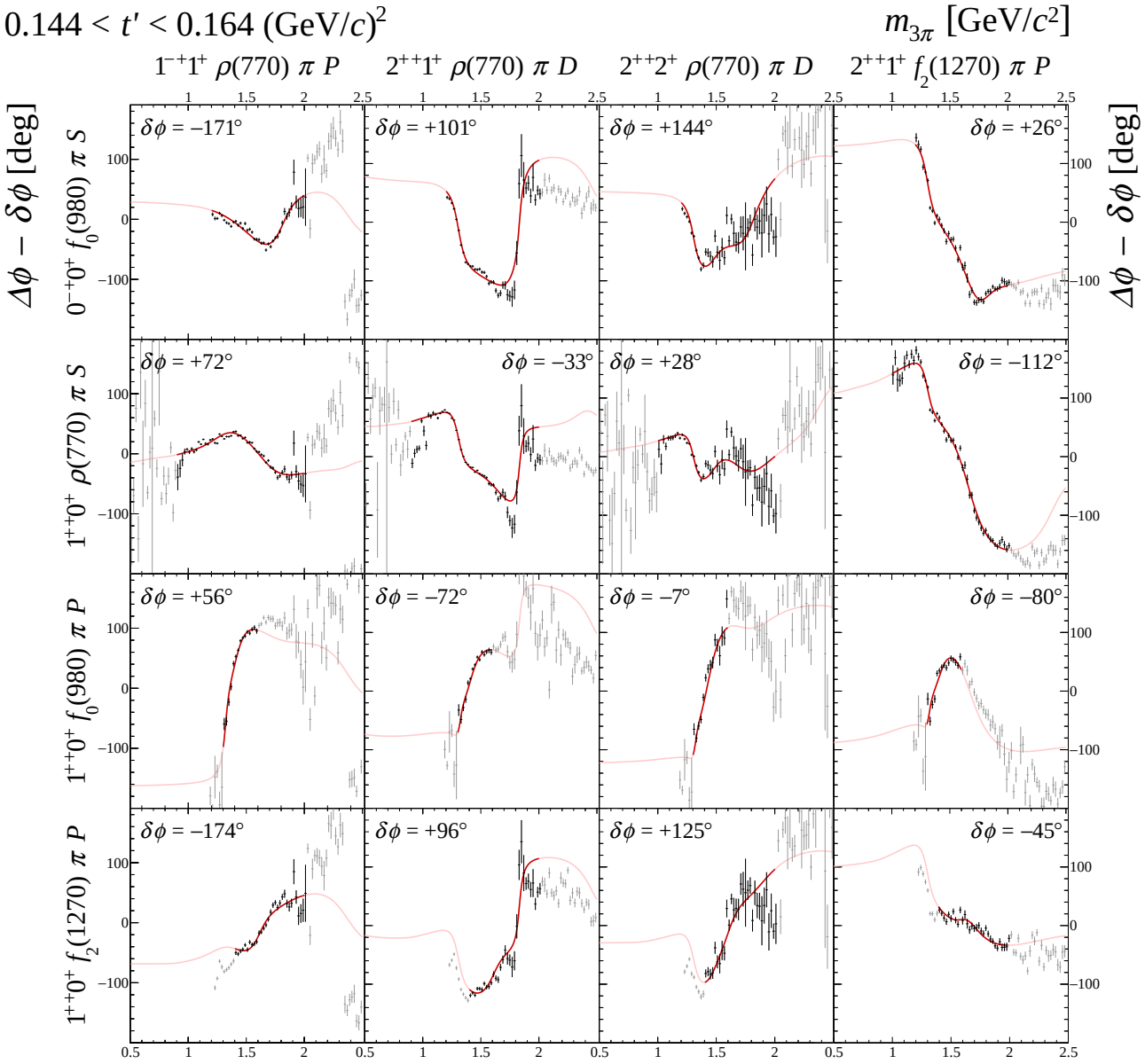

FIG. 71: Submatrix B of the 14 × 14 matrix of graphs that represents the spin-density matrix (see Table 8).

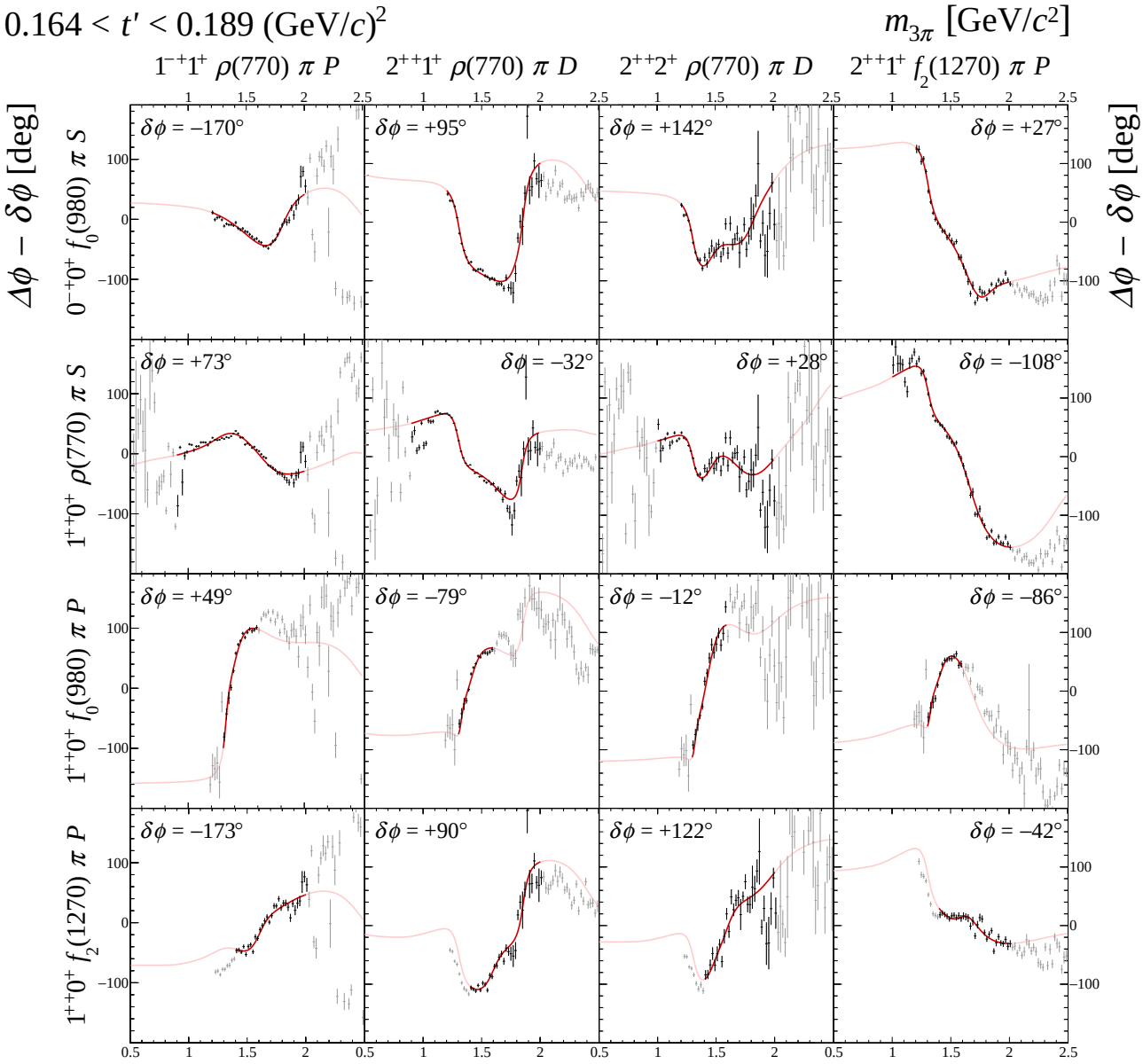

FIG. 72: Submatrix B of the 14 × 14 matrix of graphs that represents the spin-density matrix (see Table 8).

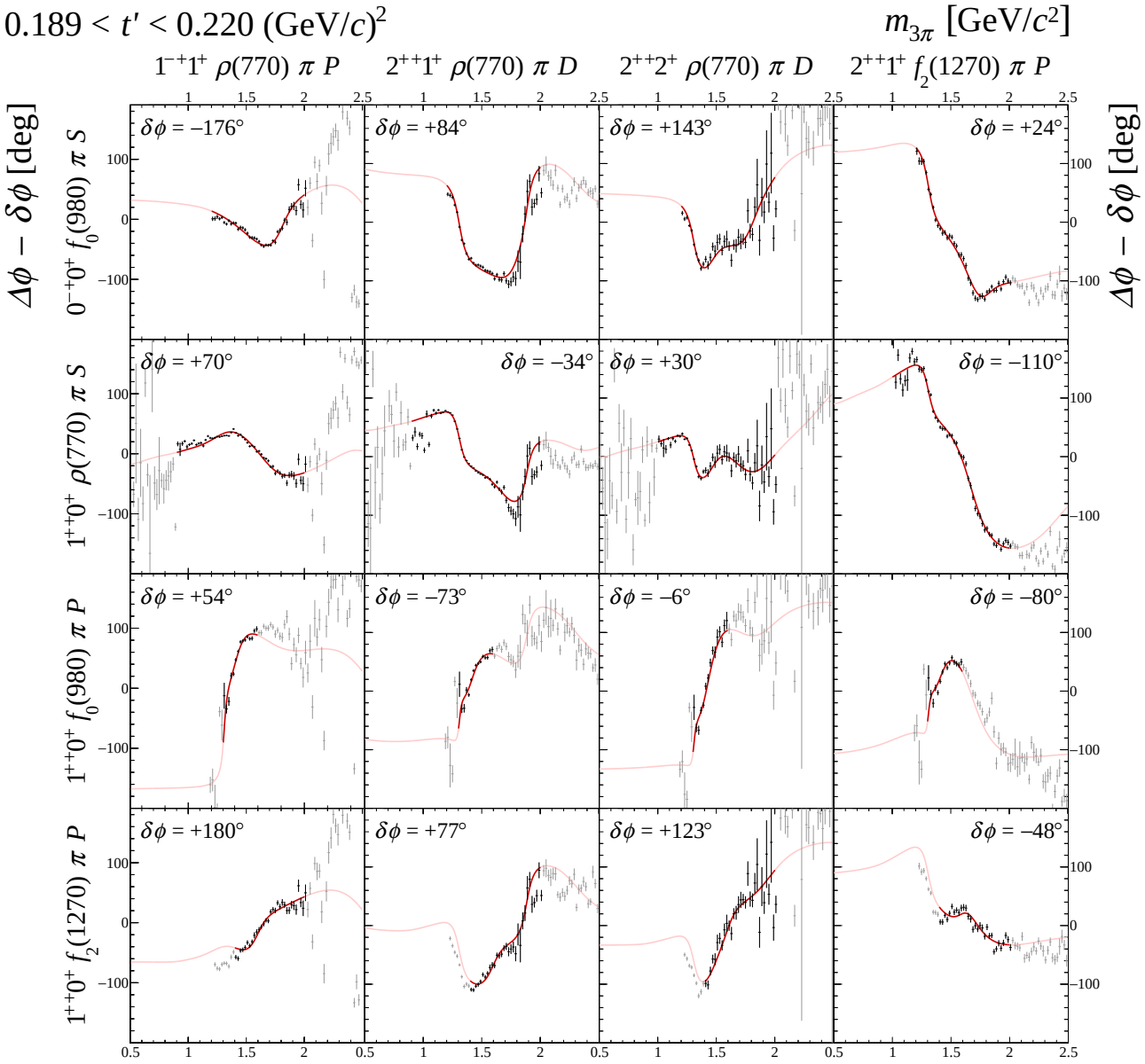

FIG. 73: Submatrix B of the 14 × 14 matrix of graphs that represents the spin-density matrix (see Table 8).

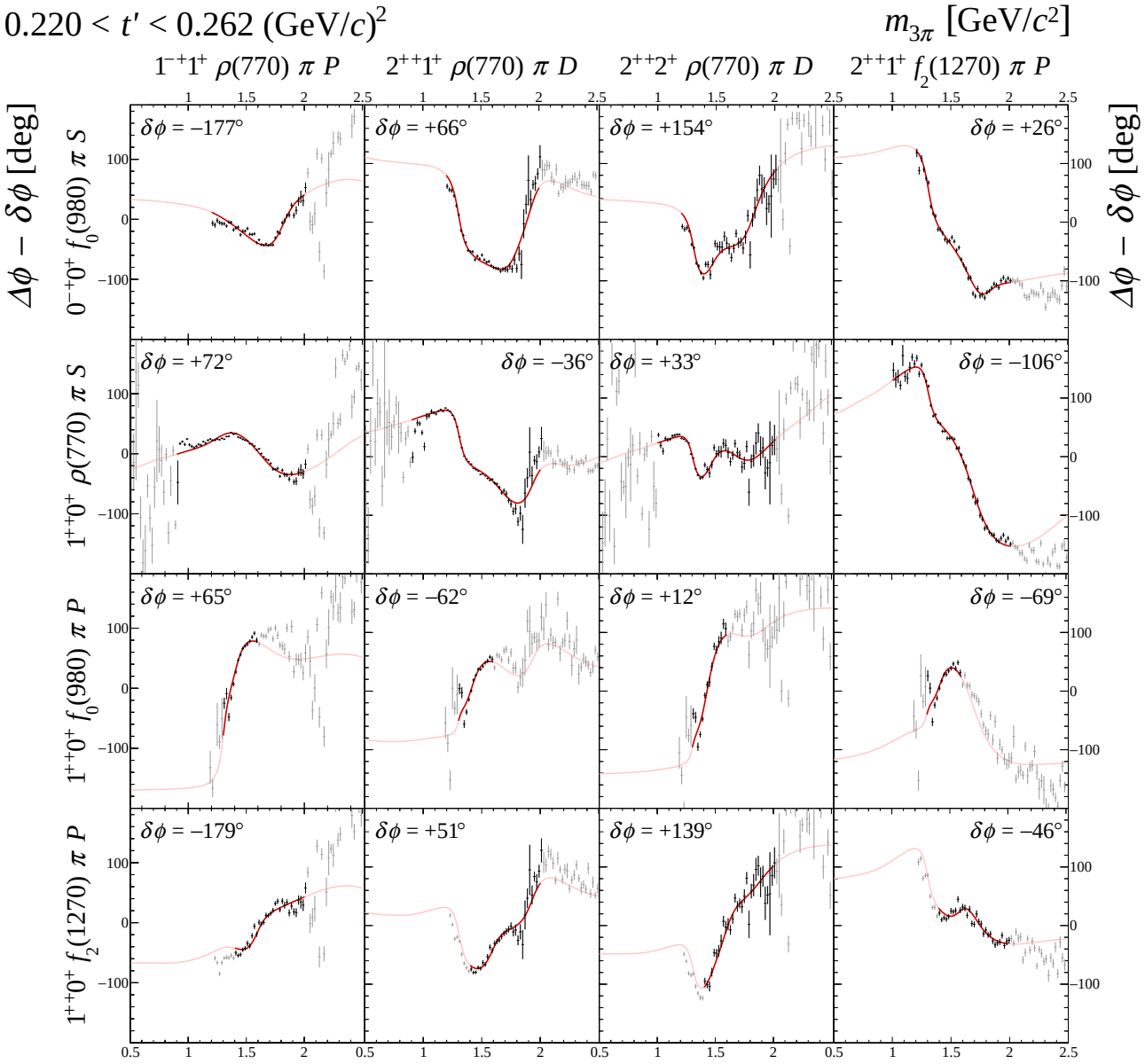

FIG. 74: Submatrix B of the 14 × 14 matrix of graphs that represents the spin-density matrix (see Table 8).

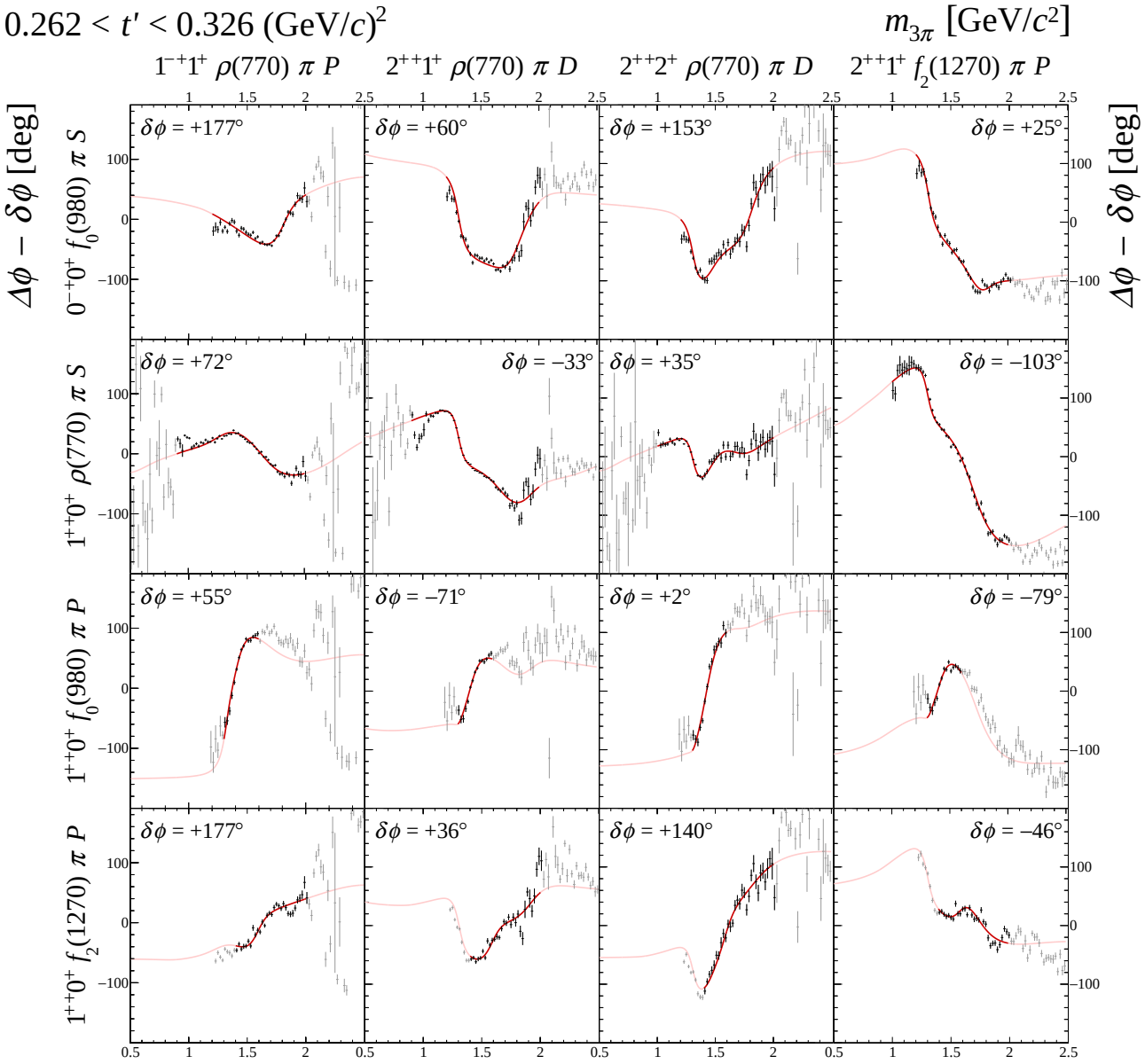

FIG. 75: Submatrix B of the 14 × 14 matrix of graphs that represents the spin-density matrix (see Table 8).

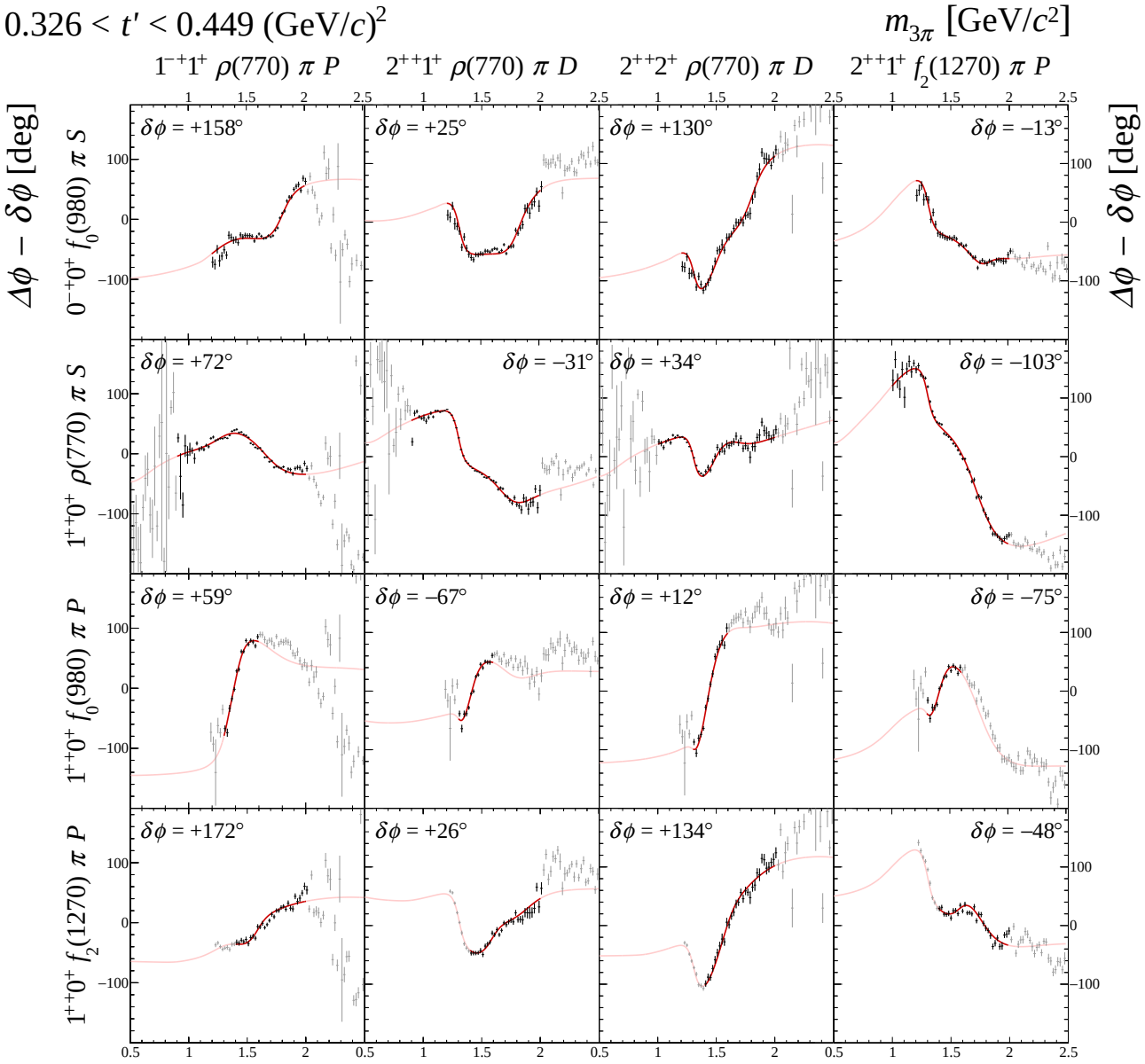

FIG. 76: Submatrix B of the 14 × 14 matrix of graphs that represents the spin-density matrix (see Table 8).

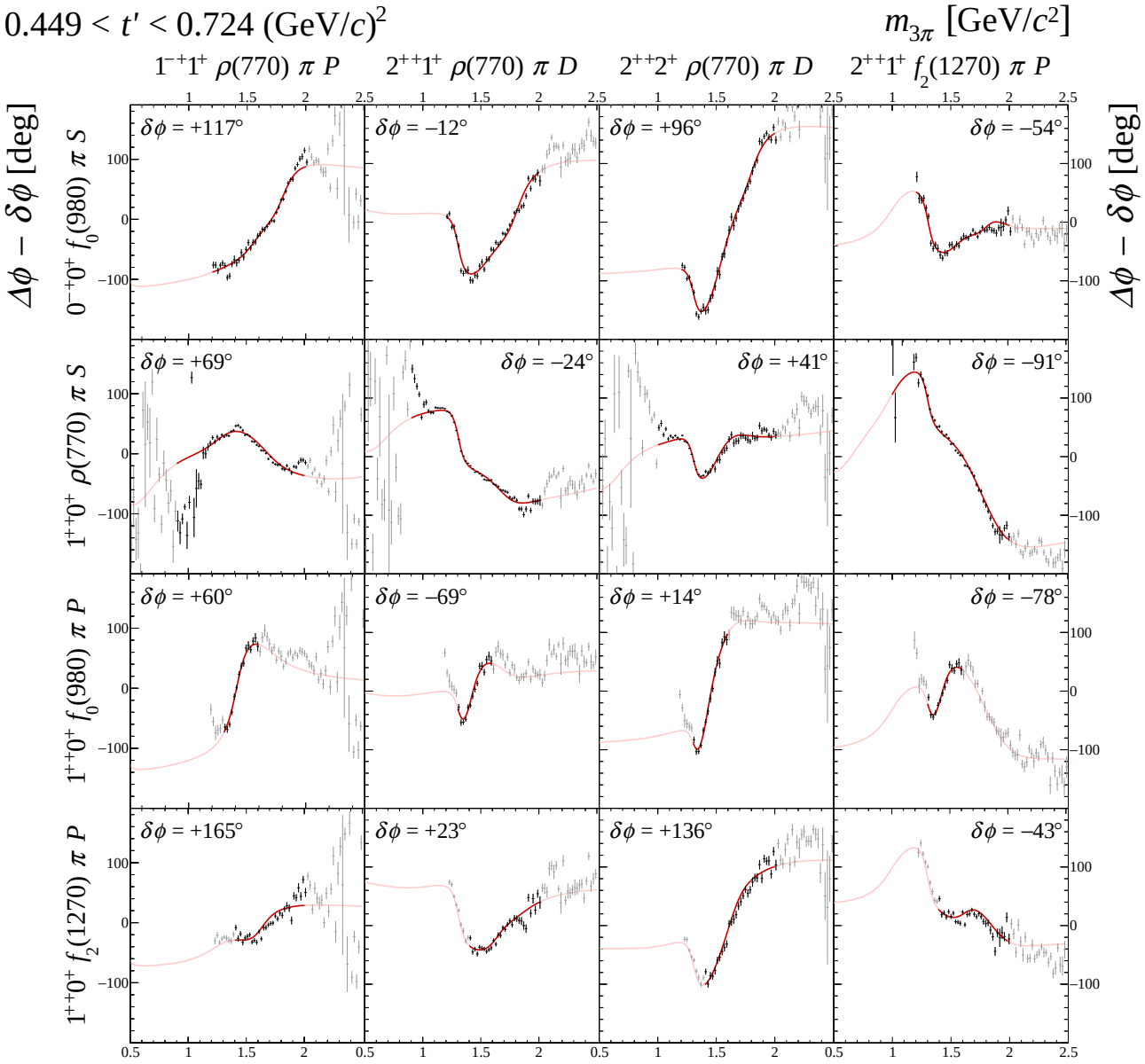

FIG. 77: Submatrix B of the 14 × 14 matrix of graphs that represents the spin-density matrix (see Table 8).

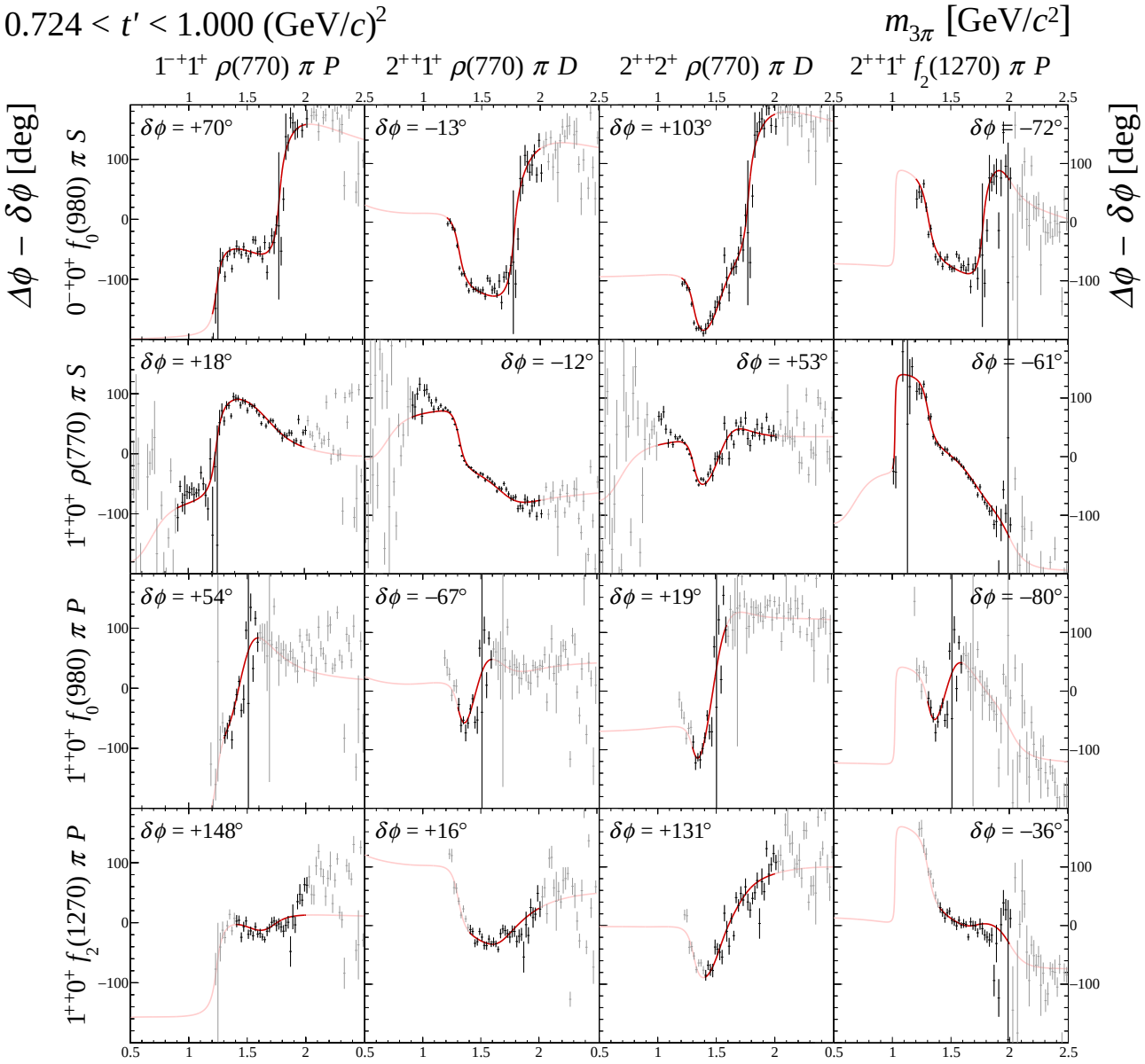

FIG. 78: Submatrix B of the 14 × 14 matrix of graphs that represents the spin-density matrix (see Table 8).

3 Submatrix C

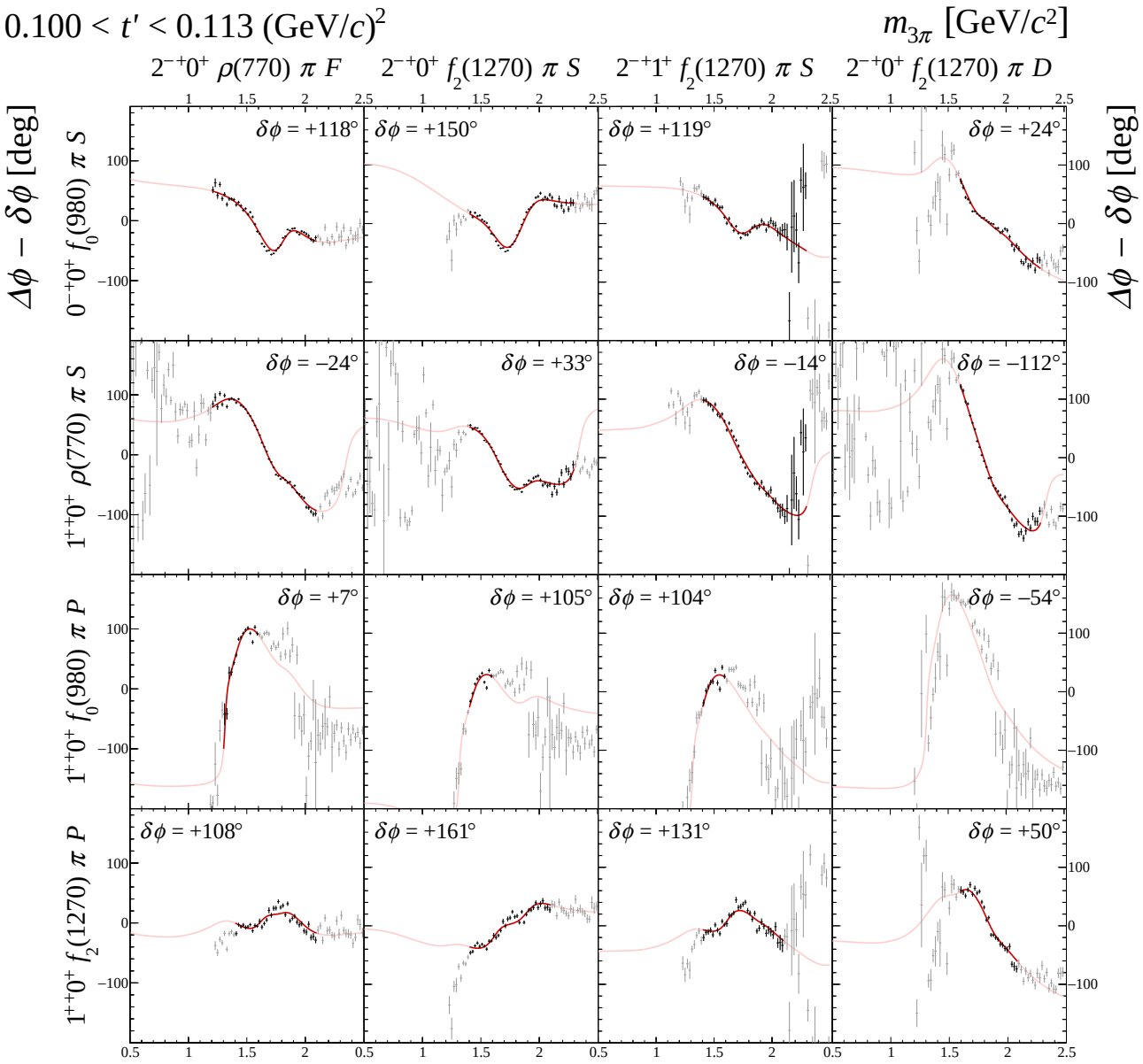

FIG. 79: Submatrix C of the 14 × 14 matrix of graphs that represents the spin-density matrix (see Table 8).

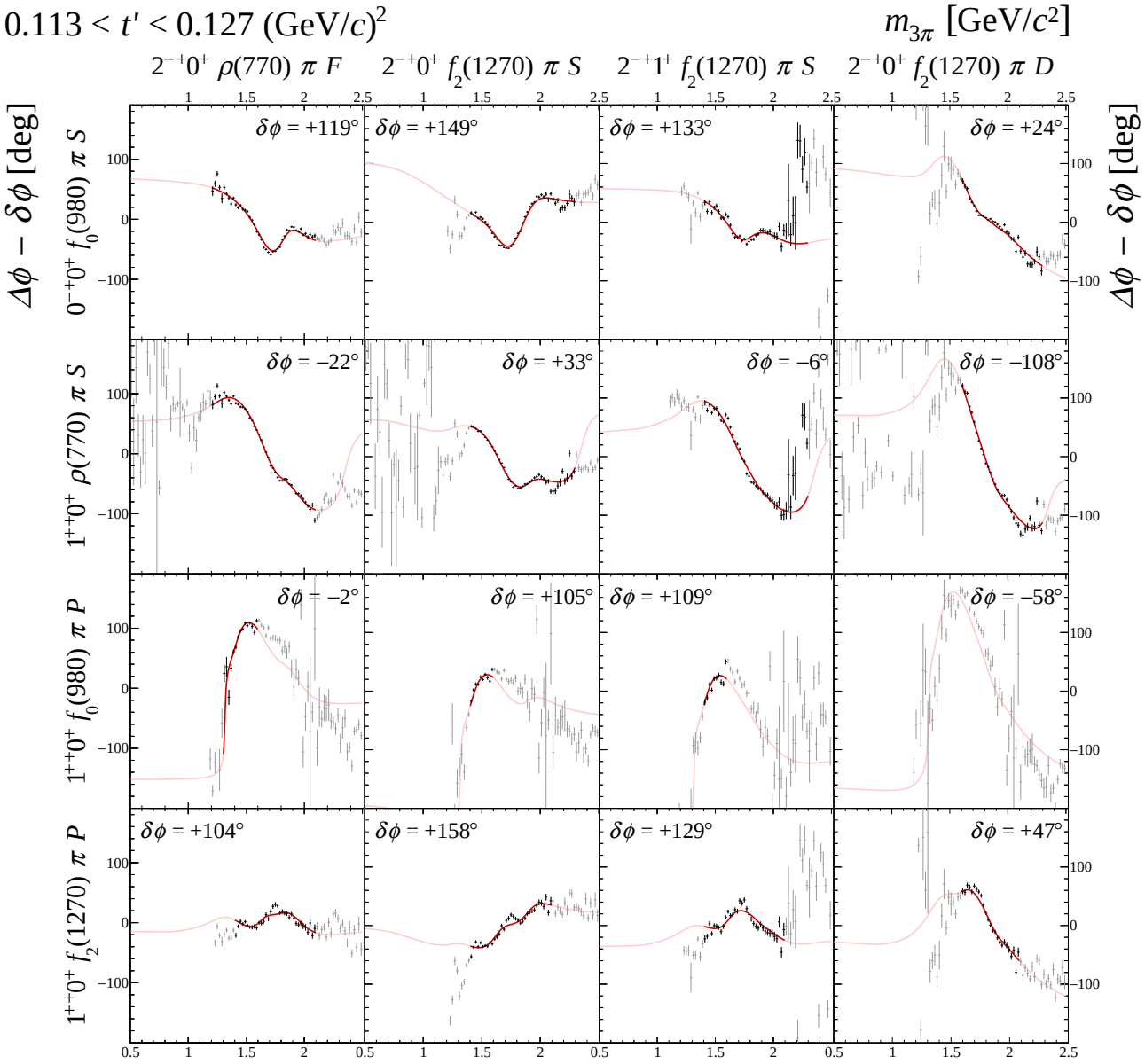

FIG. 80: Submatrix C of the 14 × 14 matrix of graphs that represents the spin-density matrix (see Table 8).

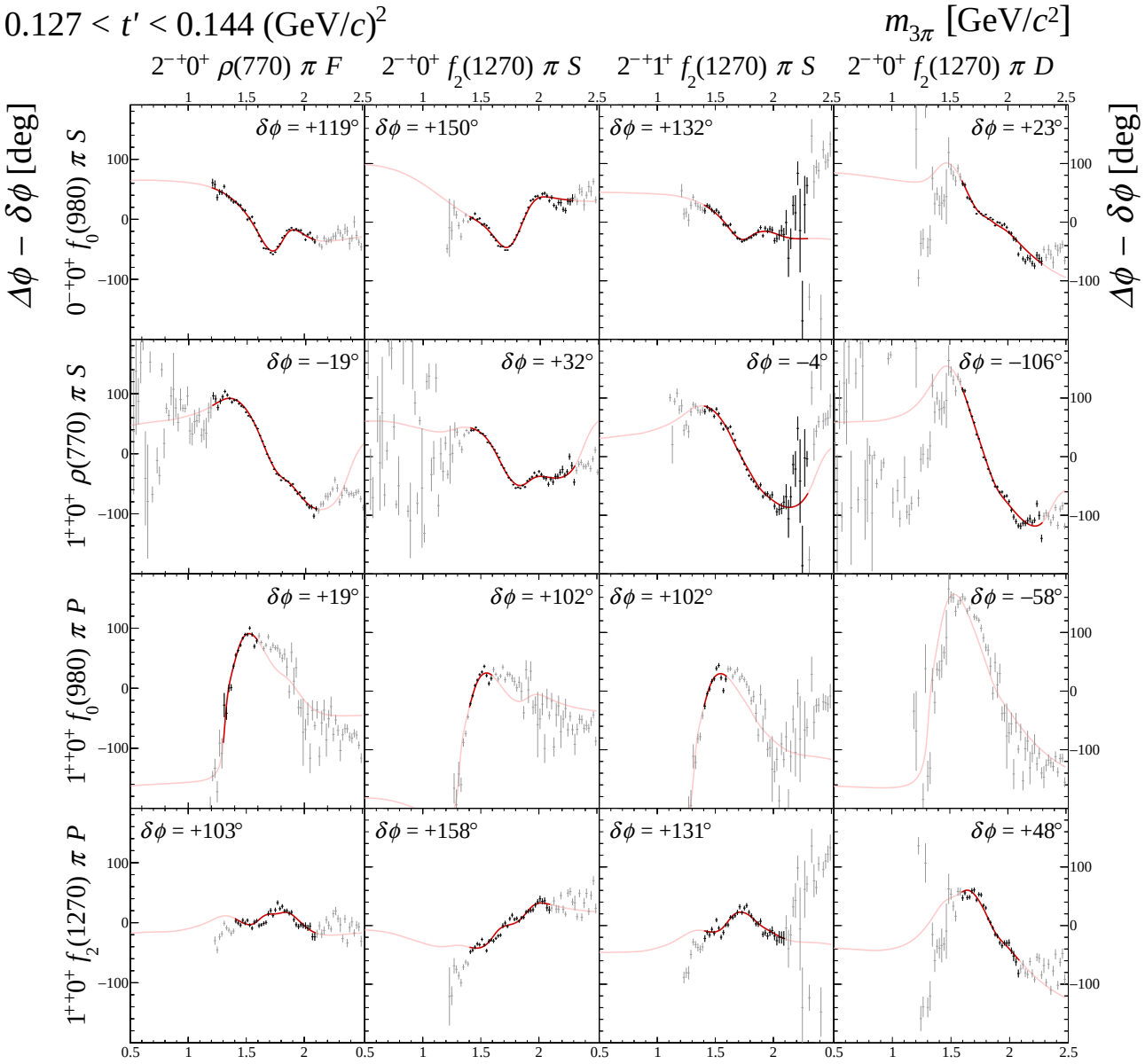

FIG. 81: Submatrix C of the 14 × 14 matrix of graphs that represents the spin-density matrix (see Table 8).

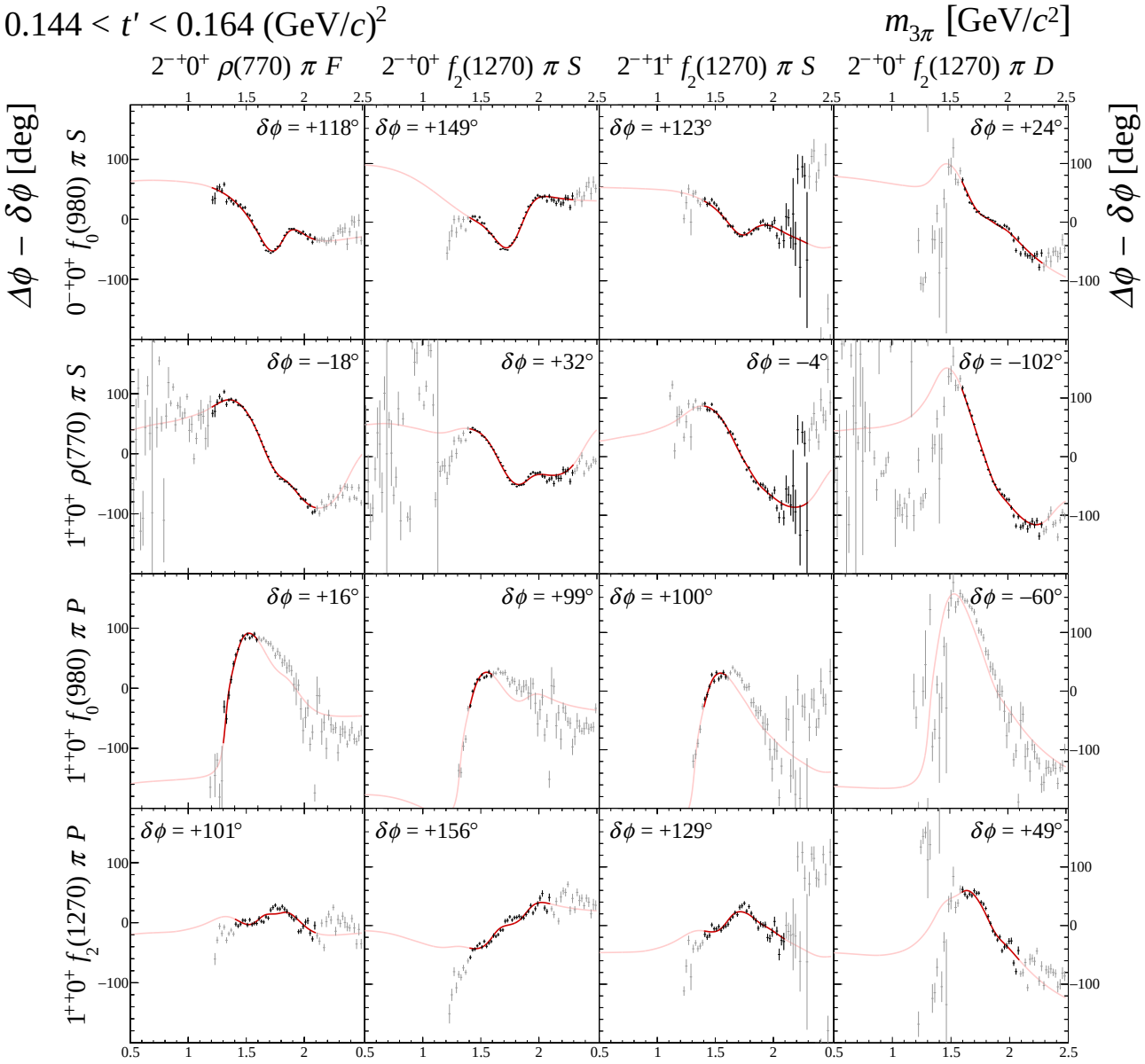

FIG. 82: Submatrix C of the 14 × 14 matrix of graphs that represents the spin-density matrix (see Table 8).

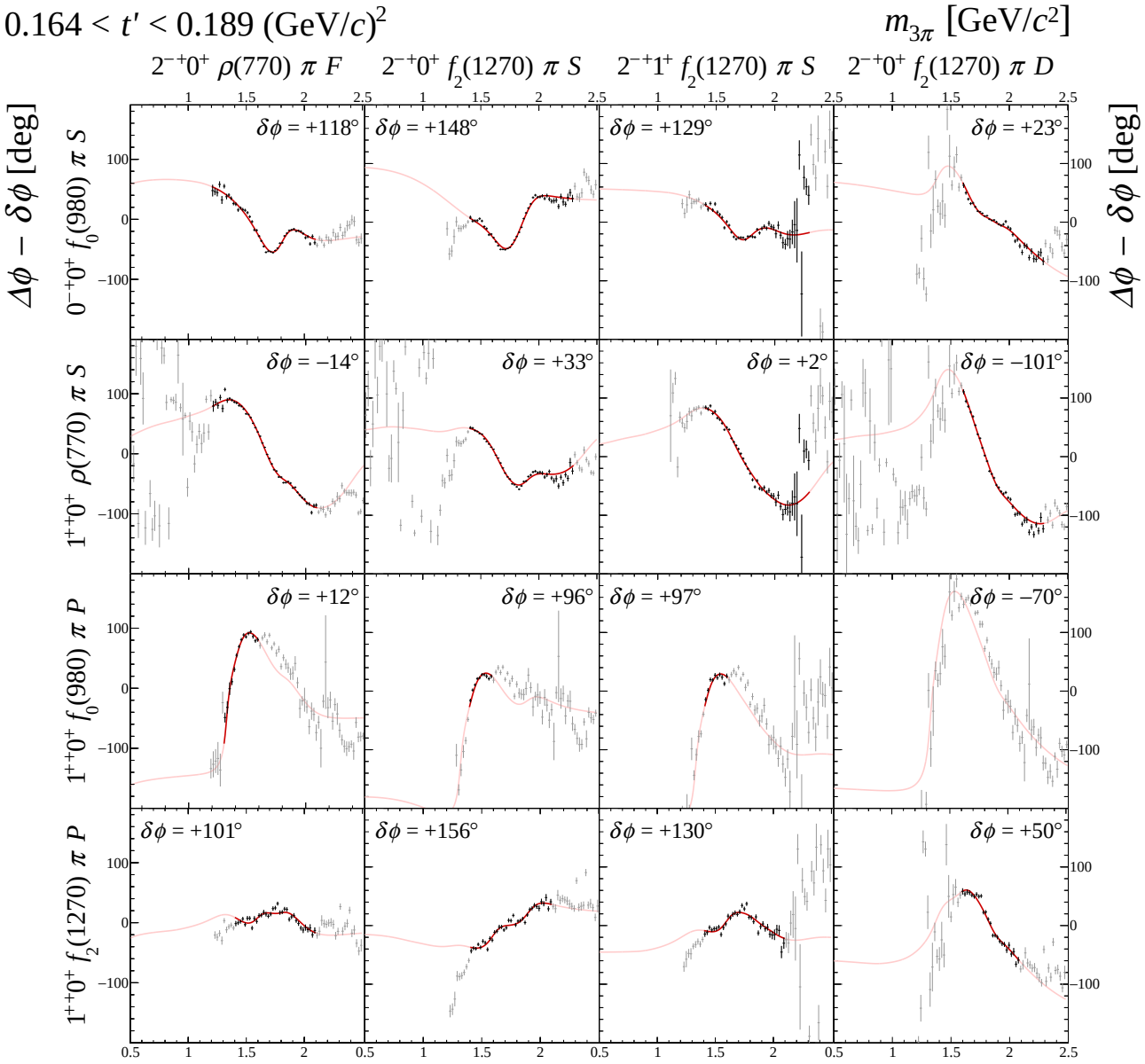

FIG. 83: Submatrix C of the 14 × 14 matrix of graphs that represents the spin-density matrix (see Table 8).

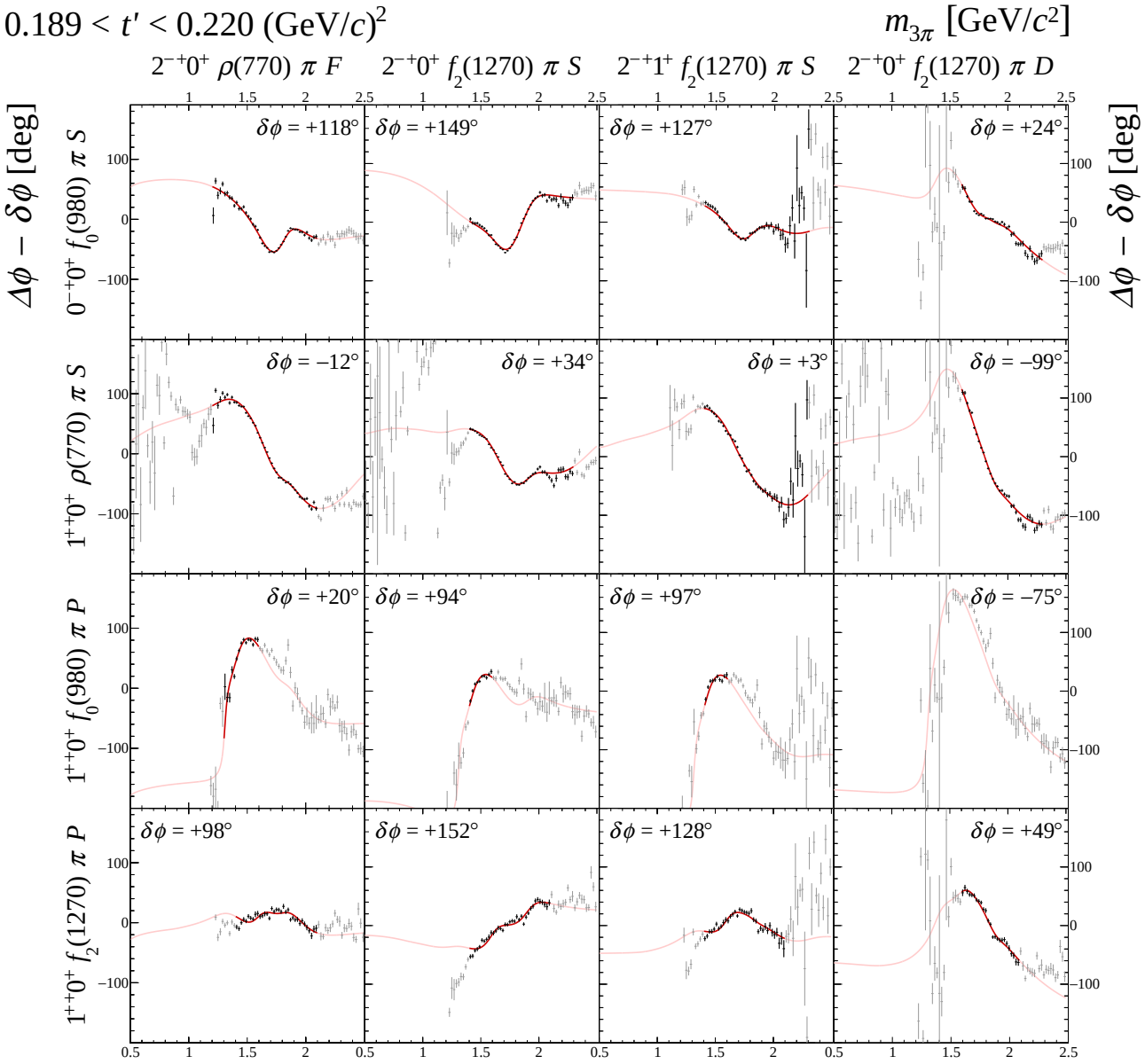

FIG. 84: Submatrix C of the 14 × 14 matrix of graphs that represents the spin-density matrix (see Table 8).

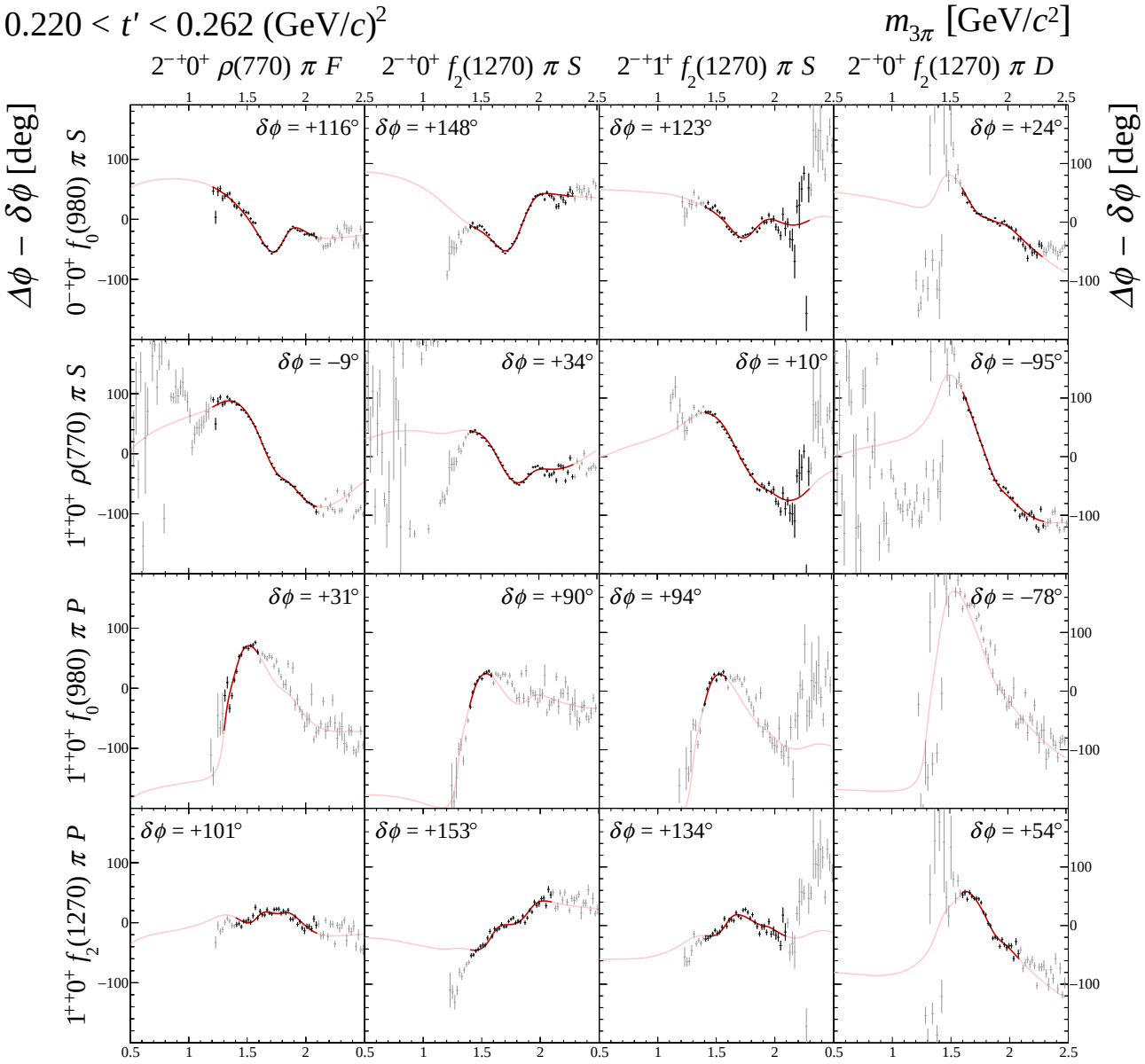

FIG. 85: Submatrix C of the 14 × 14 matrix of graphs that represents the spin-density matrix (see Table 8).

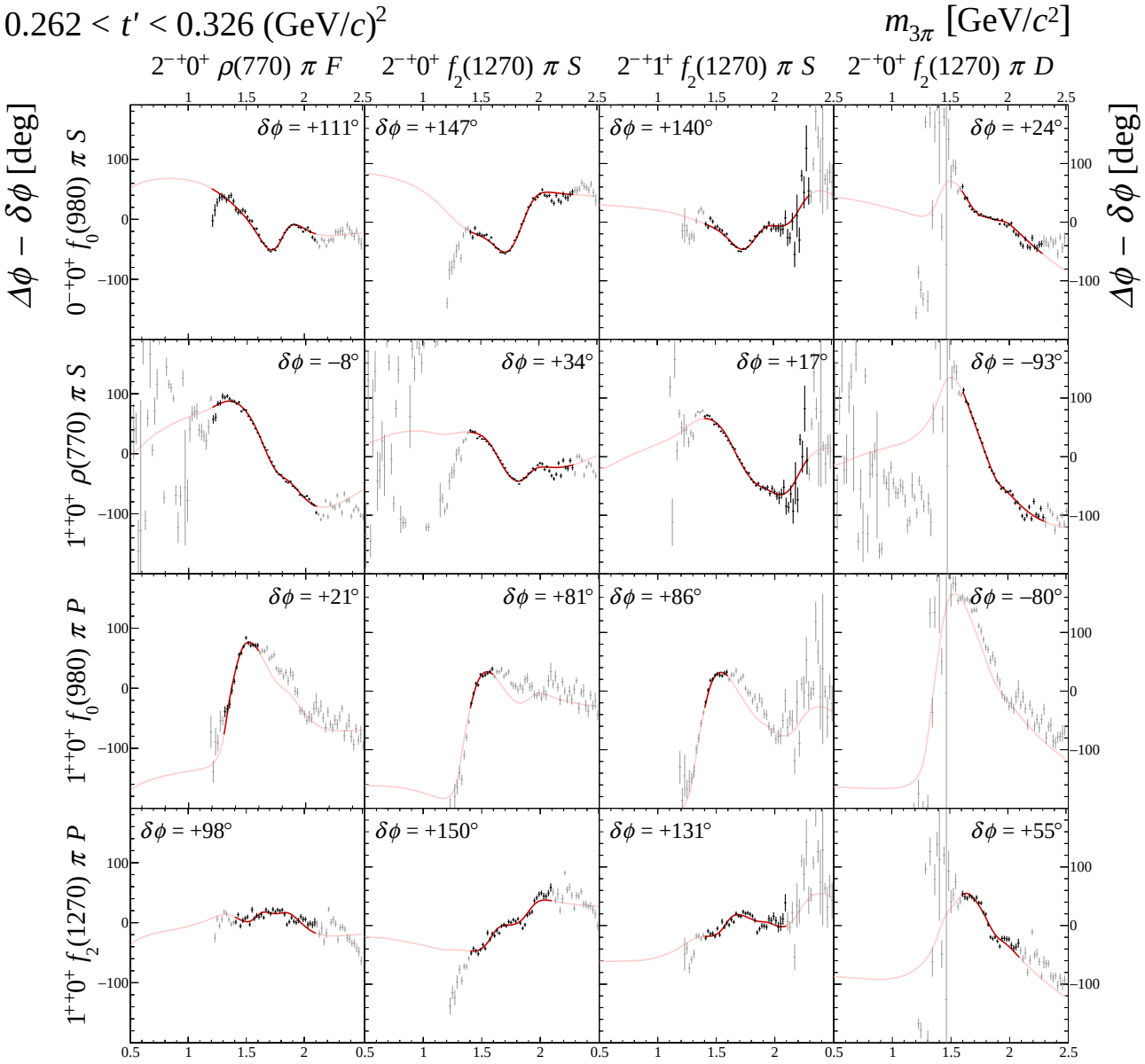

FIG. 86: Submatrix C of the 14 × 14 matrix of graphs that represents the spin-density matrix (see Table 8).

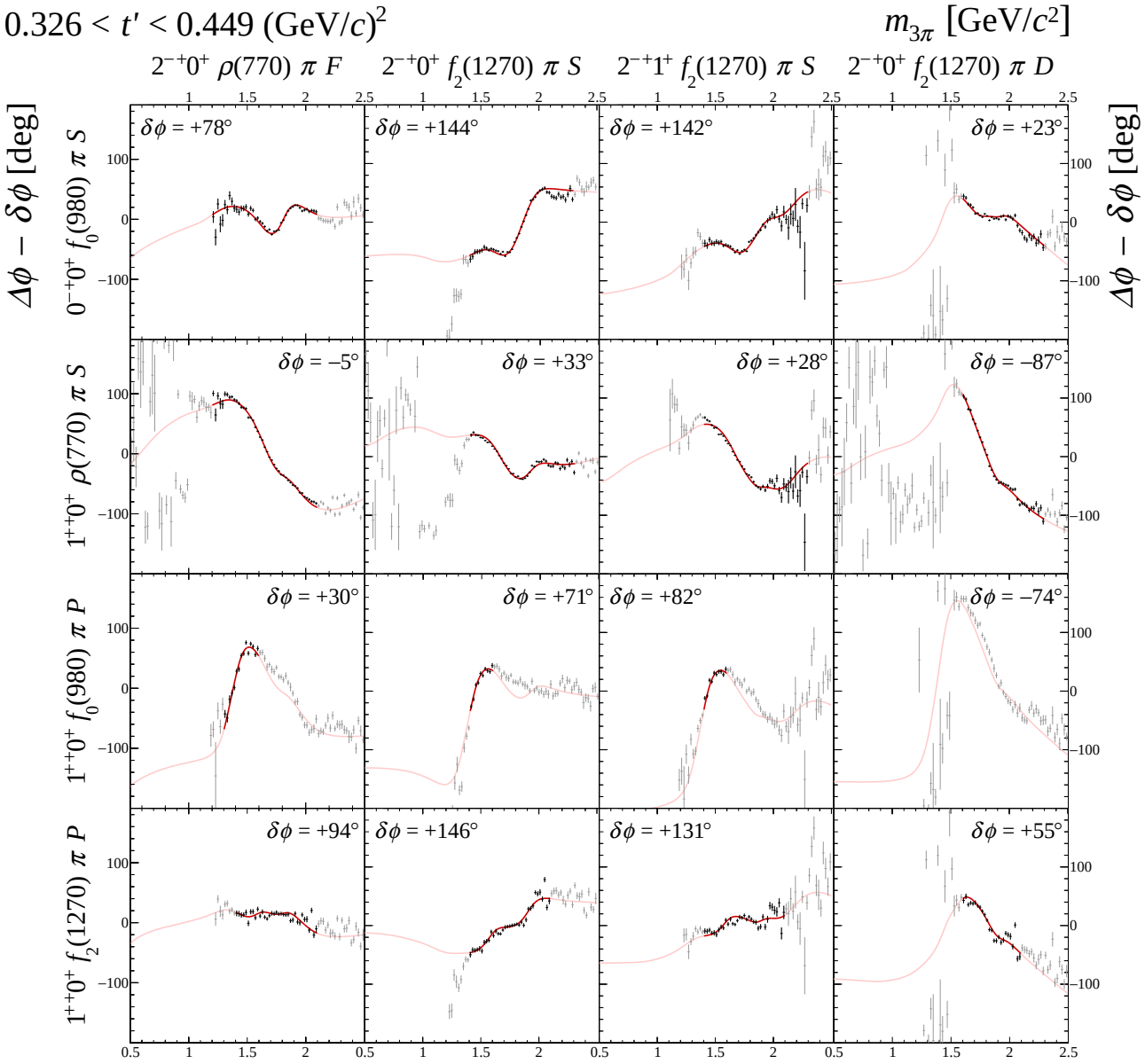

FIG. 87: Submatrix C of the 14 × 14 matrix of graphs that represents the spin-density matrix (see Table 8).

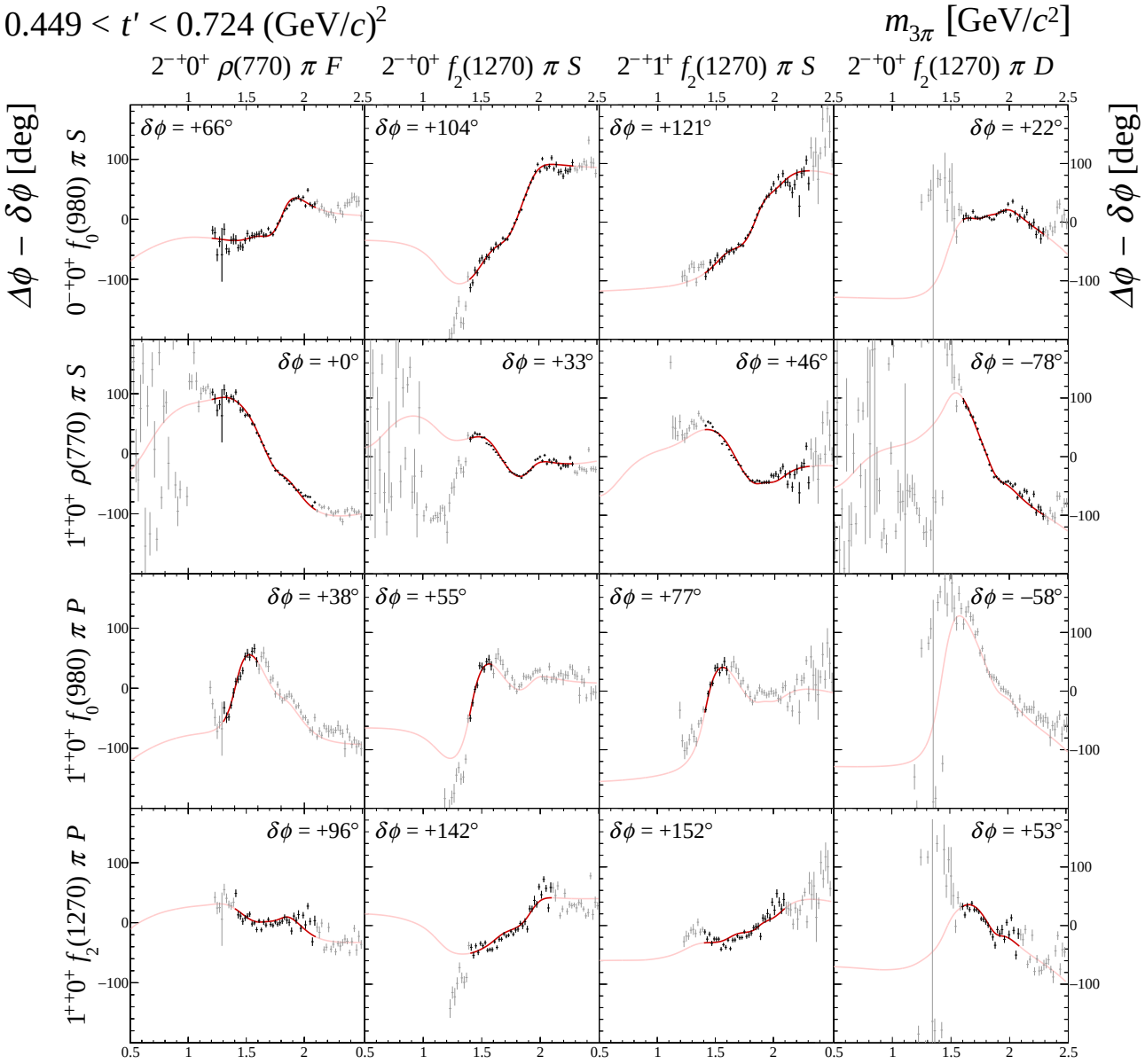

FIG. 88: Submatrix C of the 14 × 14 matrix of graphs that represents the spin-density matrix (see Table 8).

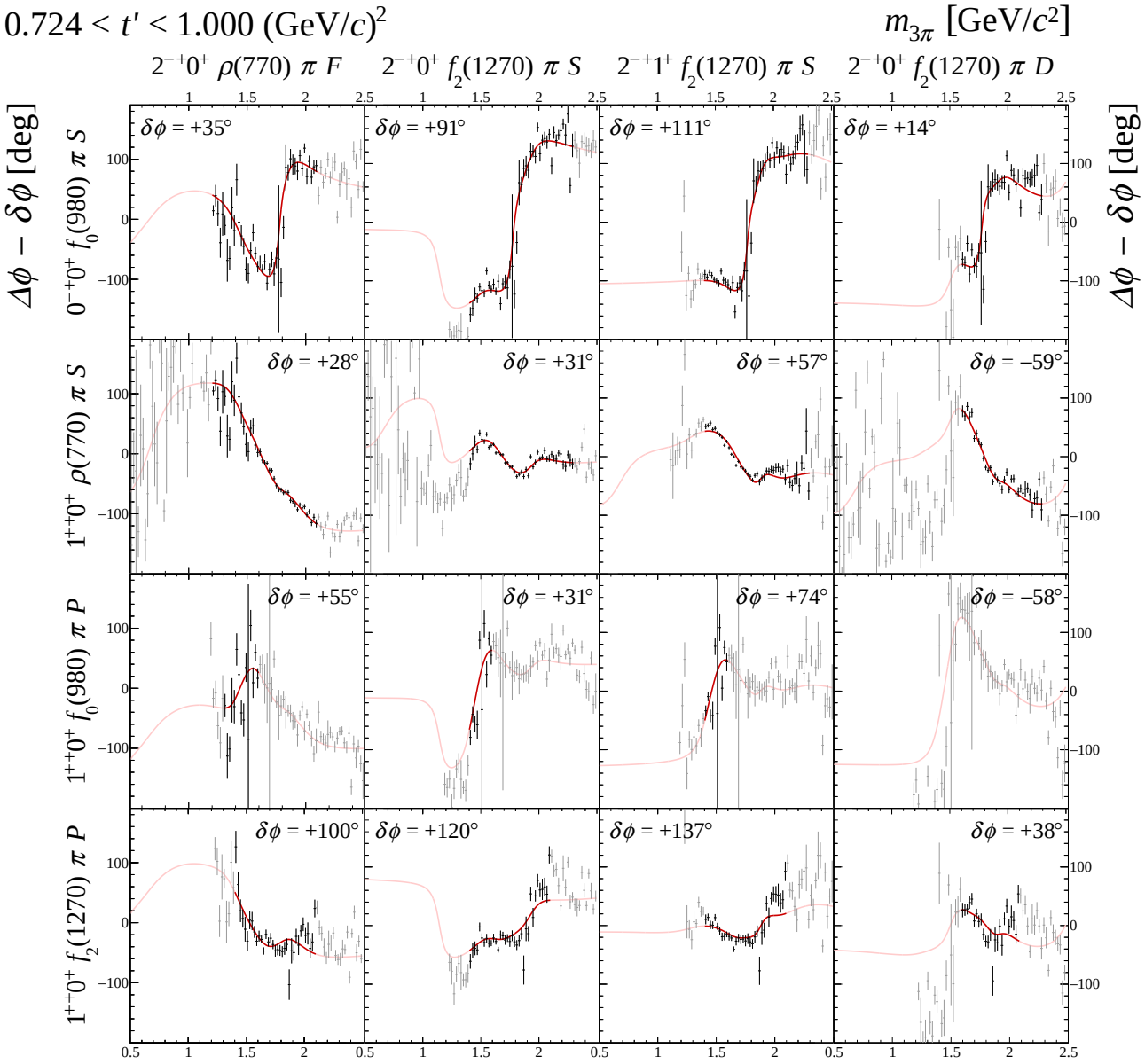

FIG. 89: Submatrix C of the 14 × 14 matrix of graphs that represents the spin-density matrix (see Table 8).

4 Submatrix D

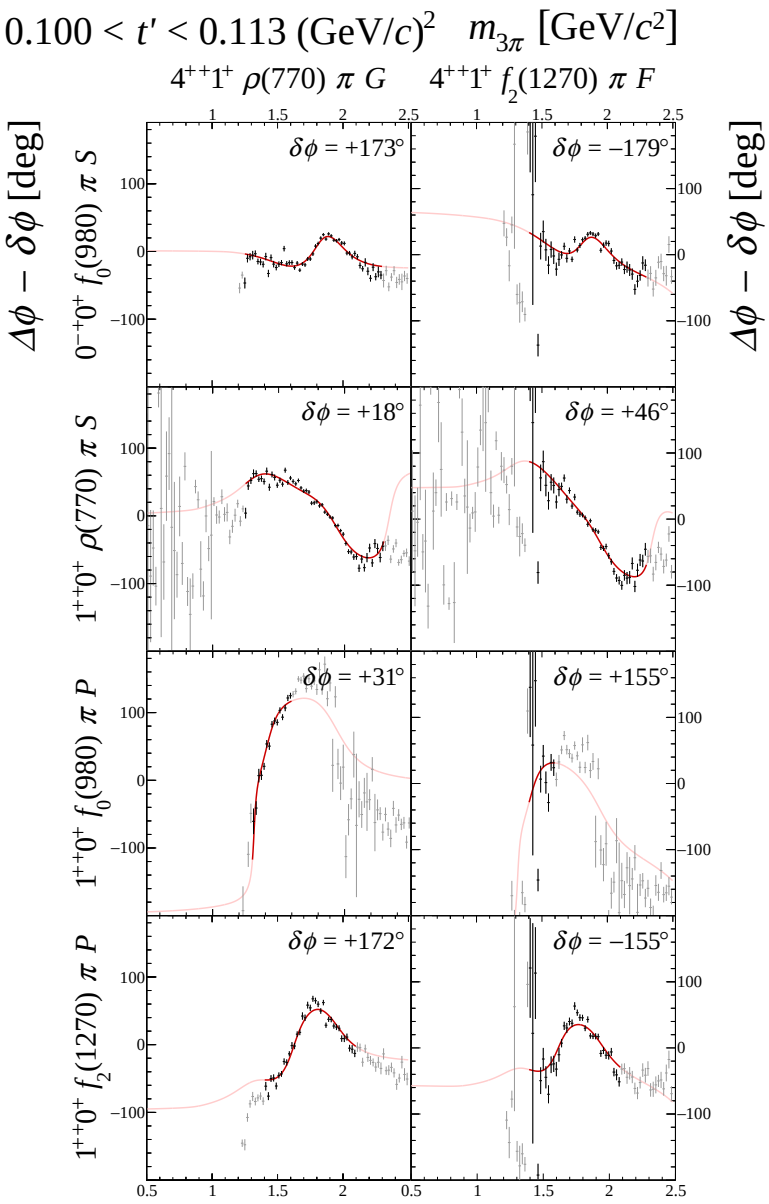

FIG. 90: Submatrix D of the 14 × 14 matrix of graphs that represents the spin-density matrix (see Table 8).

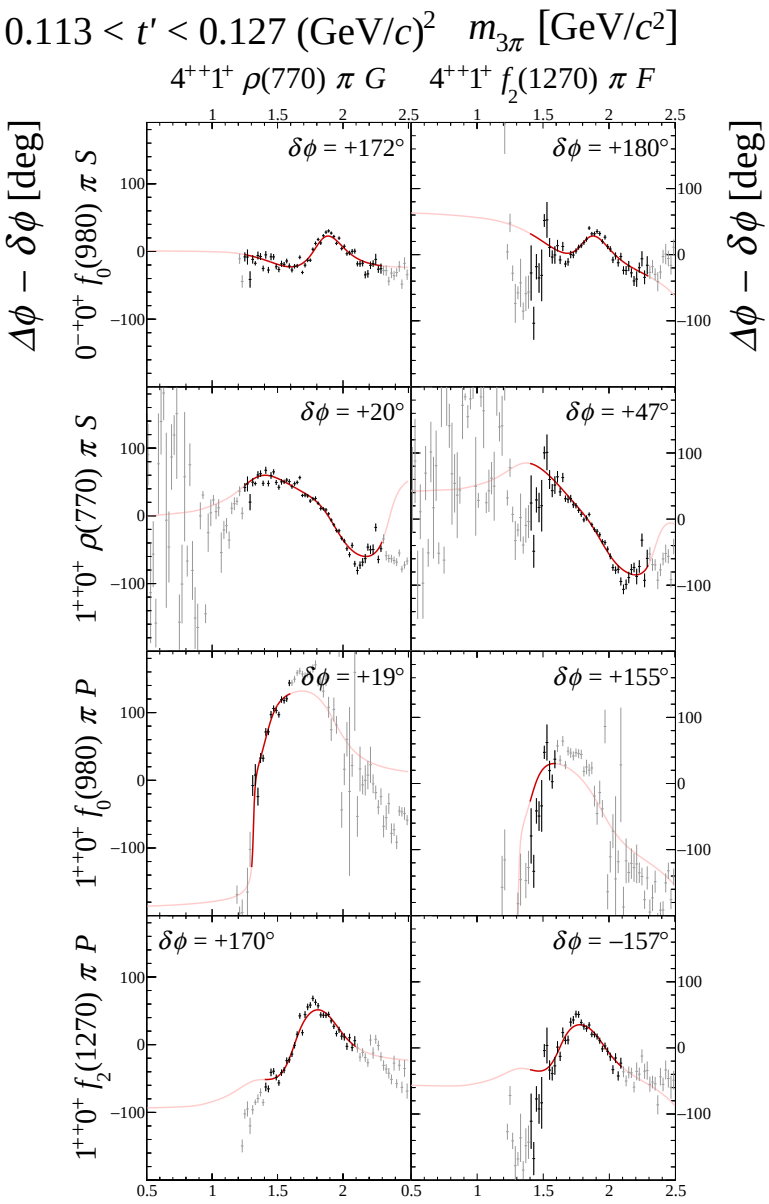

FIG. 91: Submatrix D of the 14 × 14 matrix of graphs that represents the spin-density matrix (see Table 8).

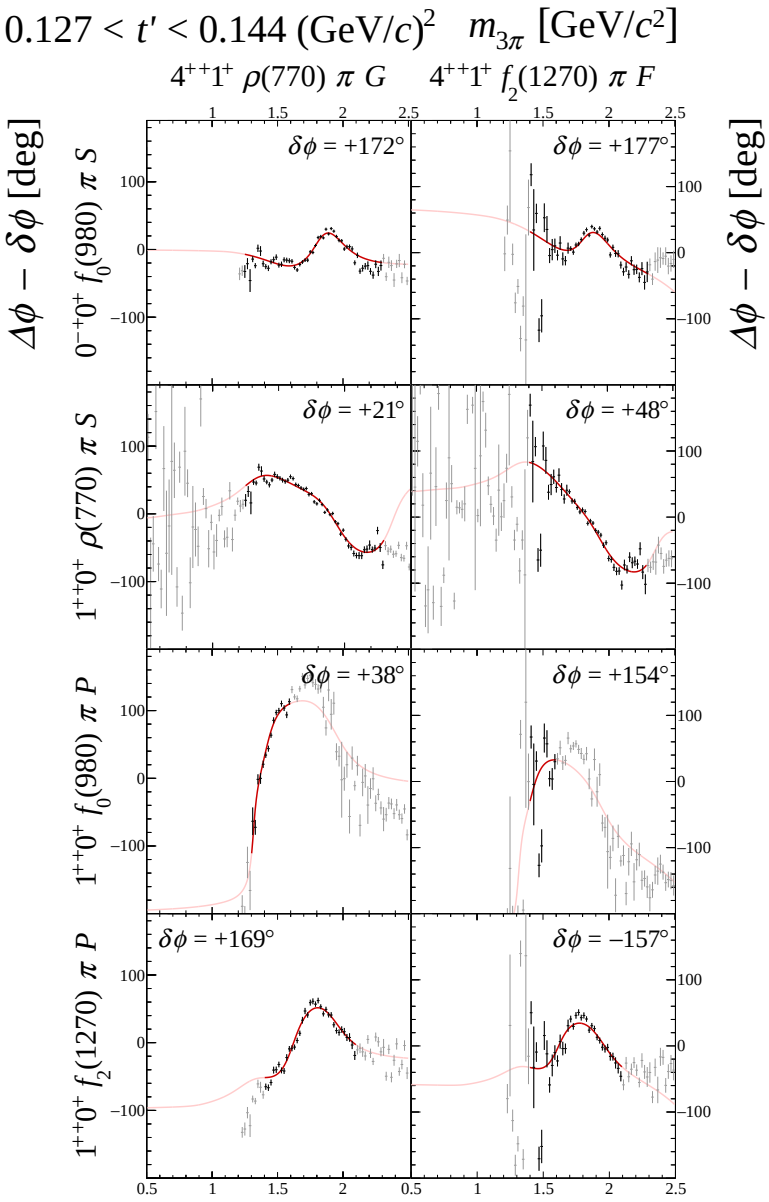

FIG. 92: Submatrix D of the 14 × 14 matrix of graphs that represents the spin-density matrix (see Table 8).

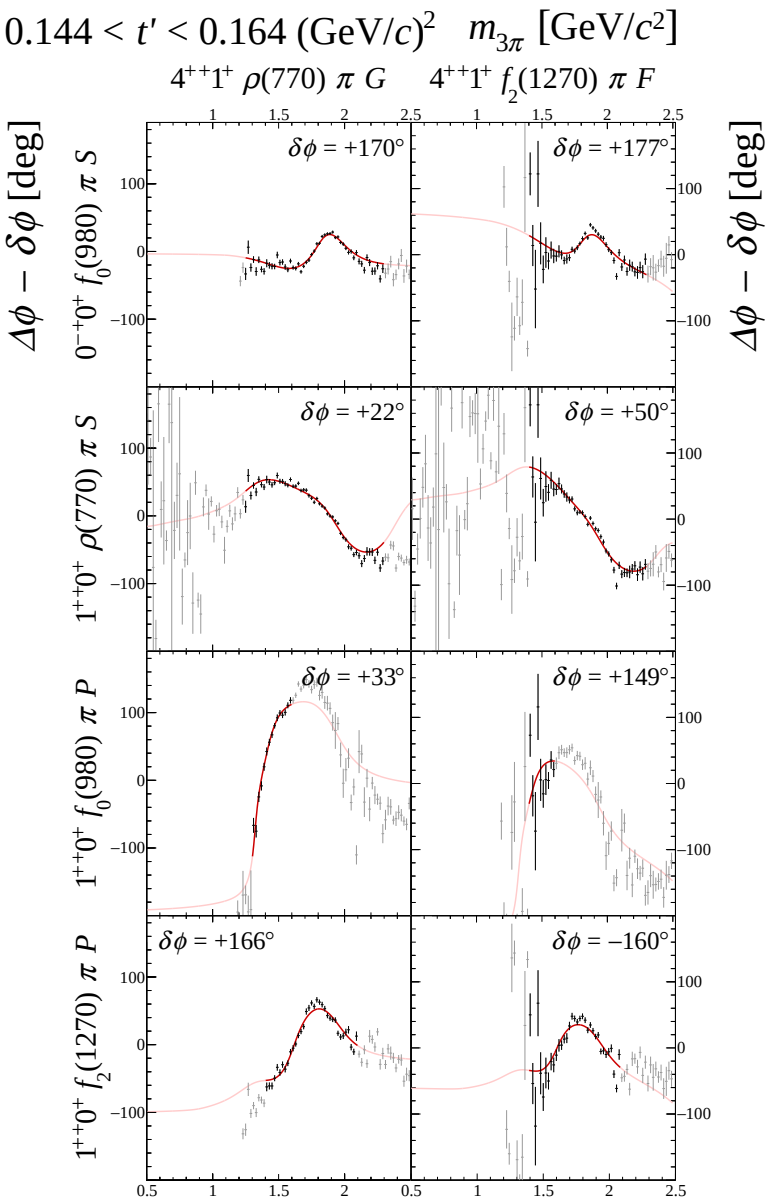

FIG. 93: Submatrix D of the 14 × 14 matrix of graphs that represents the spin-density matrix (see Table 8).

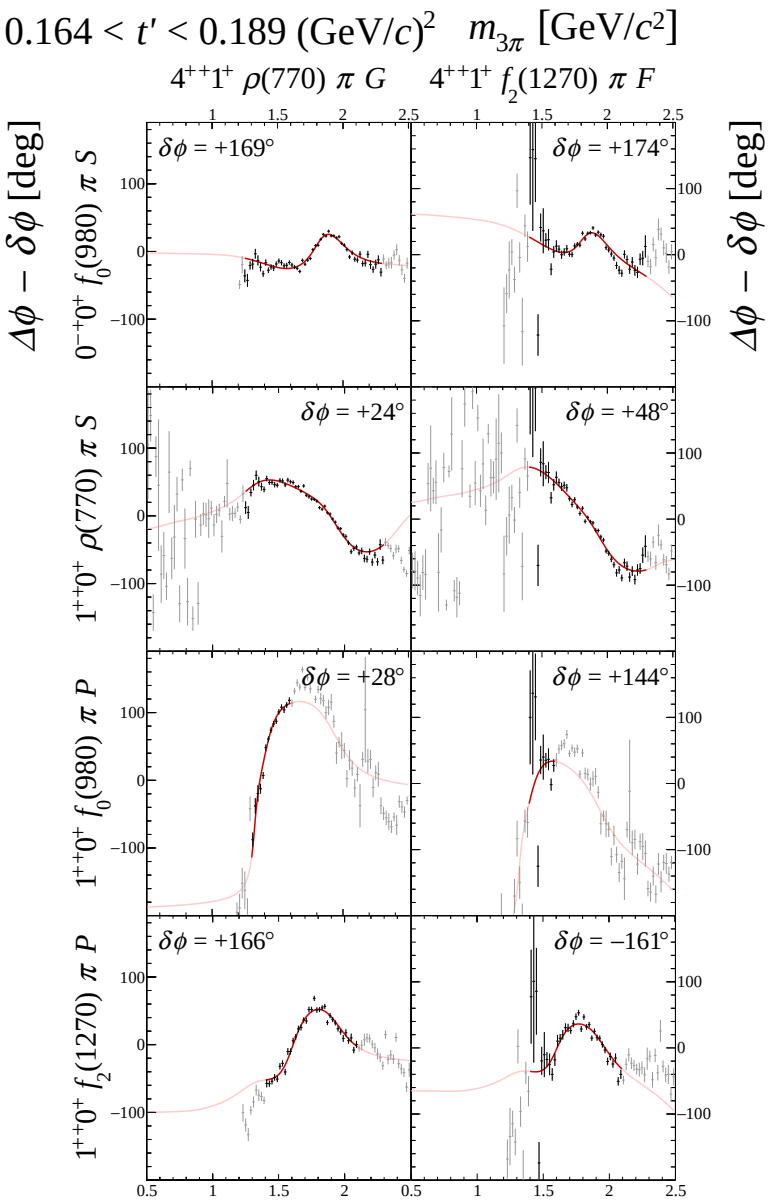

FIG. 94: Submatrix D of the 14 × 14 matrix of graphs that represents the spin-density matrix (see Table 8).

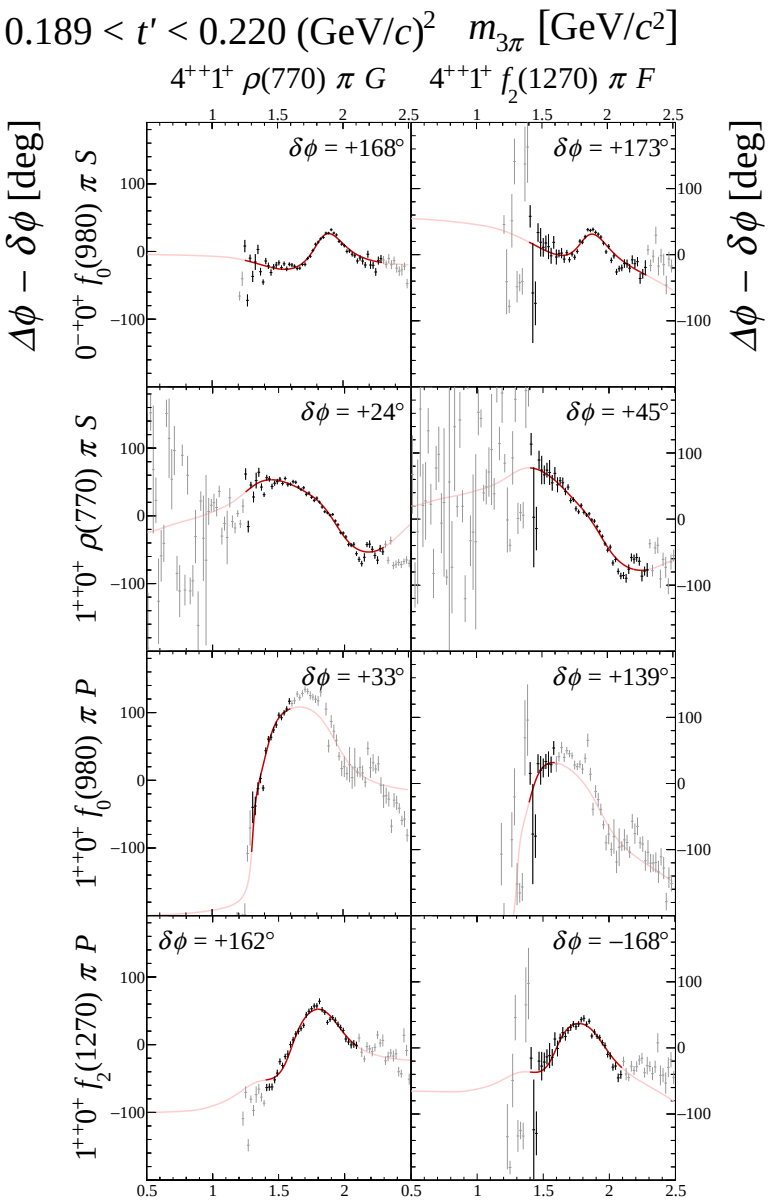

FIG. 95: Submatrix D of the 14 × 14 matrix of graphs that represents the spin-density matrix (see Table 8).

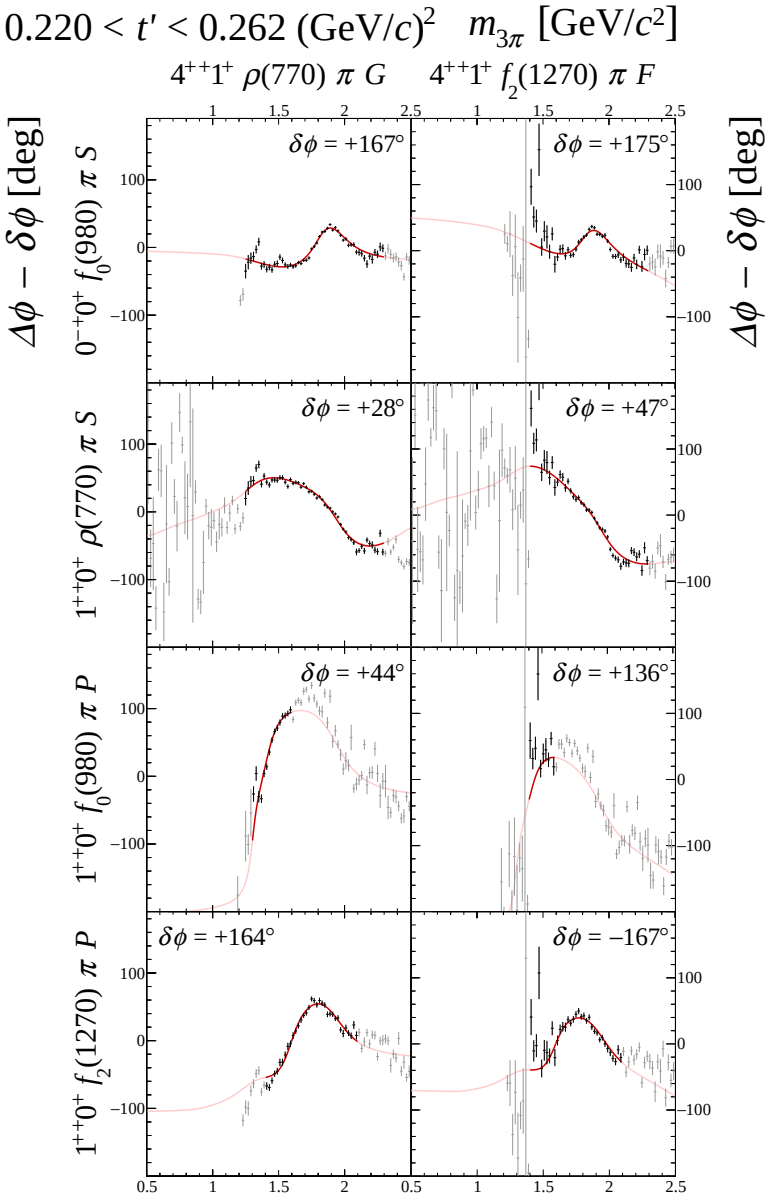

FIG. 96: Submatrix D of the 14 × 14 matrix of graphs that represents the spin-density matrix (see Table 8).

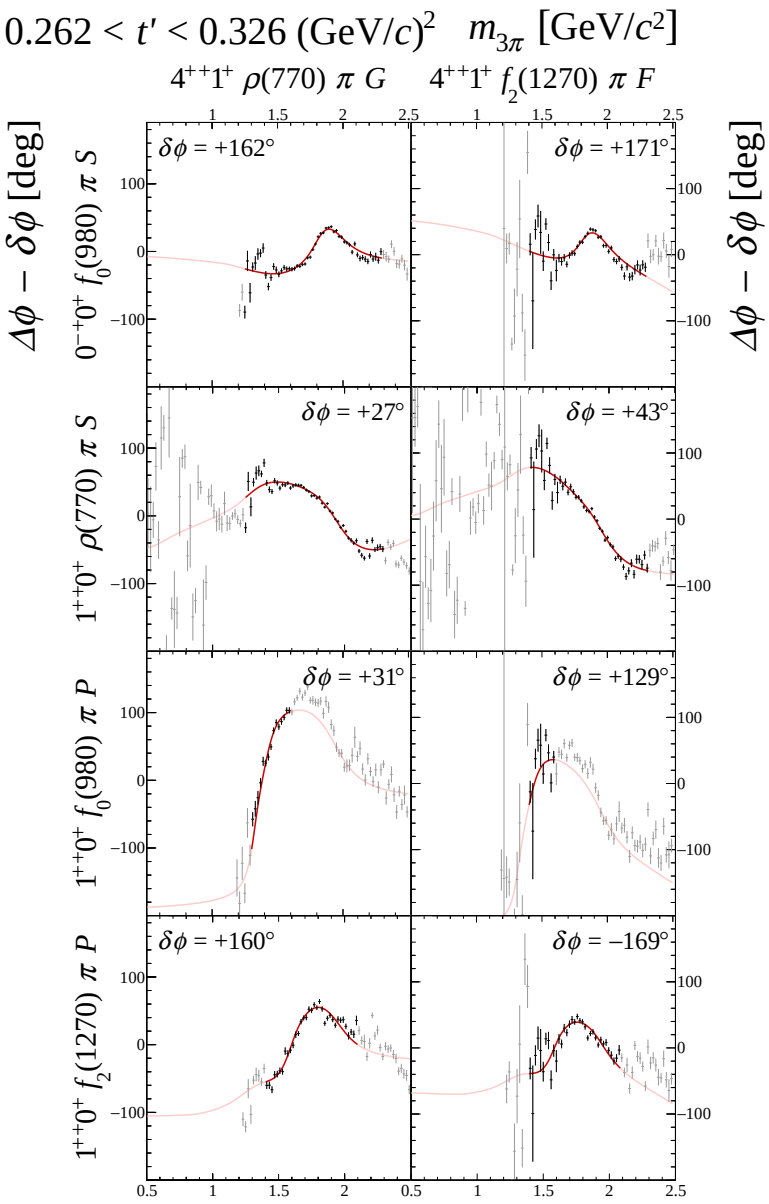

FIG. 97: Submatrix D of the 14 × 14 matrix of graphs that represents the spin-density matrix (see Table 8).

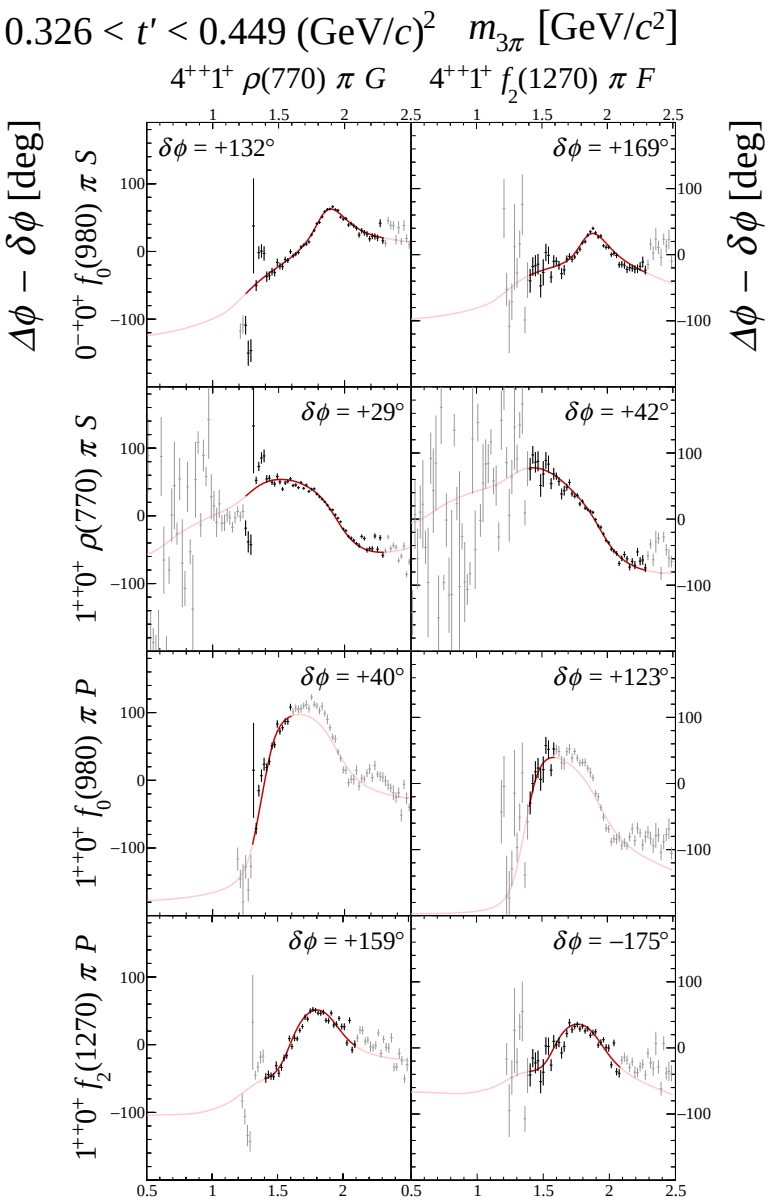

FIG. 98: Submatrix D of the 14 × 14 matrix of graphs that represents the spin-density matrix (see Table 8).

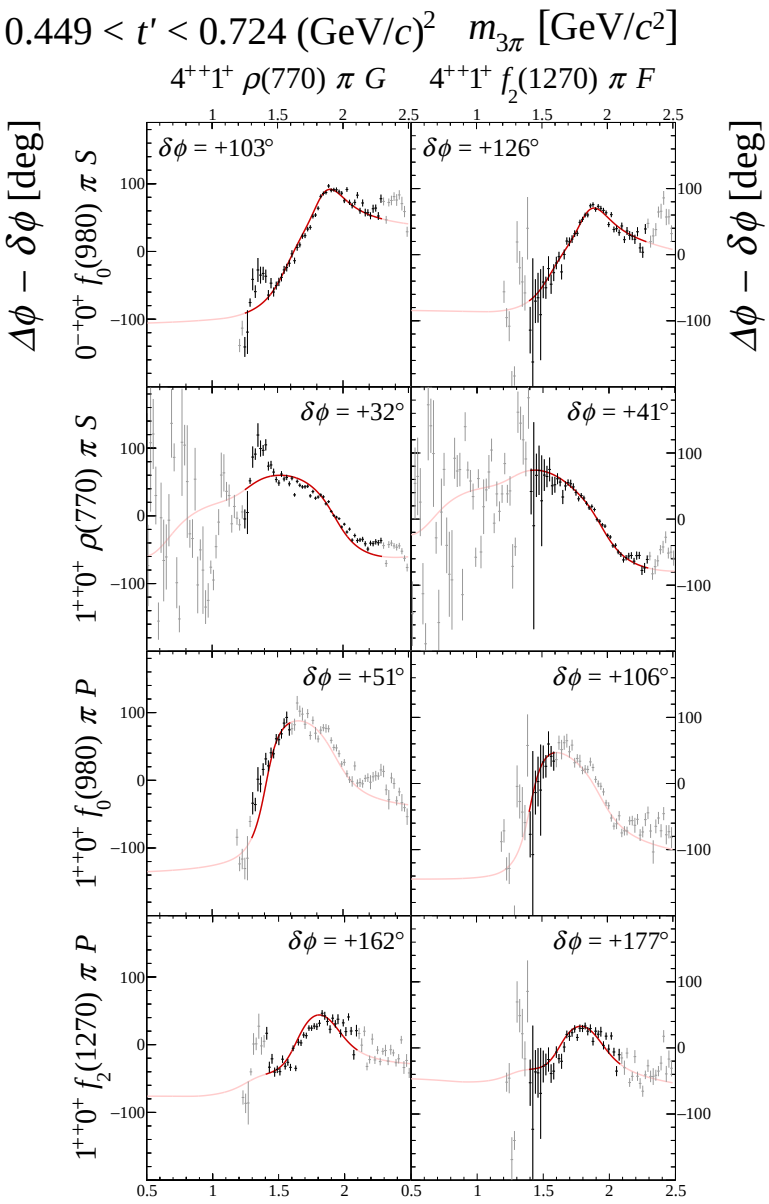

FIG. 99: Submatrix D of the 14 × 14 matrix of graphs that represents the spin-density matrix (see Table 8).

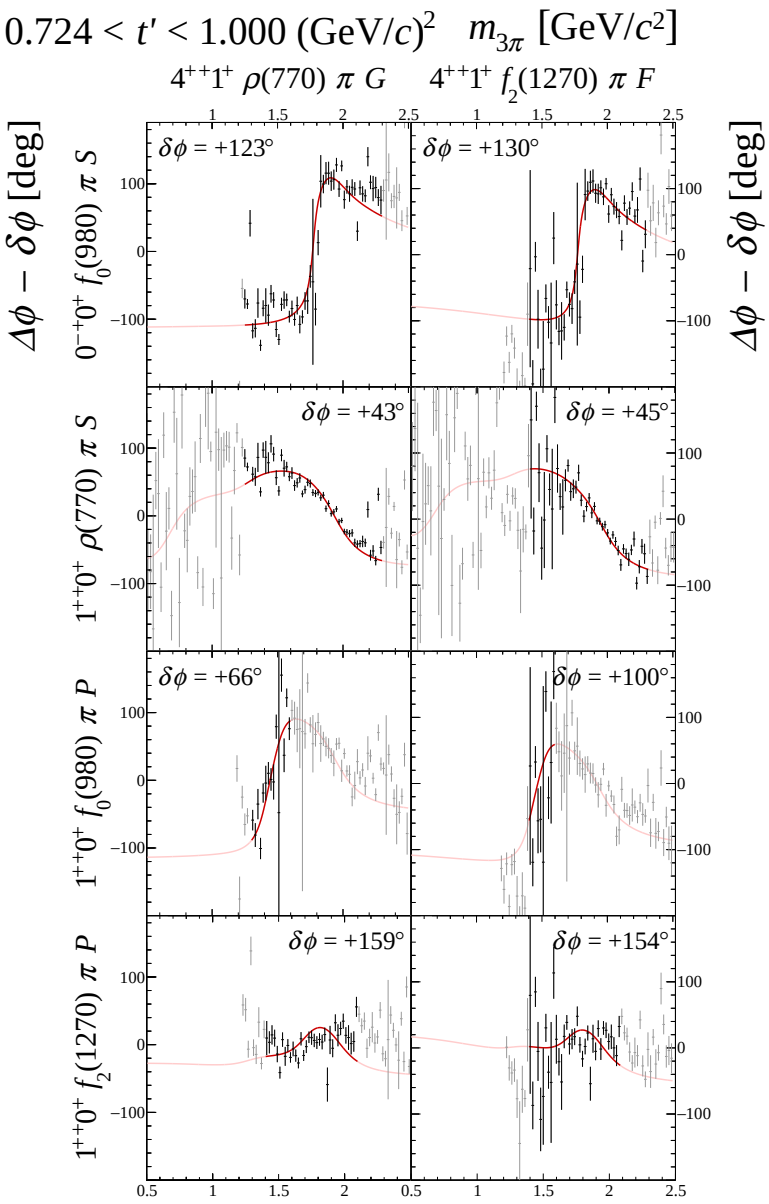

FIG. 100: Submatrix D of the 14 × 14 matrix of graphs that represents the spin-density matrix (see Table 8).

5 Submatrix E

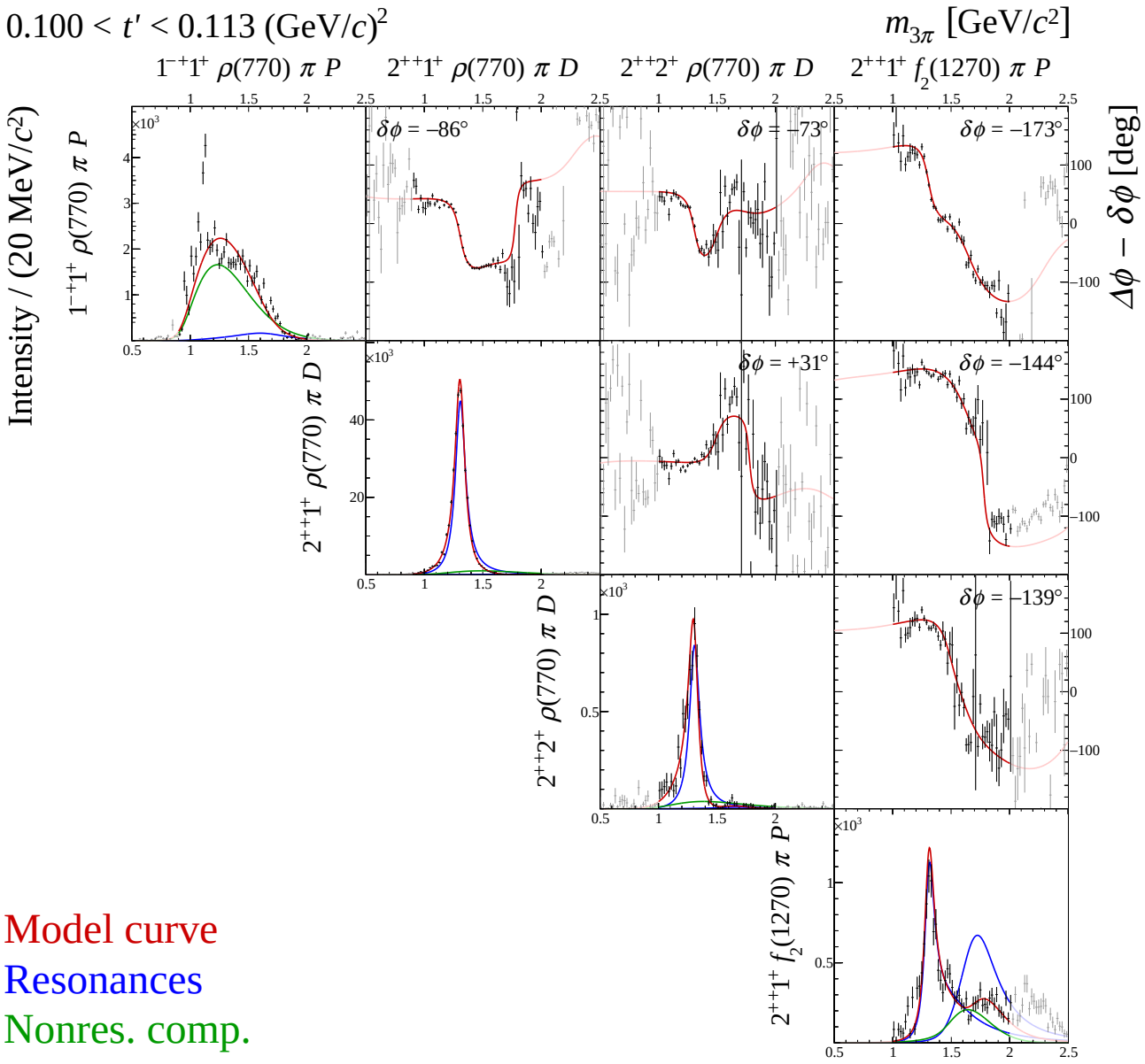

FIG. 101: Submatrix E of the 14 × 14 matrix of graphs that represents the spin-density matrix (see Table 8).

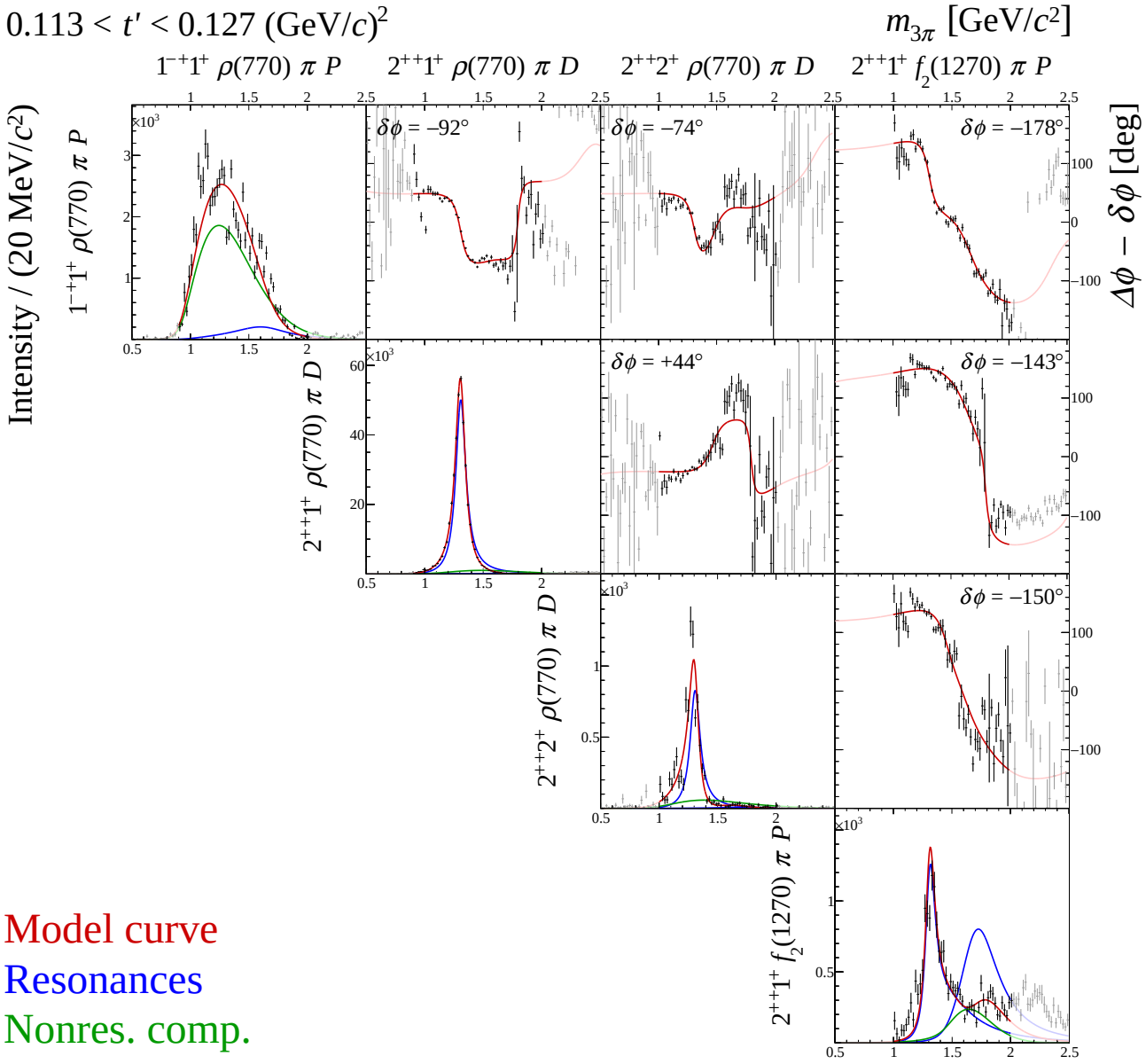

FIG. 102: Submatrix E of the 14 × 14 matrix of graphs that represents the spin-density matrix (see Table 8).

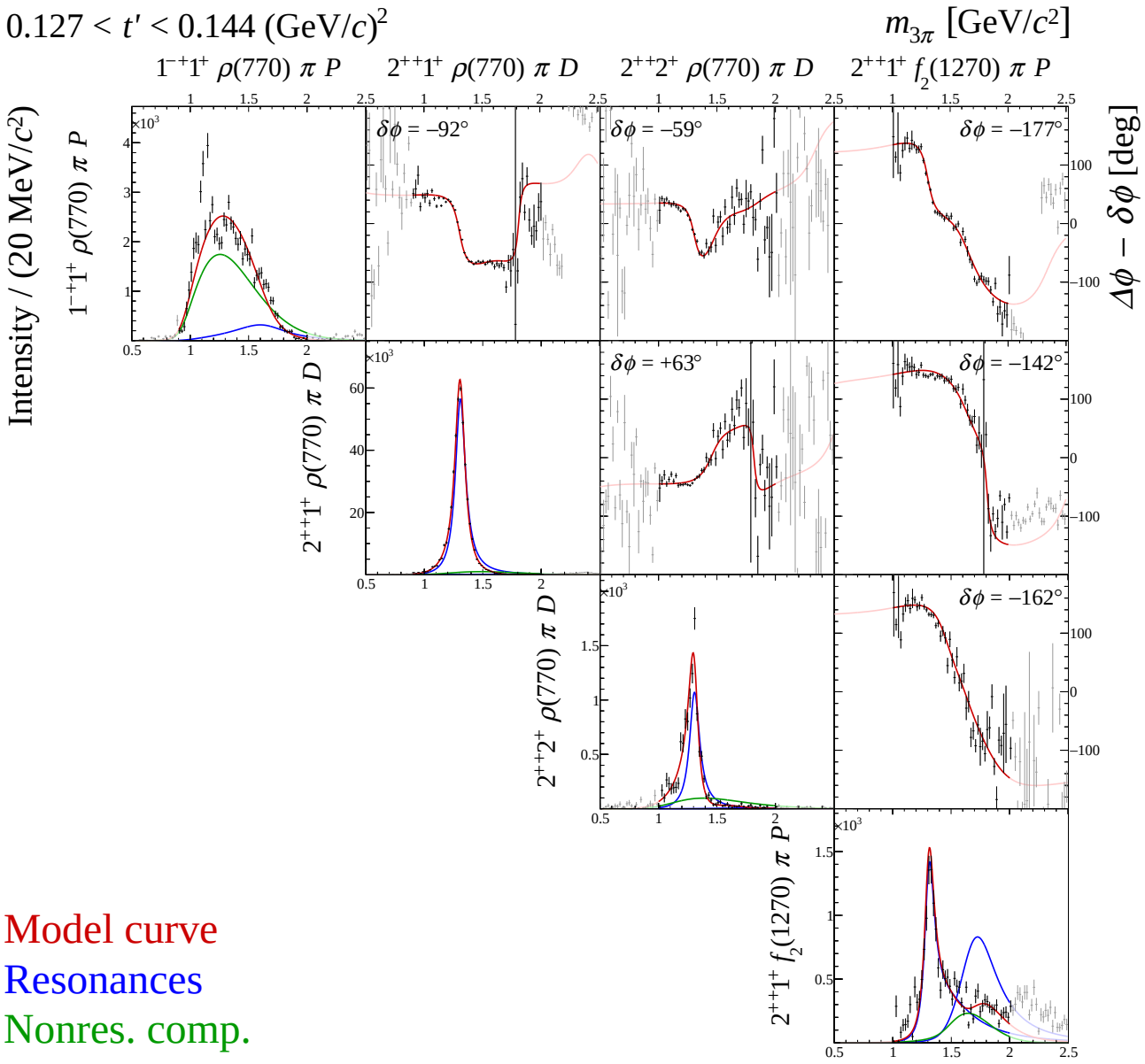

FIG. 103: Submatrix E of the 14 × 14 matrix of graphs that represents the spin-density matrix (see Table 8).

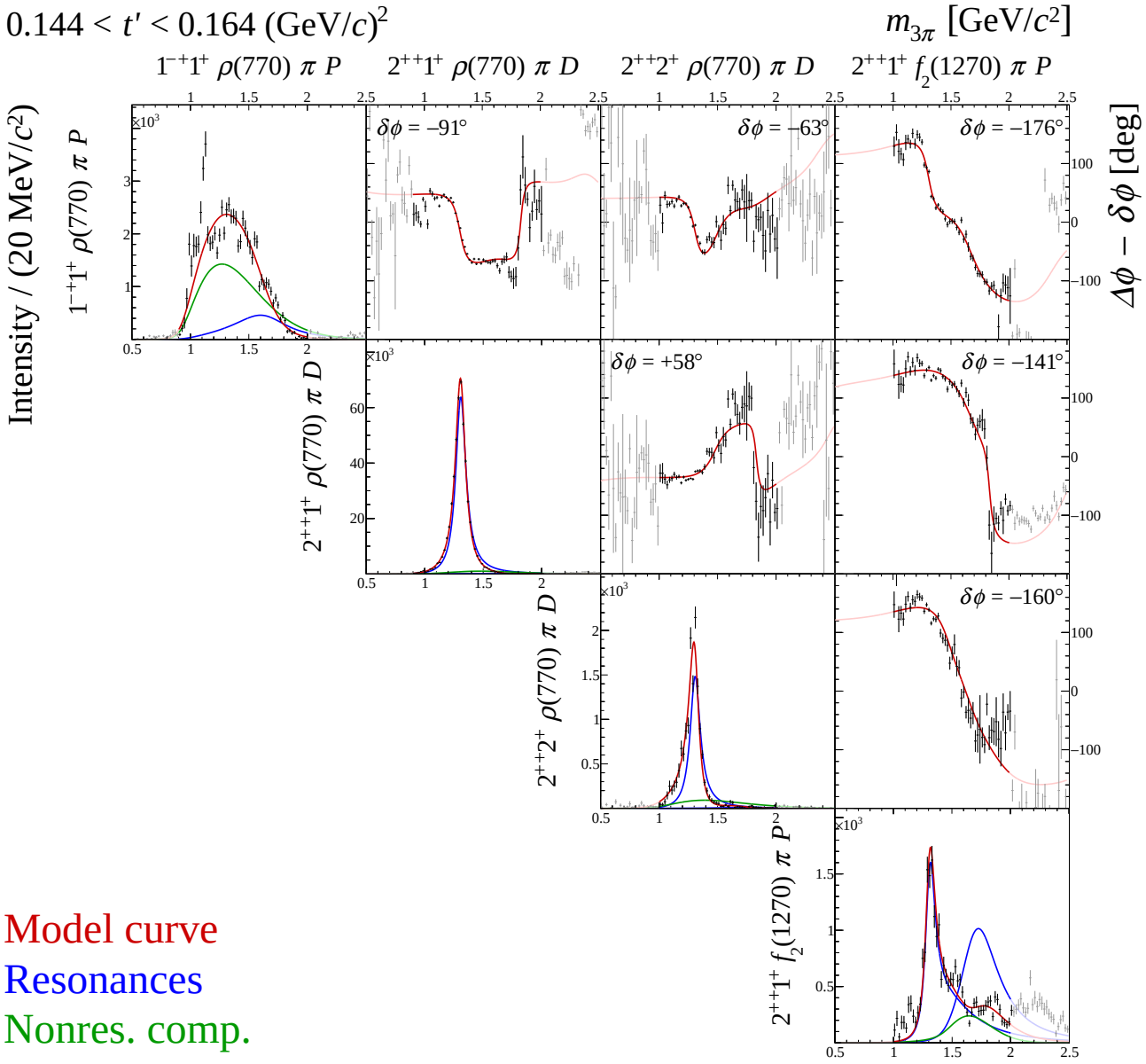

FIG. 104: Submatrix E of the 14 × 14 matrix of graphs that represents the spin-density matrix (see Table 8).

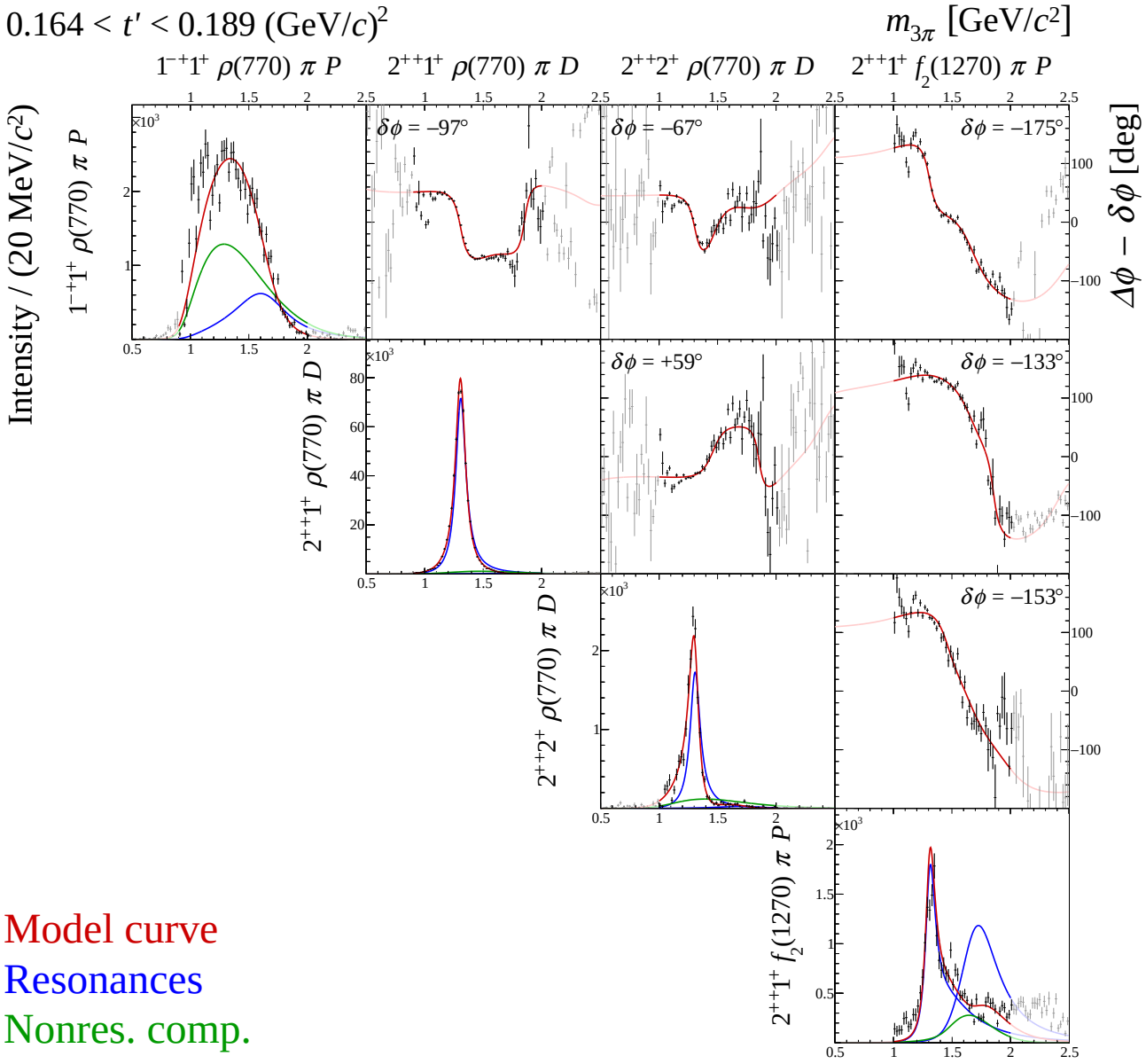

FIG. 105: Submatrix E of the 14 × 14 matrix of graphs that represents the spin-density matrix (see Table 8).

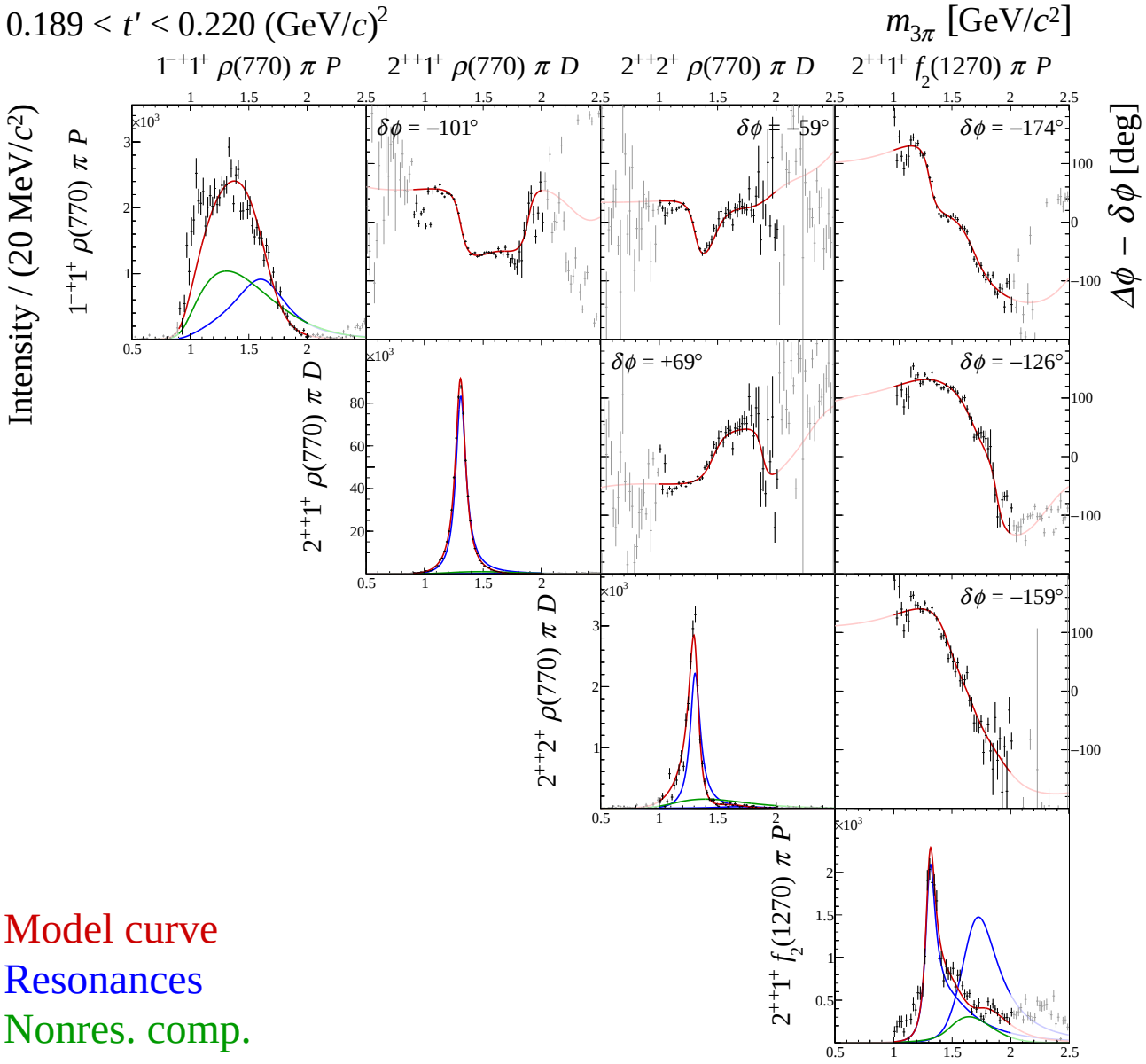

FIG. 106: Submatrix E of the 14 × 14 matrix of graphs that represents the spin-density matrix (see Table 8).

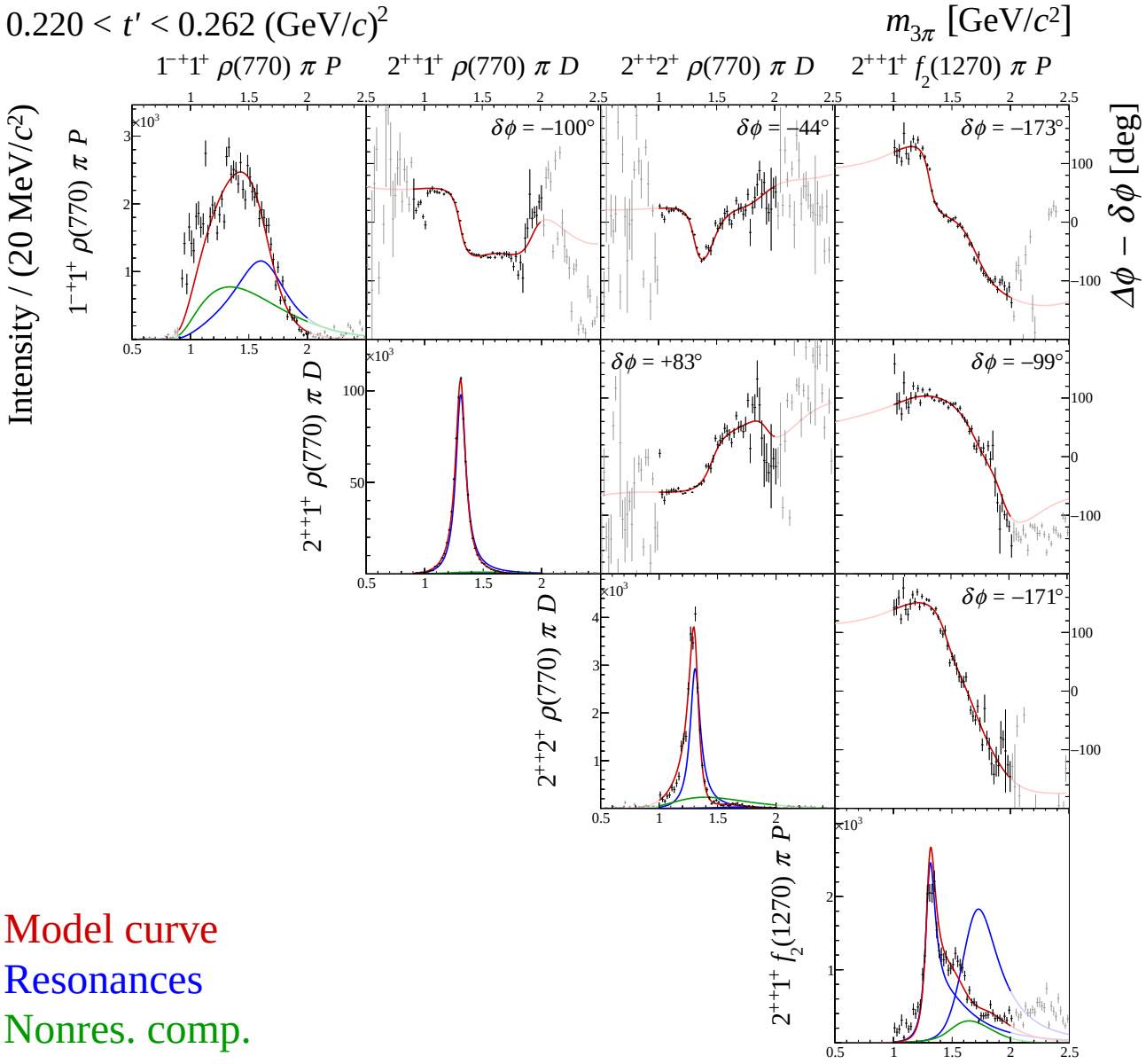

FIG. 107: Submatrix E of the 14 × 14 matrix of graphs that represents the spin-density matrix (see Table 8).

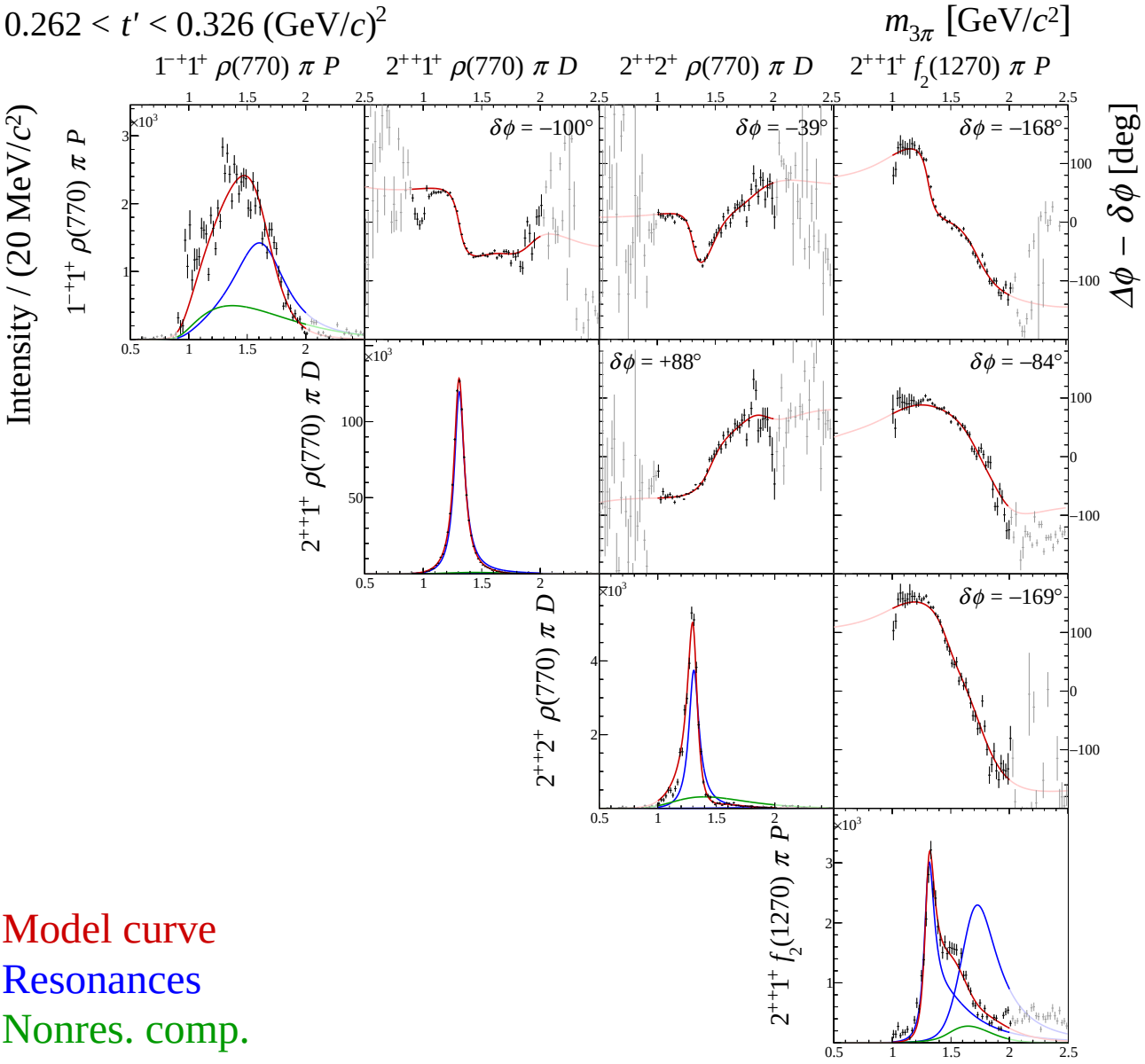

FIG. 108: Submatrix E of the 14 × 14 matrix of graphs that represents the spin-density matrix (see Table 8).

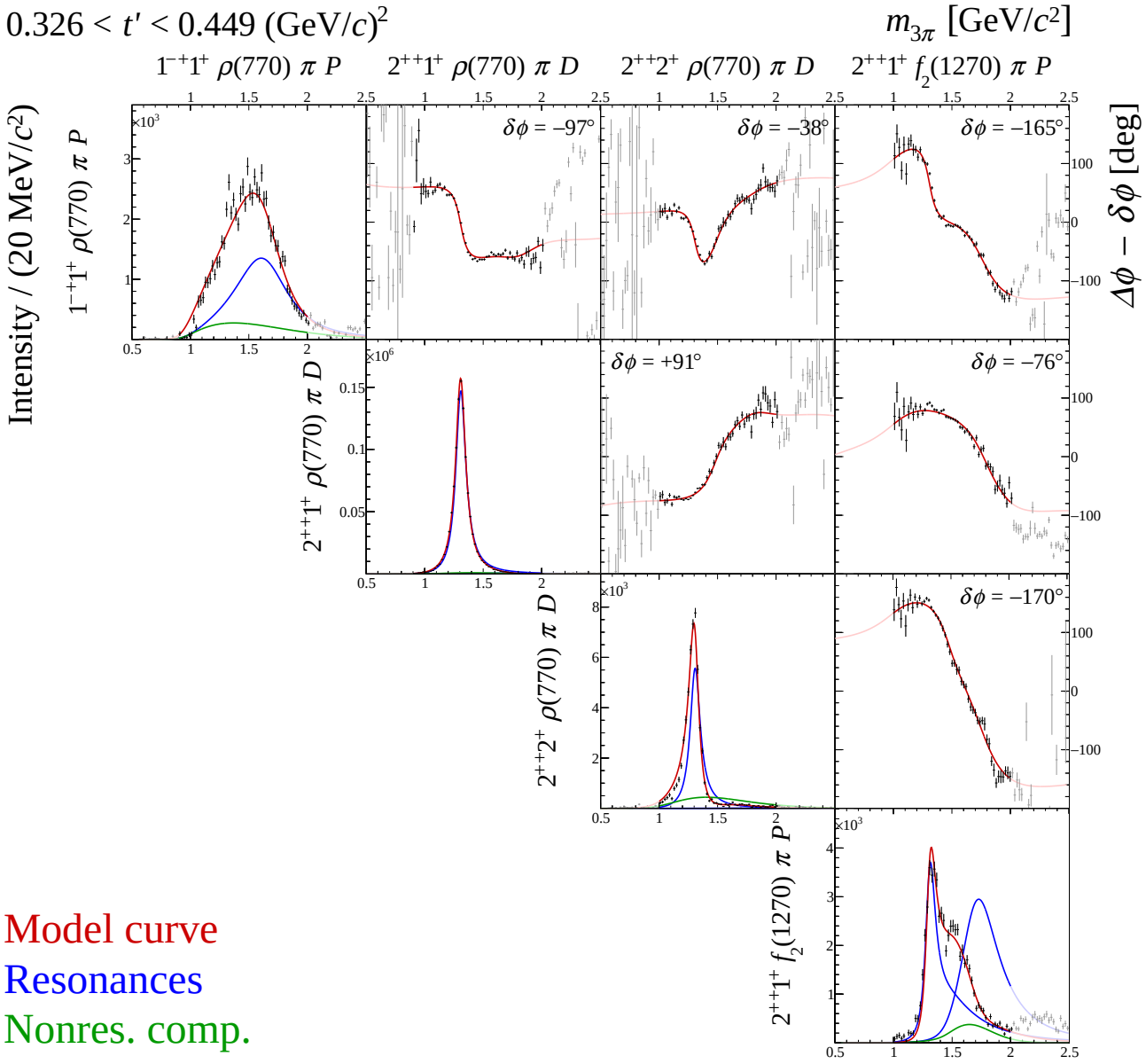

FIG. 109: Submatrix E of the 14 × 14 matrix of graphs that represents the spin-density matrix (see Table 8).

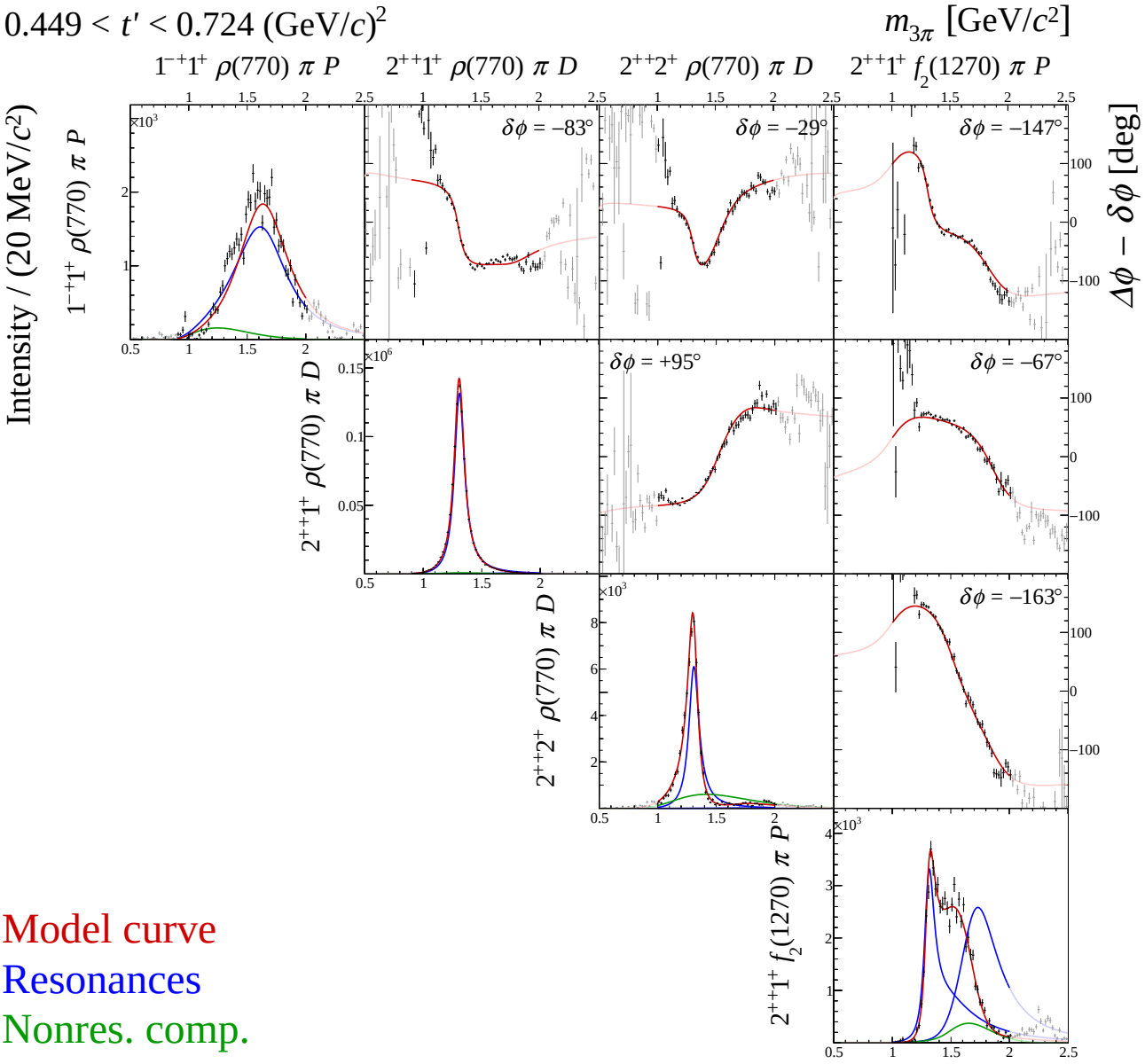

FIG. 110: Submatrix E of the 14 × 14 matrix of graphs that represents the spin-density matrix (see Table 8).

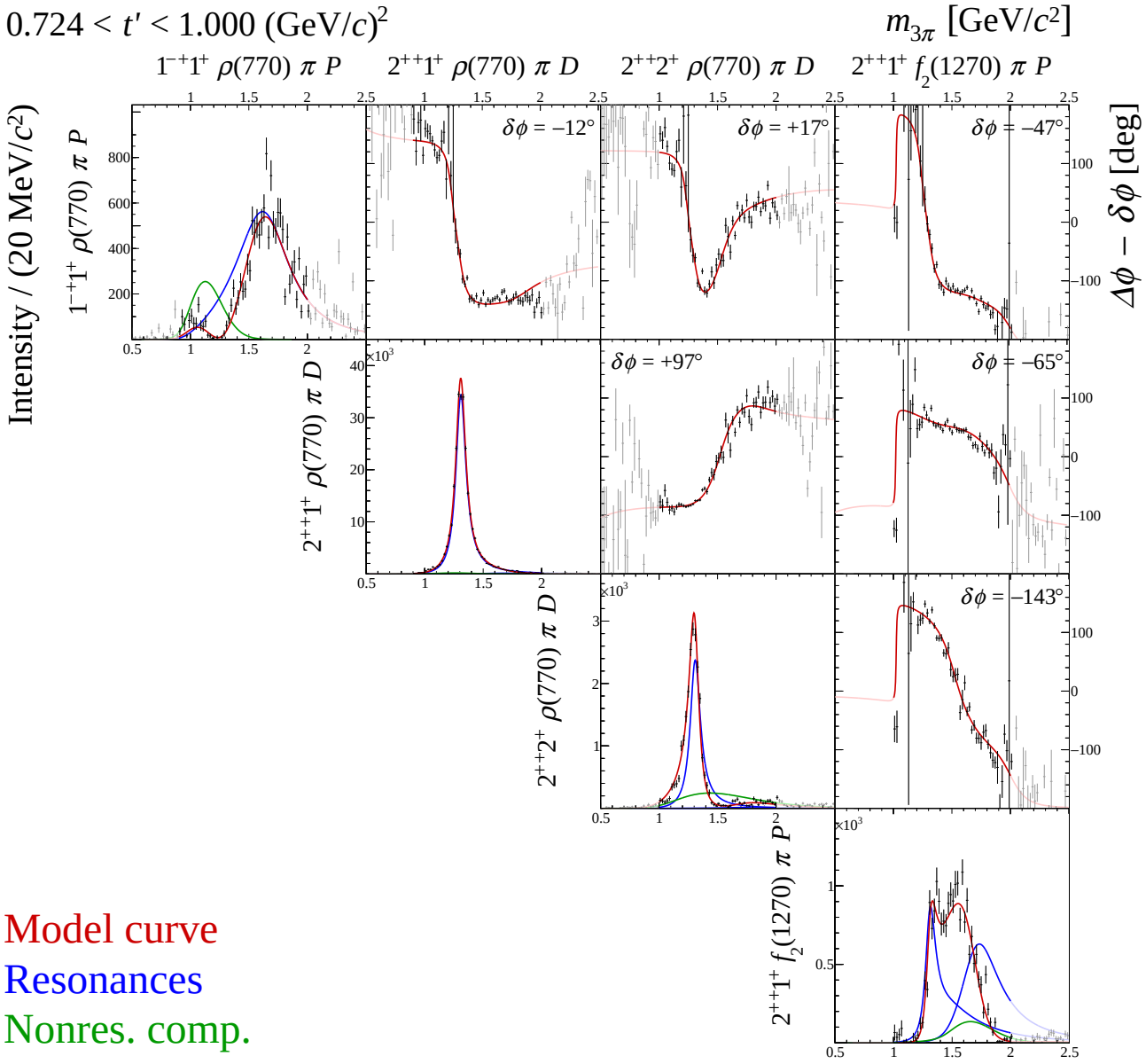

FIG. 111: Submatrix E of the 14 × 14 matrix of graphs that represents the spin-density matrix (see Table 8).

6 Submatrix F

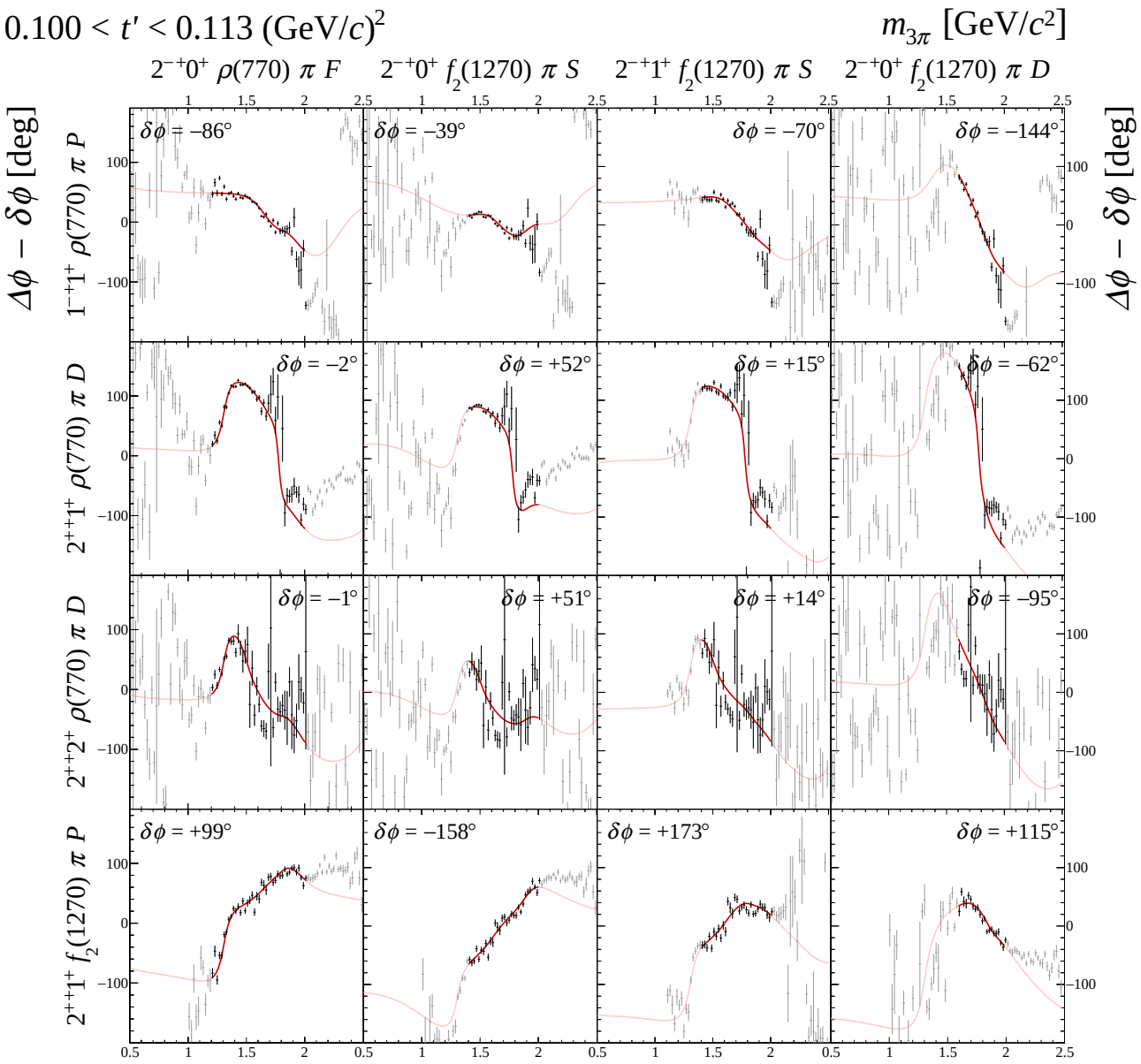

FIG. 112: Submatrix F of the 14 × 14 matrix of graphs that represents the spin-density matrix (see Table 8).

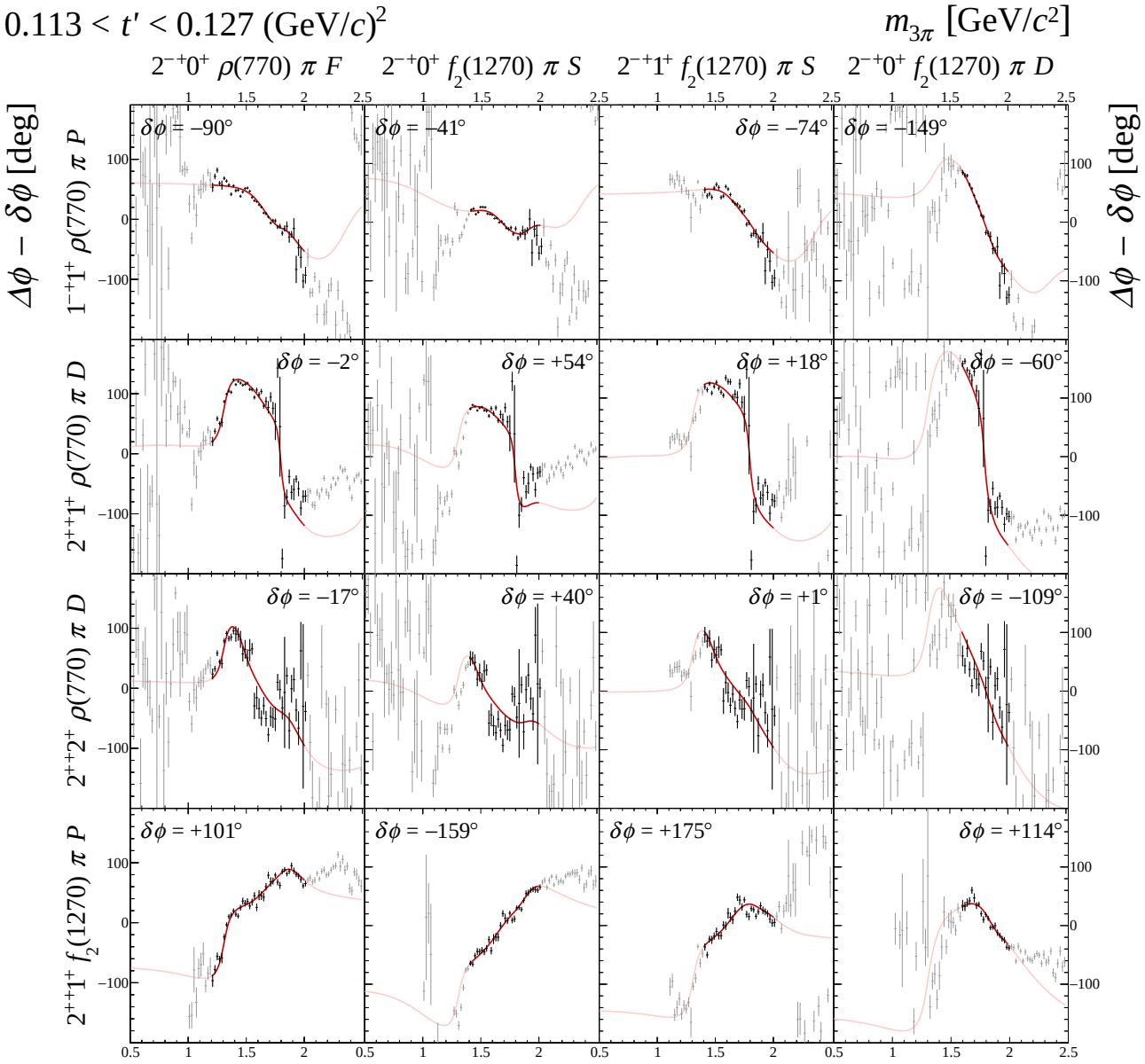

FIG. 113: Submatrix F of the 14 × 14 matrix of graphs that represents the spin-density matrix (see Table 8).

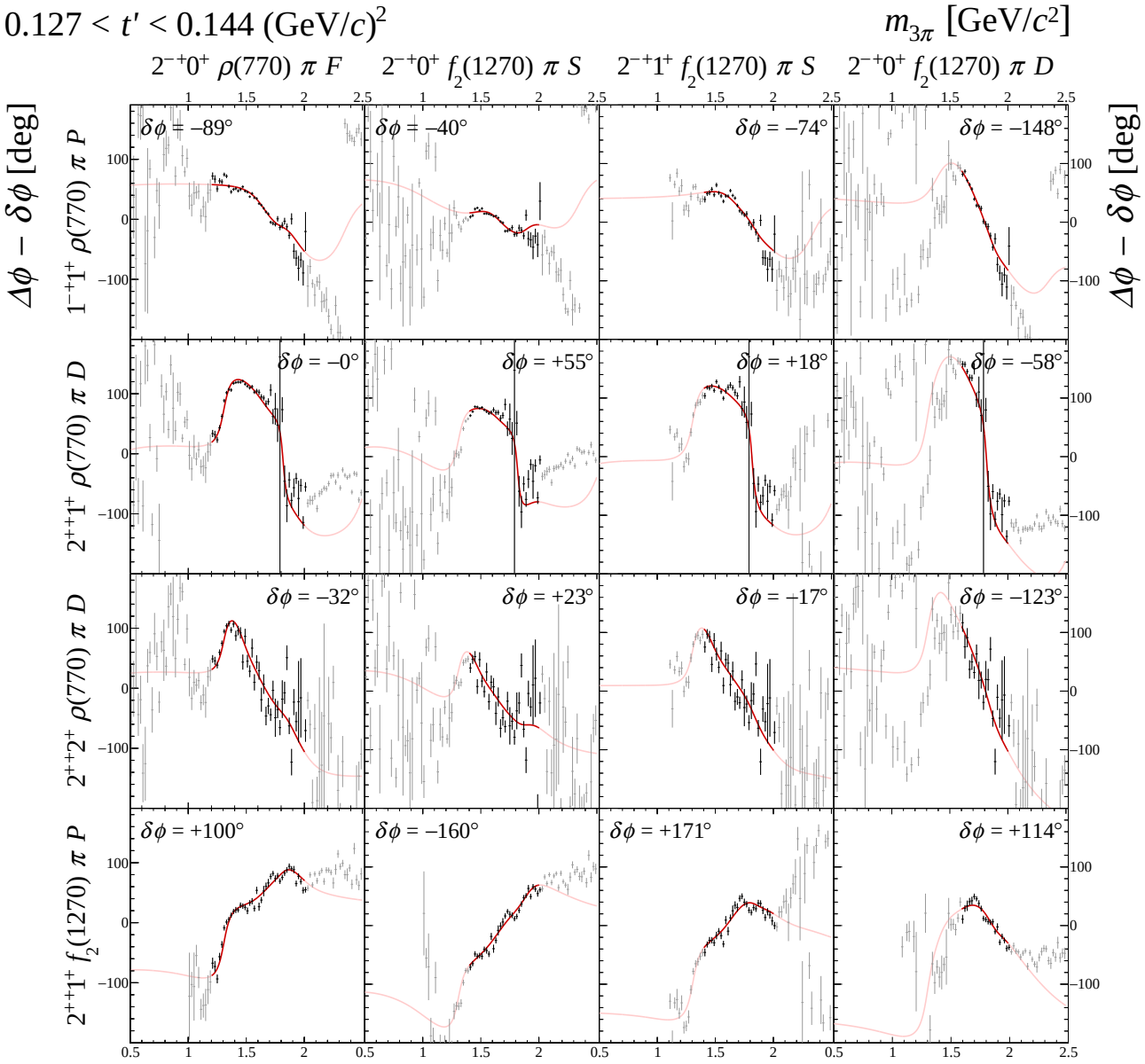

FIG. 114: Submatrix F of the 14 × 14 matrix of graphs that represents the spin-density matrix (see Table 8).

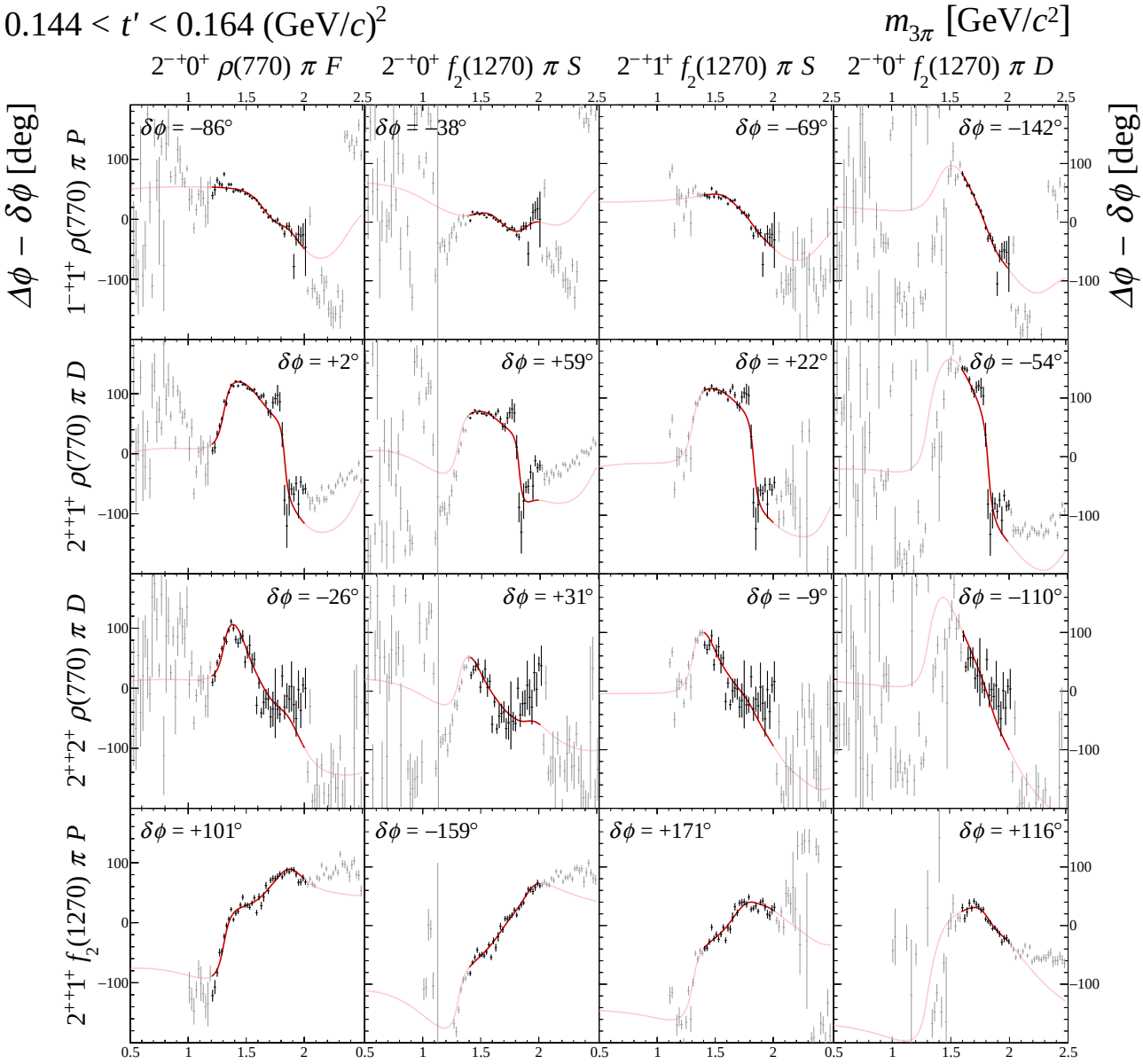

FIG. 115: Submatrix F of the 14 × 14 matrix of graphs that represents the spin-density matrix (see Table 8).

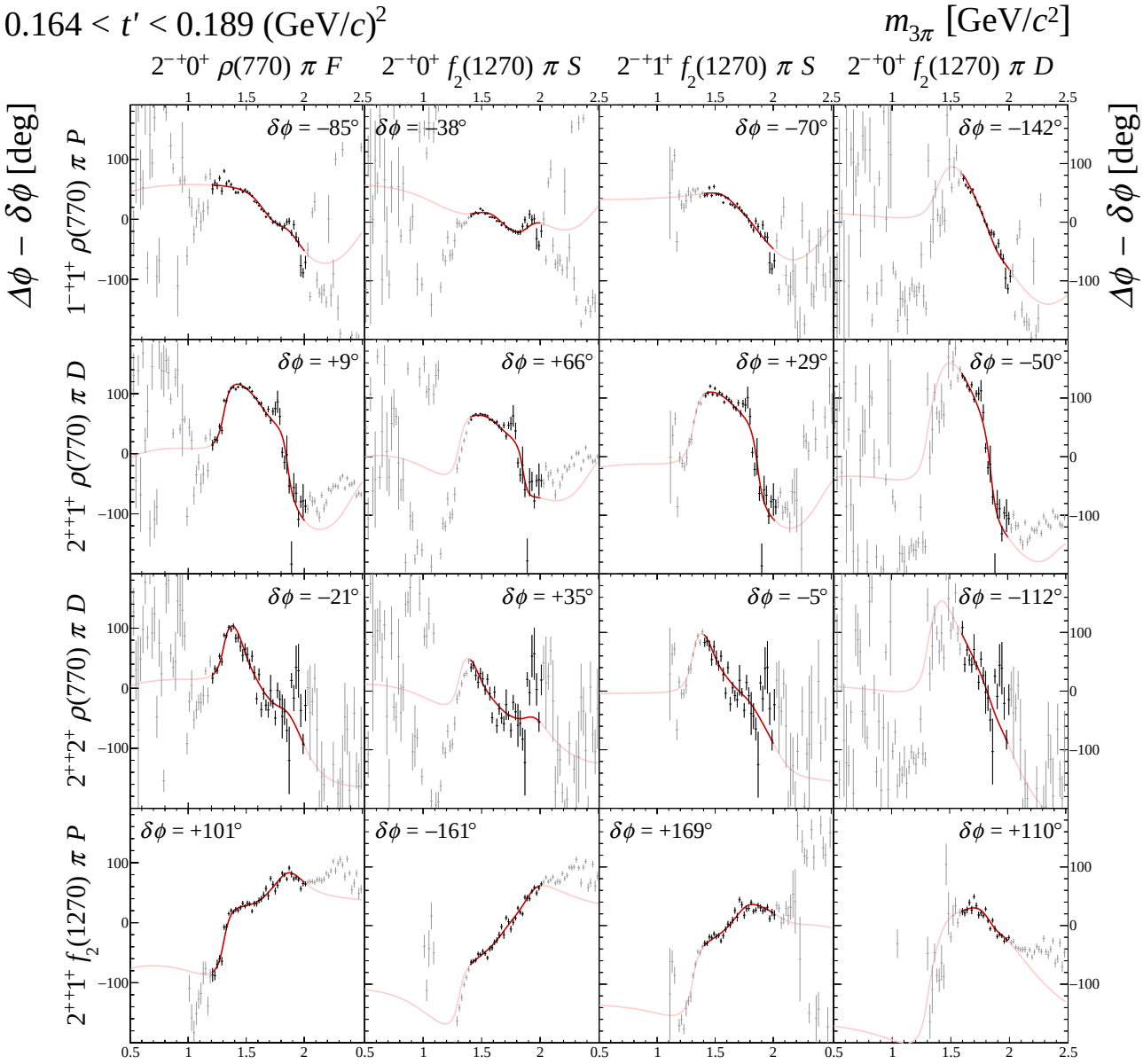

FIG. 116: Submatrix F of the 14 × 14 matrix of graphs that represents the spin-density matrix (see Table 8).

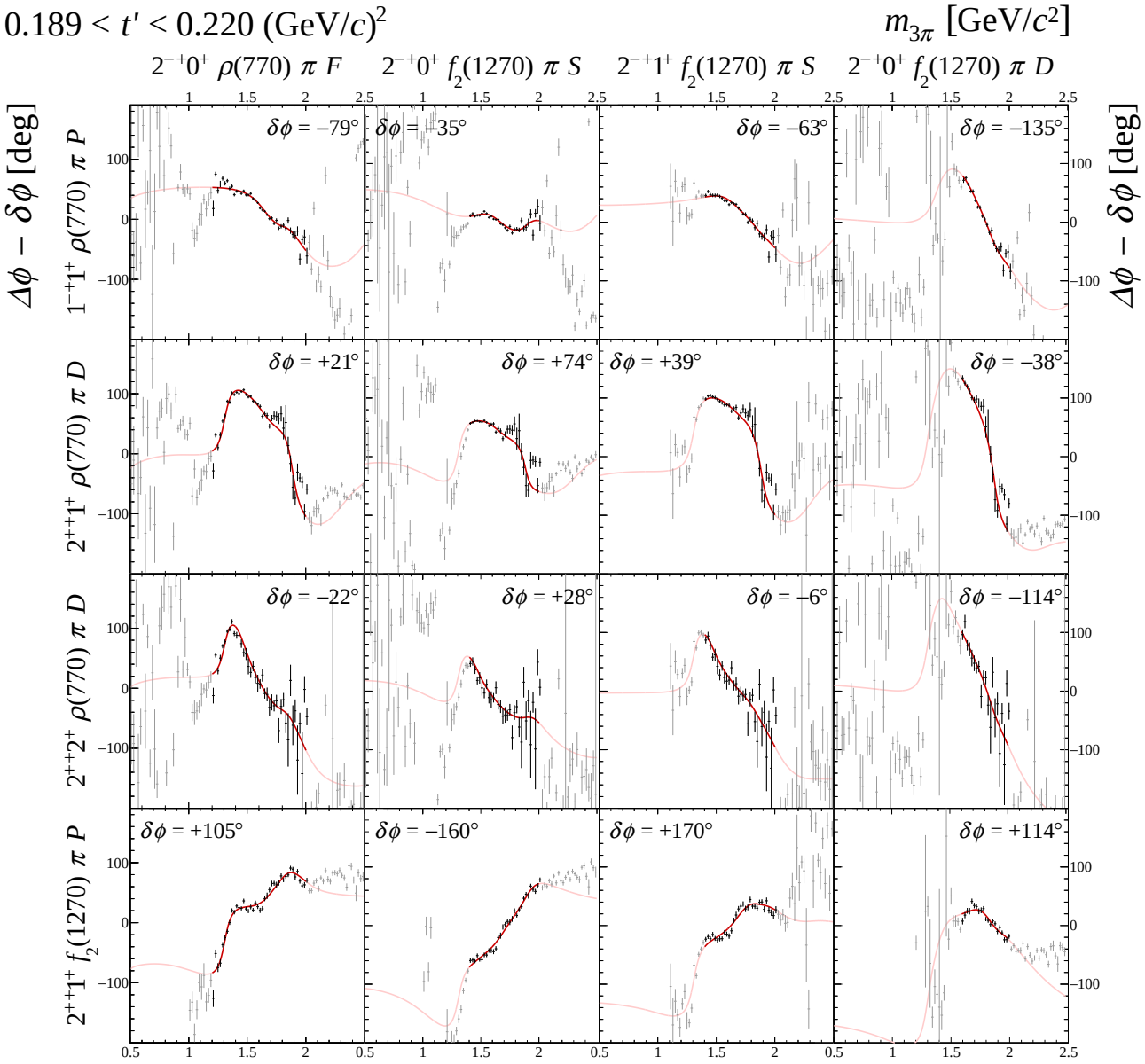

FIG. 117: Submatrix F of the 14 × 14 matrix of graphs that represents the spin-density matrix (see Table 8).

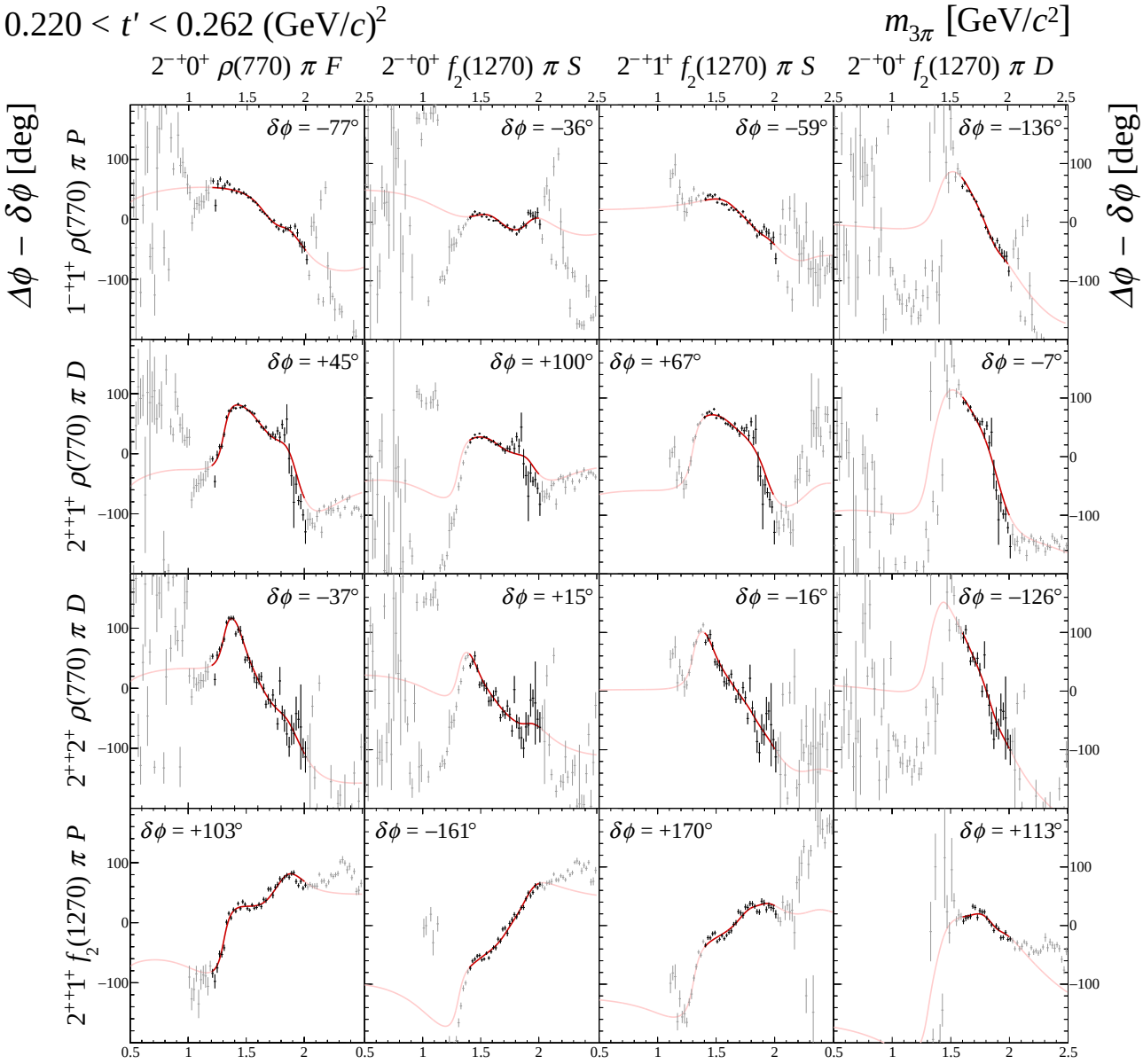

FIG. 118: Submatrix F of the 14 × 14 matrix of graphs that represents the spin-density matrix (see Table 8).

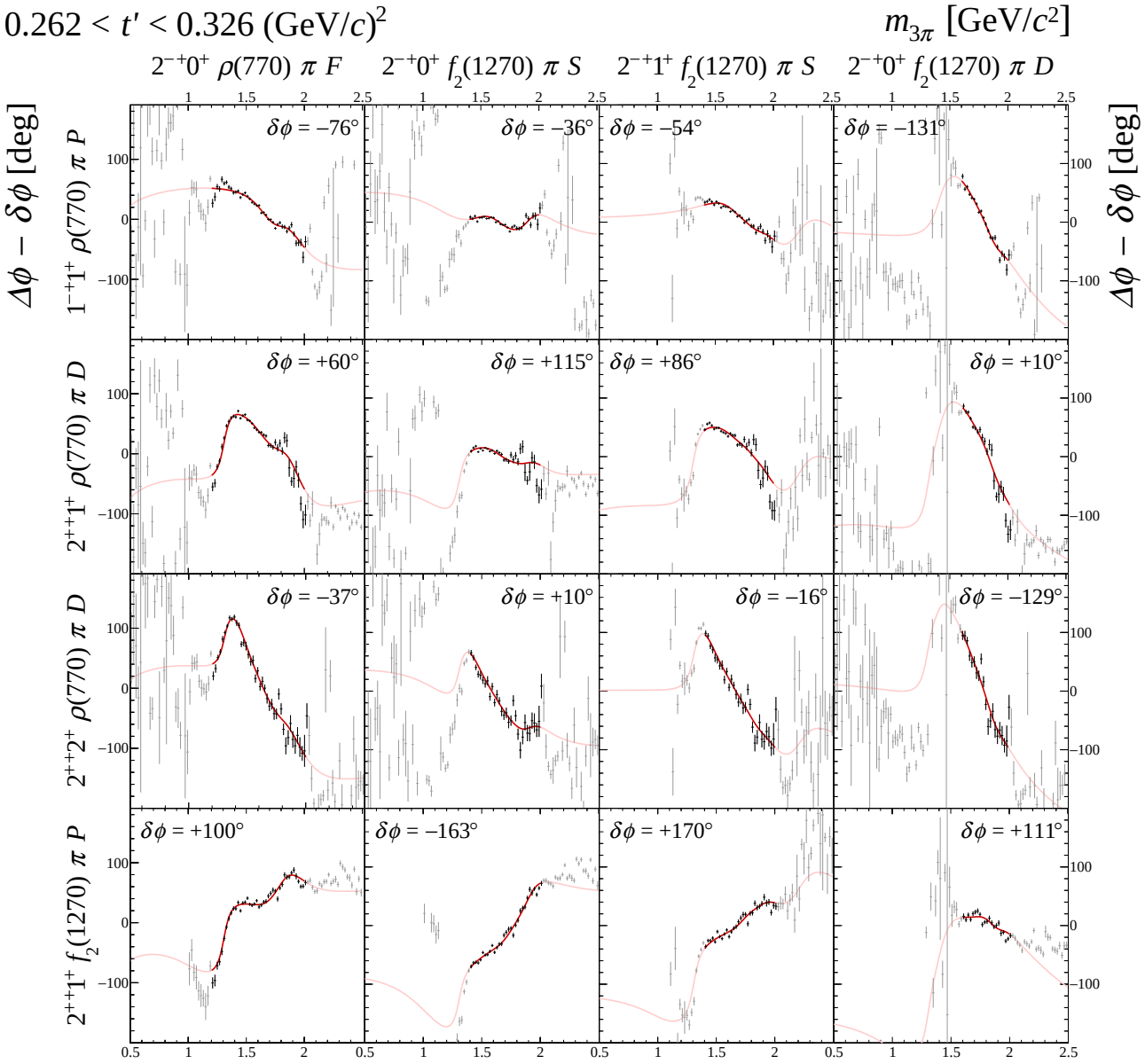

FIG. 119: Submatrix F of the 14 × 14 matrix of graphs that represents the spin-density matrix (see Table 8).

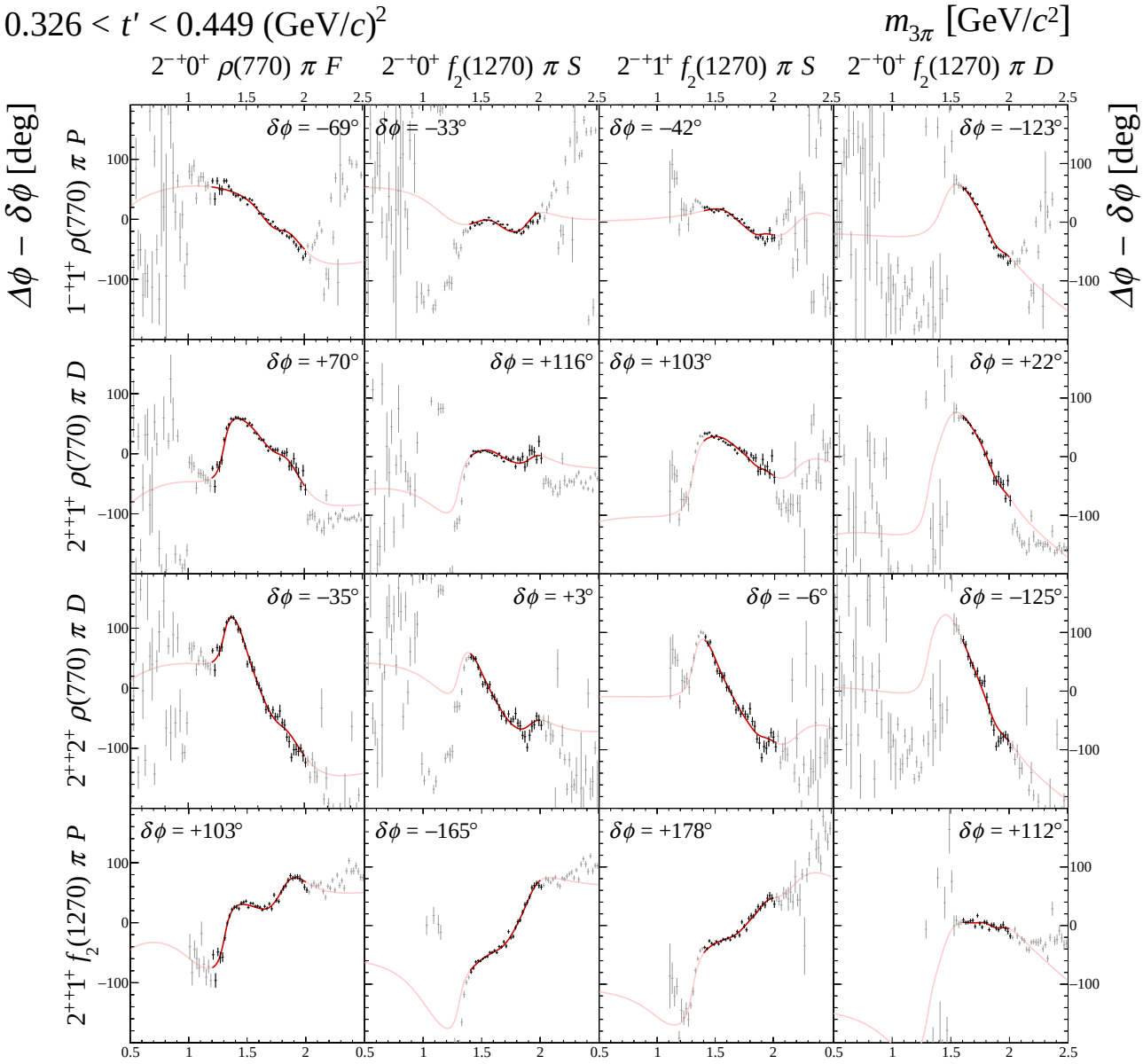

FIG. 120: Submatrix F of the 14 × 14 matrix of graphs that represents the spin-density matrix (see Table 8).

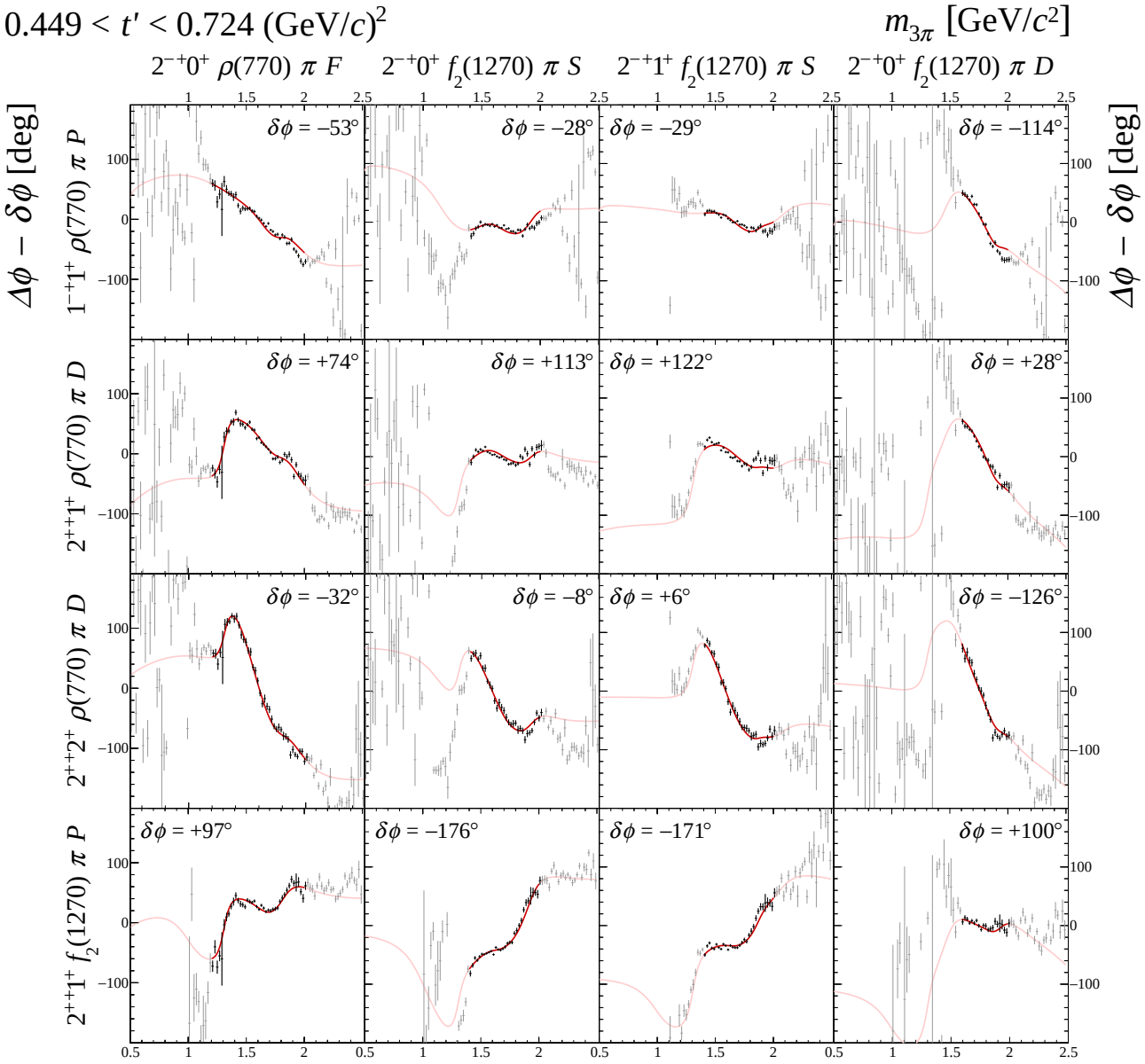

FIG. 121: Submatrix F of the 14 × 14 matrix of graphs that represents the spin-density matrix (see Table 8).

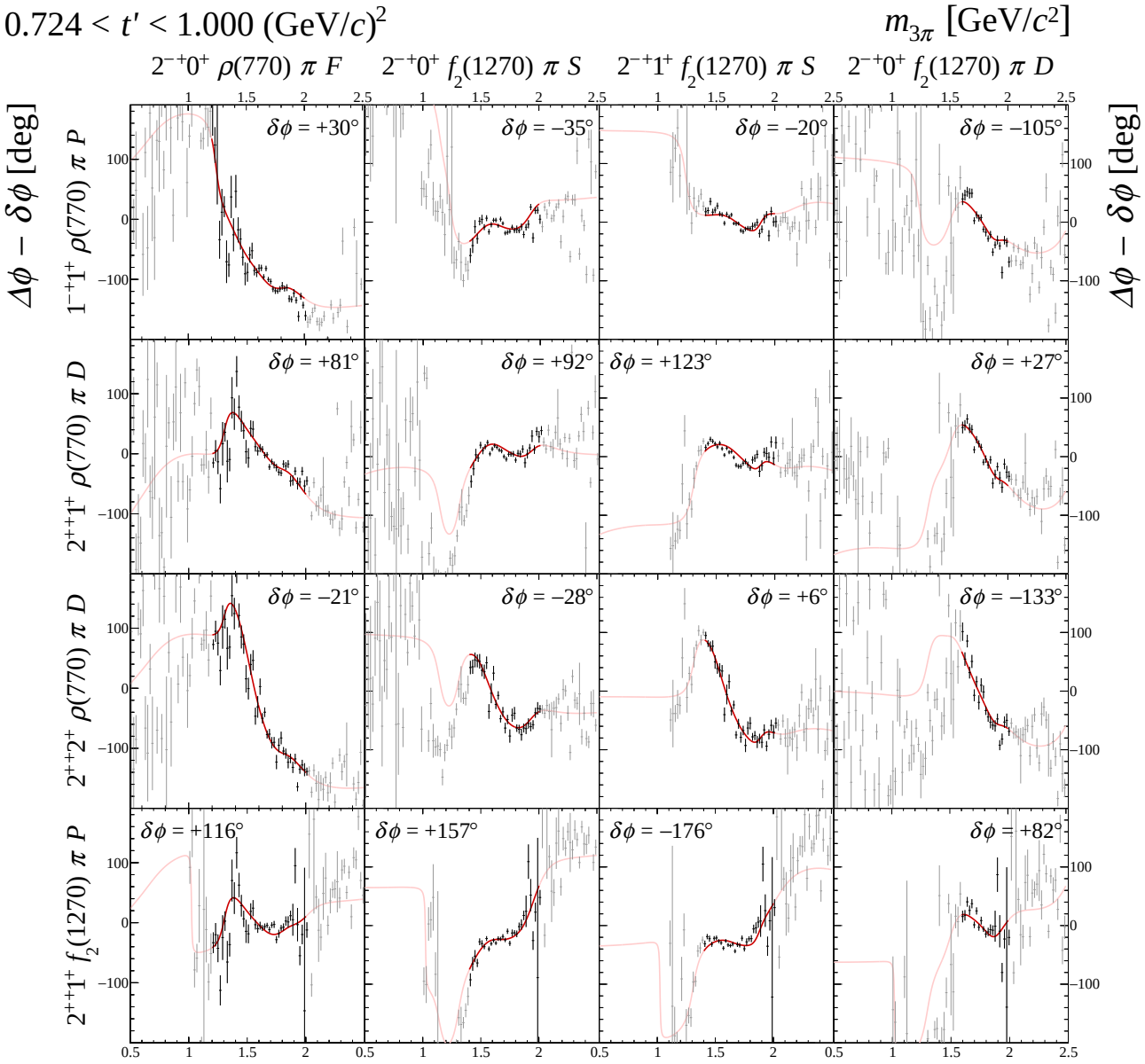

FIG. 122: Submatrix F of the 14 × 14 matrix of graphs that represents the spin-density matrix (see Table 8).

7 Submatrix G

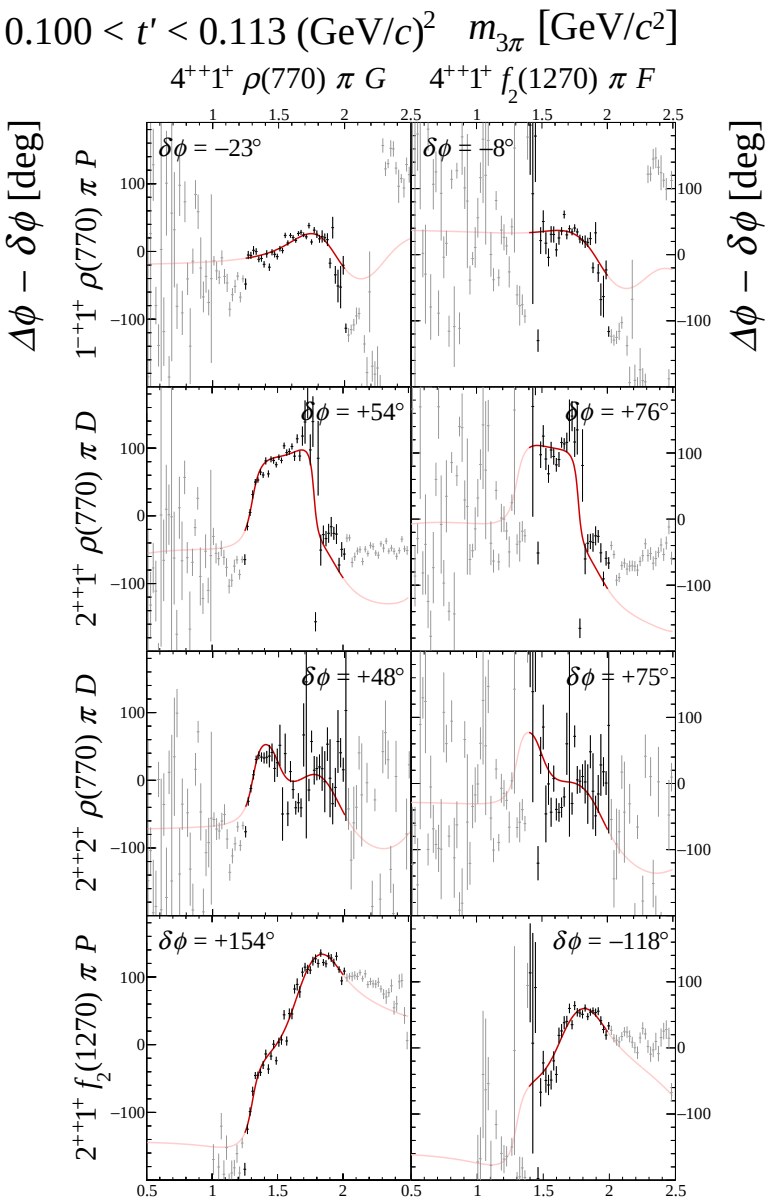

FIG. 123: Submatrix G of the 14 × 14 matrix of graphs that represents the spin-density matrix (see Table 8).

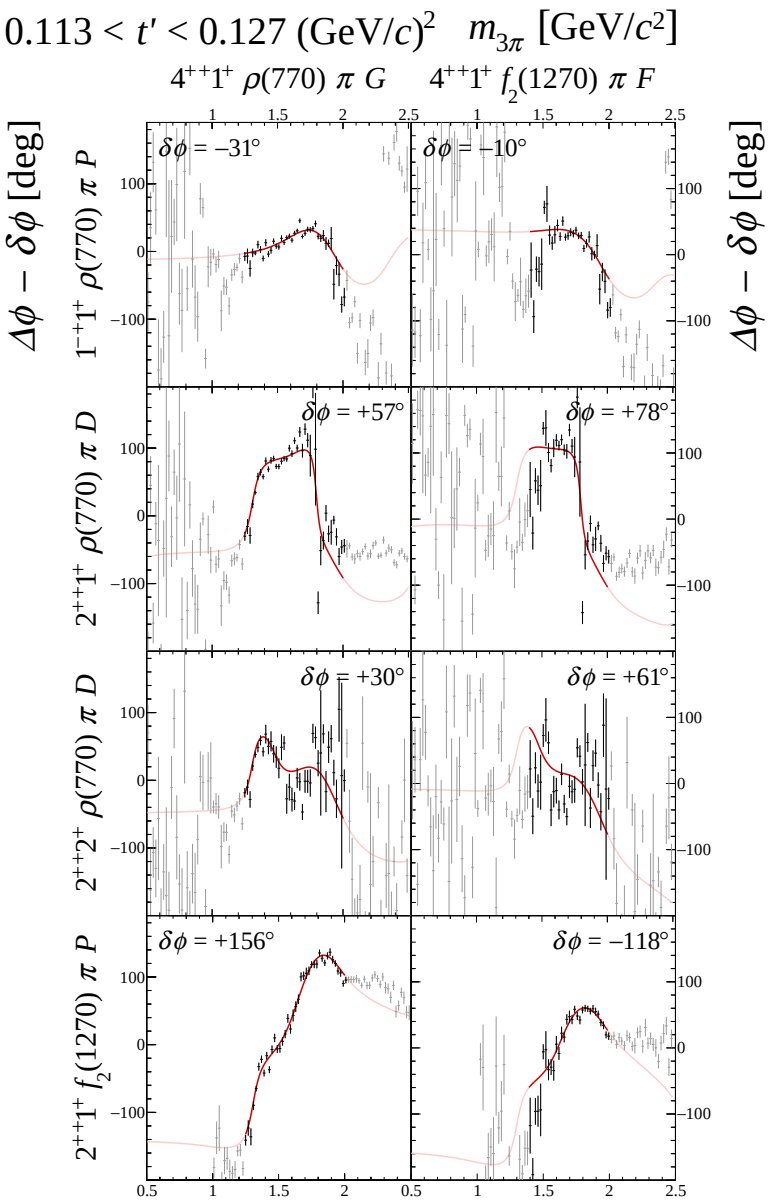

FIG. 124: Submatrix G of the 14 × 14 matrix of graphs that represents the spin-density matrix (see Table 8).

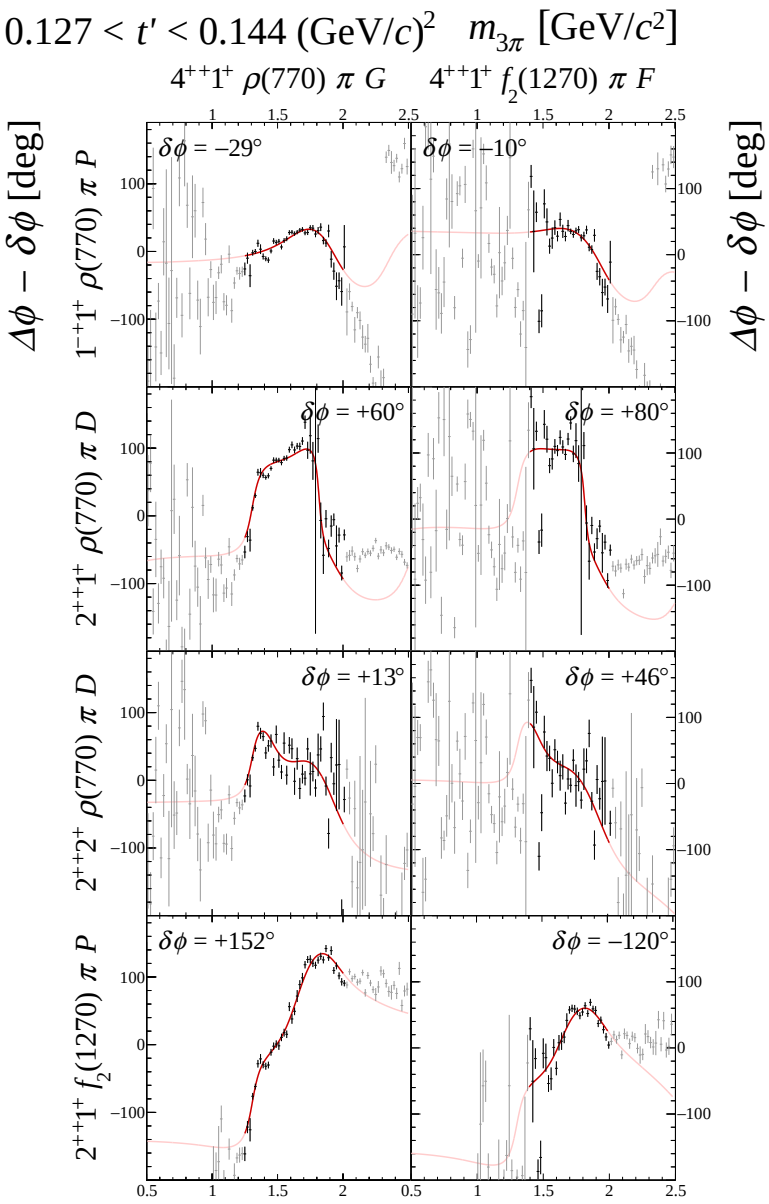

FIG. 125: Submatrix G of the 14 × 14 matrix of graphs that represents the spin-density matrix (see Table 8).

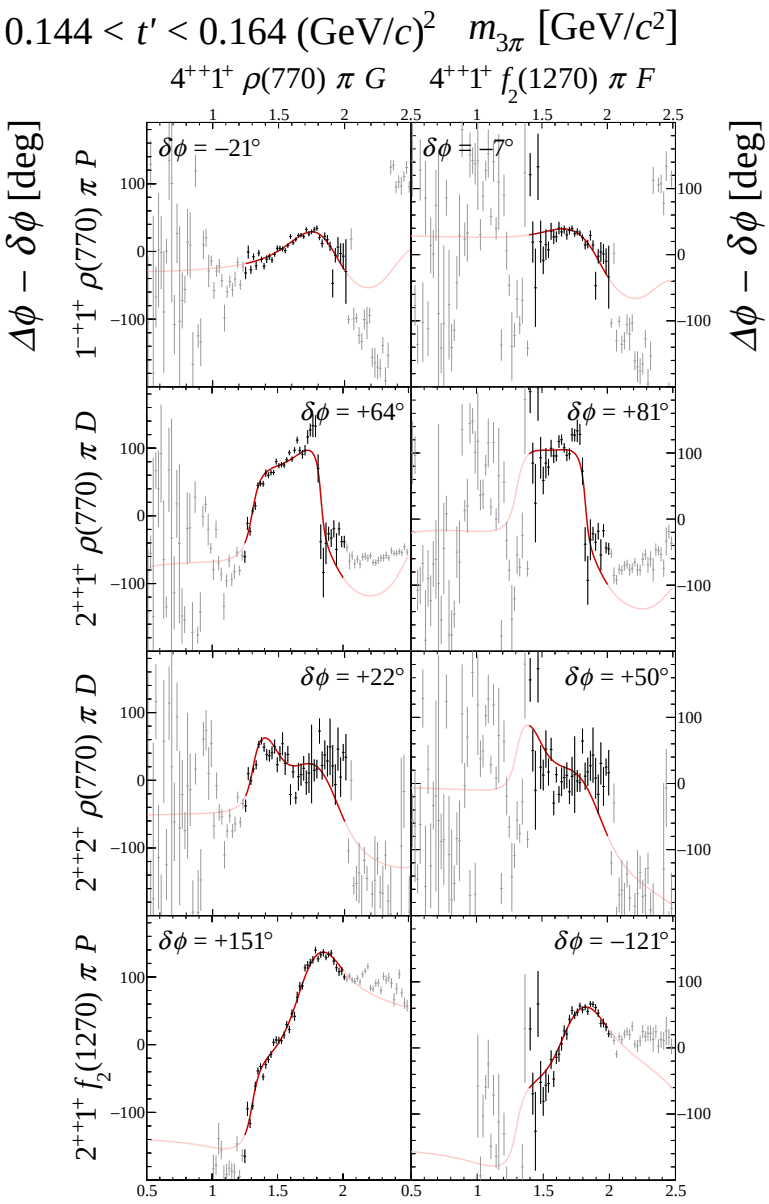

FIG. 126: Submatrix G of the 14 × 14 matrix of graphs that represents the spin-density matrix (see Table 8).

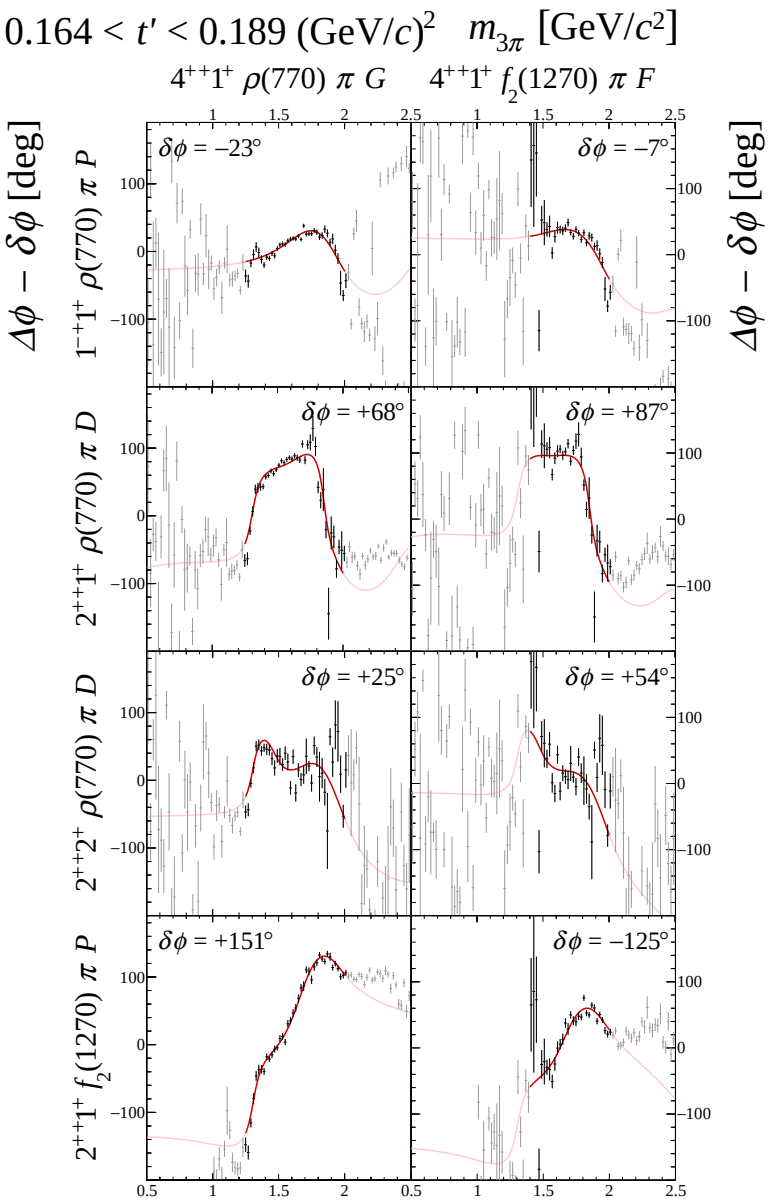

FIG. 127: Submatrix G of the 14 × 14 matrix of graphs that represents the spin-density matrix (see Table 8).

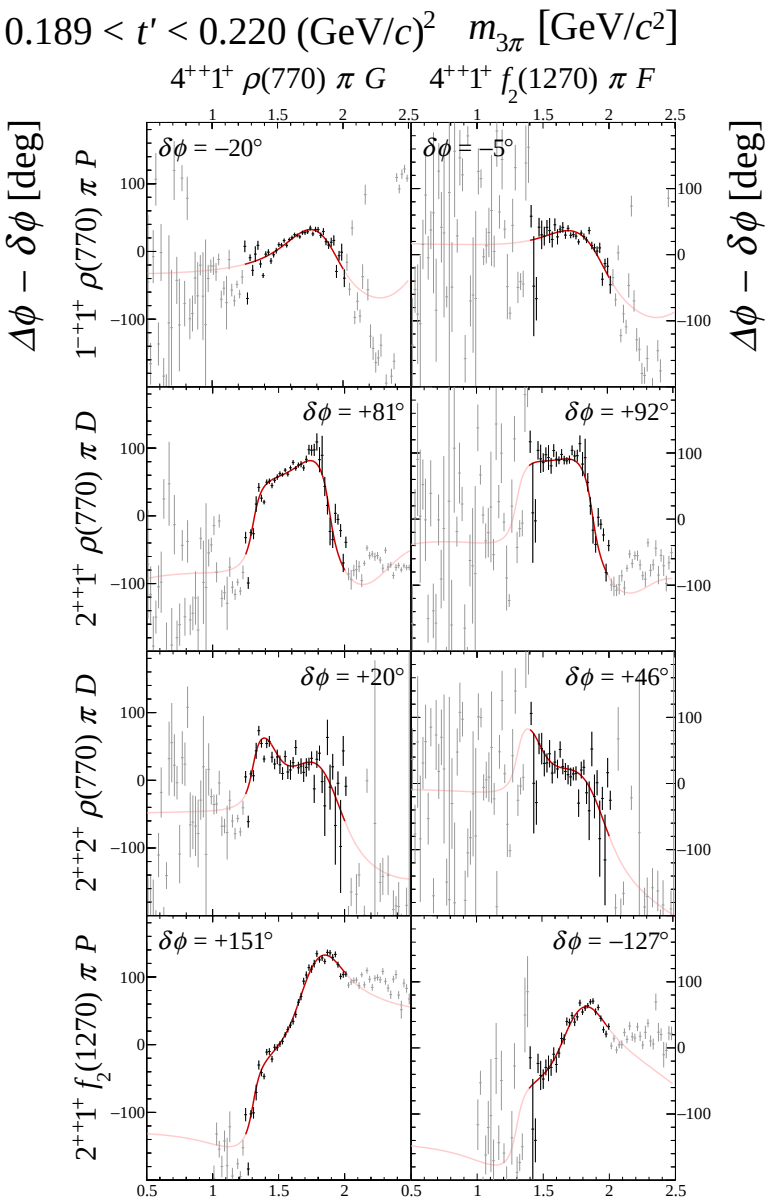

FIG. 128: Submatrix G of the 14 × 14 matrix of graphs that represents the spin-density matrix (see Table 8).

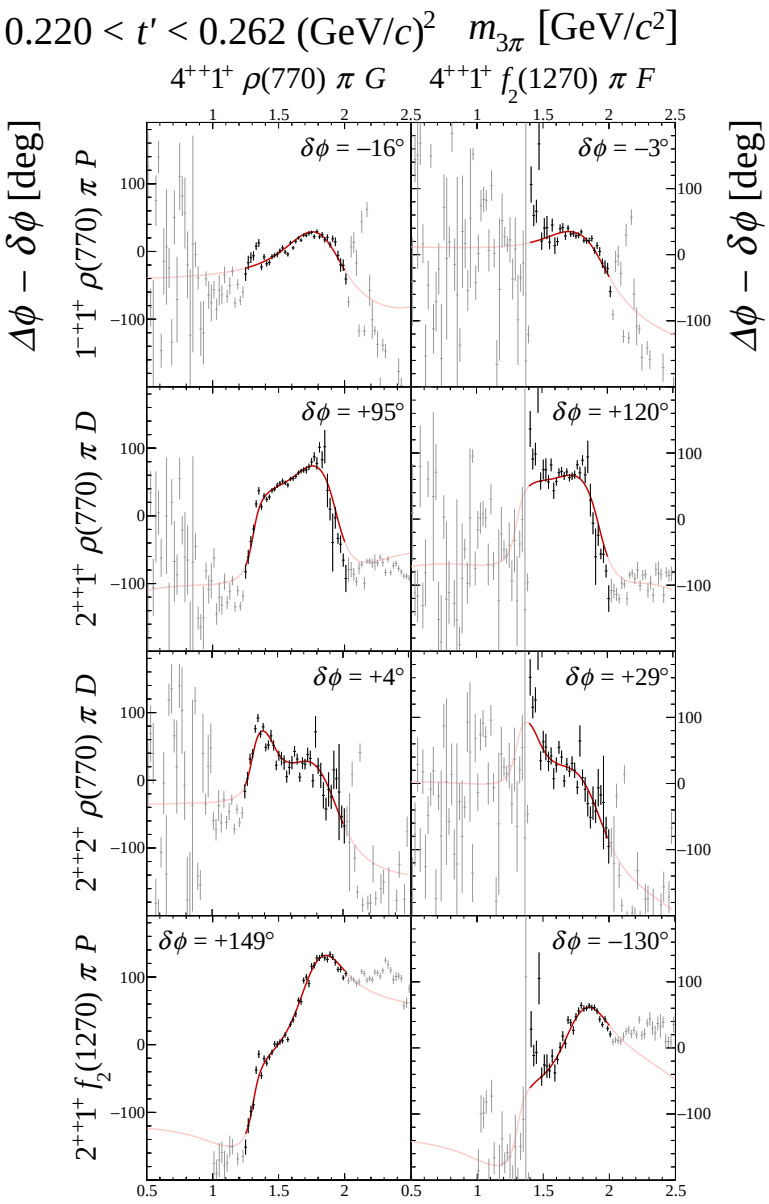

FIG. 129: Submatrix G of the 14 × 14 matrix of graphs that represents the spin-density matrix (see Table 8).

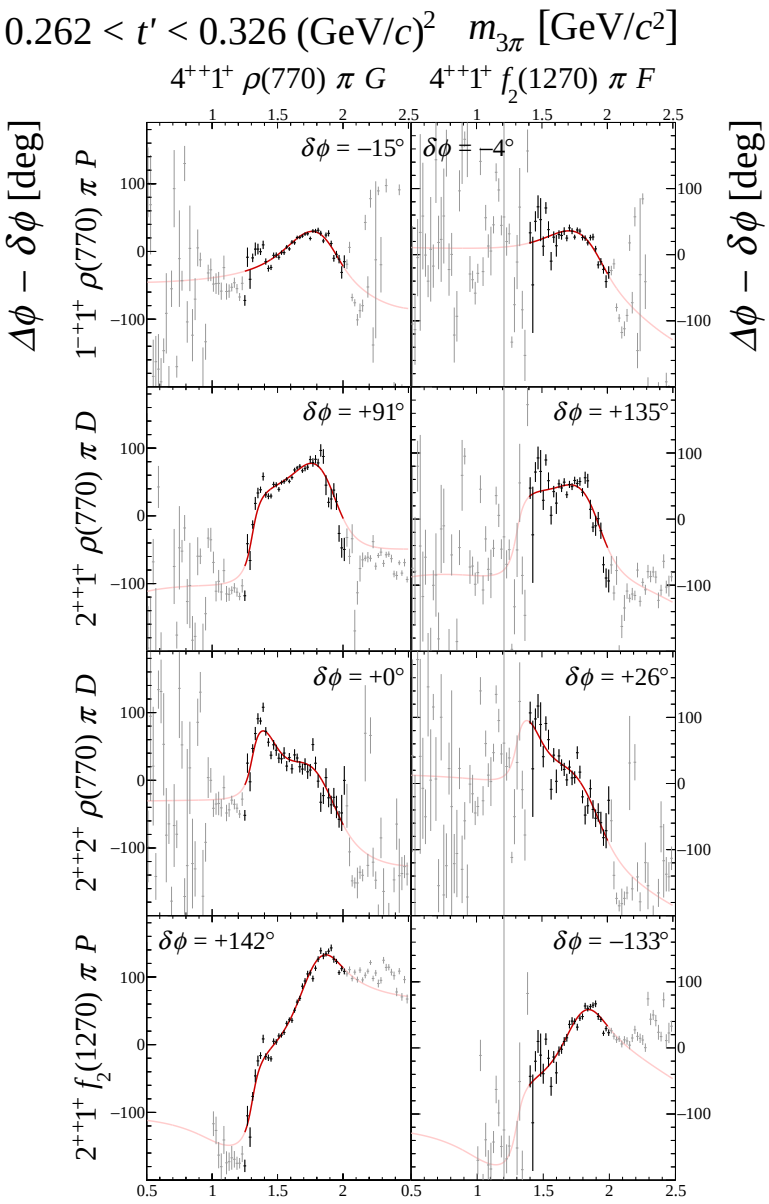

FIG. 130: Submatrix G of the 14 × 14 matrix of graphs that represents the spin-density matrix (see Table 8).

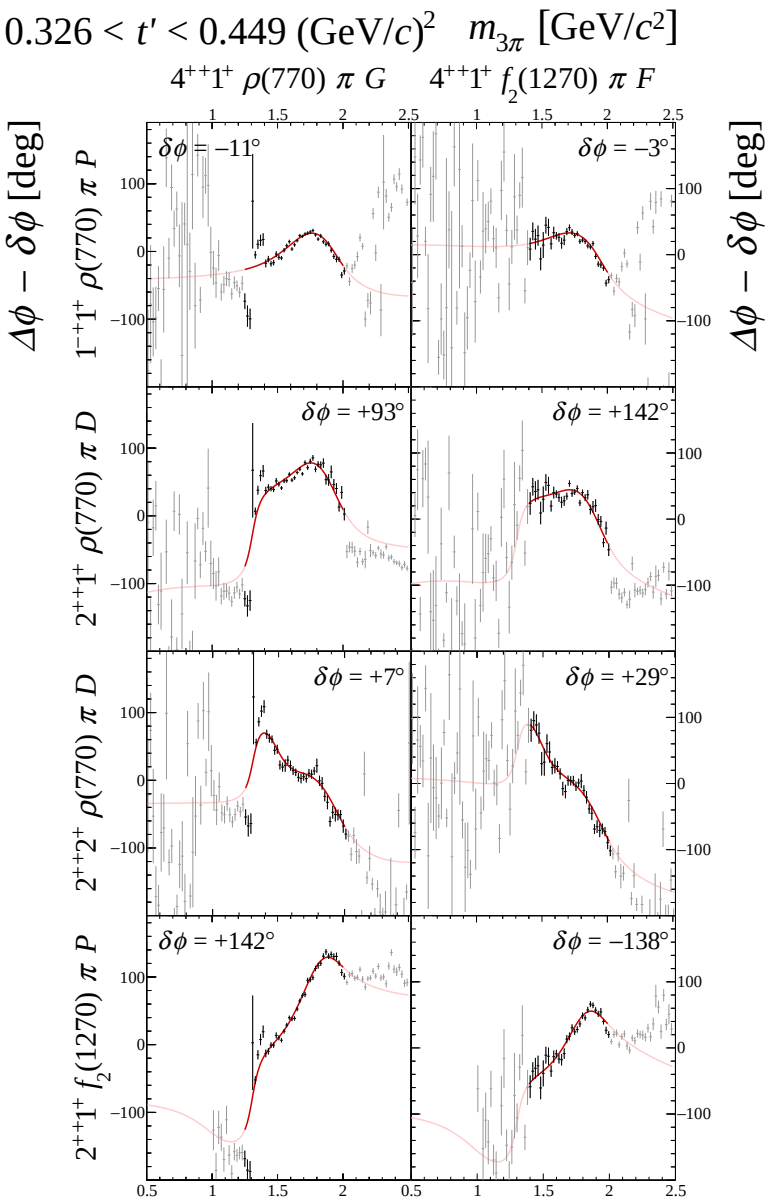

FIG. 131: Submatrix G of the 14 × 14 matrix of graphs that represents the spin-density matrix (see Table 8).

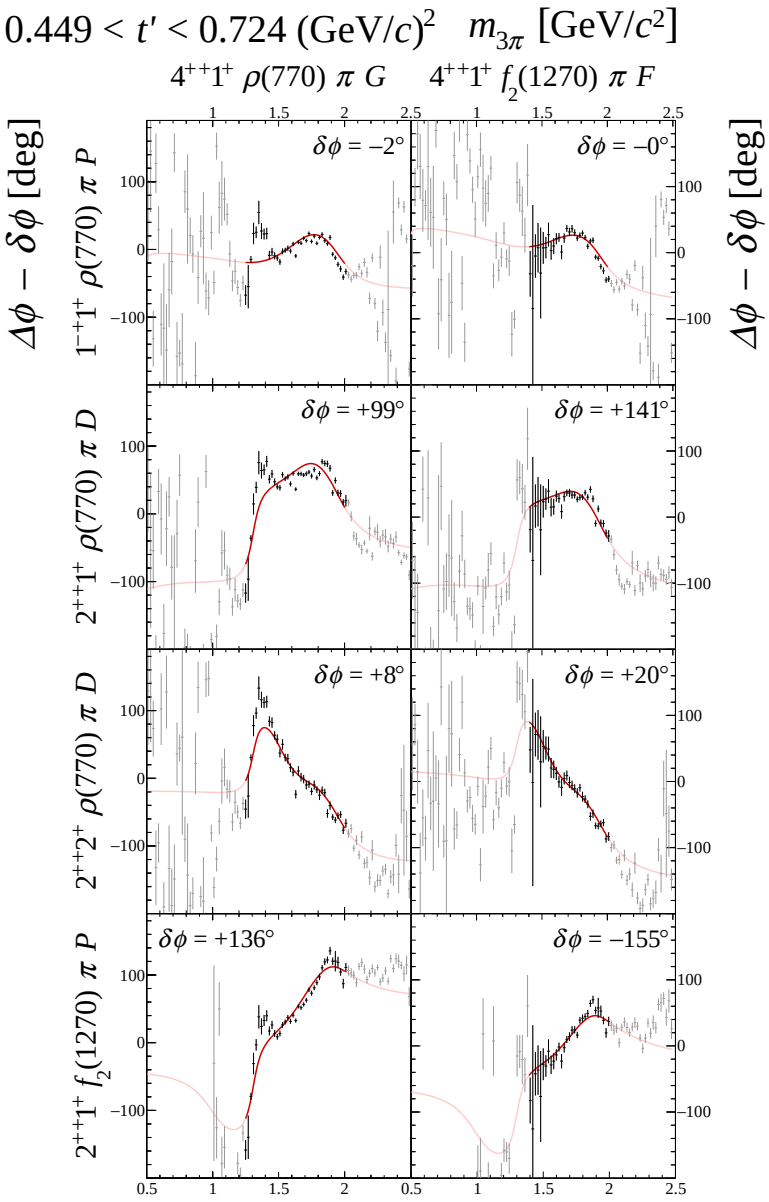

FIG. 132: Submatrix G of the 14 × 14 matrix of graphs that represents the spin-density matrix (see Table 8).

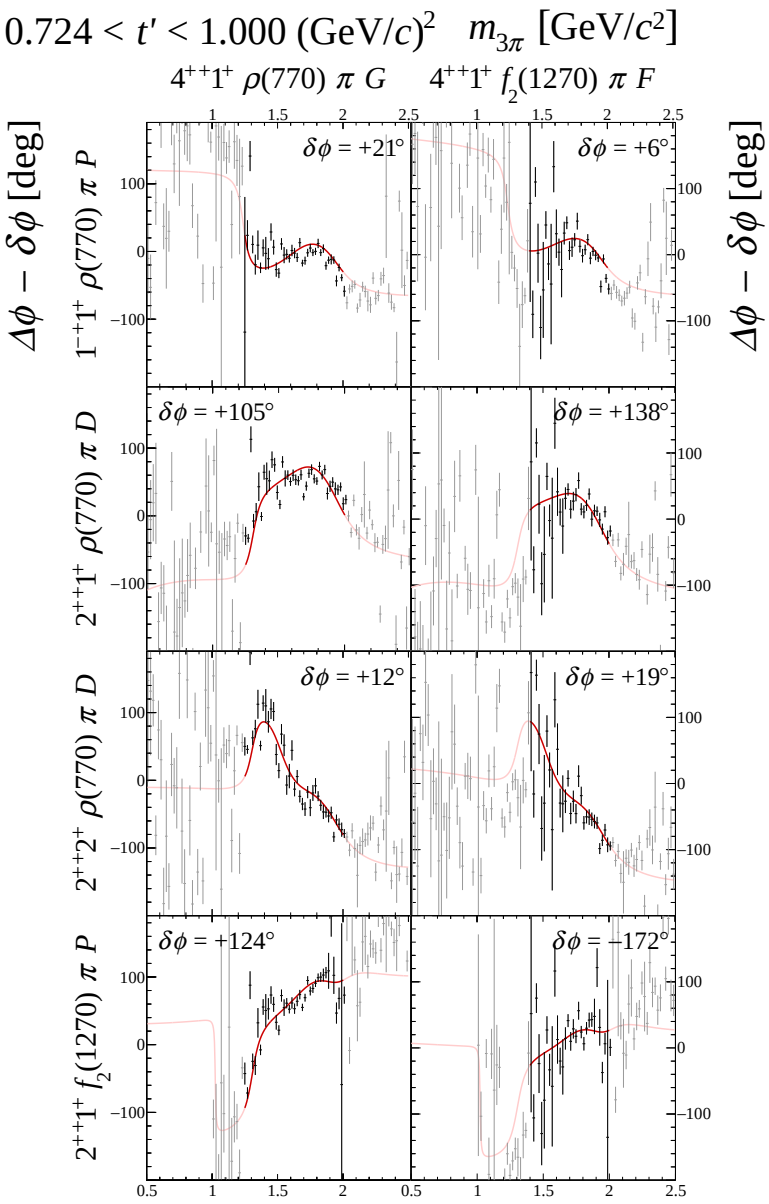

FIG. 133: Submatrix G of the 14 × 14 matrix of graphs that represents the spin-density matrix (see Table 8).

8 Submatrix H

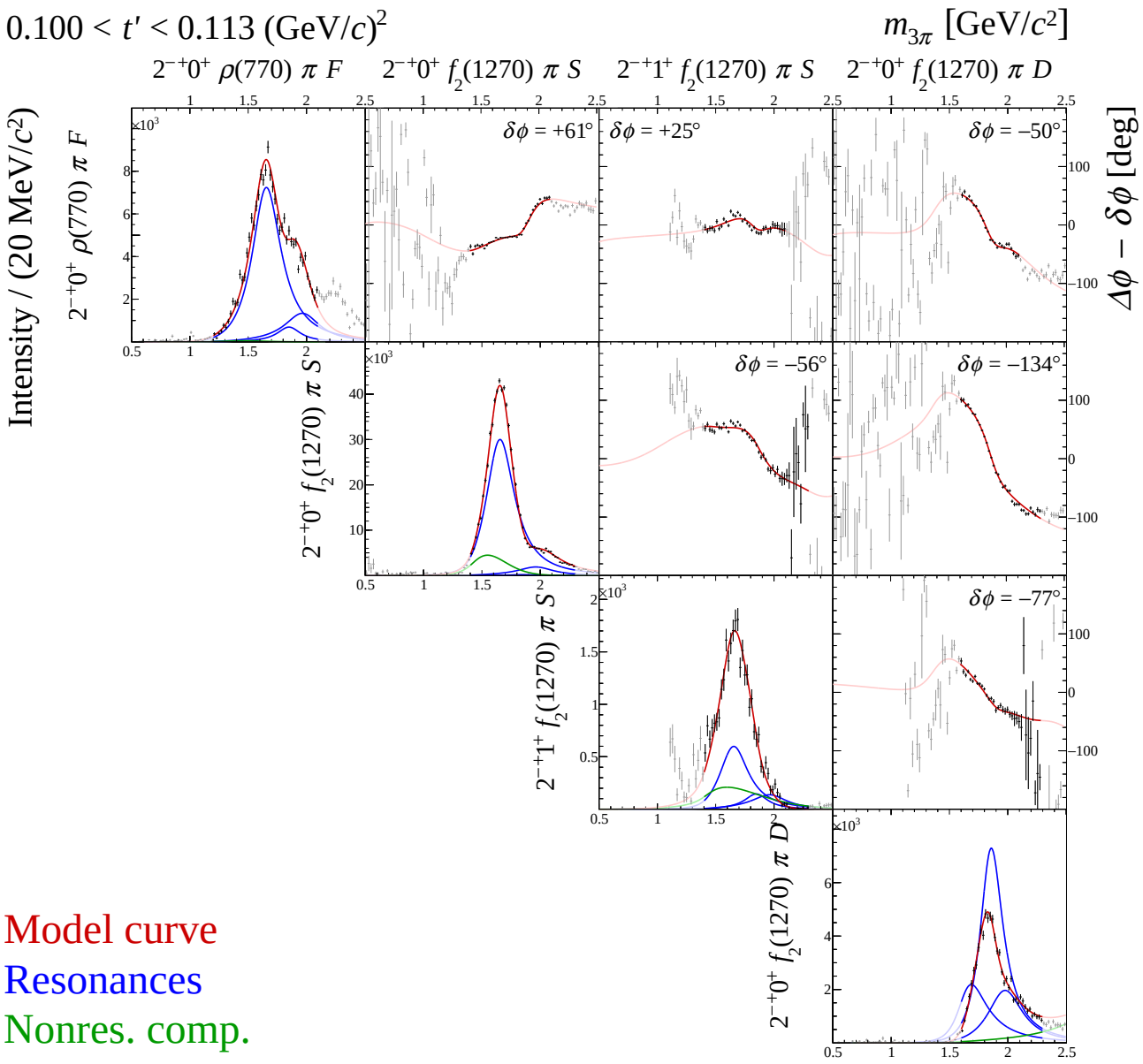

FIG. 134: Submatrix H of the 14 × 14 matrix of graphs that represents the spin-density matrix (see Table 8).

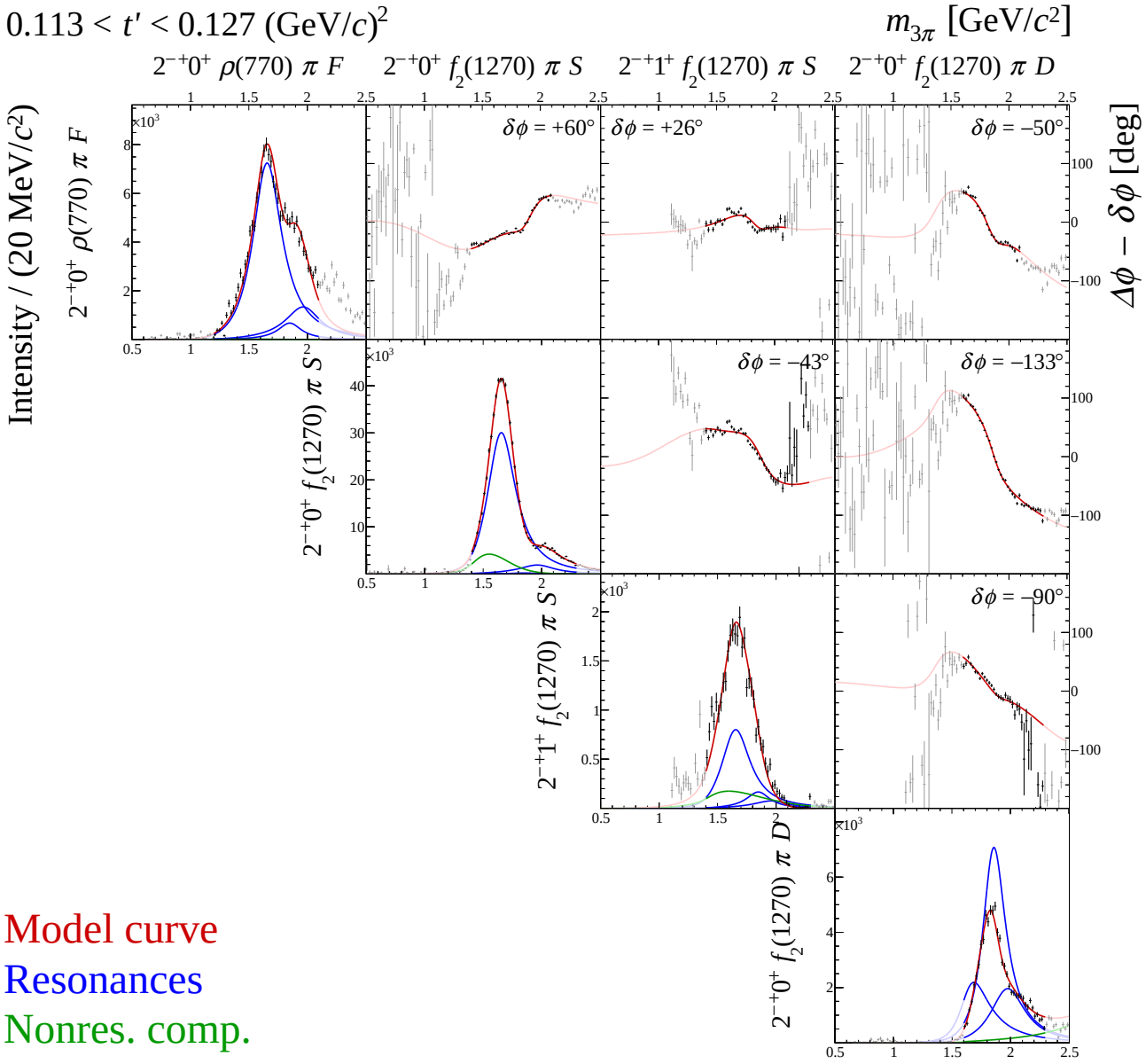

FIG. 135: Submatrix H of the 14 × 14 matrix of graphs that represents the spin-density matrix (see Table 8).

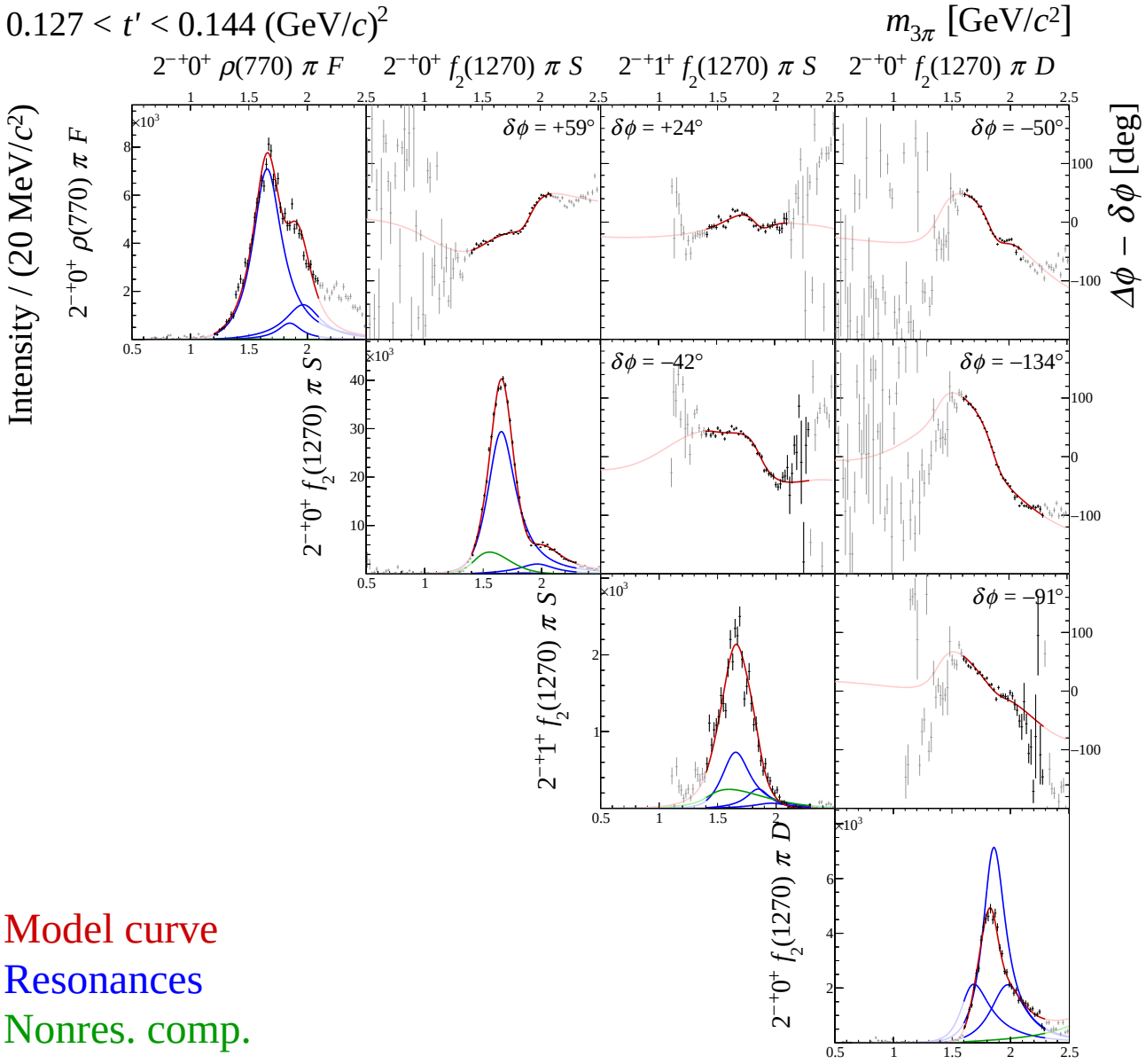

FIG. 136: Submatrix H of the 14 × 14 matrix of graphs that represents the spin-density matrix (see Table 8).

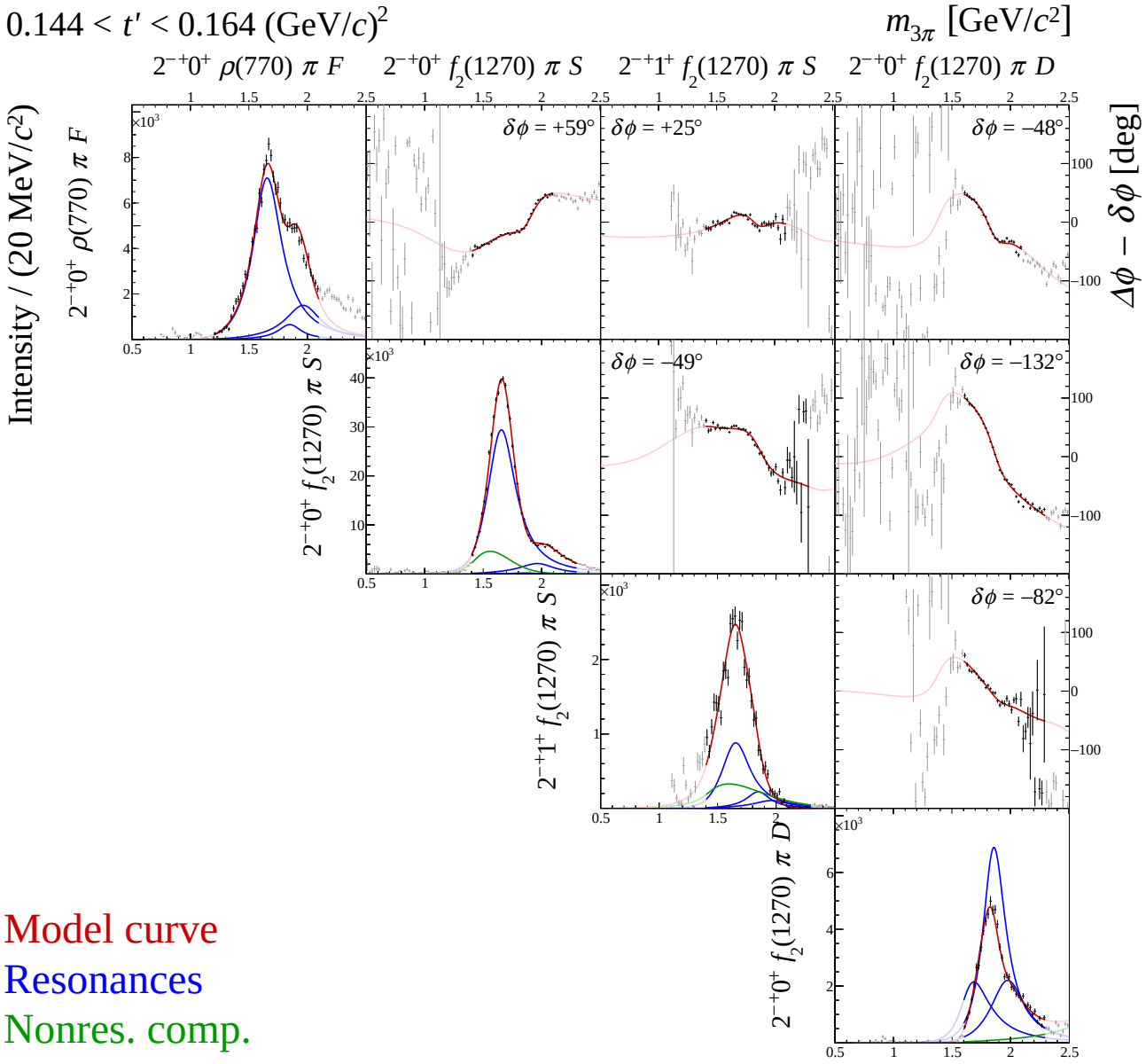

FIG. 137: Submatrix H of the 14 × 14 matrix of graphs that represents the spin-density matrix (see Table 8).

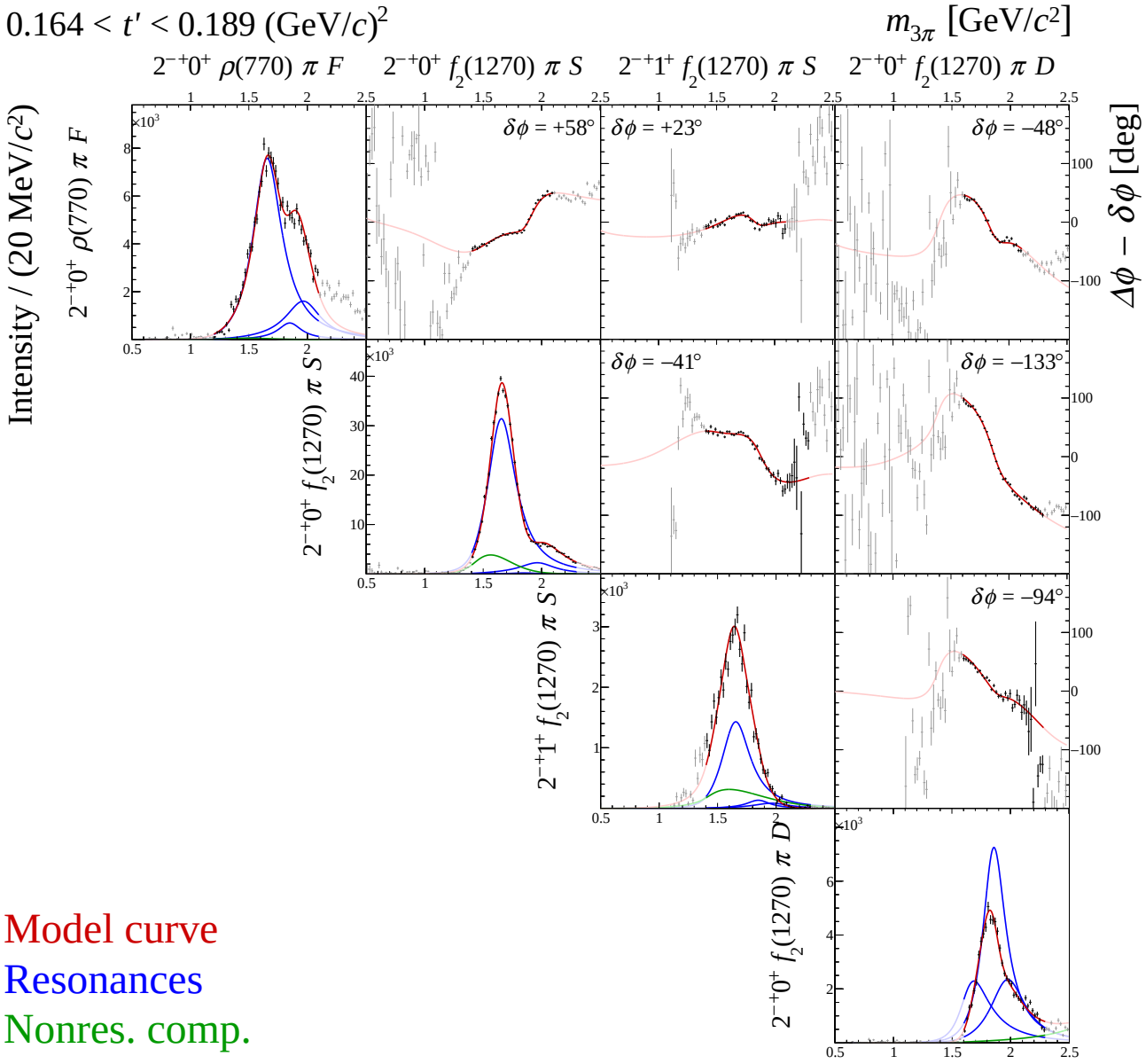

FIG. 138: Submatrix H of the 14 × 14 matrix of graphs that represents the spin-density matrix (see Table 8).

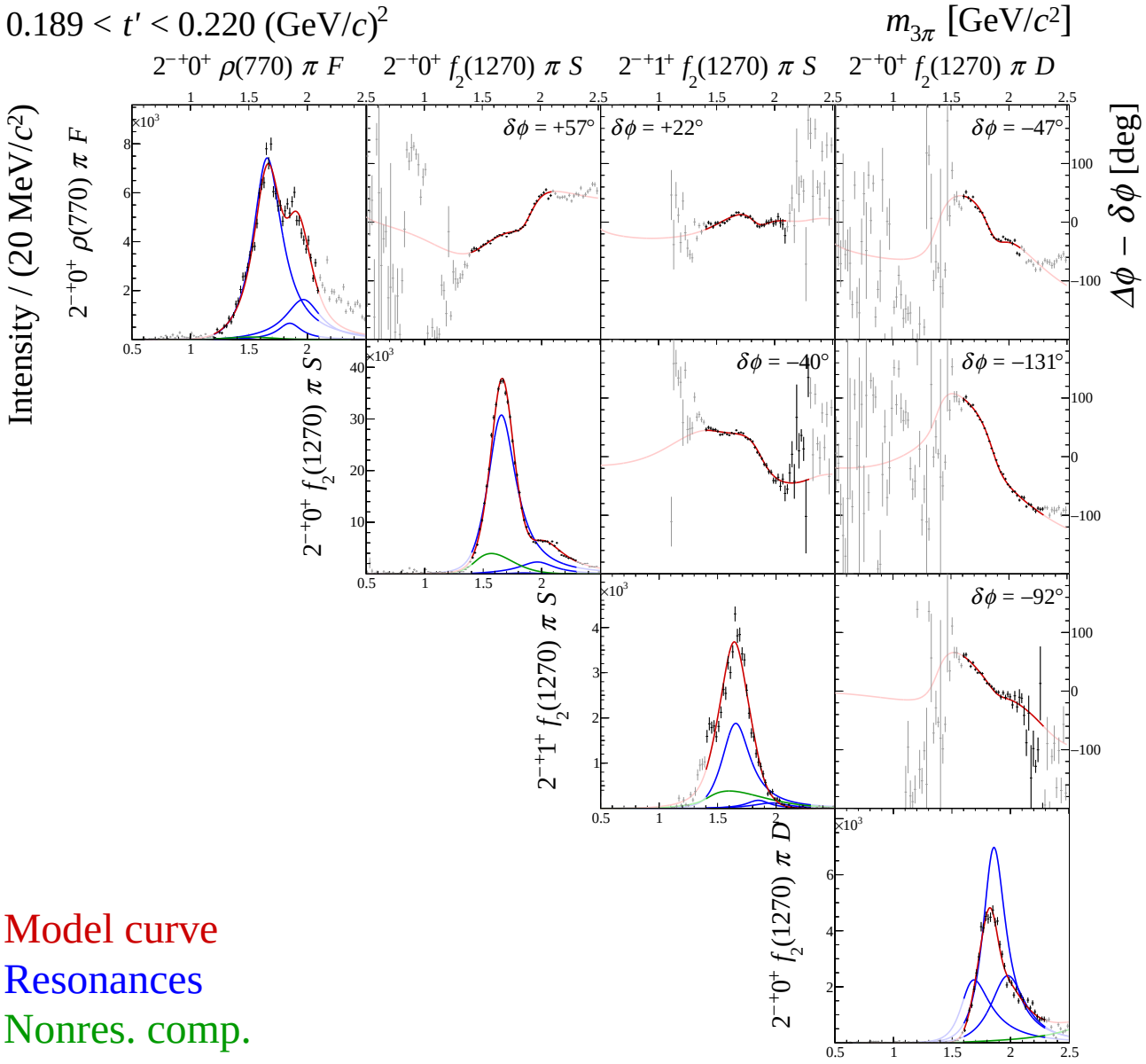

FIG. 139: Submatrix H of the 14 × 14 matrix of graphs that represents the spin-density matrix (see Table 8).

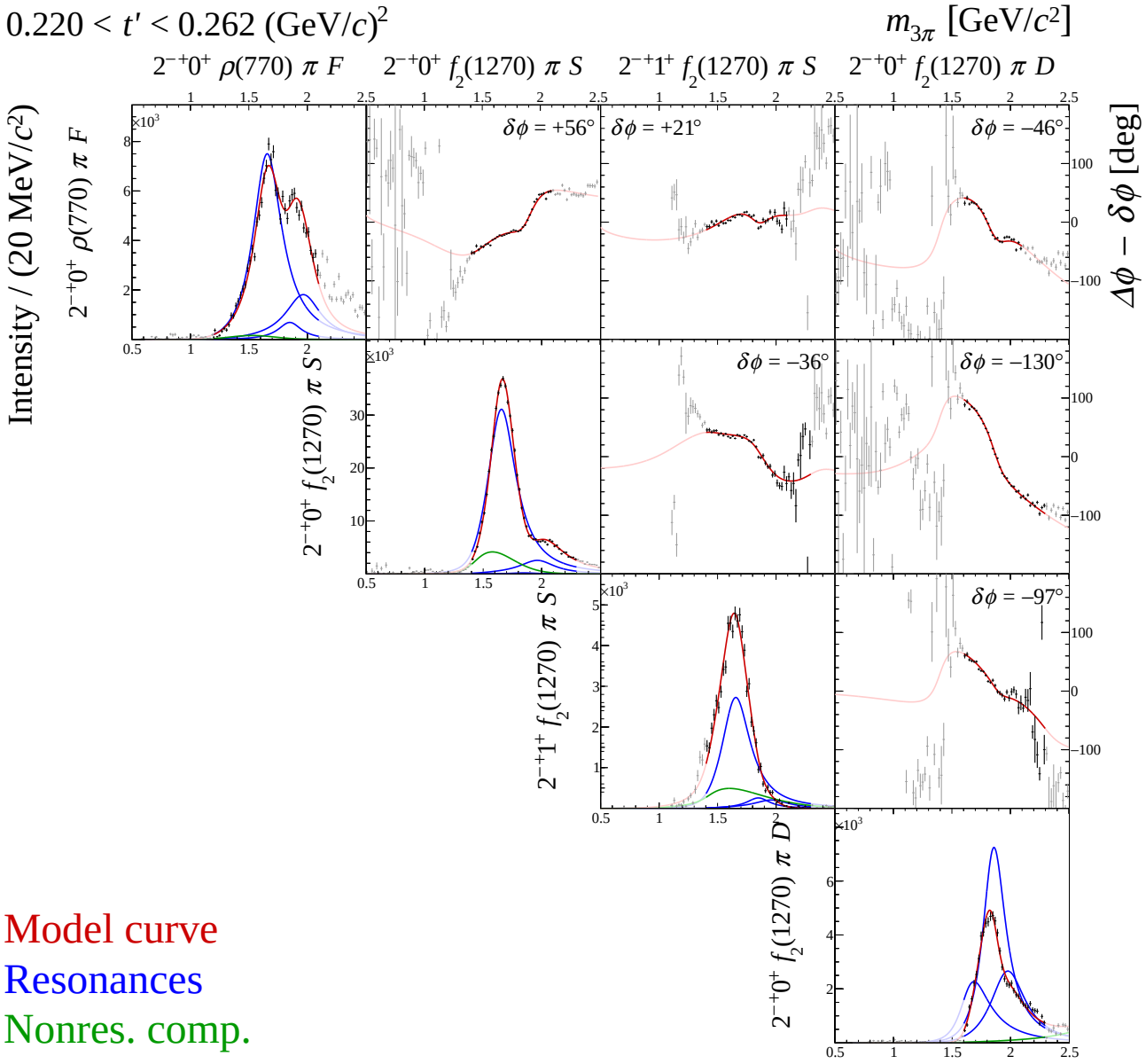

FIG. 140: Submatrix H of the 14 × 14 matrix of graphs that represents the spin-density matrix (see Table 8).

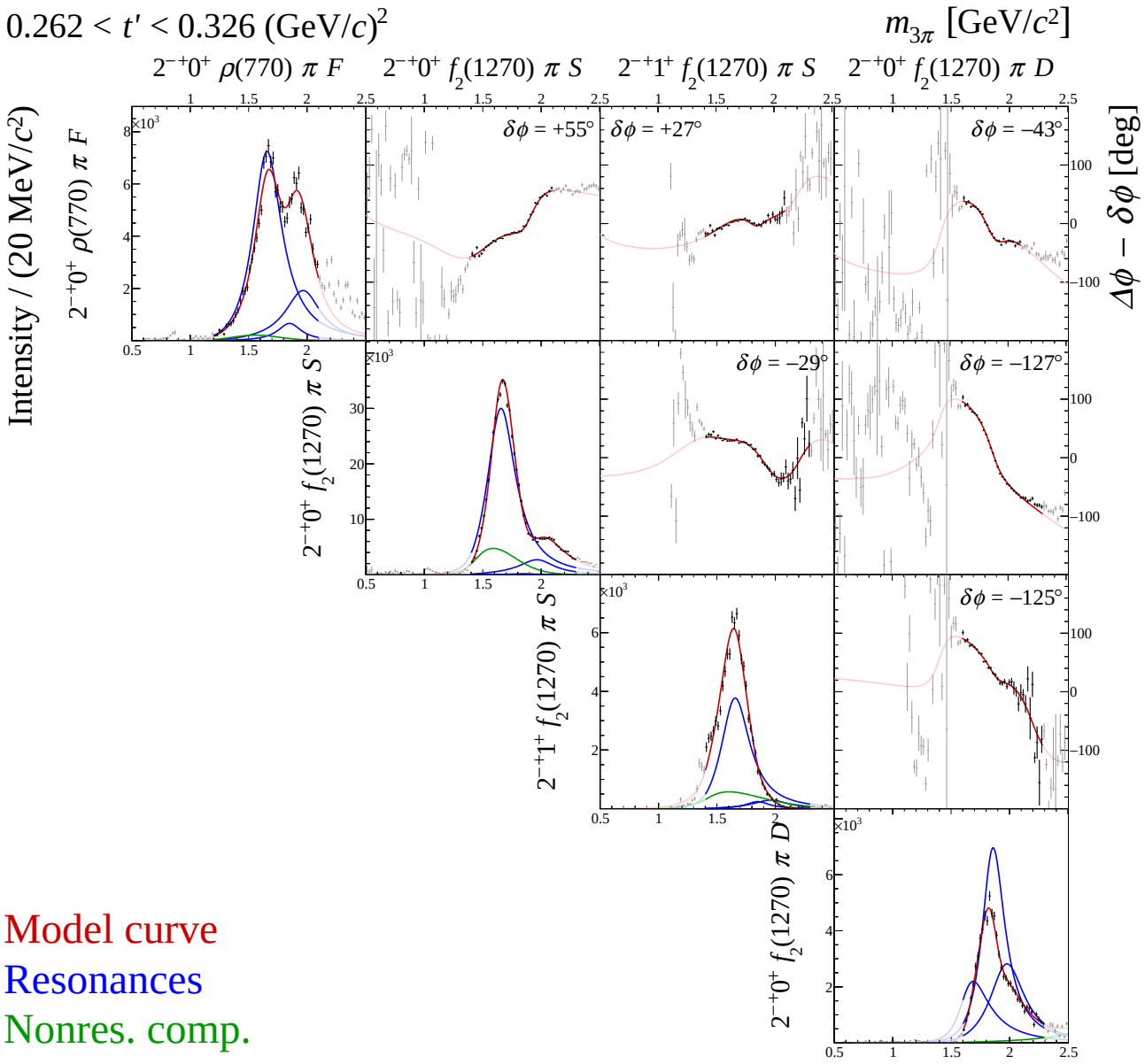

FIG. 141: Submatrix H of the 14 × 14 matrix of graphs that represents the spin-density matrix (see Table 8).

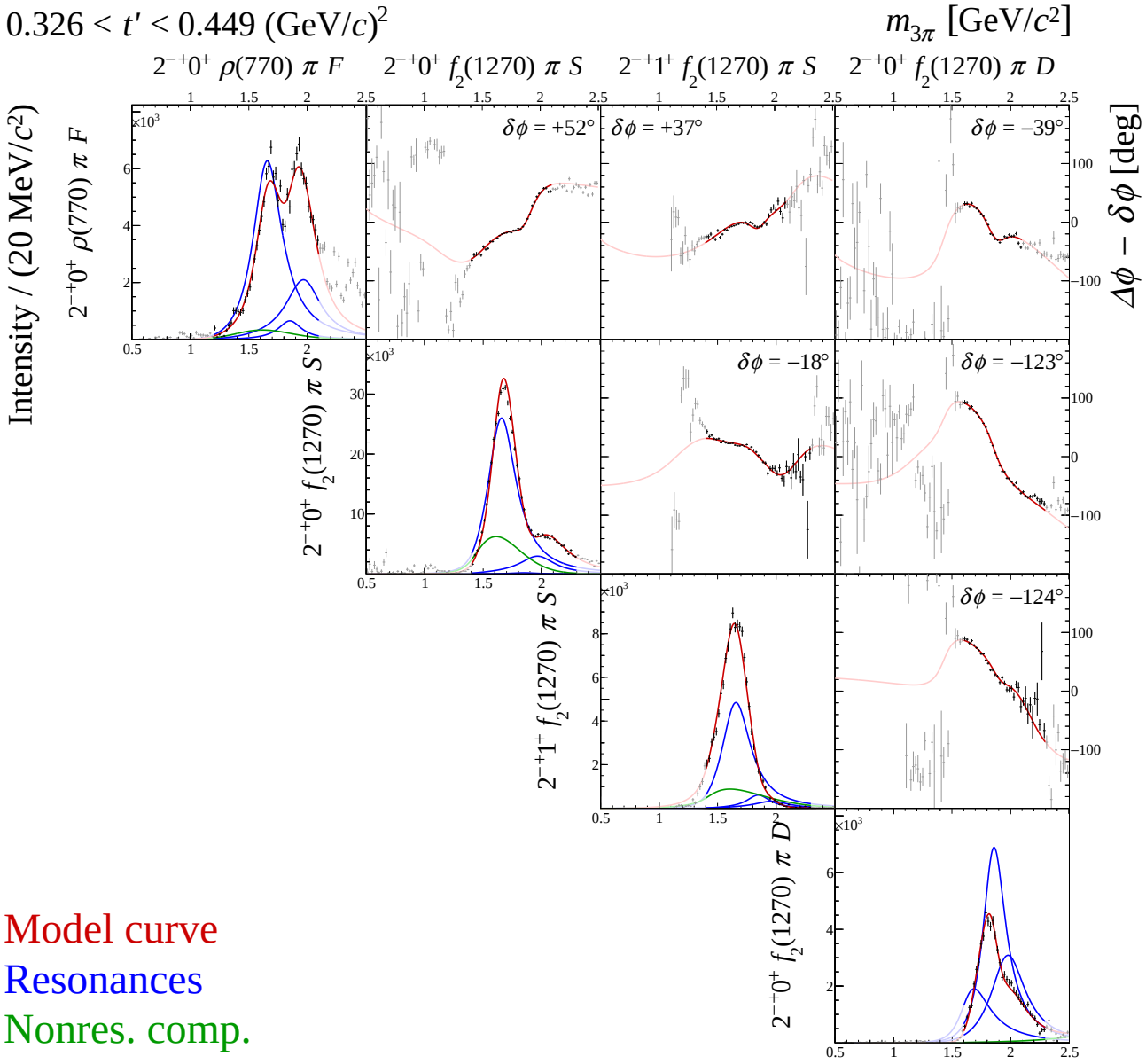

FIG. 142: Submatrix H of the 14 × 14 matrix of graphs that represents the spin-density matrix (see Table 8).

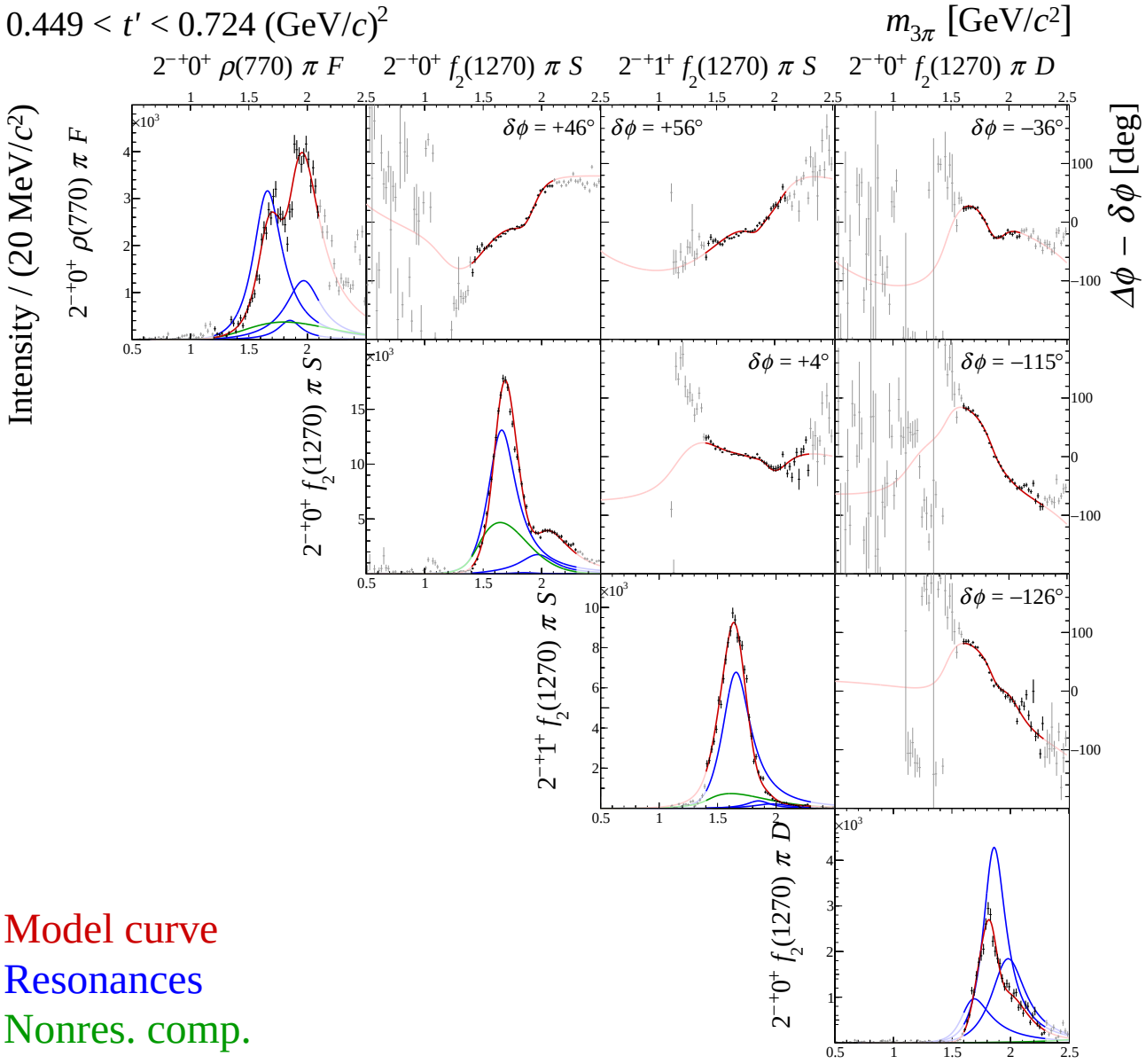

FIG. 143: Submatrix H of the 14 × 14 matrix of graphs that represents the spin-density matrix (see Table 8).

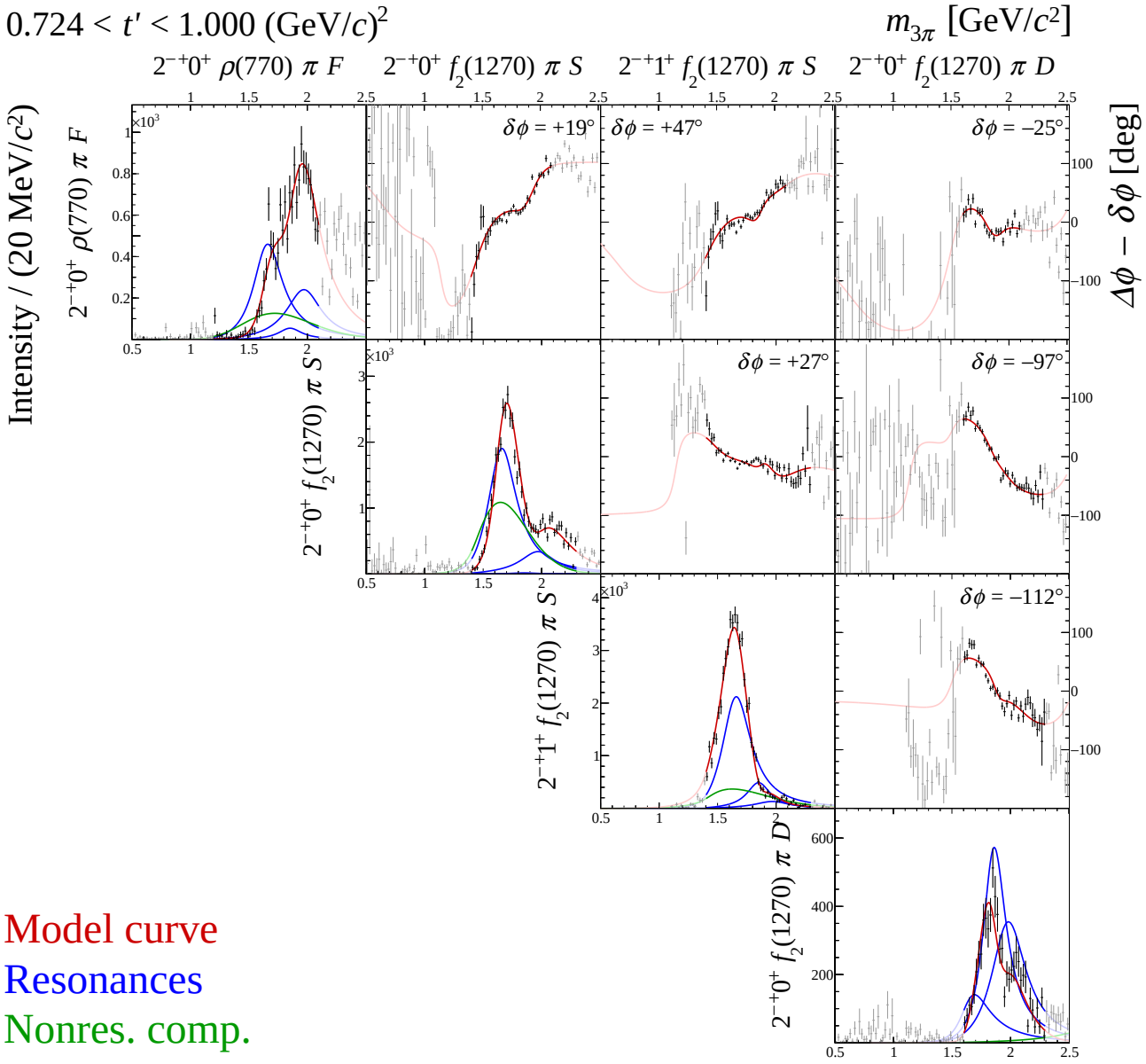

FIG. 144: Submatrix H of the 14 × 14 matrix of graphs that represents the spin-density matrix (see Table 8).

9 Submatrix I

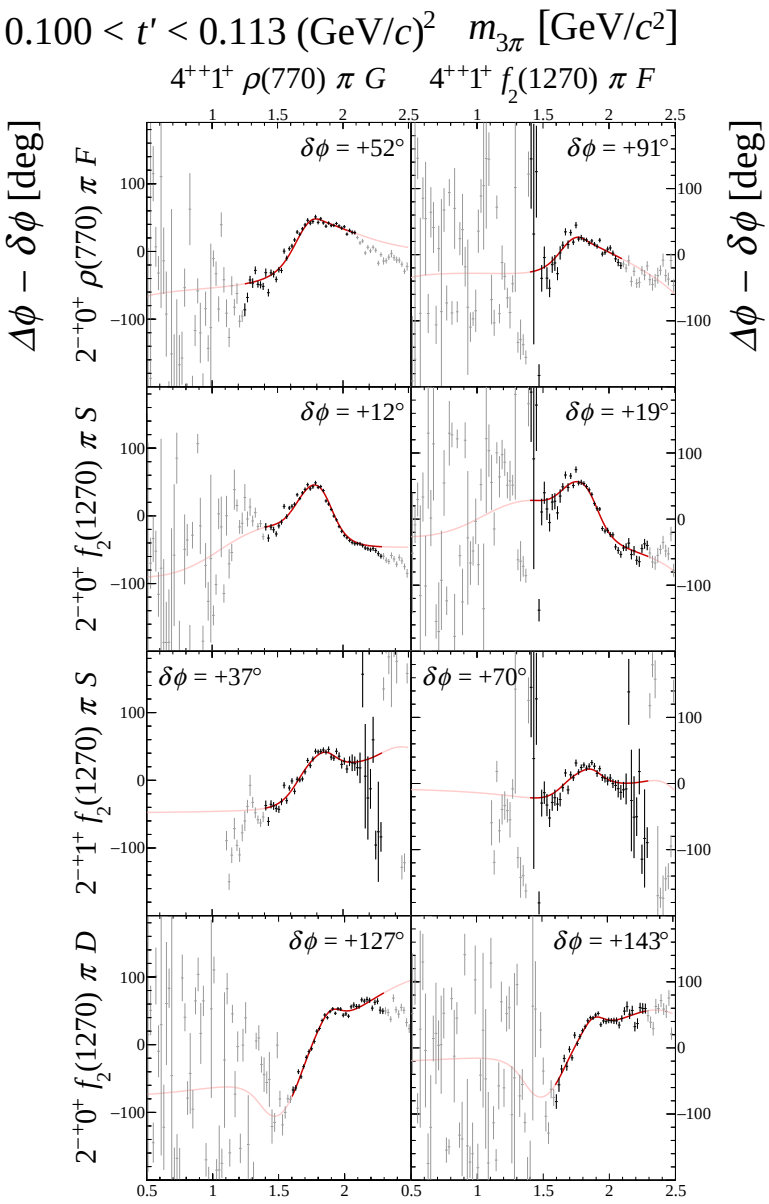

FIG. 145: Submatrix I of the 14 × 14 matrix of graphs that represents the spin-density matrix (see Table 8).

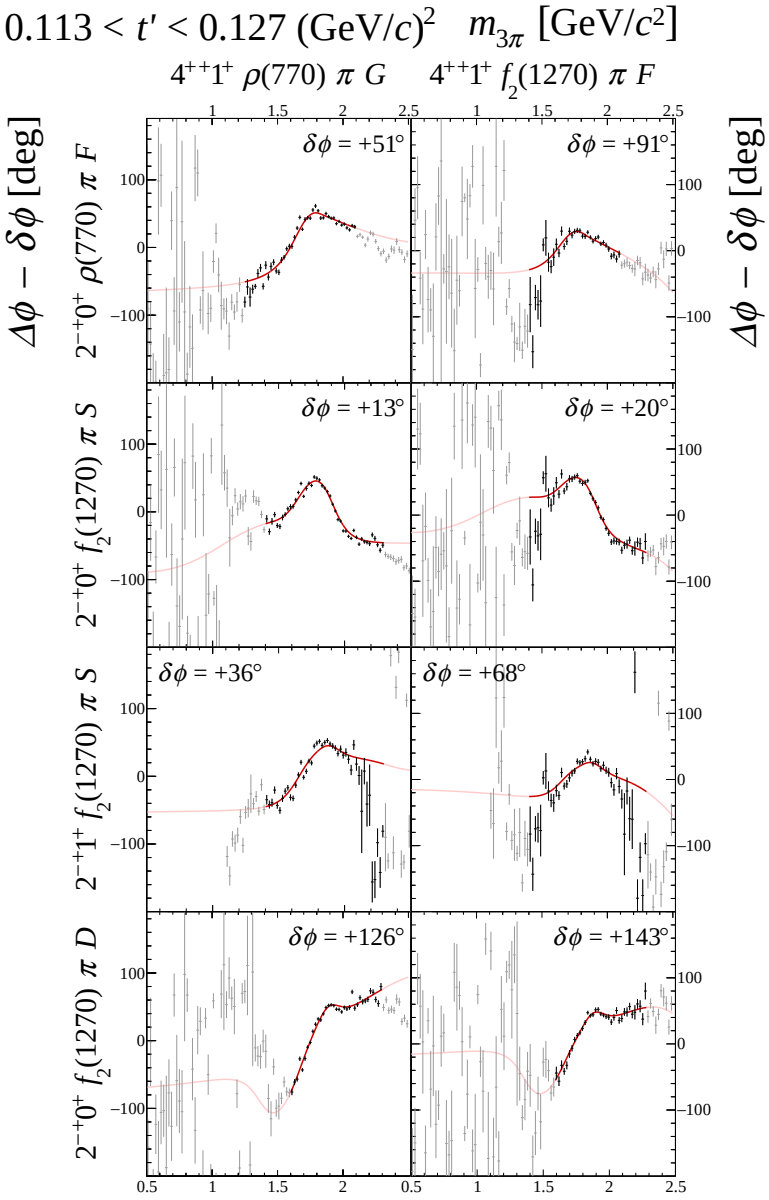

FIG. 146: Submatrix I of the 14 × 14 matrix of graphs that represents the spin-density matrix (see Table 8).

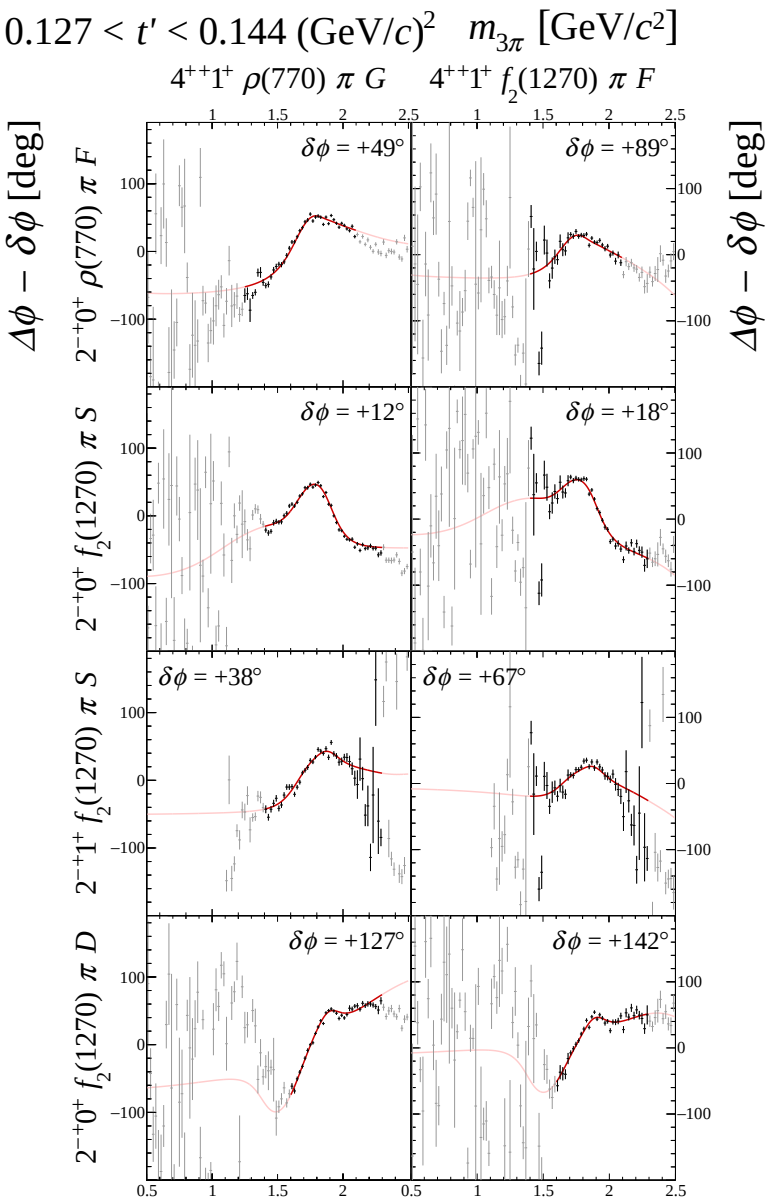

FIG. 147: Submatrix I of the 14 × 14 matrix of graphs that represents the spin-density matrix (see Table 8).

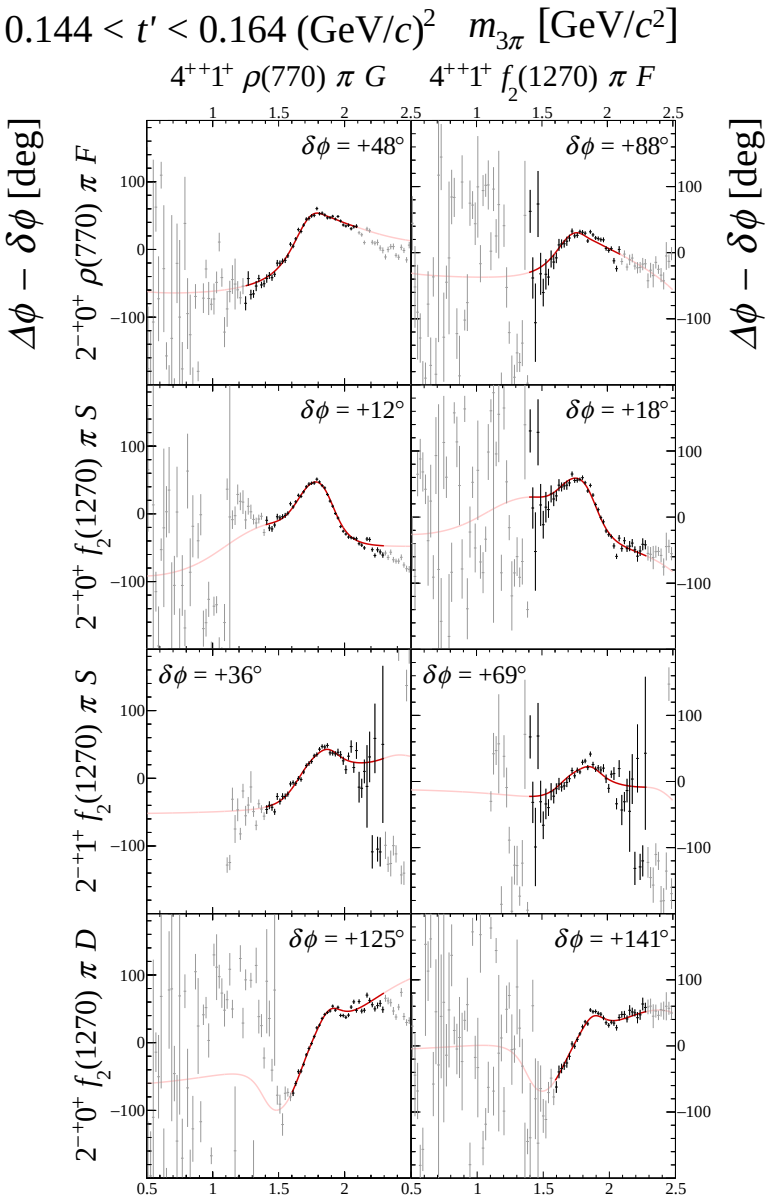

FIG. 148: Submatrix I of the 14 × 14 matrix of graphs that represents the spin-density matrix (see Table 8).

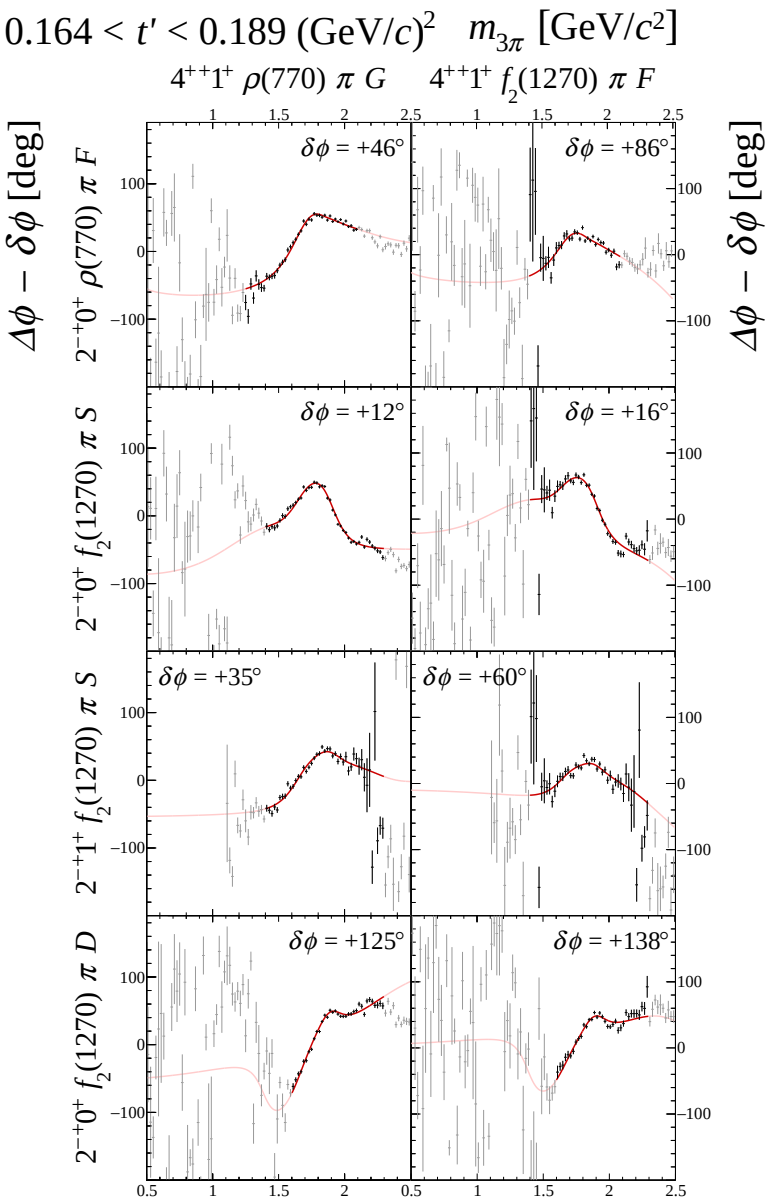

FIG. 149: Submatrix I of the 14 × 14 matrix of graphs that represents the spin-density matrix (see Table 8).

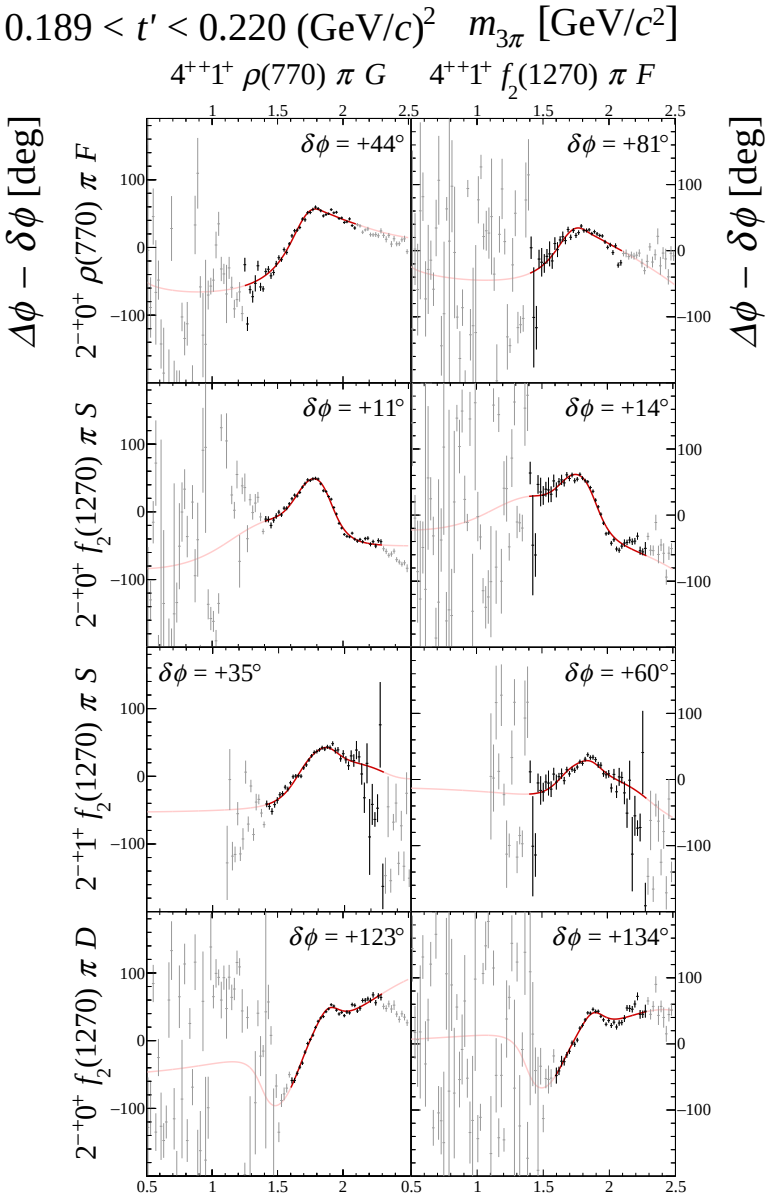

FIG. 150: Submatrix I of the 14 × 14 matrix of graphs that represents the spin-density matrix (see Table 8).

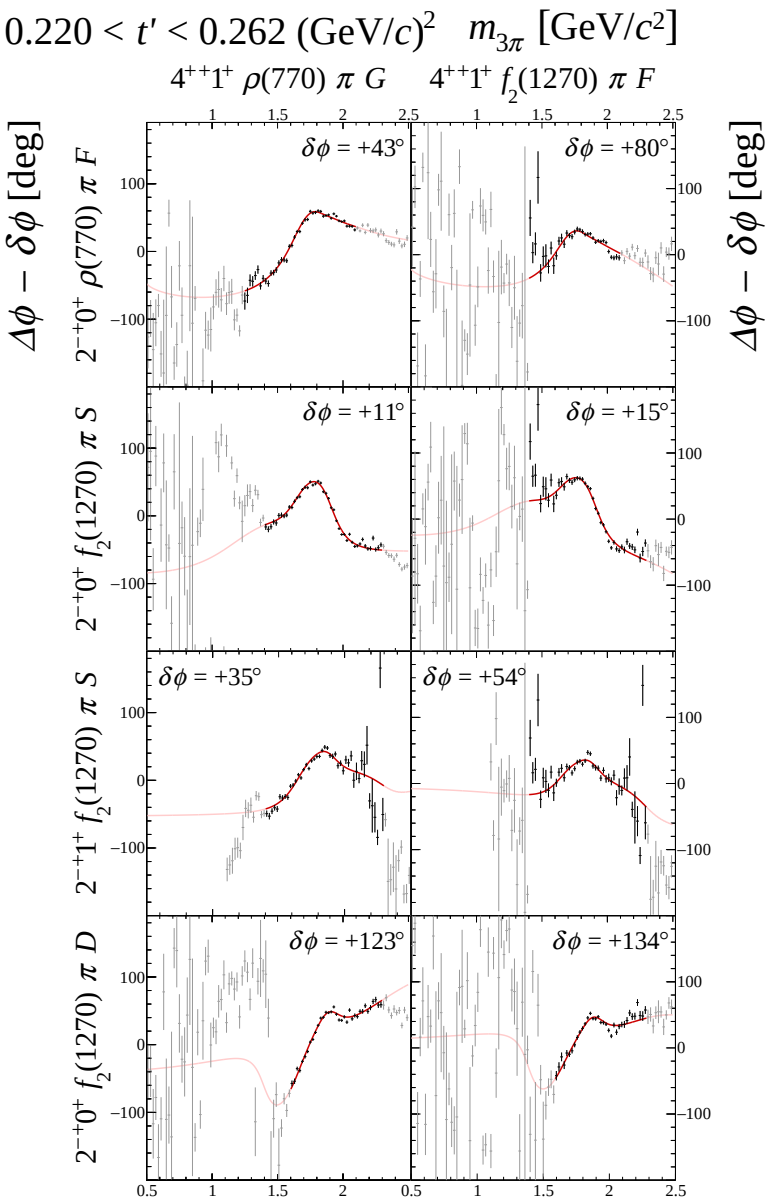

FIG. 151: Submatrix I of the 14 × 14 matrix of graphs that represents the spin-density matrix (see Table 8).

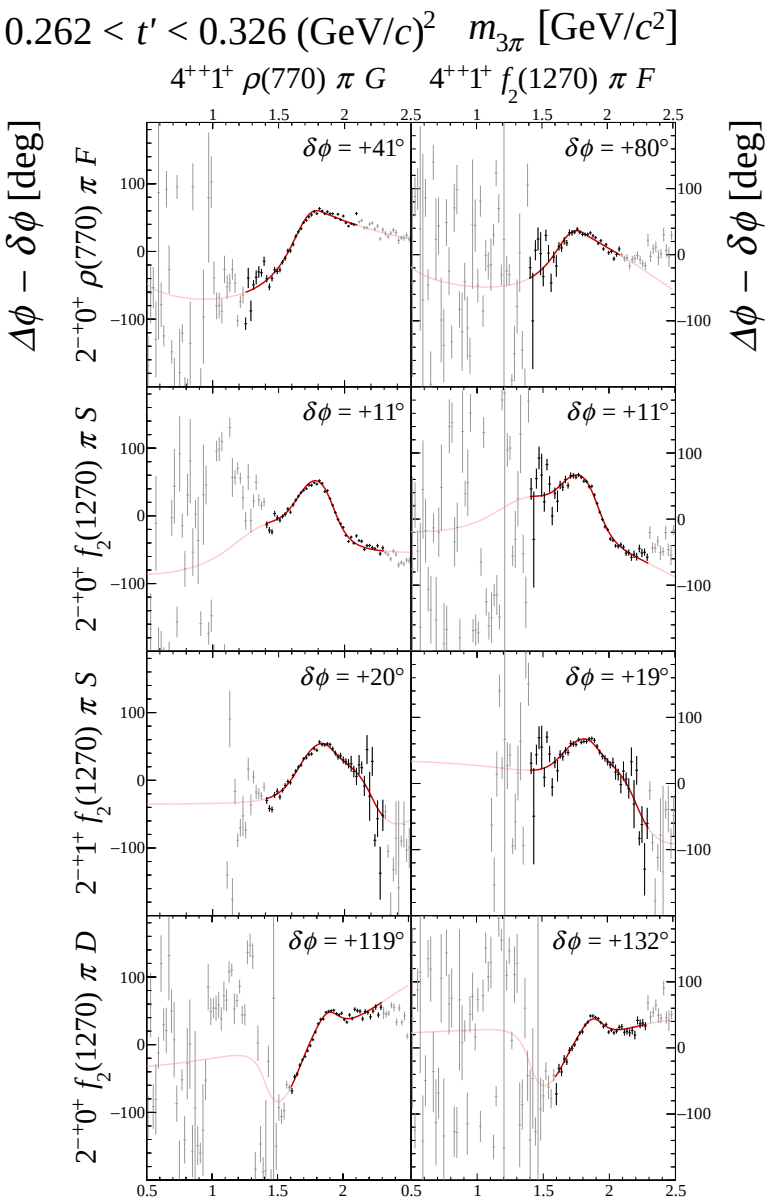

FIG. 152: Submatrix I of the 14 × 14 matrix of graphs that represents the spin-density matrix (see Table 8).

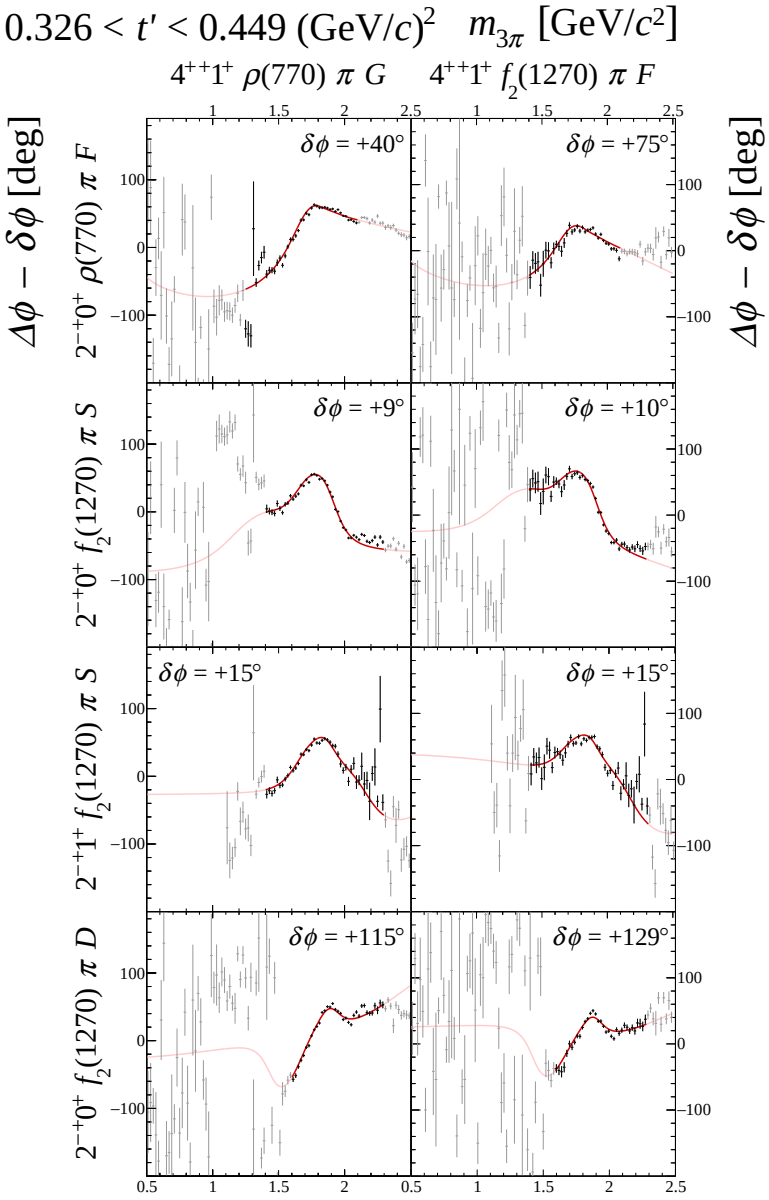

FIG. 153: Submatrix I of the 14 × 14 matrix of graphs that represents the spin-density matrix (see Table 8).

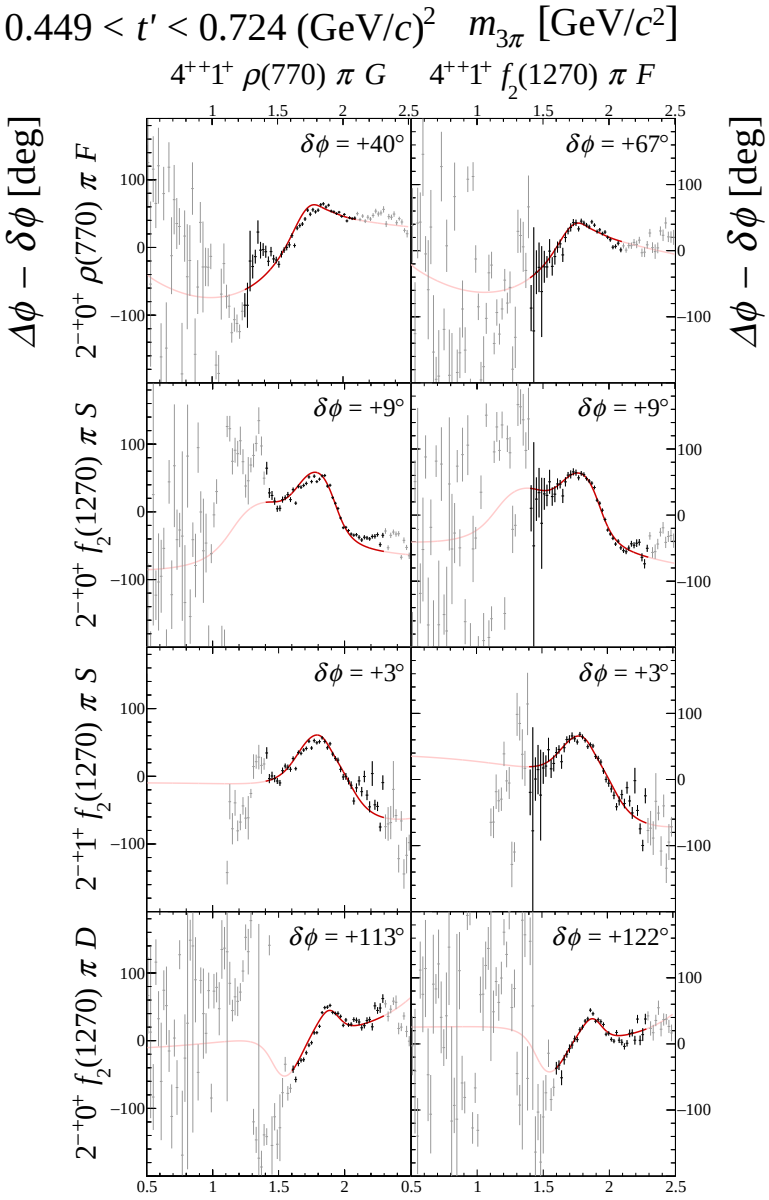

FIG. 154: Submatrix I of the 14 × 14 matrix of graphs that represents the spin-density matrix (see Table 8).

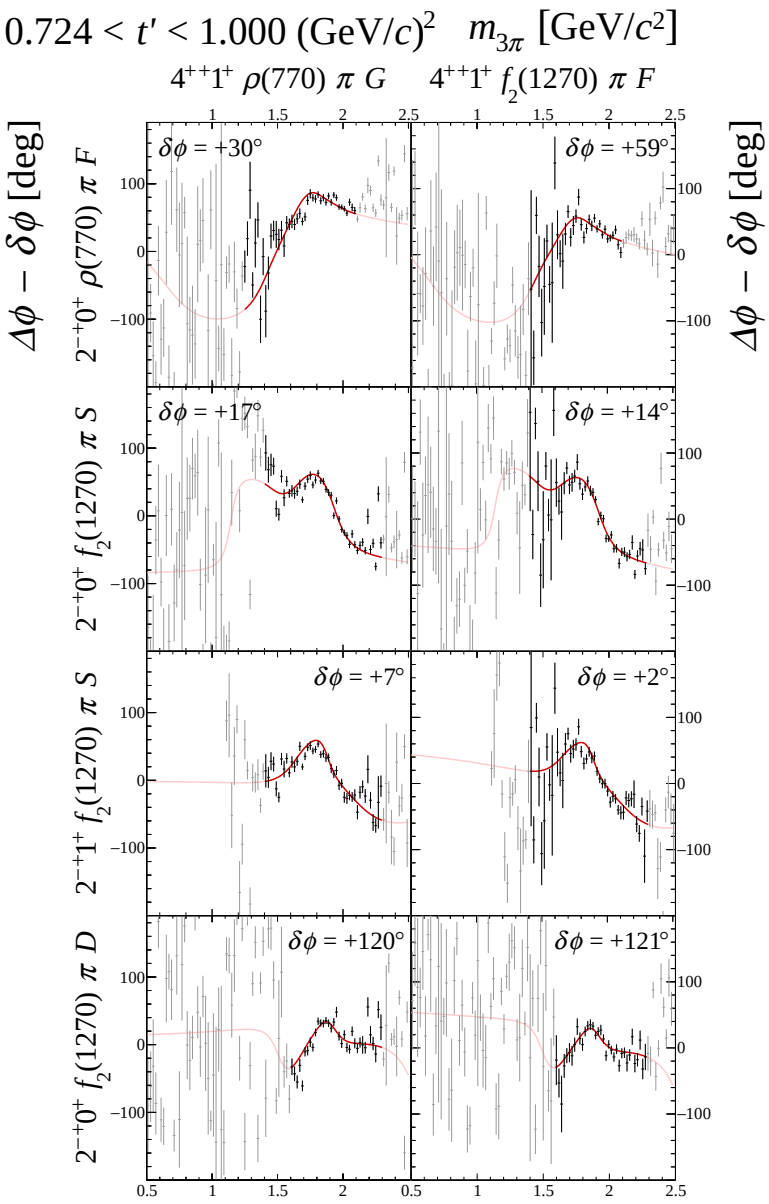

FIG. 155: Submatrix I of the 14 × 14 matrix of graphs that represents the spin-density matrix (see Table 8).

10 Submatrix J

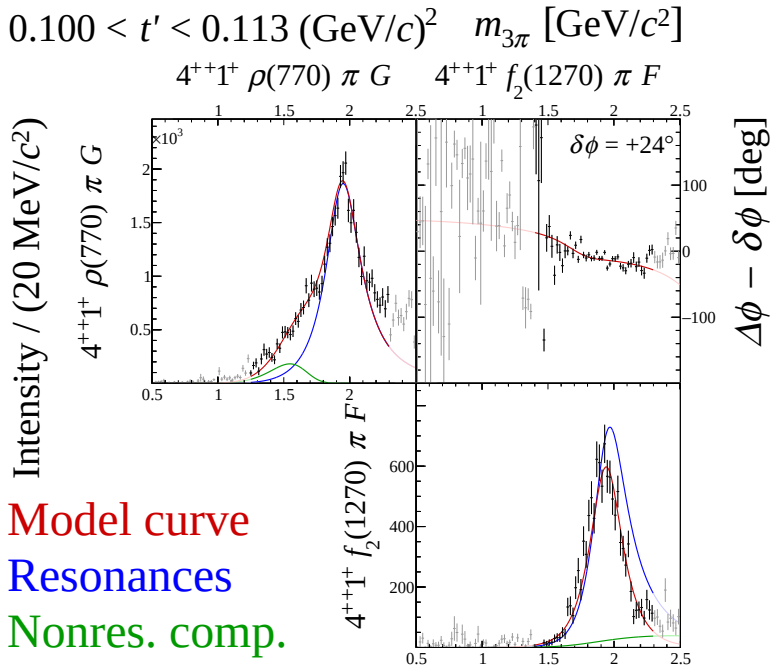

FIG. 156: Submatrix J of the 14 × 14 matrix of graphs that represents the spin-density matrix (see Table 8).

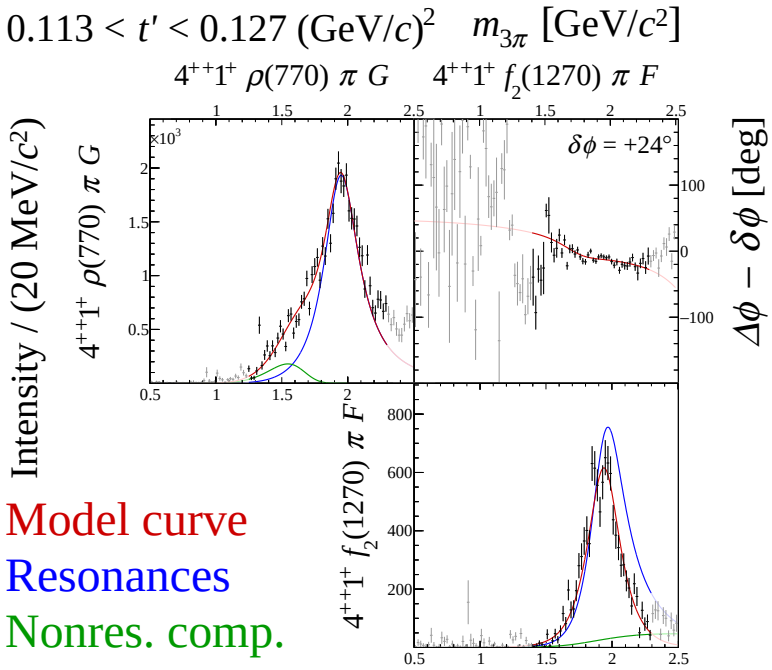

FIG. 157: Submatrix J of the 14 × 14 matrix of graphs that represents the spin-density matrix (see Table 8).

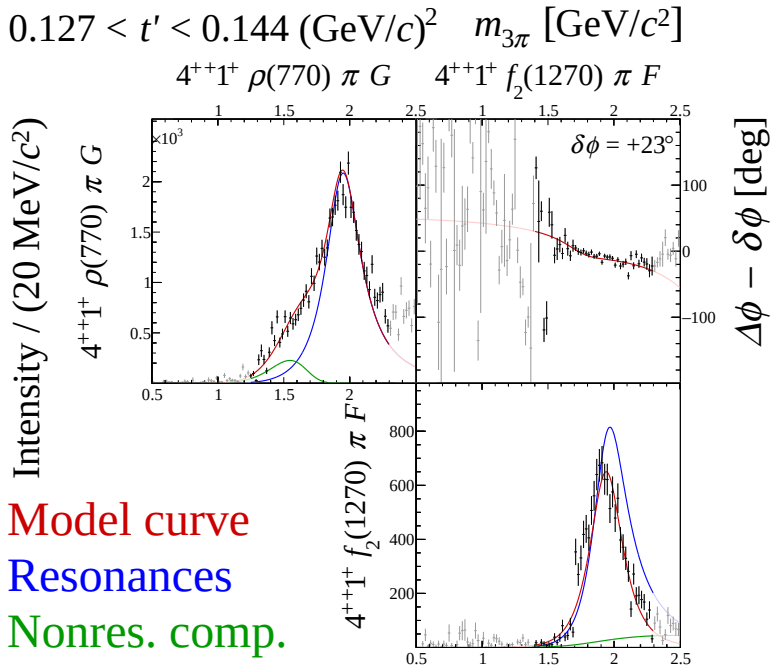

FIG. 158: Submatrix J of the 14 × 14 matrix of graphs that represents the spin-density matrix (see Table 8).

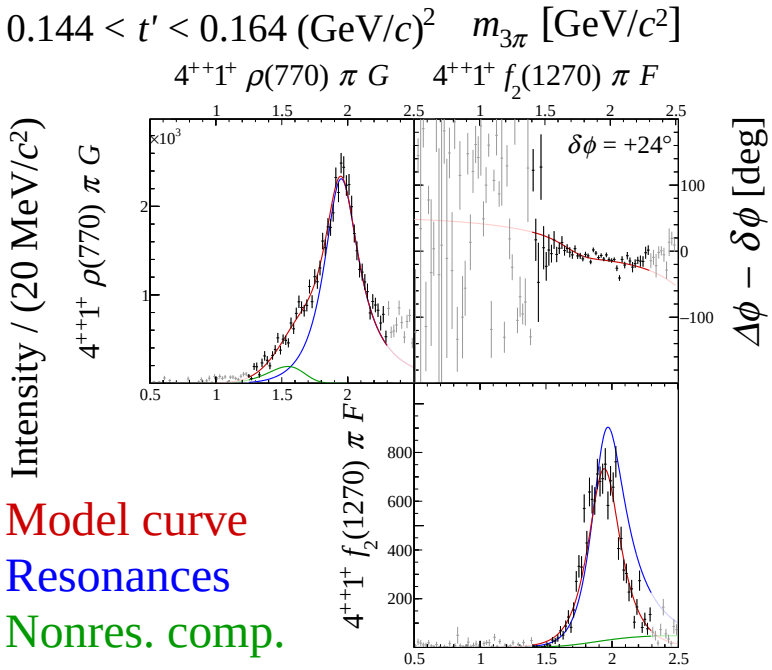

FIG. 159: Submatrix J of the 14 × 14 matrix of graphs that represents the spin-density matrix (see Table 8).

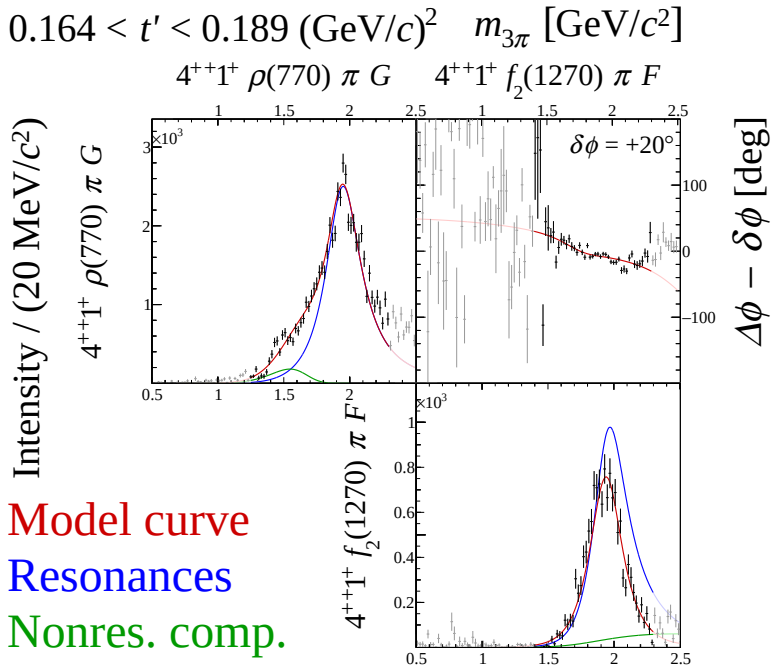

FIG. 160: Submatrix J of the 14 × 14 matrix of graphs that represents the spin-density matrix (see Table 8).

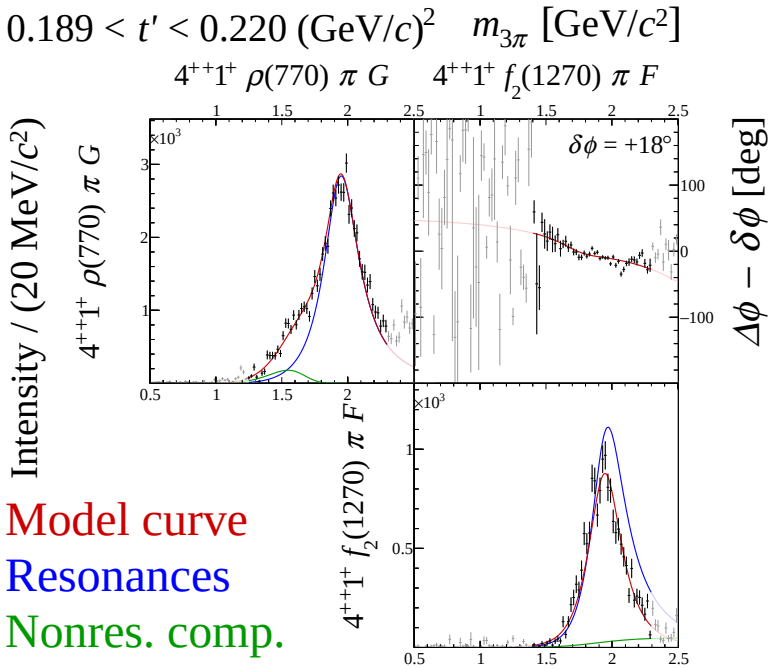

FIG. 161: Submatrix J of the 14 × 14 matrix of graphs that represents the spin-density matrix (see Table 8).

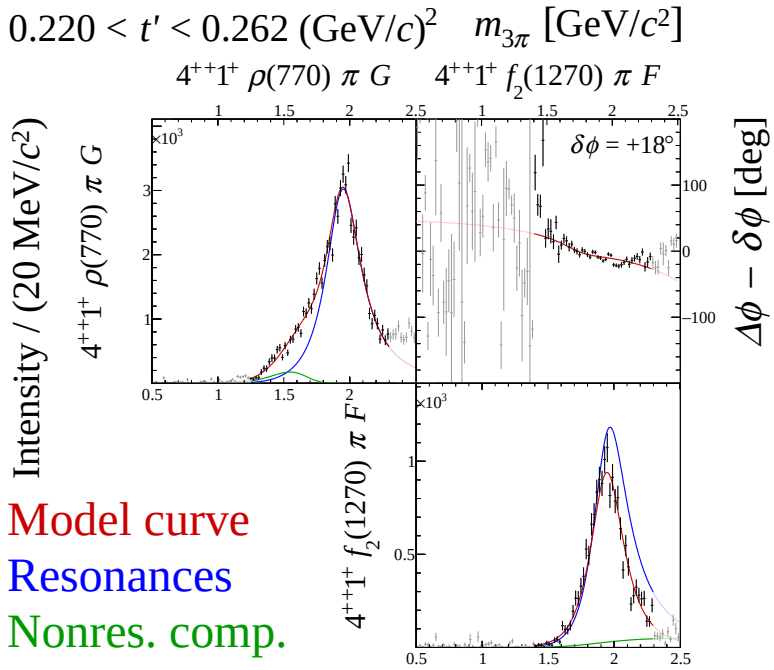

FIG. 162: Submatrix J of the 14 × 14 matrix of graphs that represents the spin-density matrix (see Table 8).

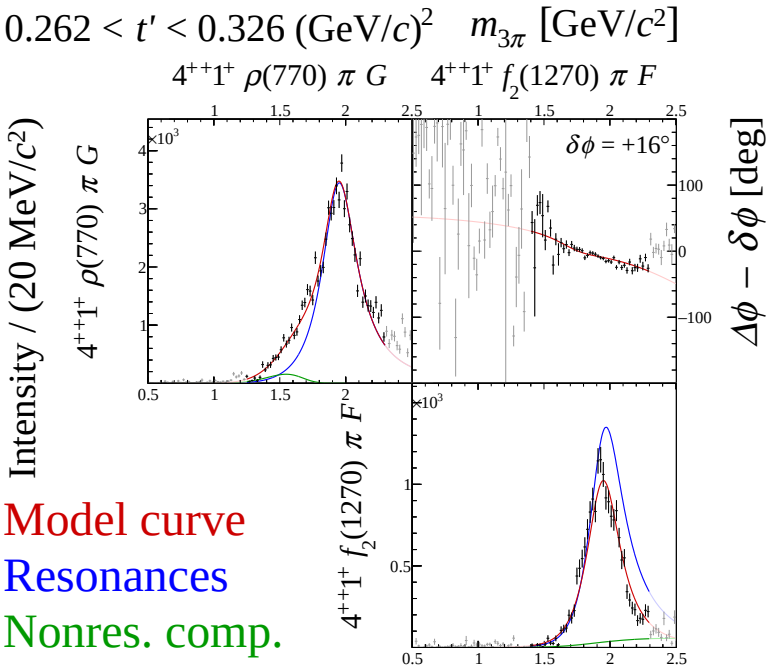

FIG. 163: Submatrix J of the 14 × 14 matrix of graphs that represents the spin-density matrix (see Table 8).

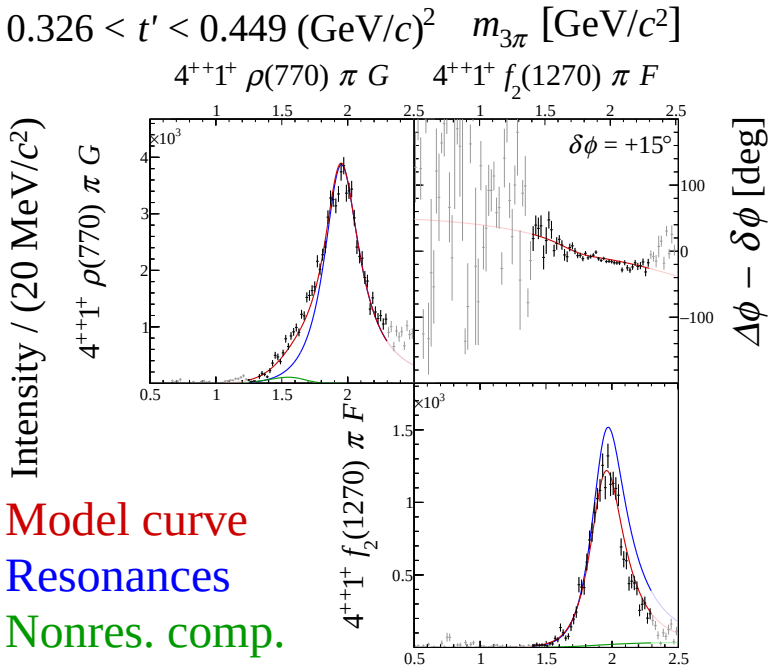

FIG. 164: Submatrix J of the 14 × 14 matrix of graphs that represents the spin-density matrix (see Table 8).

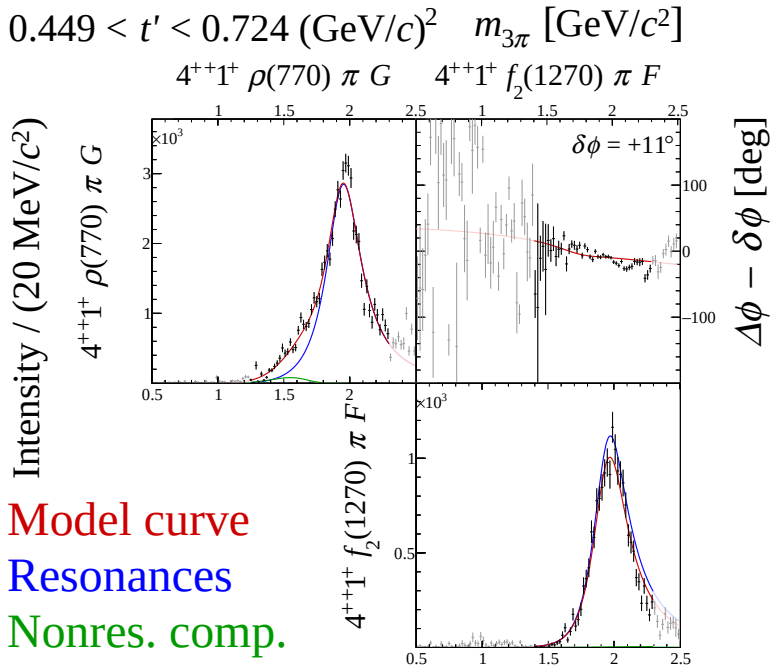

FIG. 165: Submatrix J of the 14 × 14 matrix of graphs that represents the spin-density matrix (see Table 8).

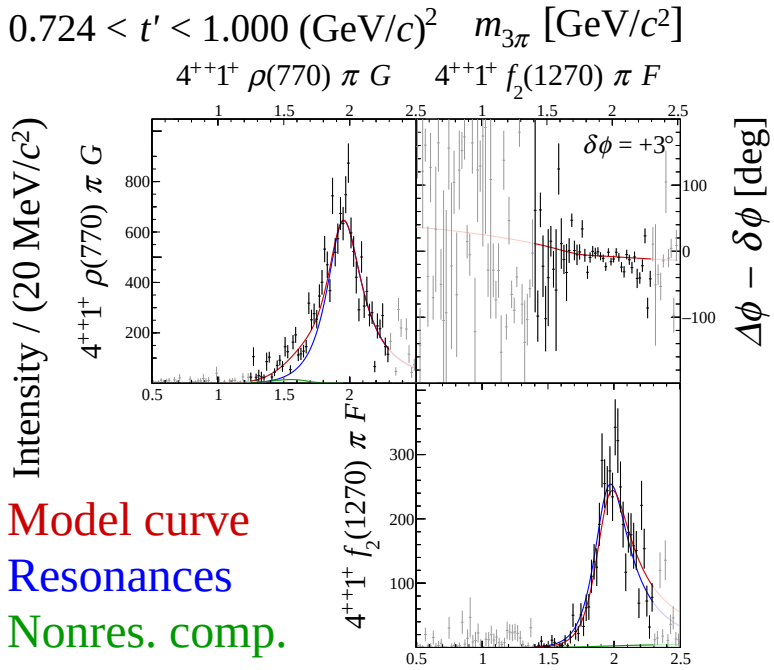

FIG. 166: Submatrix J of the 14 × 14 matrix of graphs that represents the spin-density matrix (see Table 8).

F Decay phase-space integrals for partial waves

Figures 167 to 172 show for each of the 14 waves in the resonance-model fit the $m_{3\pi}$ dependence of the phase-space integrals I_{aa} as defined in Eq. (6). The phase-space integrals are normalized to their maximum value in the shown mass range $0.5 < m_{3\pi} < 2.5\,\mathrm{GeV}/c^2$.

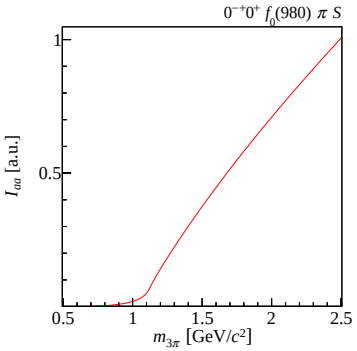

FIG. 167: Phase-space integral I_{aa} for the $0^{-+}0^{+}f_0(980)\pi S$ wave in arbitrary units as a function of $m_{3\pi}$ [see Eq. (6)].

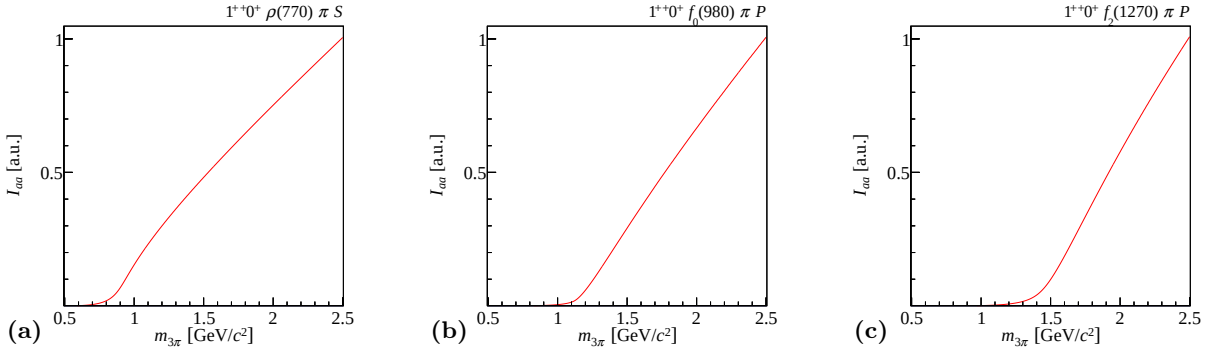

FIG. 168: Phase-space integrals I_{aa} for (a) the $1^{++}0^{+}\rho(770)\pi S$, (b) the $1^{++}0^{+}f_0(980)\pi P$, and (b) the $1^{++}0^{+}f_2(1270)\pi P$ wave in arbitrary units as a function of $m_{3\pi}$ [see Eq. (6)].

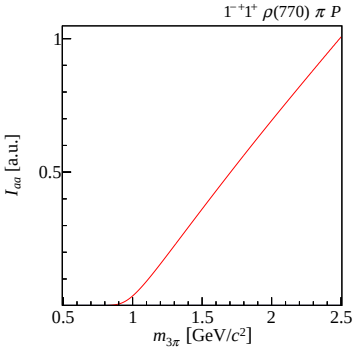

FIG. 169: Phase-space integral I_{aa} for the $1^{-+}1^{+}\rho(770)\pi P$ wave in arbitrary units as a function of $m_{3\pi}$ [see Eq. (6)].

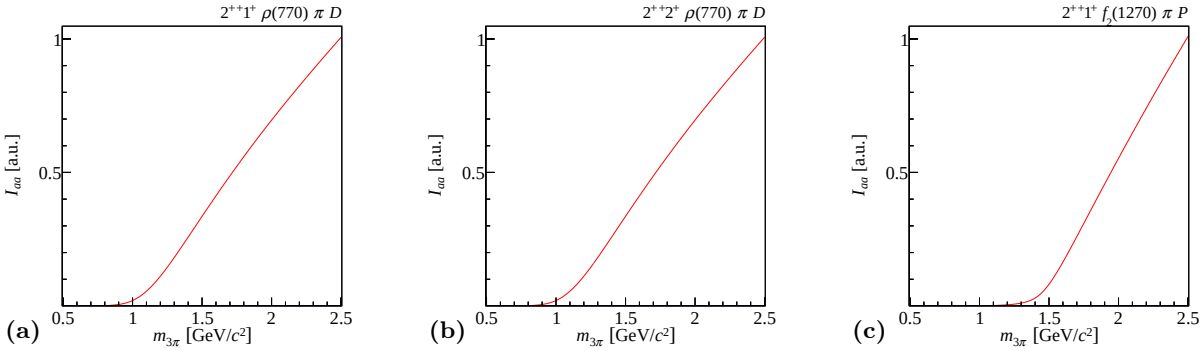

FIG. 170: Phase-space integrals I_{aa} for (a) the $2^{++}1^{+}\rho(770)\pi D$, (b) the $2^{++}2^{+}\rho(770)\pi D$, and (c) the $2^{++}1^{+}f_2(1270)\pi P$ wave in arbitrary units as a function of $m_{3\pi}$ [see Eq. (6)].

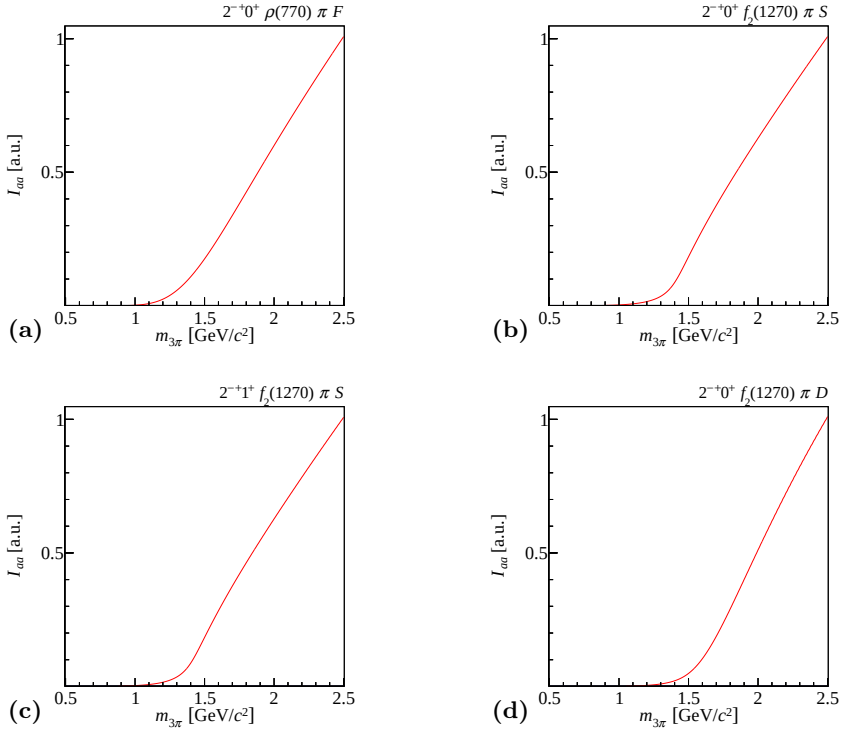

FIG. 171: Phase-space integrals I_{aa} for (a) the $2^{-+}0^{+}\rho(770)\pi F$, (b) the $2^{-+}0^{+}f_2(1270)\pi S$, (c) the $2^{-+}1^{+}f_2(1270)\pi S$, and (d) the $2^{-+}0^{+}f_2(1270)\pi D$ wave in arbitrary units as a function of $m_{3\pi}$ [see Eq. (6)].

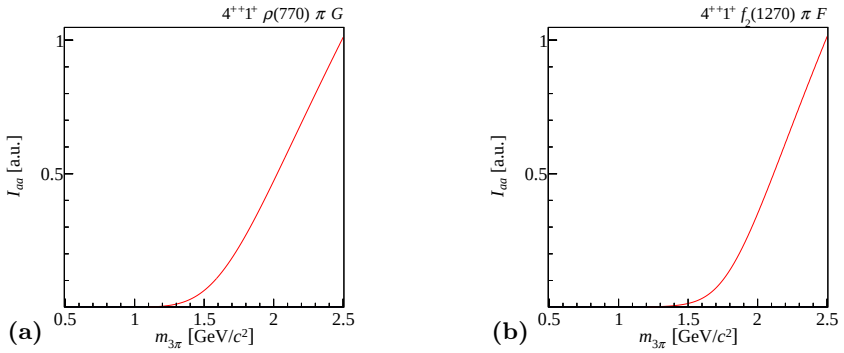

FIG. 172: Phase-space integrals I_{aa} for (a) the $4^{++}1^{+}\rho(770)\pi G$ and (b) the $4^{++}1^{+}f_2(1270)\pi F$ wave in arbitrary units as a function of $m_{3\pi}$ [see Eq. (6)].